An Infrared-Radio Study of Galaxies at High Redshift

Ariadna Manilla Robles

Supervisors: Dr. Chris Gordon
Dr. Eelco van Kampen

Department of Physics and Astronomy
University of Canterbury

This dissertation is submitted for the degree of
Doctor of Philosophy in Astronomy

August 2018

Collaborators

Dr. Loretta Dunne
School of Physics and Astronomy, Cardiff University
Institute for Astronomy, The University of Edinburgh

Dr. Steve Maddox
School of Physics and Astronomy, Cardiff University
Institute for Astronomy, The University of Edinburgh

Prof. Dr. Rob Ivison
European Southern Observatory
Institute for Astronomy, The University of Edinburgh

Dr. Ivan Oteo
Institute for Astronomy, The University of Edinburgh
European Southern Observatory

Members of the examination committee

Prof. Dr. Andrew Hopkins
Head of Research and Outreach, Australian Astronomical Observatory

Prof. Dr. Matt Jarvis
Astrophysics, University of Oxford
Physics and Astronomy Department, University of the Western Cape

"We are alive. We are intelligent. We must know."
Stephen Hawking (1942 - 2018)

To those who put stones in my path.
You did not make me fall.

Acknowledgements

I would like to express my gratitude to all the supervisors who have been involved in this thesis in one way or another. I am particularly grateful for the opportunity to start this journey. To the University of Canterbury I am grateful for its support during my time in New Zealand and in Germany.

Thanks to Jamie Stevens and Zhi-Yu Zhang for their advice with the radio observations and data reduction for ATCA and the VLA. To Ian Heywood for the HFF-VLA catalogues and Matt Jarvis for sharing his data. I would also like to thank Juan Gutiérrez Larraínzar for making some of the plots in Chapter 2.

A big thanks to Ivan Oteo for his help during my time at ESO, for reading my proposals, reports and full thesis and giving me comments that have greatly improved the manuscript. I am very grateful to Ivan as well for helping me with advice and intermediating when things were complicated during the last two years of this thesis. An unpayable debt of gratitude to Pieter De Vis for helping with the MC simulation, for the interesting and long discussions, for reading my proposals, reports and full thesis with extraordinary detail which resulted in a much better version of my thesis.

To my friends and flatmates in New Zealand I really appreciate you make me feel at home even being so far away from it. Special thanks to Nezihe and Braden for the wine and cheese, the dancing and hours of intense and interesting chatting. To Christopher, Edward, Sanjay, Alister, Katrin, Emily and Doug for making the office a great place to work everyday. To my friends from Spain Laura, Maribel, Mirian and Pedro thank you for encourage me from the distance during both the easy and the hard times of this thesis.

Nothing of this would have been possible without the great sacrifices my parents did for me to have the best educations I could have. A big part of this thesis belongs to them. Thanks to my mum for always doing her best for my wellbeing and happiness. Thanks to my dad for teaching me to have critical thinking and be brave in my decisions. I wish I could share this moment with you. To my brother I am grateful for encouraging me during the last part while writing the manuscript when the tiredness and stress was more present, and to my aunt Rosa for sending me funny emoticons from time to time just to let me know that I am in her memories even from distance.

And finally I must thank Pieter for absolutely everything. For never stopping to believe that this was possible, for being patient when I had no patience left, for just being there for me all the time without hesitating no matter what. There are not enough words to explain that I am certain that without you this thesis would have never become a success. We did it!

Table of contents

Abstract

In this thesis we use infrared and radio observations to characterise a sample of high-redshift dusty star-forming galaxies (DSFGs) selected from the *Herschel*-ATLAS (H-ATLAS) survey and the Hubble Frontier Fields (HFF). The thesis is divided into three main projects.

In the first study, we use ATCA observations at 3 and 7 mm to pinpoint the location and measure the redshift of two bright H-ATLAS DSFGs, selected because of their red colour in the SPIRE bands ($S_{250} < S_{350} < S_{500}$ and $S_{500} > 100$ mJy). We obtain, via detection of $^{12}CO(2-1)$ emission, that the spectroscopic redshift of both sources is $z \sim 3.8$. Furthermore, near-IR observations taken with GEMINI-South suggest that both DSFGs are lensed, with magnification factors $\mu \sim 3.2$ for both DSFGs. After correcting for magnification, they have high star-formation rates $\sim 2{,}400$ $M_{\odot}yr^{-1}$ and infrared luminosities $\sim 10^{13}$ $L_{\odot}$ consistent with ultra luminous infrared galaxies. With very rapid depletion times of a few Myears and CO linewidths of ~ 800 $km\,s^{-1}$, these DSFGs are consistent with merger events, and they are likely progenitors of two massive elliptical-like galaxies at $z \sim 2-3$.

Our second project aims to classify a sample of relatively faint ($S_{500} > 29$ mJy) H-ATLAS sources in terms of whether they are lensed or not via 1 arcsec resolution VLA radio continuum observations at 6 GHz. The sample is formed by all 123 H-ATLAS sources with $1.5 < z_{phot} < 2.5$ which could be efficiently observed with the VLA because they could share calibrators. We find 7% strongly gravitationally lensed galaxies, 18% potential lensed sources, 30% star-forming galaxies, 8% AGNs and 36% groups or clusters galaxies which become part of a sub-sample of proto-clusters candidates. In addition, a study of the infrared-to-radio correlation (IRRC) is presented for the star-forming galaxies. We found that the IRRC ratio, q_{TIR}, has an average value of ~ 2.42 consistent with previous studies in the literature.

The third project aims to understand the behaviour of the IRRC in different environments. We compare: i) field and cluster galaxies and ii) lensed and non-lensed galaxies. *Herschel* and deep VLA data (r.m.s. ~ 0.6 μJy/beam) at 3 and 6 GHz for three HFF clusters (MACSJ1149, MACSJ0717 and MACSJ0416) are used to create our cluster-lensed and cluster-member samples. The other two samples are obtained from a search in the literature as well as from the second project of this thesis. No significant differences are found between the different scenarios. For the lensed sources we find an evolution of the IRRC with redshift of $q_{TIR} = (2.90 \pm 0.06)(1+z)^{-0.18 \pm 0.05}$, consistent with previous studies in the literature for non-lensed sources. For the cluster-members we find tentative evidence of a slight increment in the radio luminosities compared with field galaxies and therefore a decrease in q_{TIR}. For the cluster-members the IRRC within the cluster is studied as well, finding no clear trend with distance to the centre of the cluster.

Chapter 1

Introduction

1.1 Galaxy Evolution

1.1.1 Galaxy Formation and Evolution

A few hundred million years after the Big Bang, the first stars and proto-galaxies started to form. The most accepted theory to explain galaxy formation and evolution is part of the Λ-Cold Dark Matter Cosmology model (ΛCDM; Liddle 2003). This model fits best some of the cosmological observations like the Cosmic Microwave Background (CMB), the large-scale structure in the distribution of galaxies, the abundance of hydrogen, helium and lithium and the acceleration expansion of the universe. The presence of dark energy (Λ)[1] and cold dark matter[2] are the main characteristics of ΛCDM. According to this model, quantum fluctuations after the Big Bang produce over-density regions. As the universe expands and cools, lumps of dark matter start to contract and the primordial gas starts to form (mostly hydrogen and helium). Then, dark matter and gas are gravitationally attracted to the over-dense regions and halos start to form. As the halos become more massive, they collapse under their own gravity and proto-galaxies start to form, where the hydrogen and helium gas fall into the centre and the dark matter remains in the surrounding halo. When the gas within the halos contracts sufficiently, this gas starts to form the first stars.

The evolution of galaxies is driven by ongoing star-formation. During the stars' lifetime, heavy elements are forming in their cores during the stellar nucleosynthesis. Processes associated with supernovae (SNe) and Asymptotic Giant Branch (AGB) stars heat the gas and expel metals into the interstellar medium (ISM), enriching the galactic environment. This

[1] The dark energy is an unknown form of energy which is hypothesised to be responsible for the accelerating expansion of the universe.

[2] The dark matter does not emit electromagnetic radiation nor scatters light, therefore it is dark to our observations. However, the effect of gravity in this dark matter can be observed.

heating stabilises the contraction of the primordial gas which settles in a rotational disk due to the second law of thermodynamics and the conservation of angular momentum (e.g. Fall & Efstathiou, 1980). It is believed that early galaxies had very irregular morphologies as not enough time had passed for the gas and stars to settle. The young universe is a crowded environment and therefore mergers of galaxies occur regularly. These mergers result in the collisions of clouds of gas and dust, which induce instabilities that result in the formation of new stars. When the nucleus of each galaxy takes part in the merging, a significant amount of gas is involved in the process and a starburst occurs, creating thousands of new stars per year (e.g. Mihos & Hernquist, 1994). During this phase the gas content decreases rapidly and these galaxies become quenched. The quenching can occur because the high rate of star-formation exhausts the whole gas reservoir (e.g. Barnes & Hernquist, 1992; Mihos & Hernquist, 1994) or because the gas is expelled out of the galaxy by Active Galactic Nuclei (AGN) and SNe (e.g. Springel et al., 2005; Croton et al., 2006). In isolated galaxies, star-formation appears to have evolved more steadily, at a rate dependent on the mass. This normal star-formation occurs in normal disk galaxies and is more extended over the galaxy. Therefore, two modes of star-formation are supported by observations, normal star-forming and starburst. Although, it is difficult to know which one of these two modes dominates a given galaxy population at high redshifts due to the observational limitations.

Early galaxies merged with each other forming larger galaxies as time passes. At higher redshift ($z > 0.2$) galaxy clusters seem to contain more blue and spiral galaxies than their counterparts in the local universe (e.g. Butcher & Oemler, 1978; Wirth et al., 1994). Thus, it is believed that the massive red elliptical galaxies of today's universe are the result of spiral mergers (e.g. Glazebrook, 2013). In addition, these mergers are believed to be the required fuel for AGN to occur. The different morphological classification in the local universe, i.e. spiral, elliptical, irregular, and lenticular galaxies, are due to the different initial conditions and environmental processes for each galaxy. The rate at which a galaxy evolves depends on its stellar mass and environment. Galaxies in dense environments or with massive halos go through their evolution faster and are typically lenticulars or ellipticals by the current age of the universe. In addition, interactions[3] between nearby galaxies are favorable to create irregular galaxies (e.g. Chattopadhyay et al., 2015; Nidever et al., 2013). The Hubble diagram of galaxies (Figure 1.1) classifies elliptical galaxies as Early Type Galaxies (ETGs) and spirals as Late Type Galaxies (LTGs). This classification is still used currently but it is somewhat confusing. In general, the most unevolved galaxies are spiral and irregular galaxies followed by the elliptical and lenticular galaxies.

[3] When two galaxies are close, their gravity interacts resulting in tidal distortions.

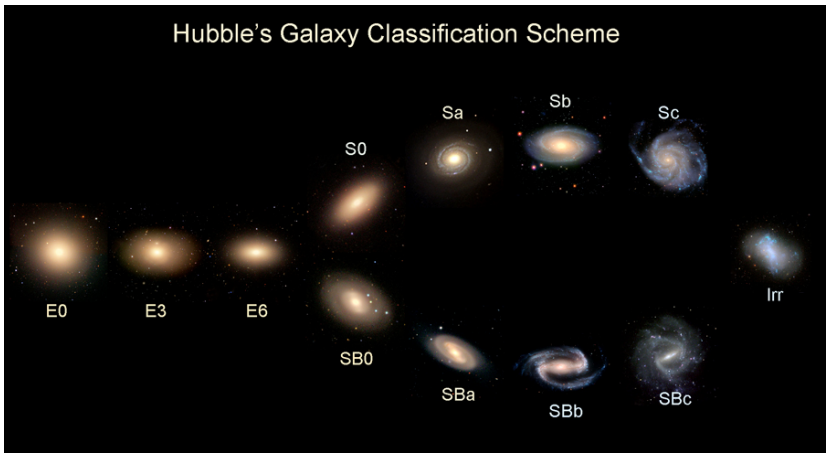

Figure 1.1 : Hubble's galaxy classification where the most unevolved galaxies are irregular (Irr) and spiral galaxies (S) and the most evolved are elliptical galaxies (E). Image credit: https://www.galaxyzoo.org

The evolution of galaxies is a very slow process and therefore it is not possible to observe any changes directly. To understand the evolution of galaxies over cosmic time, the average physical properties of galaxies at different evolutionary stages are studied, i.e. the redshift-evolution of galaxies. This approach allows us to study the average changes in the properties of the galaxies at different redshifts, thereby creating a frame work to study their evolution over cosmic times. The most distant galaxy known is GN-z11 with a confirmed spectroscopic redshift $z = 11.09$, just 400 Myr after the Big Bang (Oesch et al., 2016). The next confirmed most distant galaxy is EGSY8p7 at $z = 8.68$ (Lehnert et al., 2010). Only a few very high-redshift galaxies have been detected due to difficulties in observing such far away galaxies. Currently, ALMA has revealed more galaxies at $z > 6$ (e.g. Venemans et al., 2017; Carniani et al., 2017a;b) opening a new future for observing the high-redshift universe.

1.1.2 Galaxy Clusters

In the local universe ($z \sim 0.1$) more than half of the galaxies (54%) are concentrated in virialised stable groups and clusters (Courtois et al., 2013), around 20% appear in collapsing regions around groups and clusters (e.g. Tully, 1987; Crook et al., 2007; Makarov & Karachentsev, 2011), and the remaining 26% are isolated field galaxies were a small fraction are found to be pairs and compact groups (e.g. Xu & Sulentic, 1991; Karachentseva et al., 2010). Galaxy groups and clusters are divided according the number of galaxy members. Groups are formed by up to 50 galaxies while clusters by hundreds to thousands of galaxies. In addition, clusters are divided by their number density in rich (over a thousand galaxies with an extension of $3 - 10$ Mpc) and poor clusters (less than a thousand galaxies and an extension ~ 1 Mpc). Thus,

clusters are the most massive structures in today's universe ($\sim 10^{15} M_{\odot}$, e.g. Fouqué et al., 2001).

Local and high-redshift elliptical galaxies in clusters follow a tight correlation between colour and brightness (e.g. Bower et al., 1992; Bernardi et al., 2005), the so called red-sequence. This correlation is consistent with passive evolution models, i.e. galaxies grow redder and dimmer without high star-formation. However, this correlation evolves with redshift (De Lucia et al., 2004; 2007; Rudnick et al., 2009), indicating an evolution of the morphological evolution in galaxy clusters (Cerulo et al., 2017) and the blue star-forming fraction of galaxies in the cluster. The morphological distribution of galaxies in the clusters is driven by its density, where high density regions present more elliptical and lenticular galaxies and low density regions mainly spirals. This distribution is similar for both rich clusters and loose groups where clusters are dominated by higher densities than groups (Dressler, 1980a;b). In the core of the cluster ($R < 0.5$ Mpc) most of the galaxies are elliptical and lenticular while there is almost no presence of spiral galaxies. The opposite is found in the outskirts of the cluster, with a presence of spiral galaxies of $\sim 60\%$. For distant clusters the fraction of lenticular galaxies is lower and the fraction of spiral galaxies is larger than for nearby clusters, which indicates a morphological evolution (Dressler et al., 1997; Fasano et al., 2000; Postman et al., 2005).

The effect of the cluster environment on member galaxies is a well-established field of study. Observations have shown that the fraction of blue galaxies in clusters at $z \sim 1$ is $\sim 70\%$ while at low-redshift, $z \sim 0.1$, is $\sim 3\%$. Thereby this effect demonstrates evolution in the cluster environment (Butcher & Oemler, 1978). When spiral and irregular galaxies fall into the cluster, they lose their gas due to interactions within their ISM and their star-formation activity is quenched. At $z \sim 0.5$ it is believed the in-fall is more effective but it is harder to observe.

The physical processes acting in clusters are still under big debate. Local clusters are used to study these interactions at high-resolution. Different models have been developed to understand the interactions between galaxies and with the ISM. The main two models are gravitational (i. e. interactions between galaxy-galaxy, galaxy-cluster, and harassment) and hydrodynamic where the interaction between the ISM and the intra-cluster medium (ICM) is studied (i.e. ram-pressure, viscous stripping, and thermal evaporation). There are as well some hybrid models where the gravitation and the hydrodynamic mechanisms are studied together like starvation and preprocessing models (see Boselli & Gavazzi 2006 for a review).

One of the most often used mechanism is ram-pressure stripping (Gunn & Gott, 1972). This model suggests that a galaxy passing through the ICM suffers an external pressure proportional to the gas density of the ICM and the relative speed of the galaxy to the ICM. This pressure strips gas out of the galaxy if the ICM 'wind' overcomes the gravitational potential of the galaxy. It is believed that this process has a large impact in the evolution of clusters galaxies. Many

observational evidence of stripped galaxies have been reported in the literature in different nearby clusters (e.g. Bravo-Alfaro et al., 2000; Kemp et al., 2005; Crowl et al., 2005; Rasmussen et al., 2006). Ram-pressure features have also been found in distant clusters ($z > 0.2$, Cortese et al., 2007; Ebeling et al., 2014).

1.1.3 Gravitational Lensing

Gravitational lensing was first theoretically predicted by Newton and Laplace among others, but first observed in the past century (Walsh et al., 1979). This effect is a direct consequence of Einstein's General Theory of Relativity. The gravitational field of a massive object bends the spacetime around it, which bends the path of the photons (radiation) passing nearby. Depending on how much light is deflected and where, three different types of gravitational lensing are defined: *strong lensing*, *weak lensing* and *microlensing*. The difference between them depends on the position of the background and foreground sources, the position of the observer and the mass and shape of the lens. When the lens is very massive and the source is well aligned with the lens, the light is strongly bent and more than one images from the background source appear producing a *strong lensing* effect (see Treu 2010 for a review). If the effect of the lensing is not strong enough to form multiples images, but the light is still bent the lensing is defined as *weak* (see Kilbinger 2015 for a review). With *microlensing* the mass of the lens is too low (mass of a planet or a star) for the displacement of the light to be easily detected, although we can study the apparent brightness of the background source. When the lens (i.e. a planet) pass in front of a bright background source, its apparent brightness changes due to the transient phenomenon producing the *microlensing* effect. This effect is used to detect exoplanets as well as binary stars for instance (see Rahvar 2015 for a review).

Some of the main astrophysical issues that can be studied with the use of *strong lensing* are: i) the spatial distribution of mass at big scales where dark matter interact with baryonic mass[4] to shape galaxies, ii) the cosmography of the universe (i.e. geometry, content and kinematics) and, iii) the study of distant astronomical objects that otherwise would be invisible to us due to the current instrumental limitations. An illustration of this effect is shown in Figure 1.2 where a massive foreground galaxy, at redshift z_l, acts as a lens for the background galaxy, at redshift z_b, resulting in a very characteristic arcs feature, the so-called 'Einstein rings', which belong to the background galaxy. Dark matter appears to only interact with gravity, so by measuring the size of this blending, the halo of dark matter of the foreground galaxy can be measured. In addition, the background galaxy can be studied as well.

[4]The baryonic mass refers to all matter made of normal atoms (i.e. excluding dark matter).

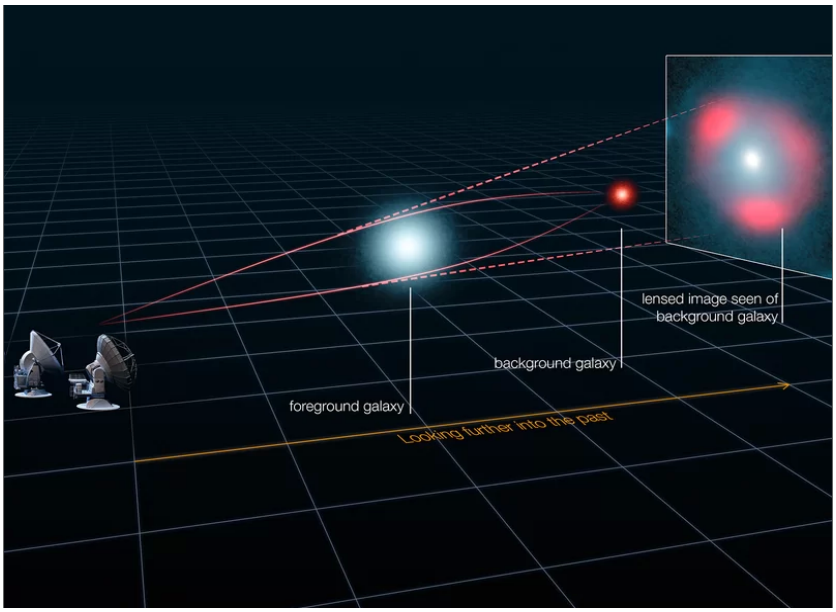

Figure 1.2 : Artistic representation of strong gravitational lensing. The white foreground galaxy acts as a lens to the red background galaxy behind it. This produces the 'Einstein rings' that can be detected by ground telescopes allowing us to study the background galaxy as well as the dark matter halo of the lens galaxy. Image credit: ALMA (ESO/NRAO/NAOJ), L. Calçada (ESO), Y. Hezaveh et al.

The more massive the lens is, the stronger is the gravitational field and therefore the blending of the light. Galaxy clusters are the most massive objects in the universe, which makes them great lenses to observe the early universe. It is believed that they are dominated by dark matter (80-85% of the total mass) so the lensing effect is mostly due to the dark matter (e.g. Babyk et al., 2012; Laporte & White, 2015).

1.2 Cosmic Dust

1.2.1 Dust in Galaxies

Interstellar dust plays an important role in the evolution of galaxies as many key processes involving dust happen in the ISM. For example, dust is a catalyst for the formation of molecular hydrogen and other molecules (Gould & Salpeter, 1963) and shields the molecules in molecular clouds by absorbing the energetic radiation from young stars. This allows the clouds to cool further and enables them to collapse to form the next generation of stars. In addition, dust also strongly influences the observations of other galaxy components. Around 30 to 50% of the radiation produced by galaxies is absorbed by dust and thermally re-emitted at far-infrared

(FIR) and submillimetre (sub-mm) (e.g. Fixsen et al., 1996; Hauser & Dwek, 2001; Driver et al., 2016). We can thus study the properties of the ISM of galaxies at these wavelengths to understand galaxy evolution. Due to the absorption or scattering of photons from the light of sight by dust, some of the environments in galaxies are hidden by obscuration. Not all wavelengths are equally affected by obscuration, with shorter wavelengths being more affected than longer wavelengths.

This obscuration by dust modifies the observed spectral energy distribution (SED) of galaxies. A system in quasi-thermal equilibrium emits the same amount of energy it absorbs. Therefore, the amount of energy absorbed by dust have to be equal to the energy emitted by it. In Figure 1.3 we can see examples of two SEDs from a more evolved galaxy NGC4030 (top) and a more immature/young galaxy UGC09299 (bottom). The blue line represents the stellar radiation before obscuration and the black line at $\lambda \lesssim 5\mu$m shows the attenuated/observed SED. The emission at $\lambda \gtrsim 5\mu$m is the re-radiated dust emission. Thus, the difference between the stellar radiation before and after obscuration is equal to the dust emission. Studying these two plots we see that the evolved galaxy NGC4030 is much more obscured than the immature galaxy UGC09299, where the obscured and unobscured curve are much closer to each other.

Dust is continuously produced and destroyed during its life cycle. Dust grains are formed in the cooling gas of stellar outflows (Yamamoto & Hasegawa, 1977; Draine & Salpeter, 1979). When low-to-intermediate mass stars reach the AGB stage, part of the heavy elements synthesised in these stars condenses as dust grains in the winds of these stars (Ferrarotti & Gail, 2006; Sargent et al., 2010). For massive stars, when their core collapse into SNe, and subsequently explodes the heavy elements produced during their lifetimes are ejected and a fraction again condenses as dust grains (e.g. Dunne et al., 2003; Barlow et al., 2010; Gomez & Matsuura, 2012; Gall et al., 2014). Some of the metals and dust produced dissipate into the ISM, and some stay in the molecular clouds were they formed becoming part of the new generation of stars when these clouds collapse. The dust in the consumed molecular clouds will thus be destroyed as it becomes part of the star. Once the dust is injected into the ISM the grains suffer different destruction processes as SNe shocks (e.g. Barlow, 1978; Draine & Salpeter, 1979; Jones et al., 1994) and collisions between dust grains (Jones et al., 1996). Other processes as thermal sputtering, and ionising destruction by cosmic-rays reduce the dust mass (see Jones 2004 for a review). The predicted timescale for dust destruction in the ISM (10^8 years) suggest that the majority of the dust grains must be re-formed there (Jones & Nuth, 2011), and therefore dust grain growth in the ISM is necessary. The increasing dust-to-metal ratio as galaxies evolve can also only be explained as a result of dust grain growth (De Vis et al., 2017b).

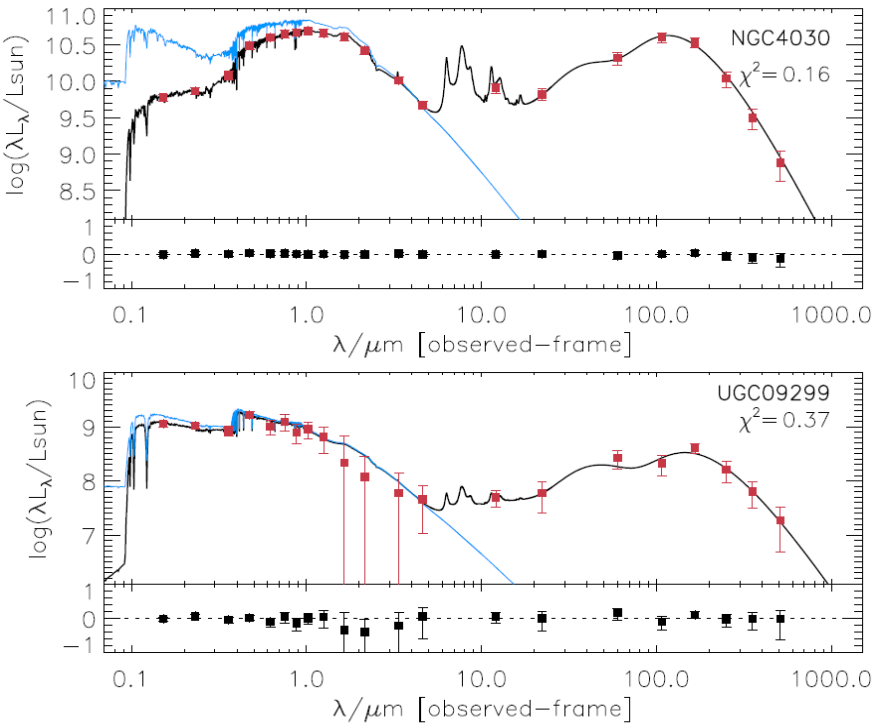

Figure 1.3 : From top to bottom, SEDs for the evolved galaxy NGC4030 and for the more immature galaxy UGC09299. The red-squares correspond to the observed fluxes to which the model is compared to. The black curve shows the best fit model SED to the observations and the blue curve shows how the stellar part of the SED would look without any obscuration. We can see how for the more evolved galaxy there are much more obscuration and therefore the dust emission is higher than for the more immature galaxy. Image credit: De Vis et al. (2017a)

1.2.2 Dust Emission

Dust is composed of grains of different size, broadly from ~ 10 nm to ~ 10 μm (Kim et al., 1994). There are thus, two emission regimes within the dust SED of a galaxy, one for the small dust grains and another for the large dust grains. The first type produces non-local thermal equilibrium or polycyclic aromatic hydrocarbon molecules (PAHs). Briefly, when a very small grain absorbs an optical/UV photon, the internal energy of the grain is highly boosted such that its temperature reaches a much higher temperature than the surrounding environment. In this situation the dust grain emits at mid-infrared wavelengths ($5\ \mu\text{m} < \lambda < 20\ \mu\text{m}$) (Camps et al., 2015). For the larger dust grains the absorption of a single photon does not excite the grain to very high energy levels remaining in a local thermal equilibrium with their environment.

The temperature of a blackbody emitter in local thermal equilibrium is described by the Stefan-Boltzmann law:

$$\mathrm{T}^4 = \frac{\mathrm{Qc}}{4\sigma} \tag{1.1}$$

where Q is the local radiation heat, c is the speed of light, and σ is the Stefan-Boltzmann constant. The spectrum of a blackbody at this temperature as a function of frequency ν, is given by the Plank function:

$$\mathrm{B}_\nu(\mathrm{T}) = \frac{2\mathrm{h}\nu^3}{\mathrm{c}^2 \mathrm{e}^{\frac{\mathrm{h}\nu}{k\mathrm{T}}} - 1} \tag{1.2}$$

where h is the Planck constant and k is the Boltzmann constant. The fluxes S_ν of a source are proportional to mass of dust $\mathrm{M_d}$, and inversely proportional to the distance squared, D^2. For a blackbody emitter, the spectrum will thus be given by:

$$\mathrm{S}_\nu = \frac{\kappa_\nu \mathrm{M_d B}_\nu(\mathrm{T})}{\mathrm{D}^2} \tag{1.3}$$

where κ_ν is the dust mass absorption coefficient, which for a blackbody emitter is a constant. However, dust is not an ideal emitter and therefore cannot be described as such ideal blackbody. To account for changes in the emission at different frequencies, we make κ_ν frequency dependent. At FIR/sub-mm frequencies, this can be described as:

$$\kappa_\nu \simeq \kappa_{\nu_0} \left(\frac{\nu}{\nu_0}\right)^\beta \tag{1.4}$$

where β is the emissivity index, defined as the spectral index of the power-law slope of the Rayleigh-Jeans tail. Thus, it is possible to determine this factor studying the SED of galaxies. Observational studies suggest $\beta = 2$ an appropriate value for cold dust in local spiral galaxies (Dunne & Eales, 2001; Clemens et al., 2013; Smith et al., 2013). Although, for different types of dust this value is found to be $1 \leqslant \beta \leqslant 2$. The spectrum of large dust grains radiating as a

Modified Black Body (MBB) can be described as:

$$S_\nu = \frac{\kappa_{\nu_0} \nu^\beta M_d B_\nu(T)}{D^2 \nu_0^\beta} \tag{1.5}$$

κ_{ν_0} is a not well constrained value as it depends on the properties of the dust grains as size, density and shape. The uncertainty thus, is thought to be one order of magnitude (James et al., 2002). Two values are normally used, $\kappa_{850} = 0.077$ m^{2}kg^{-1} (Dunne et al., 2000; James et al., 2002) and $\kappa_{350} = 0.192$ m^{2}kg^{-1} (Draine, 2003). However, it is possible that this factor varies from galaxy to galaxy which would bias our understanding of dust masses in galaxies.

The dust in any given galaxy will not be at a constant temperature but within a range of different temperatures. Due to the limited amount of observed wavelengths it is not possible to disentangle the MBB for all different temperatures. A common approach is to model the dust emission using a limited number of dust components. The most normal approximation is to use a cold ($10 < T < 30$ K) dust component which correspond with the bulk of the dust mass, and a warm ($30 < T < 60$ K) component which can represent a significant fraction of the dust luminosity ($L_d \propto T^{4+\beta}$). These two-components MBB have been used in this thesis to model the infrared luminosity.

1.2.3 Herschel Space Observatory

Cosmic dust has been studied for decades using infrared (IR) space telescopes (e.g. IRAS; Neugebauer et al. 1984, ISO; Kessler et al. 1996 and Spitzer; Werner et al. 2004) as well as sub-mm ground telescopes such as the James Clerk Maxwell Telescope (JCMT) with the Submillimeter Common-User Bolometer Array SCUBA (Holland et al., 1999) and SCUBA2 (Holland et al., 2013) , and APEX with LABOCA (Siringo et al., 2009). The opacity of the atmosphere at FIR and sub-mm wavelengths makes it nearly impossible to observe these frequencies from ground telescopes (Figure 1.4). Some atmospheric windows at long wavelengths in the sub-mm range are possible to observe from ground telescopes located in very high and arid places as Atacama in Chile and Mauna Kea in Hawaii. However, FIR wavelengths need to be observed from space. The study of the cold universe entered a new era with the launch of the *Herschel Space Observatory* (hereafter *Herschel*, Pilbratt et al. 2010). *Herschel* was designed to offer a larger telescope and to extend the spectral coverage further into the FIR and sub-mm wavelengths (Figure 1.5). Launched by the European Space Agency's (ESA) on May 2009, with a 3.5 m diameter primary mirror, *Herschel* was the largest telescopes of its kind. It was active almost for 4 years when the liquid helium used to cool down the telescope's mirror boiled off. It covered photometry and spectroscopy at wavelengths $52 - 670$ μm, sensitive to

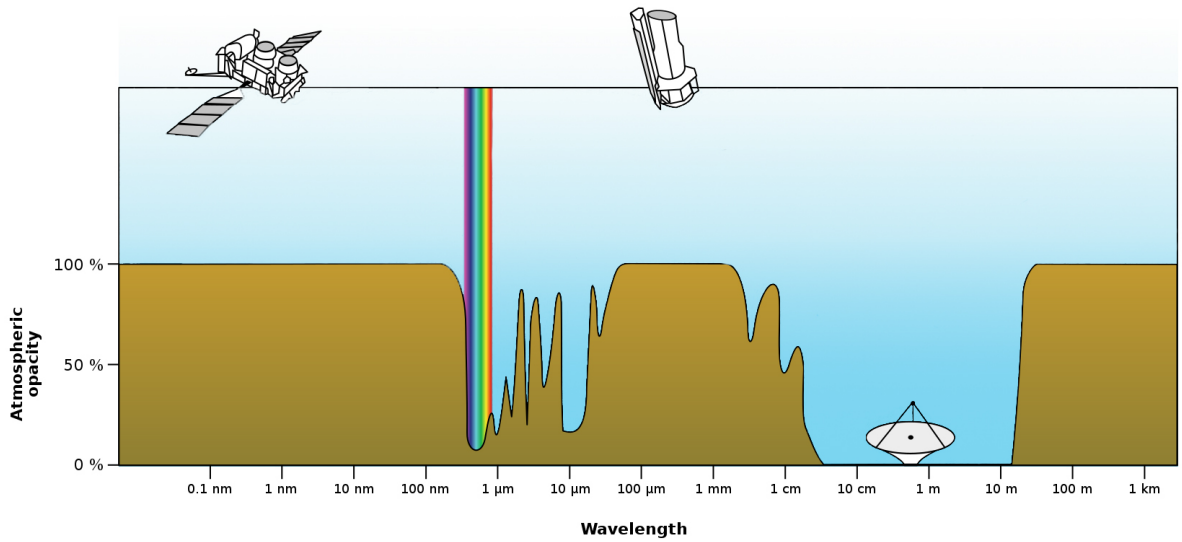

Figure 1.4 : Presence of the atmospheric opacity along the electromagnetic spectrum. At radio wavelengths we can see that there is no opacity and therefore we can observe those from ground. However at FIR as well as Gamma rays, X-rays and UV for instance we need space telescope to observe at these ranges. Image credit: https://commons.wikimedia.org

the diffuse cold dust (T $<$ 30 K) that dominates the dust mass in galaxies. There were three main reasons for using a big mirror: i) To obtain better resolution; Due to the diffraction limit $\theta \simeq 1.22\frac{\lambda}{D}$ where θ is the resolution, λ is the wavelength and D is the diameter of the primary mirror, at sub-mm wavelengths the resolution is $\sim 1,000$ times worse than in the optical and a large mirror is necessary. ii) To limit the confusion between sources; At high redshift multiple unresolved sources are located with smaller angular separation than the resolution of the observations and therefore it is not possible to determine how much flux belongs to each galaxy. iii) To increment the sensitivity in the observations; Sensitivity scales with the squared radius of the primary mirror. Therefore, the size of the mirror was as big as possible for it to fit inside the Ariane V rocket used to launch *Herschel* into orbit.

Herschel had on board three instruments, PACS, SPIRE and HIFI. HIFI was a very high-resolution spectrometer and PACS and SPIRE were direct detection cameras with medium resolution spectrometers. In this thesis only PACS and SPIRE photometers are used, and we thus provide some additional information here. The Photodetector Array Camera and Spectrometer (PACS; Poglitsch et al., 2010) was sensitive at $60-210\mu$m range with 3 different bands at 70, 100 and 160μm. However, only two bands could be observed simultaneously (160μm together with one of the shorter wavelength bands) as PACS only had two filled arrays of bolometers. The 160μm was observed with a 512 element array with pixel size 6.4 arcsec, while the other two bands with a 2048 element array with pixel size 3.2 arcsec. The field-

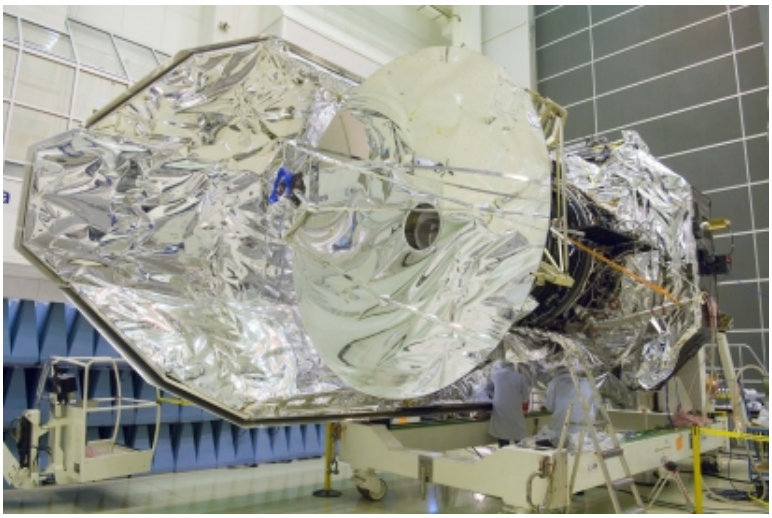

Figure 1.5 : *Herschel Space Observatory* during its assembly at ESA. Image credit: https://herschelmission.wordpress.com

of-view (FOV) for both bolometers was 3.5×1.75 arcmin^2. The Spectral and Photometric Imaging Receiver (SPIRE; Griffin et al., 2010) operated at $194 - 672\mu$m with bands centred at $250, 350$ and 500μm. The three bands were observed simultaneously with bolometer arrays of 139, 88 and 45 elements respectively, pixel sizes 6, 10 and 14 arcsec, and FOV 4×8 arcmin^2.

The *Herschel*-Astrophysical Terahertz Large Area Survey (H-ATLAS) is the largest extragalactic sub-mm survey covering 600 deg^2 in 5 photometric bands, using in parallel mode PACS and SPIRE instruments (Eales et al., 2010). With 600 hours of observations this survey is the largest *Herschel* open time single key-project. H-ATLAS have developed their own program to detect sources on *Herschel* images (MADX; Maddox et al., in preparation), such that only sources with a measured flux density $> 4\sigma$ in at least one of the SPIRE bands are included in the H-ATLAS catalogue (Valiante et al., 2016; Smith et al., 2017). This survey covers a relatively shallow area of sky measuring the dust masses and dust-obscured star-formation rate (SFR) for thousands of local (Dunne et al., 2011) and high-redshift galaxies (e.g. Lapi et al., 2011; González-Nuevo et al., 2012; Pearson et al., 2013). The H-ATLAS observed fields were selected to avoid bright continuum emission from dust in the Galaxy and to provide the maximum amount of data in other wavelengths (e.g. GALEX; Martin & GALEX Team 2005, WISE; Wright et al. 2010, UKIDSS-LAS; Smith et al. 2014, VIKING; Edge et al. 2013, KiDS; de Jong et al. 2013). Thus, five fields were selected: one close to the North Galactic Pole (NGP) with an area of ~ 170 deg^2, one field in the South Galactic Pole (SGP) of ~ 285 deg^2, and 3 GAMA fields (Driver et al., 2009) at right ascension of approximately 9, 12 and 15 hours (GAMA9, GAMA12 and GAMA15) each of them with an area of 54 deg^2. Sources from all these different fields have been studied in this thesis.

1.3 Dusty Star Forming Galaxies

1.3.1 Identification of Dusty Star Forming Galaxies

During the 1990s with the use of SCUBA at 850μm a new population of high-redshift galaxies was uncovered (Smail et al., 1997). This population of extremely bright sources at sub-mm and FIR wavelengths are though nearly optical invisible. This revolutionised the field of galaxy formation and the field of high-redshift dusty galaxies became one of the fastest growing areas in extragalactic astronomy.

Dusty Star Forming Galaxies (DSFGs) are abundantly present in the early universe where the first assembly of galaxies occurs. High SFRs results in many new massive young stars which emit UV radiation. This radiation is absorbed by dust grains and re-emitted at FIR wavelengths, making this type of galaxies specially bright at infrared luminosities ($L_{TIR} > 10^{12}$ $L_{\odot}$) and mostly obscured in the optical and UV regime. Thus, it is important to study these galaxies at their peak of emission at FIR. DSFGs are the most intense starburst in the universe and they represent more than half of the FIR background (Devlin et al., 2009). Therefore, it is important to understand the start and end of the dusty starburst phase as they represent half of the star-formation activity in the universe. Observations suggest that DSFGs are strongly clustered (Weiß et al., 2009b), and that they contain big amount of gas reservoirs. These two characteristics makes the DSFGs the best candidates to be the progenitors of massive elliptical galaxies (Swinbank et al., 2006).

Semi-analytic models predict that the DSFGs population is dominated by merging star-forming galaxies rather than normal star-formation. However, the estimation at high redshift of major merger rates and the short duty cycle of merging starbursts suggest a lack of major mergers to account for the DSFGs population. Therefore, a significant fraction of this population must be massive discs fuelled by minor mergers and smooth accretion (Carilli et al., 2010). The dominant mode of star-formation for the DSFGs population is still an open debate. One tool to understand the nature of the extreme starburst found in many high-redshift galaxies is the study of the very dense gas. A very high fraction of molecular gas is found at these high-redshifts which explain the high SFRs compared with the most active present-day counterparts.

The low-resolution of the sub-mm observations first done with SCUBA gives a positional uncertainty of tens of arcseconds, so the number of counterparts at other wavelengths is therefore tens. Interferometric observations at radio wavelengths allow us to narrow the position of these sources. Radio sources are much more rare than optically-bright sources (Ivison et al., 2007) so while tens of optical sources can be detected within the sub-mm beam, it is rare to have more than one radio-bright galaxy. Once we have the radio position, follow up at other wavelengths is easier. However, a big fraction of sub-mm sources do not have radio counterparts (for sources

brighter than $S_{850} > 5$ mJy, 66% were found to have radio counterparts brighter than 30 μJy; Chapman et al. 2003; Barger et al. 2007) which might bias our interpretation of this population. The reason for this could be that galaxies at high redshifts ($z \gtrsim 3.5$) are very difficult to detect in radio due to the lack of negative K-correction at radio wavelengths (see next section), or that high-redshift DSFGs have weaker radio counterparts, which would imply a variation in the infrared-to-radio correlation (see Section 1.5).

The bulk of DSFGs peaks at $z \sim 2.2$ (e.g. Chapman et al., 2004; 2005; Amblard et al., 2010), but the detection of galaxies at $z \sim 4-5$ has increased during the last years. This leads one to believe that a significant number of DSFGs could lie at $z > 4$. This implies that the sample of galaxies selected is often limited to the brightest galaxies or to fainter ones in small area fields. It is important to note that these $z > 4$ studies are in its infancy, and may even point to the existence of a new or different DSFGs population (Wall et al., 2008).

1.3.2 Negative K-correction

The reason why many sub-mm and FIR sources can be detected at high redshift is due to the *negative* K-correction. The K-correction is applied to the flux of an observed source to convert this flux from the observed-frame into the rest-frame. This correction depends only on the shape of the galaxy's SED. Typically, a positive K-correction is defined when the flux density decreases with increasing redshifts, and a negative when it increases with redshift, i.e. the larger the redshift the fainter the galaxy as its flux is inversely proportional to its distance:

$$S = \frac{L_{rest}\, K_{corr}}{4\pi D_L^2} \tag{1.6}$$

where S is the flux of the source, L_{rest} is its luminosity at rest-frame, D_L is the luminosity distance and K_{corr} refers to the K-correction. At high redshifts the peak of the FIR emission at rest-frame is shifted into the mm and sub-mm part of the SED. In Figure 1.6 we can see that considering a given luminosity, the flux density of galaxies at redshifts $1 < z < 8$ remains approximately constant at mm wavelengths. At shorter wavelengths ($250-350-450-500\mu$m) the negative K-correction is still appreciable but less strong. For the rest of the bands this correction is positive instead, as the fluxes decrease with redshift. The reason for this is that the dust emission in this type of galaxies resembles a MBB (Dunne & Eales, 2001) which peaks at rest-frame wavelength at ~ 100 μm and the long-wavelength portion of the spectrum is the Rayleigh-Jeans regime. Beyond ~ 3 mm the dominant emission is not coming from the dust but for a mix of synchrotron and free-free emission, where the K-correction is positive. Other wavebands for which the galaxy SED is more flat do not benefit from this effect so the DSFGs

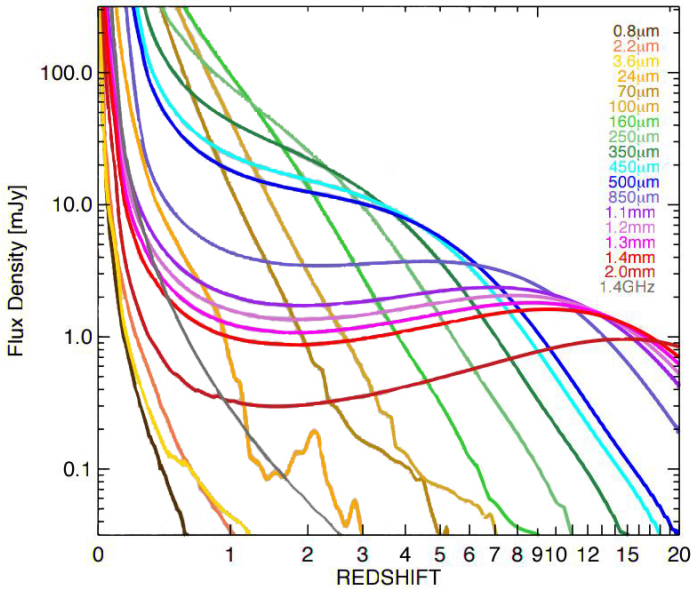

Figure 1.6 : The observed flux densities for a galaxy with infrared luminosity $L_{IR} \sim 10^{12.5}\ L_{\odot}$. We can see how the flux densities vary with redshift at different wavelengths. The flux density remains almost constant at mm wavelengths at redshifts $1 < z < 8$ due to the negative K-correction. Image credit: Casey et al. (2014)

counterparts are usually very faint. Additionally, optical observations also suffer from high levels of extinction due to the large amounts of dust present in these systems.

1.3.3 Local Luminous Infrared Galaxies

With the use of IRAS and ISO, the local luminous infrared galaxies (LIRG; $10^{11} < L_{IR} < 10^{12}\ L_{\odot}$) and a small sub-sample of ultra luminous infrared galaxies (ULIRGS; $10^{12} < L_{IR} < 10^{13}\ L_{\odot}$) were discovered (e.g. Sanders et al., 2003; Blain, 1999). Detailed studies of these galaxies revealed that most of them with infrared luminosities $\sim 10^{11.5}\ L_{\odot}$ were major mergers of two or more galaxies with similar masses (e.g. Soifer et al., 1984; Lonsdale et al., 1984; Veilleux et al., 2002). Despite it not being clear yet if there is a close relationship between this population of galaxies and the DSFGs, there are certain similarities between them: high infrared luminosities (associated with merger), massive molecular gas reservoirs, comparable CO linewidths and similar IR/radio and IR/CO luminosity ratios. In the evolutionary sequence (U)LIRGs are located in a large evolutionary stage where two gas-rich disk galaxies merge producing an intense phase of start-formation due to the fast compression and cooling of the gas. During this phase, the dust grains absorb rest-frame optical and UV emission coming from the blue young stars and re-emit this radiation at IR and sub-mm wavelengths during the

(U)LIRGs phase. This phase is thought to be short-lived due to the limited gas supply and high SFRs. The two supermassive black holes merge during the final coalescence generating an AGN which is fed by an accretion disk of material. Eventually there is no more available gas in the galaxy and it becomes an elliptical galaxy characterised by and old stellar population. This explains quite good how the most massive elliptical galaxies in the universe were formed. Although, (U)LIRGs are very rare comparing with the 'normal' Milky Way type of galaxies and are not thought to contribute substantially to the cosmic star-formation rate density of today's universe. Therefore, if high-z (U)LIRGs are more common than local (U)LIRGs, this could mean that at early times cosmic star-formation was dominated by mergers, or a different physical process that we do not know yet could explain this.

1.3.4 Molecular Lines

Since it is generally accepted that molecular gas is the fuel for star-formation, this active star-formation must be reflected by the morphology of the ISM. H_2 and CO are the most abundant molecules in the ISM. However, H_2 is difficult to observe due to its symmetry, as the molecule has no dipole moment and as a result its vibrational and rotational energy levels are close together. This results in a whole forest of potential emission lines which makes H_2 optically thick. It is thus hard to identify which line is being observed at any given time. On the other hand, CO molecules are polar[5] and therefore easier to observe as the rotational energy levels of polar molecules are well separated. The quantised rotational kinetic energy can be expressed as:

$$\mathrm{E_{rot}} = \frac{\mathrm{J(J+1)}\hbar^2}{2\mathrm{I}}, \mathrm{J} = 0, 1, 2, ... \tag{1.7}$$

where I is the moment of inertia, $\hbar$ is the reduced Plank constant and J correspond to the angular-momentum quantum number corresponding to the upper energy level. Molecules are excited into $\mathrm{E_{rot}} > 0$ states by collisions in the gas and ambient radiation. Different temperatures and densities in the gas will produce different J energy levels that when they return to lower energy levels radiate CO emission at different energy levels. These emission lines together form the CO emission *ladder*. Low energy J transitions originate in low density and colder regions while high energy J transitions correspond to warmer and denser regions. Multiple-J CO observations allow us to constrain the physical conditions (e.g. temperature, density and radiation field) within the emitting gas and the primary source responsible for heating the gas (e.g. cosmic-rays, UV photons, X-ray and shocks).

The CO lines are used to deduce the mass and distribution of molecular hydrogen in galaxies as well as reliable dynamical mass and size estimates. To comprehend the evolution of galaxies,

[5] They have a non-zero permanent electric dipole moment.

it is essential to understand the different phases of the molecular gas in the galaxies. The study of molecular lines at high redshift allows us to determine the total molecular gas mass of the galaxy, and therefore to know how long star-formation can be maintained at the current rate, and how much stellar mass can be assembled without a source of molecular gas supply.

DSFGs have star-formation rates of $\gtrsim 1,000$ $M_{\odot}yr^{-1}$ which can be explained by either larger reservoirs of molecular gas ($10^{10}-10^{11}M_{\odot}$, $\sim 40\%$ of their total mass) or higher star-formation efficiency (SFE), traced by the ratio between the FIR and CO luminosities (Frayer et al., 2011). The relation between the SFR and the amount of gas is found through the Kennicutt-Schmidt law (Kennicutt & Evans, 2012). To determine the gas mass, the measured gas tracer (the CO line) needs to be converted to the total amount of gas in the galaxy. Though, this conversion is still not well defined and still remains an open debate. The choice of this conversion factor, which ranges between $\alpha \sim 0.8-1.6$ $[M_{\odot}(K\ km/s\ pc^2)^{-1}]$, will influence the inferred relation (see Bolatto et al. 2013 for a review).

Other ladders of CO contribute to the insight into the temperature and density of the gas. The detection of other molecules such as HCN, HCO+, HNC, CN, and H_2O are less present in the literature but have enabled studies of the chemical composition (for a review see Solomon & Vanden Bout 2005; Carilli & Walter 2013).

Determining the redshifts of DSFGs at rest-frame UV and optical wavelengths is very difficult as these galaxies suffer from optical extinction, and thus the photometric redshifts are less reliable (Casey et al., 2012). Furthermore, the poor spatial resolution at mm and sub-mm continuum maps ($\sim 10-20$ arcsec) makes it more difficult to determine the counterparts as many sources might be within the beam. Therefore, the use of CO emission lines at mm and cm wavelengths become a great tool to determine redshifts of distant galaxies. This technique has been proved successful in many studies in the literature and with many different telescopes like IRAM, ALMA, ATCA (e.g. Weiß et al., 2005; 2009b; Fudamoto et al., 2017; Venemans et al., 2017; Greve et al., 2005; Coppin et al., 2010; Emonts et al., 2011). With the identification of at least two CO lines from the molecular ladder, we can identify their redshift mostly unambiguously. In addition, the CO lines arise from the molecular gas, so it is then possible to relate this galaxy component with its sub-mm counterpart.

1.3.5 Gravitationally Lensed DSFGs

Identifying gravitational lensing systems is often very time consuming and it involves sifting through large volumes of imaging or spectroscopic data to find a few candidates. Lensed galaxies at sub-mm wavelengths are rare and finding them thus requires large areas of sky. The use of *Herschel* to find lensed galaxies at these wavelengths has a great potential. A significant fraction of the bright-end number counts of wavelengths above 500μm are gravitationally

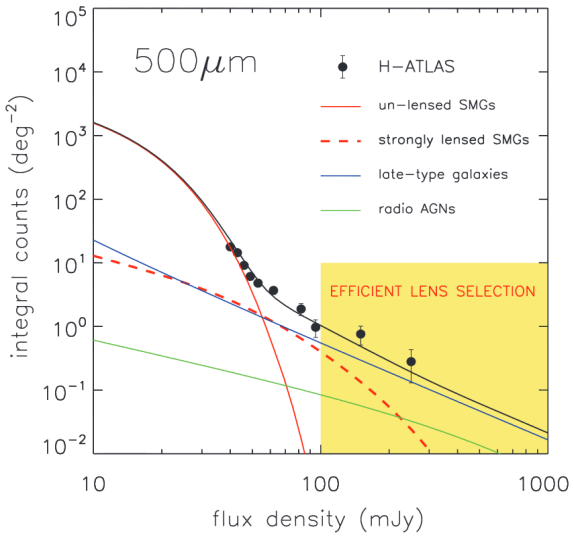

Figure 1.7 : We can see how the steepness of the number of counts changes above 100 mJy for H-ATLAS (solid-black line). The yellow region indicates where the best area to identify lensed galaxies might be. Image credit: Negrello et al. (2010)

lensed DSFGs as first predicted by Blain (1996). This is due to two main reasons: i) The number counts of sub-mm galaxies are steep and have a sharp cut-off. Thus, the magnification factor due to the gravitational lensing moves the sources from the faint-end to the bright-end as shown in Figure 1.7. ii) Due to the negative K-correction at longer wavelengths, high-redshift galaxies are expected to be detected where the optical depth to lensing is rapidly increasing (Weiß et al., 2013). At shorter wavelengths than 500μm the bright-end counts are dominated by star-forming galaxies at low-redshifts where the lensed counts do not make up an appreciable fraction (Negrello et al., 2007; Bussmann et al., 2013; Wardlow et al., 2013). The bright-end number counts is therefore a mix of local galaxies, blazars and distant lensed infrared galaxies. Therefore it is easy to identify good candidates of lensed galaxies with the number counts. Theoretical predictions argue that there are no DSFGs with intrinsic flux at 500μm above 80 mJy (Negrello et al., 2007). Follow-up for the lensed candidates is needed at other wavelengths to achieve sub-arcsecond resolution to untangle the background galaxies.

1.4 Synchrotron Radiation

When a charged particle moves through a strong magnetic field, this particle is accelerated along a spiral path, thereby emitting radio waves. When the particle reaches relativistic velocities this emission is called synchrotron radiation (Figure 1.8). The radio signature is correlated to the strength of the magnetic field.

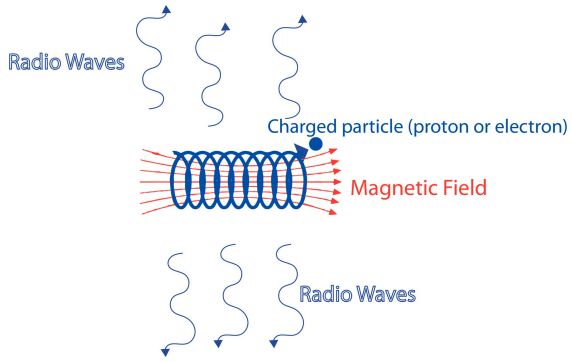

Figure 1.8 : Schematic representation of the synchrotron emission emitted by a charge particle when it passes through a magnetic field. Image credit : Juan Gutiérrez Larraínzar

In normal galaxies, those not dominated by an AGN, most of the radio emission is due to a mix of synchrotron radiation from relativistic electrons and free-free emission from ionised gas[6] (Klein et al., 1988; Carlstrom & Kronberg, 1991). As shown in Figure 1.9, synchrotron radiation (dot-dashed-green line) dominates the spectrum of the very well studied starburst M82 at low frequencies (below $\nu \sim 30$ GHz). The free-free emission (dashed-blue line) is coming from H_{II} regions ionised by massive ($M > 15M_{\odot}$) main-sequence stars and is distributed along the galaxy. This emission absorbs some of the synchrotron radiation and thus flattens the overall spectrum (solid-black line) at the lowest frequencies. The synchrotron radiation is believed to be a consequence of SNe explosions of massive stars ($M > 8M_{\odot}$). The relativistic electrons accelerate in the shock fronts of SNe remnants propagating into the ISM and moving through interstellar magnetic fields. The relativistic particles spinning around the magnetic field emit synchrotron radiation over a large range of radio wavelengths, increasing its intensity with wavelength.

Massive stars with $M > 8M_{\odot}$ have main-sequence lifetimes $\tau < 3 \times 10^7$ yr, while relativistic electrons in typical interstellar magnetic field have lifetimes $\tau < 3 \times 10^8$ yr. Thus, the radio continuum emission from normal galaxies is unconfused from older stars an it is an extinction-free tracer of recent star-formation. In addition, the sub-arcsecond position accuracy and resolution of radio maps allow us to identify regions of higher star-formation within the galaxy and resolve the most compact ones. The most intense starburst are only transparent at radio and FIR wavelengths, thus the observed flux densities at these frequencies are accurately proportional to intrinsic luminosities (Condon, 1992).

[6]Free-free emission or thermal bremsstrahlung emission is produced by free electrons scattering off ions without being capture. The electrons are free before and after the interaction.

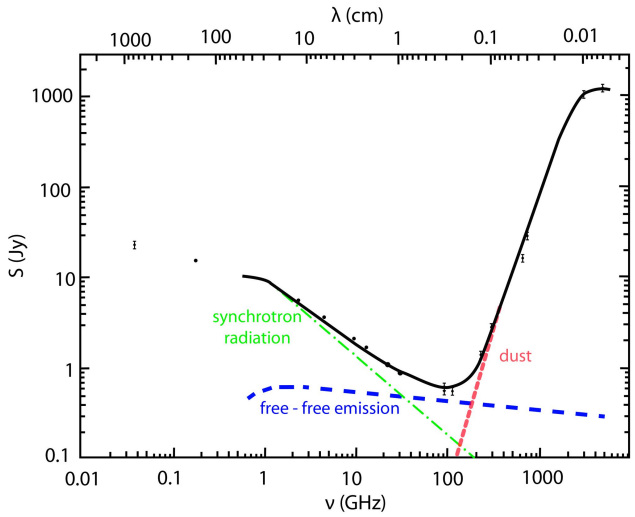

Figure 1.9 : The observed FIR and radio part of the SED of M82 (solid-black line). This spectrum is the sum of synchrotron (dot-dashed-green line), free-free (dashed-blue line) and dust (dotted-red line) components. Image credit: Klein et al. (1988), modified by Juan Gutiérrez Larraínzar

1.5 The Infrared-to-Radio Correlation

1.5.1 The Infrared-to-Radio Correlation in Star Forming Galaxies

The tight correlation between the infrared (L_{TIR}) and radio luminosity ($L_{1.4GHz}$) of a galaxy is very well studied in the literature (e.g. de Jong et al., 1985; Yun et al., 2001; Ivison et al., 2010; Delhaize et al., 2017). This correlation is known to be followed by all star-forming galaxies not dominated by AGNs, and it extends over five orders of magnitude (Wunderlich et al., 1987; Yun et al., 2001). The ultimate driver of the so-called InfraRed Radio Correlation (IRRC)[7] is believed to be the star-formation in galaxies. The exact process is still unclear but it is believed that young massive stars emit UV radiation which is absorbed by dust grains and re-emitted at IR frequencies. A few Myr after, these stars end their lives as SNe where cosmic-rays are created that travel through the interstellar magnetic fields producing the synchrotron radiation detected at radio wavelengths.

One of the controversies of this correlation is due to the amount of radio emission in different galaxies. The radiation emitted by each electron in the ISM is proportional to the magnetic energy density, $U_B = B^2/(8\pi)$. The magnetic field for different galaxies varies from $B \sim 10$ μG in normal galaxies (Basu & Roy, 2013), $B \sim 100$ μG in M82 (Adebahr et al., 2013), and $B > 1,000$ μG in a luminous starburst galaxy such as Arp220 (Batejat et al., 2011).

[7]Note that in some of these studies the Far-Infrared-to-Radio Correlation was studied. Here, we refer to the IRRC indistinguishable to one or another.

Therefore, the synchrotron radiation emitted for each cosmic-ray electron in the different galaxies should vary by up to several orders of magnitude, but all these galaxies follow the same IRRC.

Several theoretical models have been developed to explain the IRRC on global scales, such as the calorimetry model (Voelk, 1989), the optically-thin scenario (Helou & Bicay, 1993) and the conspiracy model (Lacki et al., 2010). On more local scales models such as the small-scale dynamo effect (Schleicher & Beck, 2013; Niklas & Beck, 1997) attempt to explain this correlation. All these models assume that both the production of cosmic-rays and the production of UV light are proportional to the SN rate (and thus the SFR). The differences lie in the ratios between i) the production of cosmic-rays and the emission of synchrotron radiation (which depends on the strengrh of the magnetic field and how long the cosmic-rays are trapped in this field) and ii) the UV radiation and FIR emission (which is mostly determined by the optical depth i.e. the amount of dust, and the length of the path through the dust). For the IRRC to be tight, these two ratios have to correlate with eachother or with SFR. However, none of these models successfully reproduce all observational constraints.

The IRRC can be quantified by the parameter q_{TIR} defined as:

$$q_{TIR} = \log\left(\frac{L_{TIR}}{3.75\times10^{12}\mathrm{Hz}}\right) - \log\left(\frac{L_{1.4GHz}}{\mathrm{WHz}^{-1}}\right) \tag{1.8}$$

where L_{TIR} is in units of W and it represents the total infrared luminosity $\lambda(8-1000\ \mu\mathrm{m})$. This value is divided by the central frequency 3.75×10^{12} Hz such that q_{TIR} becomes dimensionless.

Several theoretical predictions have been done to study whether the IRRC evolves with redshift finding different results. Murphy (2009) predict an increment of the IRRC at $z>3$ due to the increase of the cosmic microwave background energy density (UCMB) with redshift ($U_{CMB}\propto(1+z)^4$). At higher redshifts the non-thermal radio emission would be suppressed by the dominant Inverse-Compton (IC) scattering[8]. Thus, only the thermal component would be detected. This increment in the IRRC increases with the magnetic field. In this situation galaxy-scale magnetic fields are built up over time, so field strengths should be typically weaker in the past. How the amplification of weak, seed magnetic fields in the halos of proto-galaxies eventually translates into galaxy-scale fields is still uncertain. Schober et al. (2016) present a model to predict the evolution of synchrotron emission and find as well an increment of q_{TIR} with redshift. However, Lacki et al. (2010) model the cosmic-ray scale heights and find a slight decrease in the IRRC at $z\gtrsim2$.

[8]The Inverse Compton scattering occurs when ultra-relativistic electrons scatter low energy photons to high energies, i.e. the photons gain and the electrons lose energy.

Observational evidence shows a slight evolution in the IRRC with redshift (e.g. Delhaize et al., 2017; Sargent et al., 2010; Magnelli et al., 2015) finding a discrepancy between some models and the observations so far. One of the explanations for this discrepancy can be contamination from indistinguishable AGNs or an increment of the radio continuum emission as a result of other processes like an increment in the strength of the magnetic field (Morić et al., 2010)

1.5.2 The Infrared-to-Radio Correlation in Galaxy Clusters

The IRRC in local galaxy clusters has been widely studied in the literature (e.g. Niklas et al., 1995; Reddy & Yun, 2004; Omar & Dwarakanath, 2005). The correlation has been found to have lower FIR/radio ratios in clusters than in field galaxies likely due to the cluster environment (Miller & Owen, 2001; Andersen & Owen, 1995). The main driver responsable for this radio enhancement in cluster galaxies is the increment on the strength of the magnetic fields. To explain the lower FIR/radio ratios in clusters several models have been used with different mechanisms. The main idea suggest an increment on the strength of the magnetic fields due to compression of the gas in the ISM. This compression can be due to i) thermal pressure by the ICM, and/or ii) ram-pressure due to galaxies moving in the ICM (e.g. Rengarajan et al., 1997; Miller & Owen, 2001; Andersen & Owen, 1995; Murphy et al., 2009). When galaxies moves throught the ICM the relative movement causes the outskirts of the galaxies (perpendicular to the movement) to be stripped. At the same time this movement makes that at the front of the galaxy, the ISM and ICM collide and as a result the ISM compresses. This compression results in higher magnetic fields, which result in a radio enhancement in the cluster galaxies and therefore lower FIR/radio ratios.

A correlation of the radio luminosity with radial distance to the center of the cluster has been found, with the radio luminosity being stronger in the core of the cluster (Reddy & Yun, 2004; Miller & Owen, 2001). Such a correlation was not found for the FIR luminosity, what implies that the IRRC is expected to be radially dependend within the cluster. This excess of radio emission is higher in rich clusters than poor clusters which can be because the ICM density is higher in rich clusters so the compression of the ISM is stronger (both ram pressure and thermal pressure) which means that the radio enhancement would be stronger and so would be the FIR/radio ratios. Alternatively, there could be a greater contribution of AGNs as a consequence of frequent galaxy-galaxy collisions (e.g. Moss & Whittle, 1993; Lake et al., 1998) and/or to the radio overluminosity coming from spirals which in clusters develop radio sources more frequently than other galaxies in the cluster or isolated galaxies (Andersen & Owen, 1995; Gavazzi & Boselli, 1999; Rengarajan et al., 1997)

Not many studies of the IRRC have been done in clusters at high redshifts. Randriamampandry et al. (2015) study the Far-Infrared-to-Radio Correlation for a single cluster at $z \sim 0.54$. A big number of galaxies present an excess in their radio fluxes when compared to low-redshift clusters, suggesting an enhancement of radio-excess in earlier epochs, although no radio-excess correlation is found with radius in this one cluster as found in nearby clusters.

1.6 Thesis Overview

In this thesis we present a classification of high-redshift dusty star-forming galaxies (DSFGs). With the use of the *Herschel Space Observatory* and radio observations with ATCA and the VLA, we identified some of the reddest sources in the H-ATLAS catalogue as well as some gravitational lensing systems at photometric redshifts $1.5 < z_{phot} < 2.5$. In particular, we aim to obtain a large sample of candidate lensed galaxies to use in follow-up studies investigating cosmography. Additionally we will study the fraction of lensed galaxies in this redshift range down to lower fluxes than previous studies in the literature (e.g. Negrello et al., 2010; Bussmann et al., 2013). Next, a study of the Infrared-to-Radio Correlation (IRRC) for different types of galaxies is performed to analyse how different environments affect this correlation. Studies comparing cluster and field galaxies have been performed in the local universe, but little work has been done at higher redshifts (see Section 1.5.2). We will present the first study of the IRRC using *Herschel* fluxes for intermediate-redshift ($z \sim 0.5$) cluster galaxies and also a comparison of lensed and non-lensed galaxies for a wide range of redshifts ($0.18 < z < 3.7$).

Three different studies are presented in this thesis, which is divided as follows. In Chapter 1 the introduction of this thesis is presented. Chapter 2 is dedicated to the fundamentals of interferometry. In this chapter we explain the principles of interferometry and the necessary steps to calibrate the observed visibilities. In addition, the main characteristics of the two radio telescopes used in this work can be found in here. In Chapter 3 our study on the identification and classification of two very red DSFGs in the H-ATLAS catalogue is presented. Spectroscopic redshifts from the $^{12}CO(2-1)$ emission line via ATCA observations were determined as well as the potential lensing origin with near-IR (NIR) GEMINI observations. In Chapter 4 a sample of 123 sources at $1.5 < z_{phot} < 2.5$ and $S_{500} > 29$ mJy from the Thousand Lens Survey (TLS) is analysed. A morphological study via NIR and VLA continuum maps was done to determine the fraction of lensed galaxies in the sample. Chapter 5 is focussed on the study of the IRRC in different environments, i.e. field and cluster galaxies, and lensed and not-lensed galaxies. A study of the evolution of the IRRC with redshifts is presented and possible explanations for its behaviour are exposed in this chapter. Finally, in Chapter 6 the conclusion of this thesis are explained.

Throughout this thesis we use cosmological constants: $H_0 = 70$ km/s/Mpc, $\Omega_m = 0.3$, $\Omega_\Lambda = 0.7$.

Chapter 2

Radio Interferometry

The first radio signals from space were detected in 1932 by Karl Jansky, revealing an unseen universe unlike the one observed at optical wavelengths. A wide variety of astronomical sources, from thermal and non-thermal radiation mechanisms, can be observed at radio waves. Some of the major discoveries are neutron stars, pulsars, quasars or the CMB from the hot Big Bang. Most continuum radio sources are extragalactic, which allows astronomers to study the universe over cosmic time.

Due to the long wavelength of radio waves (~ 0.3 mm $-$ 30 m), to obtain a resolution similar to optical telescopes a huge collecting area is needed, i.e. a very large diameter dish. The angular resolution of a telescope is defined by its diffraction limit $\Theta \simeq 1.22\frac{\lambda}{D}$, D being the diameter of the lens, mirror, or dish, depending on the type of telescope. For example, observing with VISTA[1], with a 4.1 m primary mirror, at 2.15 μm a maximum resolution of 0.1 arcsec can be achieved. However, to obtain similar resolution at a radio wavelength of 5 cm, for instance, with a single radio antenna, a dish of $\sim$ 126 km diameter would be required. Building such telescopes would be impossible. In addition, the differences in the paths of radio waves arriving at different positions on such a large dish would require extra corrections to be applied due to an unstable atmosphere[2]. Fortunately, the use of interferometry solves this problem. Different telescopes linked together to obtain a final image after combining the signals coming from the different telescopes is called an interferometer array. The resolution of these interferometers depends on the maximum separation (or 'baseline') between telescopes, obtaining the equivalent resolution to one obtained from a single, much larger telescope. Therefore, larger arrays give better resolution while smaller compact arrays yield better surface brightness sensitivity [3].

[1] VISTA is an ESO telescope located at the Paranal Observatory, Chile.

[2] The corrections that need to be applied to the incoming signal that pass through the atmosphere are more complex with bigger telescopes or shorter wavelengths.

[3] A better surface brightness sensitivity with compact arrays is due to a better sampling of the u,v-plane (see Section 2.3).

Interferometers though are blind to certain scale called the 'largest angular scale', which is determined by λ/b_{min} , b_{min} being the shorter baseline in the configuration array. The primary beam is defined by the diameter of the antennae and the observed wavelength by $P = \lambda/D$.

Since the use of the first radio telescopes, the study of the long wavelength universe has been expanding with the use of over one hundred telescopes (including single dishes and interferometric arrays) all around the wold. The wide atmospheric window at radio frequencies ($\sim$ 10 MHz – 1 THz) allow us to study a wide variety of astronomical sources but a wide variety of radio telescope and different observing techniques are needed to cover all of this frequency window. New radio observatories such as ALMA and SKA open a new era of radio astronomy with much higher resolution and better sensitivity.

In this chapter we explain the fundamentals of radio interferometry, from the measurement of the radio waves to the synthesis imaging. The chapter is organised as follows. In Section 2.1 the visibility function is explained. Section 2.2 illustrates the mechanism of the interferometers to obtain the output signal. In Section 2.3 the synthesis imaging is described. Section 2.4 is dedicated to the calibrations needed during the radio observations. Finally, Section 2.5 explains the main characteristics of the two radio interferometric arrays used in this thesis.

2.1 The Visibility Function

The basic idea of an interferometer is that the spatial intensity distribution of a radio source at a particular frequency can be reconstructed from the spatial coherence function measured at different points, i.e. by the different antennae of the interferometer. As Clark (1999) defined it: 'An interferometer is a device for measuring the spatial coherence function'.

A radio source at a location $\mathbf{R}$[4] generates an electric field $\mathbf{E}_\nu(\mathbf{R},t)$ whose electromagnetic wave propagates towards us at the point $\mathbf{r}$ (Figure 2.1). Assuming that this radiation is monochromatic we can define $\mathbf{E}_\nu(\mathbf{r})$ at our location as:

$$\mathbf{E}_\nu(\mathbf{r}) = \int\int\int P_\nu(\mathbf{R},\mathbf{r})\mathbf{E}_\nu(\mathbf{R})dxdydz \tag{2.1}$$

where $P_\nu(\mathbf{R},\mathbf{r})$ is called the *propagator* and describes how the electric field at $\mathbf{R}$ influences the electric field at $\mathbf{r}$. $\mathbf{E}_\nu(\mathbf{r})$ is the sum of all the waves emitted by the source at frequency ν. In this thesis, the effect of polarization was not studied in any of the different chapters, thus we can consider a scalar field as a fair approximation for our purposes. In addition we can assume that the sources are very far away and therefore there is no depth information and only the

[4]Boldface symbols indicate vectors.

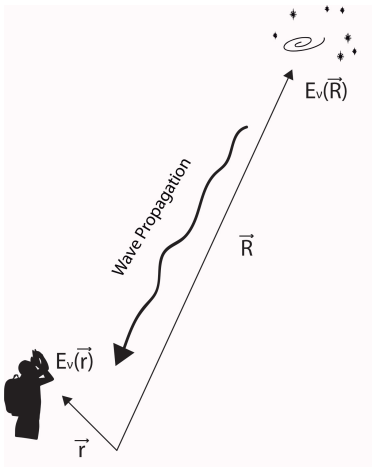

Figure 2.1 : An object located in **R** emits and electromagnetic wave $\mathbf{E}_\nu(\mathbf{r})$ which propagate in space towards the observer located at **r**. Image credit: Juan Gutiérrez Larraínzar

surface brightness of the object is measured[5]. With these assumptions and following Huygens' principle[6] we can rewrite equation 2.1 as:

$$\mathrm{E}_\nu(\mathbf{r}) = \int \mathrm{E}_\nu(\mathbf{R}) \frac{\mathrm{e}^{(2\pi i \nu(\mathbf{R}-\mathbf{r})/\mathrm{c})}}{|\mathbf{R}-\mathbf{r}|} \mathrm{dA} \tag{2.2}$$

where dA is the element of area at distance $|\mathrm{R}|$. An important property of $\mathrm{E}_\nu(\mathbf{r})$ is the correlation function at two points

$$\mathrm{V}_\nu(\mathbf{r_1}, \mathbf{r_2}) = \langle \mathbf{E}_\nu(\mathbf{r_1}) \mathbf{E}^*_\nu(\mathbf{r_2}) \rangle \tag{2.3}$$

which describes how similar the measured electromagnetic field is at these two points. The $*$ indicates the complex conjugate and $\langle\rangle$ is a time average. In this scenario, assuming that the radiation from astronomical objects is not spatially coherent, (i.e. $\langle \mathbf{E}_\nu(\mathrm{r}_1) \mathbf{E}^*_\nu(\mathrm{r}_2) \rangle = 0$ for $\mathbf{R}_1 \neq \mathbf{R}_2$) the spatial coherent function of $\mathbf{E}_\nu(\mathbf{r})$ can be expressed as:

$$\mathrm{V}_\nu(\mathbf{r_1}, \mathbf{r_2}) \approx \int \mathrm{I}_\nu(\mathbf{s}) \mathrm{e}^{-2\pi\nu \mathbf{s}(\mathbf{r_1}-\mathbf{r_2})/\mathrm{c}} \mathrm{d}\Omega \tag{2.4}$$

where $\mathrm{I}_\nu(\mathbf{s})$ is the observed intensity, **s** is the unit vector pointing towards the source ($\mathbf{R}/\mid \mathbf{R} \mid$), c is the speed of light and $\mathrm{d}\Omega$ is the solid angle. Therefore the coherence function depends only on the separation of the two points $\mathbf{r_1}$ and $\mathbf{r_2}$. Inverting this equation, $\mathrm{I}_\nu(\mathbf{s})$ can be deduced by measuring the spatial coherence function V_ν as a function of $\mathbf{r_1} - \mathbf{r_2}$. To obtain the observed intensity, first we define the favoured coordinate system of the baseline vector

[5]The distances are $>> \mathrm{b}^2/\lambda$, where b is the interferometer baseline. This only matters for very long baseline observations of solar-systems objects.

[6]Every point on a wavefront is itself the source of spherical wavelets.

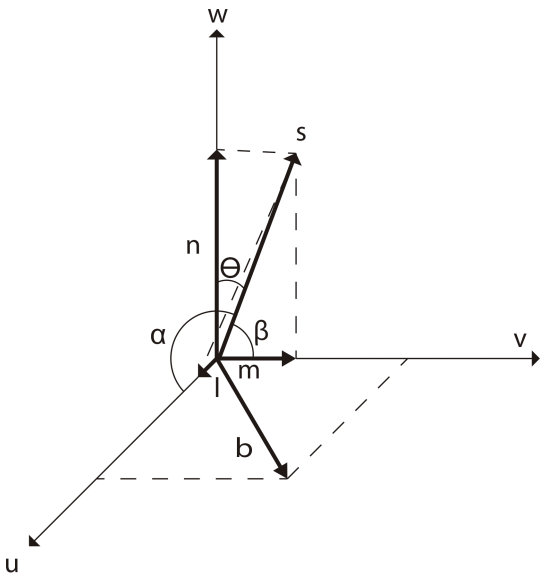

Figure 2.2 : Preferred coordinate system corresponding to the baseline vector **b**. Image credit: Juan Gutiérrez Larraínzar

b shown in Figure 2.2. We can define $\mathbf{r_1} - \mathbf{r_2} = \lambda(u,v,0)$ so that in this coordinate system $\mathbf{s} = s(l,m,\sqrt{1-l^2-m^2})$. Inserting these coordinates in the previous coherent function we obtain:

$$V_\nu(u,v,w\equiv 0) = \int\int I_\nu(l,m)\frac{e^{-2\pi i(ul+vm)}}{\sqrt{1-l^2-m^2}}dl\,dm \tag{2.5}$$

In most cases the denominator is close to one due to the small size of l and m. In addition, the source size is normally small compared with the beam size of the antenna and the variation of gain with angle is then negligible. Taken the small angle approximation and in terms of the intensity distribution, $I_\nu(l,m)$, we obtain:

$$V_\nu(u,v) = \int\int I_\nu(l,m)e^{-2\pi i(ul+vm)}dl\,dm \tag{2.6}$$

The direct inversion of this equation gives the observed intensity:

$$I_\nu(l,m) = \int\int V_\nu(u,v)e^{2\pi i(ul+vm)}dl\,dm \tag{2.7}$$

In order to make calculations practical another parameter needs to be added to this equation. The antennae have different sensitivities along the dishes, being most sensitive in the centre (Figure 2.3). To correct for this behaviour we introduce $A_\nu(\mathbf{l,m})$, defined as the *primary beam* or the *normalised reception pattern* of an antenna, which describes the sensitivity as a function

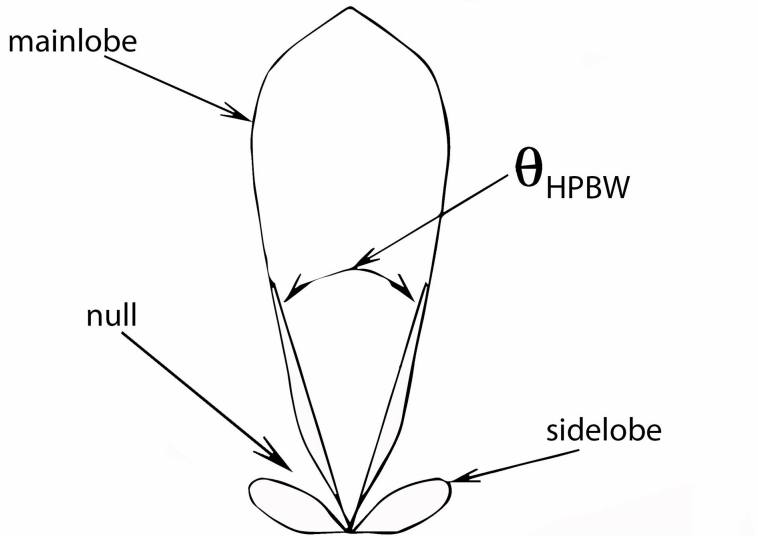

Figure 2.3 : Response of the antenna with direction. The sensitivity of the antenna is higher in the main lobe (the direction of the peak of the beam) but it is sensitive as well to sources away from the centre, the sidelobes. Ideally we want Θ_{HPBW} (FWHM) of the main lobe to be small, so the nearby sources are not confused with our target, and the sidelobes to be low to minimise the contamination from other sources.

of direction. The quantity all antennae measure is the visibility function $V'_\nu(u,v)$ (the *sampled visibility*) and it is the parameter with we will work in further analysis. It is defined as:

$$\mathrm{V}'_\nu(\mathrm{u},\mathrm{v}) = \int\int \mathrm{A}_\nu(\mathrm{l},\mathrm{m})\mathrm{I}_\nu(\mathrm{l},\mathrm{m})\mathrm{e}^{-2\pi\mathrm{i}(\mathrm{ul}+\mathrm{vm})}\mathrm{dl}\,\mathrm{dm} \tag{2.8}$$

2.2 Interferometers

The $\mathbf{E}_\nu(\mathbf{r})$ coming from a source is measured by the antennae, turned into a digital signal by their receivers, which then generates the interference pattern in a correlator. For simplicity we explain how the coherence function is measured with an interferometer comprised of just two elements. Figure 2.4 represents two antennae pointing to a source of flux density S in the direction of the unit vector $\mathbf{s}$. The vector $\mathbf{b}$ connects the phase centres of the two antennae where one of them is designated as the reference antenna. The signal arriving at antenna 2 also arrives at antenna 1, but delayed by the *geometrical delay*, $\tau_\mathbf{g} = \mathbf{b}\cdot\mathbf{s}\ /\mathrm{c}$. The radiation is collected by the dishes and passes through the receivers which incorporate a filter to select the require frequency band, $\Delta\nu$, centred at frequency ν. The measured radiation is a mix of coherent signal from the source and incoherent signal from the sky. Thus, it is easy to identify

the radiation coming from the source. Then, the amplifiers in the receivers boost the radio signal to a measurable level.

Due to the extreme sensitivity of the receivers these need to be cooled to very low temperatures to minimise interference coming from the noise generated in the system. The power received by an antenna is defined as $P_{tot} = kT_{tot}\Delta\nu$, where $T_{tot} = T_{ant} + T_{sys}$. T_{ant} is the temperature of the antenna which is proportional to the flux density of the source, S. The system temperature (T_{sys}) represent the added noise of the system and have different contributions, $T_{sys} = T_{bg} + T_{sky} + T_{spill} + T_{loss} + T_{cal} + T_{receiver}$[7,8], which we want to keep as low as possible. The first three contributions change with the position on the sky. If the system temperature changes significantly during a measurement scan, due to bad weather for instance, a meaningful measurement may be impossible. The r.m.s. noise level S_{rms} is defined as:

$$S_{rms} = \frac{2kT_{sys}}{A_v\sqrt{N_A(N_A-1)t_{int}\Delta\nu}} \tag{2.9}$$

where A_ν is the effective area of the antennae, N_A is the number of antennas, $\Delta\nu$ is the bandwidth, t_{int} is the integration time and k is Boltzmann's constant. To achieve a good sensitivity, low T_{sys} are needed as well as a large effective area and a big number of antennae. In addition, for continuum observations a large bandwidth is needed as well.

[7] T_{bg} is the noise from the microwave and galactic backgrounds. This values is ~ 3 K, except at lowest ν where the radio emission from the Galaxy becomes important.
T_{sky} noise from the atmospheric emission. Generally small but at high frequency, where the atmosphere becomes more opaque, dominates T_{sys}.
T_{spill} noise coming from the ground radiation. At low frequencies this dominates T_{sys}.
T_{loss} coming from the losses in the transmission lines.
T_{cal} noise do to unstable receiver gains.
$T_{receivers}$ the temperature coming from the receiver itself.

[8] The best $T_{reciever}$ is typically a few tens of Kelvins from 1 - 100 GHz, and around 100 K at 700 GHz.

Figure 2.4 : Schematic representation of a tow-element interferometer array. Image credit: Juan Gutiérrez Larraínzar

The measured voltages in the antennae are $V_1(t) = v_1 \cos 2\pi\nu(t-\tau_g)$ and $V_2(t) = v_2 \cos 2\pi\nu t$. The correlator multiplies the voltages $V_1(t)$ and $V_2(t)$ taking a time average, $\langle V_1(t)V_2(t)\rangle$, obtaining:

$$r(\tau_g) = v_1 v_2 \cos 2\pi\nu\tau_g \tag{2.10}$$

The cosine term varies sinusoidally with τ_g due to the Earth's rotation. This generates a *fringe pattern* due to the orientation of the antenna. The term $v_1 v_2$ represents the fringe amplitude and it is proportional to the signal power received at $\Delta\nu$ from the source element $d\Omega$. This signal is proportional to the effective area of the antennae $A_\nu(\mathbf{s})$, and the source flux S. Therefore, the correlator output in terms of baseline and source position vectors can be written as:

$$r = \Delta\nu \int_s A_\nu(\mathbf{s}) S \cos 2\pi\nu\tau_g d\Omega \tag{2.11}$$

To create an image with an interferometer a position is defined where the synthesised FOV is centred. This position is normally called *phase reference position* and it is represented by the vector $\mathbf{s_0}$. An illustration of this is shown in Figure 2.5 where we can see that $\mathbf{s} = \mathbf{s_0} + \sigma$. We can now define the *fringe visibility* which is a complex variable with dimensions of spectral power flux density ($Wm^{-2}Hz^{-1}$). It can be defined as an unnormalised measurement of the coherence of the electric field, modified by the characteristics of the interferometer:

$$V = \int_s A(\sigma) S(\sigma) e^{-2\pi i \nu \mathbf{b}\sigma/c} d\Omega \tag{2.12}$$

where $A(\sigma) = A(\sigma)/A_0$ is the normalised antenna reception pattern and A_0 the response at the beam centre. This value is computed to determine the amplitude and phase of the fringe oscillation obtaining the *observed visibility*. The amplitude and phase of the *real visibility* of the source is obtained by appropriate calibrations. These calibrations are normally referred to observations of other sources whose positions, flux densities and angular dimensions are known (more in Section 2.4). Using the system coordinates of $\mathbf{b}$ to express the *fringe visibility* we obtain:

$$V_\nu(u,v) = \int\int I_\nu(l,m) e^{(-2\pi i(ul+vm))} dl\, dm \tag{2.13}$$

which is similar to the equation 2.6. Hence, the brightness distribution of the target is obtained with the Fourier Transform (FT) of the *real visibility* data.

The *fringe visibility* produces one Fourier component of the brightness distribution. When many baselines are used in a telescope array to sample better the FT, this technique is called *aperture synthesis array*. The use of the rotation of Earth to provide continuous arc of baselines to sample better the brightness distribution is called *Earth rotation synthesis*. The coverage of

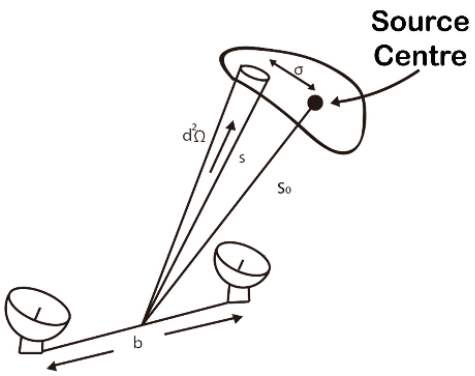

Figure 2.5 : Representation of the *phase reference position* $\mathbf{s_0}$, where the synthesised field of view is centred.

the u,v-plane depends on the configuration of the array, the number of antennae, the number of observed hours and the elevation of the target which determines the shape of the beam. For instance, during our observations with ATCA two sources were observed, one of them for 2.76 hours and the other one for 13.14 hours. The different coverage of the u,v-plane for these two sources are shown in Figure 2.6. The left image corresponds to the 2.76 hours observation where there are big gaps in the u,v-plane. However, in the right image with a 13.14 hours observations, the beam is completely sampled. The VLA has much more antennae and therefore more baselines to cover the u,v-plane. This means that with less observing time more u,v-plane is covered. Figure 2.7 shows the u,v-plane of the VLA observations for the GAMA (left) and the NGP (right) fields where the beam is completely sampled with an exposure time of 24 minutes. Both fields were observed in configuration B, however we can see the difference in elevation in the shape of the beam. While the GAMA fields have a more elongated beam shape towards declination, the NGP field is more rounded and elongated towards right ascension.

Aperture synthesis, as originally conceived, involved filling in the u,v-plane without any gaps up to some maximum baseline, b_{max}, which determines the angular resolution. Therefore to fill the gaps in the u,v-plane and obtain the final calibrated image we perform synthesis imaging with specific tools.

2.3 Synthesis Imaging

Because only a finite number of the visibility functions are measured, as we show in Figures 2.6 and 2.7, $I_V(l,m)$ cannot be obtained completely. The measured visibilities are called the *sampled visibilities*, $V'(u,v)$, and using a sampling function $S(u,v)$ we can obtain the *real*

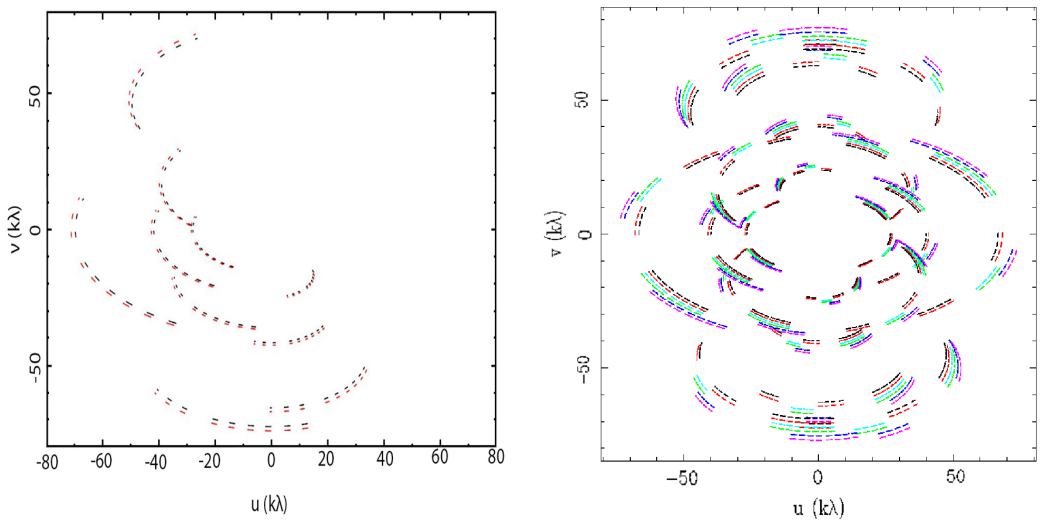

Figure 2.6 *Left*: The u,v-plane covered with ATCA in 2.76 hours observation for one of our targets. *Right*: In this case, the source was observed for a period of 13.14 hours and therefore the u,v-plane is completely sampled.

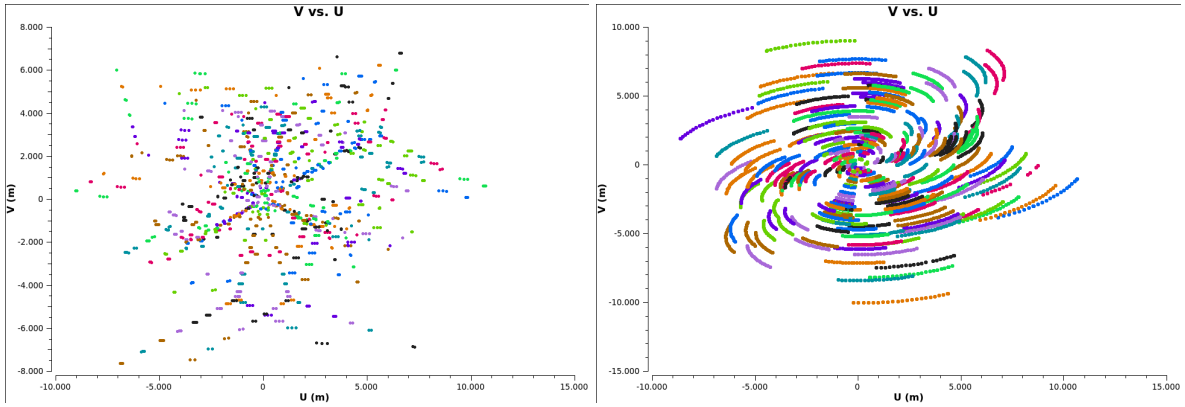

Figure 2.7 : From left to right we represent the u,v-plane of the VLA observations for GAMA and NGP fields from the TLS sample. With only 24 minutes of observation the u,v-plane is better sample than in ATCA due to the bigger number of antennae in the array.

visibilities $V(u,v)$, i.e. $V'(u,v) = S(u,v)\ V(u,v)$. The sampling function is a delta function where we take data and zero elsewhere. Thus, the FT of $S(u,v)$ is the synthesised dirty beam[9]:

$$B(l,m) = \int\int S(u,v)e^{2\pi i(ul+vm)}dudv \tag{2.14}$$

A non complete coverage of the u,v-plane gives a synthesised beam with a lot of sidelobes, i.e. a 'dirty' beam. Using the convolution theorem with the synthesised beam and the $I_\nu(l,m)$ we obtain the dirty image which is characterised as well by sidelobes:

$$I^D_\nu(l,m) = I_\nu(l,m) \otimes B(l,m) \tag{2.15}$$

$$I^D_\nu(l,m) = \int\int V_\nu(u,v)S(u,v)e^{2\pi i(ul+vm)}dudv \tag{2.16}$$

To fill in the gaps there are many different options, as the FT inversion is not unique. Obviously we aim to deconvolve our image in the best possible way to obtain the real image of the sky from the *sampled visibility*, so the deconvolution process consist of giving the best possible values to the unmeasured visibilities in order to obtain a nice Gaussian beam without sidelobes. The most well-known and successful deconvolution procedure is the algorithm CLEAN developed by Högbom (1974). This algorithm is pretty complex and many options are possible. We describe here the main characteristics of this algorithm.

Using a direct FT to invert the visibilities requires a very time consuming complex computing process. To alleviate this, the fast Fourier transform (FFT) is used instead. To do so, the u,v-plane is gridded into a 2D-array that the CLEAN algorithm can process much easier. First, a pixel size for the u,v-plane is selected so that the synthesised beam is properly sampled. Normally selecting 1/3 or 1/5 of the size of the synthesised beam for the pixel size is a good compromise. After gridding the u,v-plane, the array has some cells with data and other ones without (those which do not have measured data in that location). To fill up the empty cells, a 'weight' is assigned to the cells. There are different options to do this which affect the angular resolution and sensitivity of the final image. To determine what weighting function is the best possible in our study, there are a few questions we have to consider. How does the morphology of the source change with the weighting? How do the noise properties change with weighting? And, which weighting gives the best compromise between morphology, sensitivity and resolution? The main weighting functions are:

Natural: Assign constant weights to all visibilities assuming that each visibility has the same noise (or, more strictly, inversely proportional to the noise variance of a visibility). This

[9]The synthesised dirty beam is the PSF or diffraction pattern of the aperture.

option is normally used to obtain optimal point-source sensitivity in an image. However, the synthesised beam shape and sidelobes can be poor. Due to the low brightness of our galaxies it was key to obtain the highest possible sensitivity and therefore we used this weighting in this thesis.
Uniform: The visibilities are weighted proportionally to the number of visibilities in each resolution element. This minimises the sidelobes in the synthesised beam but produce higher noise levels.
Robust: This function allows to find a compromise between the natural and the uniform weighting functions.

With this information, CLEAN creates the dirty image. From this image it subtracts a fraction of the flux (scaled version of the dirty beam) in the brightest pixels in a defined region. This flux and the corresponding position is recorded in a model. It repeats this process iteratively until some threshold or a maximum number of iterations is exceeded. Then, the clean image is created from the information saved in the model obtaining our final deconvolved image.

2.4 Calibration

The goal of calibration is to find the relationship between the *sampled visibility*, V'(u,v), and the *real visibility*, V(u,v). The atmosphere corrupts the phase and amplitude of incoming signals which vary with time and position. In addition we have to consider that the signal is corrupted by the digital electronics, the variations in the receivers, etc. Thus, all the calibrations are antenna based as the sensitivity of the antenna varies with T_{sys}. The main idea of calibration is to measure the gains (amplitudes and phases) for known sources as a function of time and frequency and interpolate those into the target.

The first step before any calibration is applied is to flag bad data due to so-called Radio Frequency Interferences (RFIs). These interferences are normally due to cell phones, microwave ovens, mobile phones, communication satellites, wlan, TV broadcast, etc. Sometimes after flagging and performing all the needed calibrations more flagging needs to be applied as new RFIs are found. In general, flagging a little too much data is not a problem. Even flagging 25% of data results in only minor changes and is easily corrected during the deconvolution process. An example of a detected RFI while observing with ATCA is shown in Figure 2.8. How the visibility looks like before and after some flagging is shown in Figure 2.9.

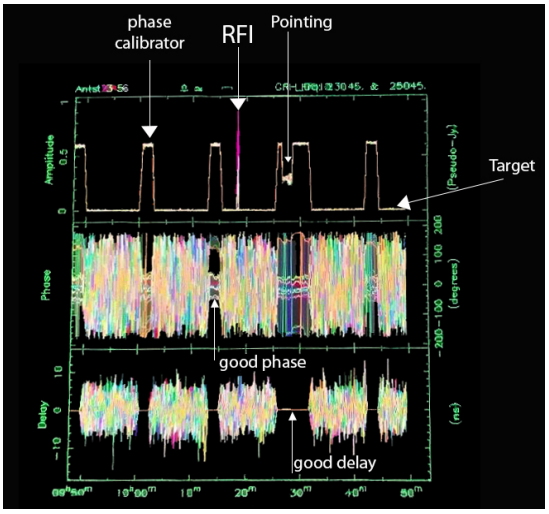

Figure 2.8 : Screen shot of the 'VIS' display window of the ATCA observing program. In the top graph, a big RFI is detected which was deleted afterwards. In addition, the pointing calibration is visible as well as the phase calibrator and the target observations. In the middle plot the phase of the antennae vs. time is represented. We see that the phases during the phase calibrator exposures are close to zero but for antenna-6. Because we were using compact configuration this antenna was ignored and therefore its calibration was not important. In the bottom graph the delay between antennae vs. time is represented. We see a good agreement in the delay of all the antennae during the exposure of the phase calibrator.

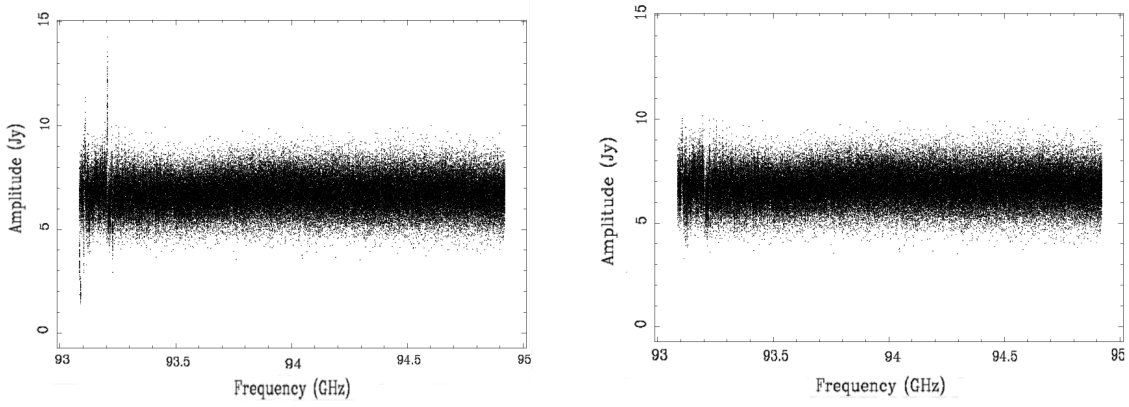

Figure 2.9 *Left*: Example of RFI affecting one of the baselines (1-4) in the flux calibrator at 3 mm band during ATCA observations. *Right*: The resulted flagged visibility.

2.4.1 Pointing Calibration

The antennae move in elevation and azimuth when moving to various sources. The *a priori* accuracy of the global pointing solution in ATCA for instance is ~ 20 arcsec. Depending on the observed frequency, this value can be a large fraction of the primary beam and because the different sensitivity response of the antenna (A_ν), we can obtain a lower sensitivity than the position of interest. Therefore, a *pointing calibration* needs to be applied during the observations as often as necessary, according with the weather conditions. Changes in temperature can make the pointing incorrect by a few arcseconds. At mm observations this means a significant fraction of the primary beam size, affecting the sensitivity of our targets. Pointing calibration was done every 10 minutes in mm observations over the *phase calibrator* with ATCA. For the VLA the recommended time for pointing calibration is every hour, achieving an accuracy of 2-3 arcsec.

2.4.2 Bandpass and Delay Calibration

The delay in the signals coming from each of the antennae causes different frequencies arriving at different phases to the bandpass, resulting in a drop in the amplitude (Figure 2.10 left). Furthermore, inaccurate antenna positions, timing, etc cause a time-constant linear phase slope as a function of frequency in the correlated data. This phase slope, known as delay, might cause decorrelation of the continuum signal and would produce an incorrect representation of the sky. To correct this effect a bright calibration source ($S \geq 1$ Jy) is observed such that the correlator can accurately determine the phase slope with frequency to correct for the delays.

In addition, due to non-uniform passbands[10] the gain responses as function of frequency are corrupted. We need to know the response of each frequency channel to a known amount of flux density to correct for this and other frequency dependent effects in the transmission of the signal. The same bright source can be used for this purpose, the so called *bandpass calibrator*. In Figure 2.10 (right) we can see the response of the bandpass after applying the calibration, where the gain is now constant with frequency.

2.4.3 Flux Calibration

To convert the gain scaling during the observations to an absolute flux density scale, the *flux calibration* is applied. For this calibration, a source[11] with well known flux density is observed,

[10] A passband is a frequency band within which signals are transmitted by a filter without attenuation.

[11] At wavelengths shorter than a few centimeters extragalactic sources are generally too variable to be used as flux calibrators, hence blackbody emission from planets are often used as flux standards.

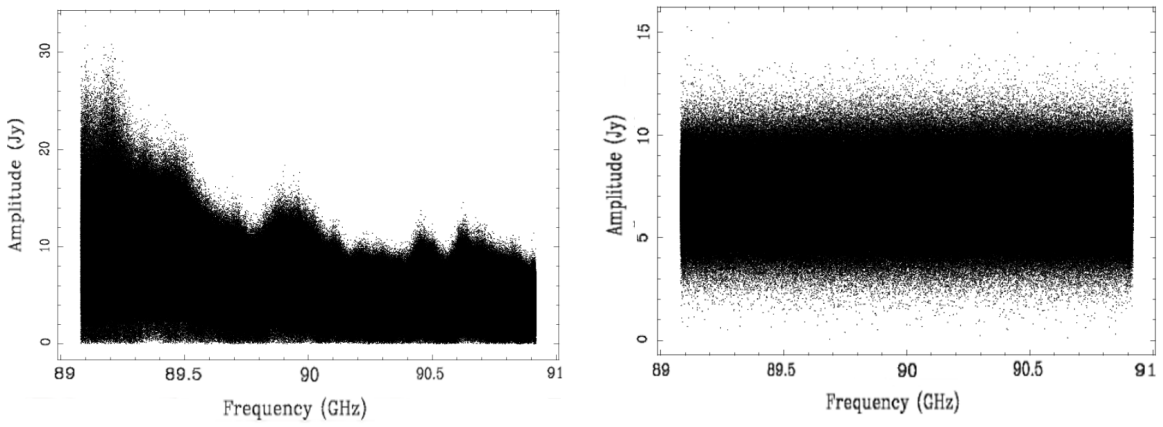

Figure 2.10 : Bandpass response along the band in one of the 2 GHz spectral windows of ATCA. *Left*: We can see how the transmission is frequency-dependent and the channels have different flux levels. *Right*: After applying the bandpass calibration the gain over the whole band is constant.

ideally at the same elevation as the target and as high in elevation as possible to reduce gain-elevation and airmass effects. However, at low frequencies these effects are not so important as the atmospheric effects are not that large. Normally, flux calibrators are observed by the observatory from time to time to determine good models to scale properly the flux density of the targets. With this model the flux calibration calculates what the flux should be on each baseline and for all frequencies across the band. Then it determines by how much the gains must be scaled by to make the observed flux at the centre of the band match the model value. Finally it scales all the data-sets it has been given by that factor.

2.4.4 Gain Calibration

The antenna gain varies significantly with time during the observations. Two main effects become significant in the gain variation of the antennae: variation in the instrument (e.g. receiver power level settings, corruption of baseband samplers, etc) and changes in the environment and atmosphere (e.g. weather conditions, position of the sun, water content). These produce thermal effects in the gain of the antennae which can vary this value up to 25% in some cases.

Assuming that these fluctuations are due to slowly varying amplitudes and phases we can correct these effects with the *gain calibration*. To do so, we need to observe the *phase calibrator* which needs to be a source close to the target ($\leq$ 10 deg). The reason for this calibrator to be close is to study the local conditions in the atmosphere which affect the visibility. Therefore, the distance between the source and the calibrator has to be such that both sources suffer from the same corruption. This calibrator is observed often enough during the whole run to track

properly the variation of the visibility with time. The time interval between phase calibrator scans has to be smaller than the coherence time of the atmosphere at the observed wavelength, the coherence time being when the visibility phase has changed one radian. These variations are slow so a relative smooth function can be interpolated which represent the real variation of the antennae. An example of the amplitude and phase gains before and after applying this correction is shown in Figure 2.11. Here, we can see in the left-hand of these plots how the amplitude and phase vary with time while in the right-hand plots, where the calibration is applied, there is no dependency of amplitude and phase with time.

After applying all these calibrations we can still have some residual errors in our data. To obtain a better model to fit, we can use our own target to create a model and calibrate over some solution interval. This process is called *self-calibration* and can be repeated to obtain a better quality in our final image. This calibration can correct for residual amplitude and phase errors as well as for direction dependency effects. However, errors in the model (in the case of low S/N) can propagate into the self-calibration solutions producing a divergence from the correct model. Due to the low signal to noise of our targets in Chapter 3 and the fact that a very accurate calibration for the sources studied in Chapter 4 was not needed, this type of calibration was not applied in this thesis.

2.5 ATCA and the VLA Facilities

For several chapters in this thesis radio observations were carried out with the Australian Telescope Compact Array (ATCA) and the Very Large Array (VLA). While the VLA observations were done in service mode, the ATCA observations were done in the control room in Narrabri or Sydney, and remotely from different locations. Here we summarise the main characteristic of these two radio telescopes.

2.5.1 Australian Telescope Compact Array

ATCA is located at the Paul Wild Observatory, in New South Wales, about 25 km west of the town of Narrabri. The observatory, together with other radio observatories in Australia, is part of the Australia Telescope National Facility (ATNF) operated by the Astronomy and Space Science division of the Commonwealth Scientific and Industrial Research Organisation (CSIRO). ATCA consists of an array of six antennae of 22 m dish diameter (Figure 2.12 left) with a Cassegrain design, located at 237 m above sea level. The array is mounted over a system of tracks such that the antennae can be moved to obtain different configurations. Five antennae can be moved along the tracks while the sixth antenna is located at a fixed position, which

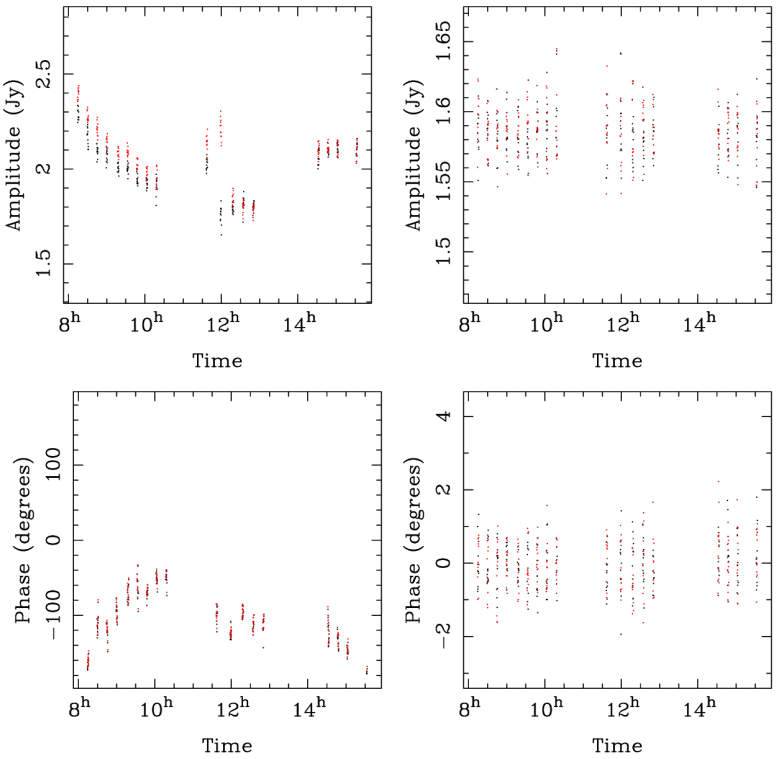

Figure 2.11 : *Top*: From left to right representation of how the amplitude of the phase calibrator varies with time before and after the gain calibration is applied. *Bottom*: Again, from left to right variation of the phase versus time before and after applying the gain calibration. We see how after the calibration the variation of the gain with time is fixed. These plots correspond to one baseline of the phase calibrator during our observations with ATCA.

Figure 2.12 *Left*: ATCA in one of its compact configurations. Image credit: David Smyth. *Right:* Picture of the VLA with its characteristic Y-shape in one of the compact configurations. Image credit: Courtesy of NRAO/AUI

results in the longest possible baseline of 6 km. Five bands can be observed, between 27 cm to 3 mm (1.1 - 105 GHz).

For the work described in this thesis we observed at 3 and 7 mm with the compact configuration H214. In this configuration antenna-6 was not used as it is located far away from the core of the configuration and therefore it only would produce a loss in sensitivity. The H214 configuration was used to increase the S/N, as we were targeting very faint sources, but not the smallest possible configuration so that the beam could be sampled better and therefore making it easier to identify our targets. With a maximum baseline of 247 m a resolution of $\sim$ 3.3 arcsec (at 91 GHz) was achieved for the 3 mm observations, and primary beam of $\sim$ 30 arcsec. With the same configuration at 7 mm we obtained a resolution of $\sim$ 6.4 arcsec (at 48 GHz), and primary beam of $\sim$ 1 arcmin.

2.5.2 The Very Large Array

The VLA is located on the Plains of San Agustin, at $\sim$ 80 km west of Socorro, New Mexico, and it is operated by the National Radio Astronomy Observatory (NRAO). The VLA consists of 27 antennae of 25 m dish diameter with a Cassegrain design in a Y-shape configuration at 2,124 m altitude (Figure 2.12 right). The antennae are located on a track with three arms of 21 km each allowing different configurations with a maximum antenna separation of 36 km. The VLA is sensitive at centimetric wavelengths covering 0.6 to 410 cm (50 GHz - 73 MHz), divided into eight different bands.

For this thesis the C-band was used, covering a bandwidth of $4-8$ GHz with primary beam of $\sim$ 7 arcmin. Observing in configurations B and BnA, with a maximum baseline of 11.1 km we obtained a synthesised beam of $\sim$ 1.1 arcsec.

Chapter 3

Dusty Star-Forming Galaxies at High Redshift

3.1 Introduction

High-redshift DSFGs comprise a population of massive, intensely star-forming galaxies in the early universe (see Section 1.3.1), representing an important phase in the assembly and evolution of massive galaxies. This important population with extreme properties, SFR $\sim 3,000$ $M_{\odot}yr^{-1}$ at $z > 4$, are the prime candidates to be the progenitors of the oldest and most massive elliptical galaxies in today's universe (e.g. Lilly et al., 1999; Swinbank et al., 2009; Casey et al., 2014; Oteo et al., 2017). Only a small number of galaxies at $z > 4$ have been found (e.g. Riechers et al., 2013; Dowell et al., 2014; Smolčić et al., 2015; Oteo et al., 2018). Currently, new wide area sub-mm/mm surveys allow us to determine their number density, where a selection based on sub-mm colour is used to look for the reddest sub-mm sources. Follow-up observations of such systems have shown molecular gas and dust content similar to the DSFGs population at $z = 2$ (i.e. molecular gas reservoirs of $\sim 10^{10}$ $M_{\odot}$, CO linewidths of $\sim 1,000$ $km\,s^{-1}$ and an implied $M_{dyn} \sim 10^{10} - 10^{11}$ $M_{\odot}$). These systems could potentially evolve into a 'red and dead' elliptical galaxy at $z = 2$ (e.g. Schinnerer et al., 2008; Riechers et al., 2010; Stach et al., 2017; Yang et al., 2017).

The DSFGs population is believed to contain a mixture of rare hyper-luminous infrared galaxies (HyLIRGs) and lower luminosity ultra-luminous infrared galaxies (ULIRGs) that are gravitationally lensed. Gravitational lensing is a powerful tool to help identify and study examples of this high-redshift population, which is believed to be responsible for the bulk of the Far-Infrared Background (Blain, 1996). The effect of lensing makes galaxies easier to detect, as it boosts the measured flux of the galaxies and improves their spatial resolution, which

otherwise result in high confusion limits. With the use of *Herschel*, a mixture of HyLIRGs ($L_{IR} > 10^{13}$ $L_{\odot}$) and gravitationally lensed ULIRGs ($L_{IR} \sim 10^{12} - 10^{13}$ $L_{\odot}$) have been revealed at the bright end ($S_{500} > 80$ mJy) of the high-redshift population (see Section 1.3.5).

In this study we present a followed-up sample of potential high-redshift *Herschel*-sources to fill in the highest end of the DSFGs redshift distribution. We classify these galaxies as lensed or intrinsical HyLIRGs and calculate their spectroscopic redshift via CO lines. Identified unlensed sources include the most intrinsically luminous starburst in the universe occurring just after the epoch of re-ionization and will become part of follow-up programs on other mm/sub-mm interferometers (ALMA/SMA). Lensed sources will become part of the lens follow-up program which aims to understand the redshift evolution of dark matter haloes to determine the cosmography of the universe. The lensing magnification will allow a dissection of their ISM structure and composition through the improvements in sensitivity and angular resolution that lensing affords.

This chapter is divided as follows. In Section 3.2 we expound the methodology followed in this work. In Section 3.3 we present the sample selection and the information related with the ATCA proposals. The radio study can be found in Section 3.4 and Section 3.5 where the observations, data reduction and data analysis for the continuum and spectroscopic data at 3 mm and 7 mm are explained respectively. In Section 3.6 the near-infrared (NIR) observations, data reduction and data analysis of the potential lens galaxies can be found to determine the lensed origin of the *Herschel*-sources. In Section 3.7 we identify and characterise these sources and compare with others in the literature. Finally, in Section 3.8 the main conclusions of this study are discussed.

3.2 Methodology

Confirming and exploring samples of potential lensed DSFGs requires the following steps:

1. Look for candidates of lensed galaxies.
2. Identify the redshifts of the *Herschel*-sources via CO redshifts surveys.
3. Study the NIR counterparts that in combination with the interferometric imaging allow us to identify if these galaxies are lensed or intrinsically luminous starbursts.
4. In the case of lensed galaxies, obtain redshifts for the lenses.
5. Obtain high resolution imaging, and multiple-J CO observations to allow full lens modelling and spatially resolved detailed investigation of the ISM conditions in the high-redshift DSFGs.

With this in mind, our first step was to select candidates of lensed galaxies. Negrello et al. (2010) showed that a high fraction (close to 100%) of the reddest sources ($S_{500} > 80$ mJy) in the H-ATLAS catalogues were most likely lensed galaxies (see Section 1.3.5). Using these catalogues[1] a colour-selection was applied to select the reddest sources. Then, photometric redshifts (z_{phot}) were determined to select the most distant galaxies for our sample. More about the sample selection can be found in Section 3.3.

To identify the redshifts of the sources via CO lines, several observations with ATCA were done. Doing a blind search of CO lines with ATCA is very time consuming due to the small size of the bandwidth in the radio antenna receivers (two spectral windows of 2 GHz width each, i.e. 4 GHz bandwidth). Thus, an estimation of the redshift became essential to determine the most likely frequency ranges where a line could be found. Following Lapi et al. (2011) we estimated z_{phot} for these sources from the *Herschel*-SPIRE bands at 250-350-500μm with a precision of $\simeq 30\%$.

The next step was to identify the NIR counterparts. González-Nuevo et al. (2012) showed that a significant number of sources from H-ATLAS with high estimated redshift were close to objects on NIR images from the VISTA survey[2]. The probability of a chance alignment was determined to be $< 10\%$, so most likely the NIR object was associated with the *Herschel*-source, either because the NIR and the *Herschel* emission were from the same galaxy or because the *Herschel* emission was being lensed by the NIR object. These objects always had much lower redshift than those estimated for the *Herschel*-sources, implying that they were the result of lensing. To carry on with the observations at NIR we observed at K_s-band with the GEMINI-South Telescope with its wide field NIR-camera FLAMINGOS-2. These data allowed us to identify the origin of the sub-mm emission, determine if these galaxies were acting as lenses and measure their stellar properties.

The final two steps to confirm the origin of our small sample (obtain optical redshift for the lenses and multiple-J CO observations to allow full lens modelling) were not possible to finish during this thesis. However, our groundwork will be part of the lens follow-up program which aims to understand the redshift evolution of dark matter halos.

3.3 Sample Selection and ATCA Proposals

Negrello et al. (2007) predicted that sources with $S_{500} > 100$ mJy in H-ATLAS comprised a mixture of lensed, high-redshift DSFGs plus 'contaminants': blazars, nearby ($z < 1$) spirals

[1] The sources in this chapter were selected from the H-ATLAS Phase-1 versions 2 and 3 internal data release.

[2] VISTA was conceived as a NIR survey telescope (Sutherland et al., 2015). With a primary mirror of 4.1 m, this telescope is the largest of its kind. VIRCAM is VISTA's IR Camera operating at $0.8 - 2.3$ μm and with a 1.65 deg diameter FOV.

and galactic sources (see Section 1.3.5). These contaminants are all easy to identify and remove via NVSS/WISE/optical data. Thus, for our first proposal (OCT2013) the sample was chosen as a pilot H-ATLAS selection from 90 deg^2 of imaging in the SGP field at $\delta \sim 33$ deg with $S_{500} > 100$ mJy. To select the reddest sources after the colour criteria, a z_{phot} selection was applied. The infrared luminosities and z_{phot} were estimated from fitting the $250-350-500\mu$m fluxes to a minimum χ^2 of three to seven SED templates[3,4] (Figure 3.1). Because we were using preliminary catalogues of H-ATLAS, an average error for the three SPIRE bands (7, 8 and 9 mJy for 250-350-500 μm) was considered in this occasion. In addition, a 7% error in quadrature was added as well following the *Herschel* manuals[5]. Our best estimation of L_{TIR} and z_{phot} was obtained by averaging the best-fit from the separate templates. Aiming for the reddest sources we selected sources which $z_{phot} > 3.8$ resulting in a sample of 3 galaxies with $S_{250} < S_{350} < S_{500}$ and $S_{500} > 100$ mJy.

To estimate the expected CO fluxes (S_{CO}) we considered the $r_{J\rightarrow J} = L_{IR}/L'_{CO}$ ratios of ~ 140 for CO(1-0) found in many studies of high-redshift DSFGs (e.g. Frayer et al. 2011). To convert to the higher-J lines transitions we used $r_{21} = 0.8$, $r_{31} = 0.6$, $r_{41} = 0.4$, which are representative of the kind of systems we were targeting (Frayer et al. 2011). The line luminosity (L'_{CO}) was converted to estimate S_{CO} using the following relation given in Solomon & Vanden Bout (2005)

$$L'_{CO} = 3.25\times10^7 S_{CO}\Delta v \upsilon_{rest}^{-2}(1+z)^{-1}D_L^2 \tag{3.1}$$

where L'_{CO} is measured in K km s^{-1} pc^2, the velocity-integrated flux ($S_{CO}\Delta v$) in Jy km s^{-1}, the rest frequency ($\upsilon_{rest} = \upsilon_{obs}(1+z)$) in GHz and the luminosity distance (D_L) in Mpc.

[3]During this study different estimations were done at different moments of this thesis. The z_{phot} for the very first sample was estimated with only three templates while for the last one seven templates were used. These templates are M82, Pearson+13 and Arp220 for the first case and Arp220, eyelash-rest (SMMJ2135-0102), Pearson+13, ALESS, G15.141, HFLS3 and Pope+08 for the other ones.

[4]**M82**, Messier 82, is a starburst galaxy about 12 millions light-years in the constellation of Ursa Major.
Arp220 is a collision between two galaxies which are now in the process of merging. Located 250 millions light-years away in the constellation Serpens, it is the 220th object in Halton Arp's Atlas of Peculiar Galaxies.
Cosmic eyelash, formally called SMMJ2135-0102, is a galaxy that lies at $z = 2.32$ and its brightness of 106 mJy at 870μm is due to the gravitational magnification caused by a massive intervening galaxy cluster.
Pearson+13 is an averaged sub-mm galaxy template derived from a sub-set of 40 H-ATLAS sources with known spectroscopic redshifts between $0.5 < z < 4.2$ (Pearson et al., 2013).
ALESS is an averaged SED of the 122 DSFGs of the ALESS-ALMA survey (da Cunha et al., 2015). This SED resembles that of local ultra-luminous infrared galaxies at infrared wavelengths, but whose stellar emission is brighter and bluer. This indicates lower dust attenuation, possibly because these galaxies are more extended.
G15.141 is a very strong lensed DSFG at $z \sim 4.24$ with estimated SFR of several hundreds $M_\odot yr^{-1}$ (Cox et al., 2011).
HFLS3 is a galaxy at $z \sim 6.34$ whose star formation rate is much faster than should be according to the existing predictions (Riechers et al., 2013).
Pope+08 is an average SED derived from dust-obscured galaxies in the GOODS-N field (Pope et al., 2008).

[5]herschel.esac.esa.int/twiki/bin/view/Public/SpireCalibrationWeb

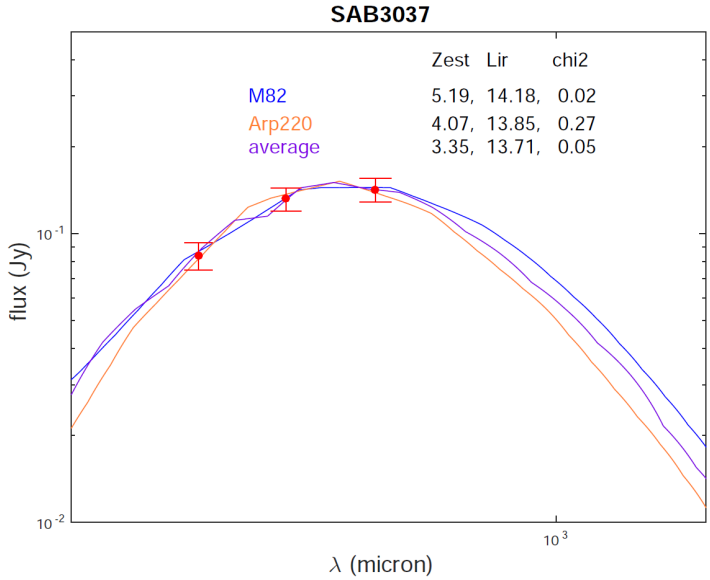

Figure 3.1 : Estimation of the z_{phot}, L_{TIR} and χ^2 for one of our targets. Three SED templates were used (M82, Arp220 and the averaged Pearson+13). The final estimation was obtained averaging the best results of the different templates.

Assuming the CO linewidth is in the range of $300-800\,\mathrm{km\,s^{-1}}$ (Harris et al., 2012), we considered a $\Delta v = 500\,\mathrm{km\,s^{-1}}$ producing peak fluxes in the range of 8 - 11 mJy for the CO(4-3) line. Using this value we estimated the sensitivity needed to detect the corresponding lines at the required bandwidth with ATCA. The information of the 3 targets observed at 3 mm with the approximated S_{CO} and z_{phot} can be found in Table 3.1. Ideally, these observations provide imaging and spectroscopic data which produce optical identification and redshift for the DSFGs. The detection of the CO line gives as well additional information on the mass of the dense gas, which allows determination of the star-formation efficiency. The linewidth gives a crude first estimation of the lensing magnification (Harris et al. 2012).

Table 3.1 : Sample for the OCT2013 proposal at 3 mm. The coordinates correspond to those at 250μm from SPIRE. Flux densities of the SPIRE bands from the H-ATLAS Phase-1 version2 catalogue were used to estimate the z_{phot}, L_{TIR} via SED fitting, and $S_{CO(4-3)}$ line fluxes.

ID	RA (deg)	DEC (deg)	S_{250} (mJy)	S_{350} (mJy)	S_{500} (mJy)	z_{phot}	log L_{TIR} ($L_\odot$)	$S_{CO(4-3)}$ (Jy km/s)
SAB3037	347.0642	-34.6326	84 ± 9	132 ± 12	142 ± 13	4.2 ± 0.6	13.94	5.6
SAB5264	340.5302	-32.7001	69 ± 8	94 ± 10	109 ± 12	4.0 ± 0.6	13.78	4.2
SAB2956	346.4423	-33.1771	83 ± 9	121 ± 12	117 ± 12	3.8 ± 0.6	13.81	4.8

An example of the estimated z_{phot} for our first sample is shown in Figure 3.2 where the flux density ratios of the SPIRE bands are represented in the x and y axes and the colour bar

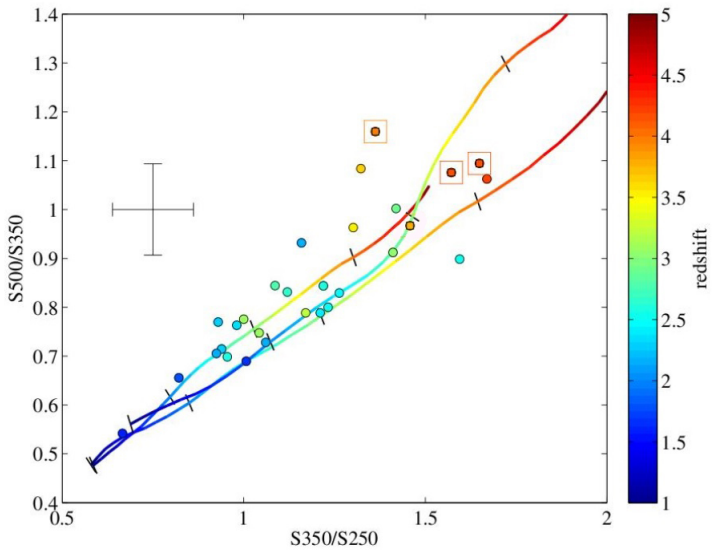

Figure 3.2 : Estimation of the z_{phot} for our first sample of galaxies. Tracks are the SED templates for M82, Arp220 and Pearson+13. The x and y axes are the flux density ratios of the SPIRE bands. The error bars can be found on the left of the image and the colour-bar to the right represents the redshifts of the SEDs templates. This plot shows the likely z_{phot} of our targets where the final sample is marked with coloured squares.

represents the z_{phot}. Our sample of red sources is highlighted with coloured squares. In this proposal we aimed to detect some of the CO J = 4-3 through 6-5 lines which for galaxies at $z > 3.5$ are located at the 3 mm band, the transition where the CO Spectral Line Energy Distribution (SLED) usually peaks (Ao et al. 2008). Figure 3.3 shows the location of our 3 targets in the 3 mm window and the range where the lines are expected to be. 36 hours were allocated for us in this semester. No lines were detected for any of the targets, although continuum was detected for two of them as explained in Section 3.4.2.

The data obtained at 3 mm showed a very high weather dependency, as we explain in Section 3.4.2, and therefore we could not assure that any of the lines could be present in some frequencies observed at this band. We decided thus, for our last two proposals (OCT2015 and APR2016) to aim for the CO(2-1) line of our two detected continuum galaxies at 3 mm, SAB3037 and SAB5264. In this case a better estimation of the z_{phot} was expected as photometry for 5 bands was available: 250-350-500μm from SPIRE, 870μm from LABOCA (Alexander Lewis, *priv. comm.*) and 3 mm from ATCA (Table 3.2). For the calibration errors we added 7% error in quadrature for SPIRE, 15% for LABOCA and 10% for ATCA. Seven templates[6] were used to estimate our needed values as explain in Section 3.2. We used the z_{phot} and L_{TIR} given by Alexander Lewis (*priv. comm.*) who used a more developed code for this purpose. However,

[6]ALESS, Arp220, Eyelash, G15.141, HFLS3, Pearson+13 and Pope+08.

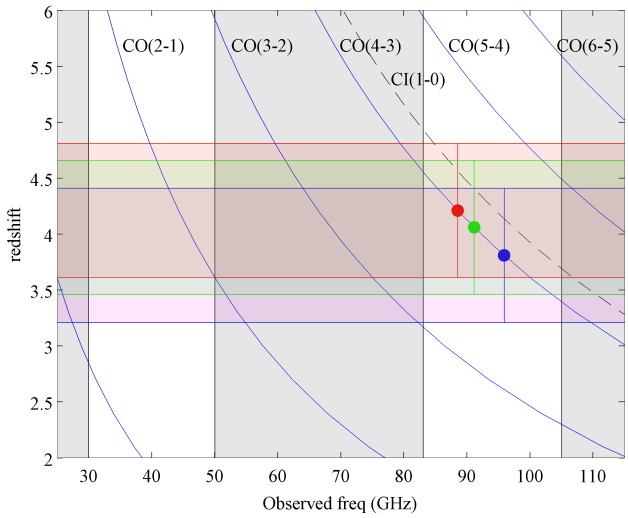

Figure 3.3 : z_{phot} of the 3 targets with their uncertainties shown as colour-shaded regions. The shifted CO lines within the ATCA bandwidths are shown in blue. The white-background windows indicate the ATCA available receivers at 3 mm (85-105 GHz) and 7 mm (30-50 GHz) and the grey-background windows represent frequency ranges not covered by ATCA.

these estimations were not as accurate as we would desire for an effective blind CO line search. In Table 3.3 the z_{phot} and χ^2 fitting of the best two out of the seven templates are shown. Here we can see for instance, that for SAB3037, similar χ^2 result in very different z_{phot}. Hence, the only assessment we assumed after studying all the fittings was that there was a tendency towards redshifts $3 < z < 4.7$. For these values of z_{phot} the CO(2-1) line is located in the 7 mm window or even outside this window as we can see in Figure 3.4. So it was possible that the line was outside the band for some of the targets and therefore not detectable. The estimated fluxes of the CO(2-1) lines are listed in Table 3.3. 19.5 + 17.5 hours were allocated in these two runs. Lines for both galaxies were detected (Section 3.5.2).

Table 3.2 : Fluxes from H-ATLAS (250, 350 and 500μm), LABOCA (870μm) and ATCA (3 mm) are shown in this table. The SPIRE fluxes were obtained from the H-ATLAS Phase-1 version 3 catalogue.

ID	S_{250} (mJy)	S_{350} (mJy)	S_{500} (mJy)	S_{870} (mJy)	S_{3mm} (mJy)
SAB3037	79 ± 8	135 ± 10	140 ± 11	55 ± 7	0.925 ± 0.133
SAB5264	73 ± 8	88 ± 9	101 ± 10	42 ± 6	0.562 ± 0.085

Table 3.3 : The best two fits of seven templates are shown for z_{phot}, χ^2, log L_{TIR} and $S_{CO(2-1)}$. We see that with very similar values for χ^2 very different z_{phot} are obtained. Hence, we can only assume that the redshifts aim to be $3 < z < 4.7$ for both our galaxies.

ID	z_{phot}	χ^2	logL_{TIR} ($L_\odot$)	$S_{CO(2-1)}$ (Jy km/s)
SAB3037	3.36-4.68	1.42-1.81	13.61-13.90	1.90-2.16
SAB5264	3.96-3.04	2.31-3.21	13.69-13.45	1.74-1.53

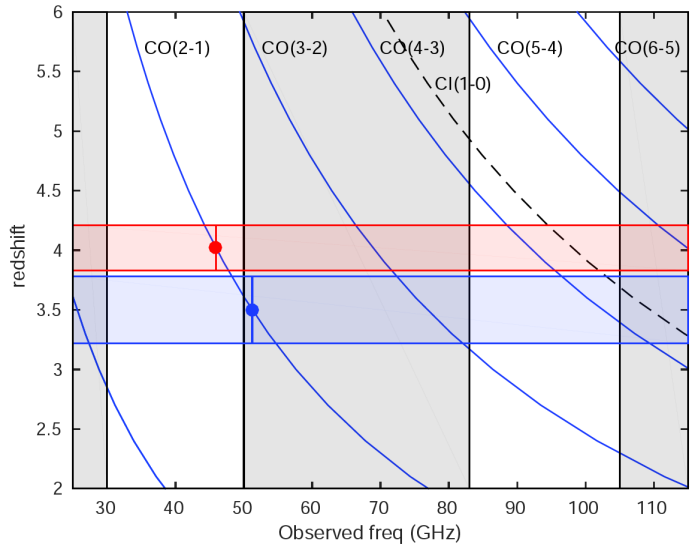

Figure 3.4 : Location of the targets in the 7 mm window in accordance with the estimated averaged z_{phot} for the seven SEDs fits. Note that the grey-background regions represent frequency ranges not covered by ATCA. We expected $z > 3.6$ so the CO(2-1) lines would be detectable, i.e. inside the 7 mm window.

3.4 Radio Observations at 3 mm

Our first run was in October 2013 over a period of 6 nights. 36 hours of allocated time were divided into 4 different targets. One of them is the so called *dusty red core* (DRC) which we observed as part of a collaboration (Oteo et al., 2018). Thus, 16 hours were used to observe our three DSFGs and 20 hours for DRC[7]. The Compact Array Broadband Backend (CABB) of 2×2 GHz bandwidth was used, with 2048 channels and 1 MHz spectral resolution. The H214 compact configuration without antenna-6 was chosen to improve the u-v coverage and to

[7]This source was found to be a proto-cluster of galaxies at spectroscopic redshifts 4.002 consisted of at least ten DSFGs. Their redshifts were determined via ATCA and ALMA observations of different lines. As part of the collaboration we carried out NIR observation with GEMINI to study the lensed origin of this source. In addition we did several observations with ATCA detecting continuum at 7 mm, 5.5 GHz and 9 GHz as well as two CO lines for one of the DSFGs.

increase the surface brightness sensitivity. The primary beam for H214 at 91 GHz is ~ 30 arcsec. The system temperature varied ± 100 K during these observations.

As explained in Section 2.4, some sources need to be observed along the observations in order to calibrate our data. The bright source, 1921-293, was visited three times (once at the start, once at the end and once sometime near the middle[8]) for 10 minutes as bandpass calibrator to determine how the bandpass solution changes over time. The flux density was calibrated with Uranus. As phase calibrator as well as paddle calibrator a bright and close source from the target was observed every 10 minutes for 2 minutes (2240-260 for SAB3037 and SAB2956; 2255-282 for SAB5264). The paddle calibration is only needed at 3 mm because the atmosphere at these frequencies is very turbulent. The purpose of this calibration is to determine how the system temperature varies, as the apparent brightness of the targets will depend on this. The pointing was updated on the phase calibrator every hour.

Following our first redshifts estimations, which indicated $z_{phot} \sim 4$, we started the observations at lower frequencies which correspond with higher redshifts ($z = (\nu_{emit} - \nu_{obs})/\nu_{obs}$). Continuum was detected for 2 out of the three targets but no lines were detected for any of them. With a synthesised beam ~ 2.2 arcsec the sources were not resolved, but more accurate positions for the DSFGs were determined.

3.4.1 3 mm Data Reduction

The data reduction was done with MIRIAD (Sault et al., 1995), a radio interferometry data reduction package specially used for ATCA data. This package allows to do the reduction of continuum and spectral lines, synthesis imaging and analysis of the products. A detailed explanation of the necessary steps for calibrating the data and create the synthesised images with an interferometer can be found in Chapter 2. Here, we point out the general steps nominating the MIRIAD-tasks for the different purposes.

1. ATCA data are initially in RPFITS format. To convert to MIRIAD's format we used the task `ATLOAD`. This task allows to process some known issues and correct them from scratch. For instance, unusable channels in the edges (~ 100 channels from the bottom and top of the channel spectrum) and those located at known wrong frequencies are flagged. With the task `ATFIX` some off-line corrections were applied at 3 mm. This task applies gain/elevation[9] effects, system temperature measurements, corrections for incorrect baselines length and instrumental phase and corrections of antenna tables (i.e

[8] Following the ATCA manual, for spectral line observations the CABB bandpass is not perfectly stable over the course of a normal 12 hours observation, so it is recommended to visit this calibrator three times during this period.

[9] Because the big size of the antennae (22 m diameter), the distortion of the dishes by gravity is also significant.

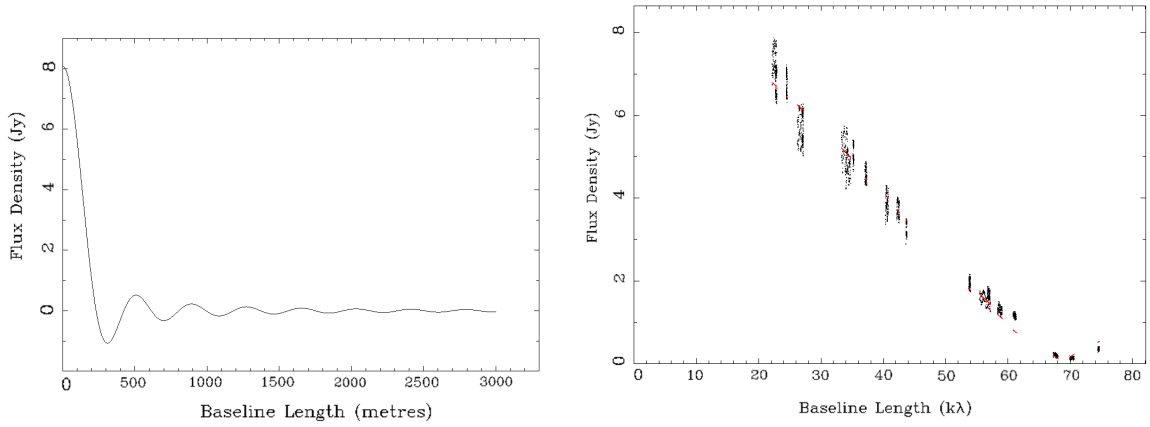

Figure 3.5 : *Left*: Variability of Uranus' visibility as function of baseline distance. *Right*: Representation of Uranus' visibility for the 3 mm observations in black dots and the best-fit model in red.

when an antenna is off-line). As mentioned before, at 3 mm it is necessary to do a paddle calibration. The 'paddle scans' are usually tens of minutes apart, during which time the system temperature recorded by the correlator does not change. To make MIRIAD interpolate the system temperature between the paddle scans `ATFIX` is used as well. The data were split with `UVSPLIT`, creating different data-sets each containing an individual source at a single central frequency.

2. Flagging was done before and after calibrating the data. MIRIAD supports two modes of flagging, automatic or manual. Due to the small amount of RFIs (see Section 2.4) at this frequency we flagged the data manually with `BLFLAG`. In case any flagging was needed after the first calibration, the data were re-calibrated.

3. The bandpass calibration was applied with `MFCAL`. The flux density model for 1921-293 at 90 GHz is S $\sim$ 6.77 Jy. The calibrated flux at this frequency resulted in a measured flux of S $\sim 6.90 \pm 0.01$ Jy, which represent an error of 2%. Then we copied this calibration to the flux calibrator with `GPCOPY`.

4. To set the proper flux scale we used the task `MFBOOT` with Uranus as flux calibrator. In Figure 3.5 (left) we can see how Uranus' flux changes with baseline distance in meters. Because we were using the H214 configuration the highest distance between baselines is 247 m. In Figure 3.5 (right) we can see how the model (in red) fits with the measured visibilities (black-dots). We copied then this calibration to the phase calibrator with `GPCOPY`.

Table 3.4 : Information for the observations at 3 mm for the continuum maps. The expected r.m.s. was calculated with the ATCA sensitivity calculator under standard weather conditions.

ID	Frequencies (GHz)	Integration time (hours)	Expected r.m.s. (mJy/beam)	r.m.s. (mJy/beam)
SAB3037	90-92	2.76	0.27	0.17
SAB5264	86-96	13.14	0.13	0.11
SAB2956[a]	90-92	2.96	0.27	0.17

[a]This source was not observed at 7 mm.

5. To determine antenna gains and leakages we used `GPCAL`. We must consider the gain variation when bootstrapping the flux density scale so to correct for this effect we use `GPBOOT`.

6. All that remains is to transfer the calibrated tables to the targets with `GPCOPY` and average (i.e. smooth) the gain solutions with `GPAVER`. Once the calibration is finished the continuum maps and/or spectral cubes from the calibrated visibilities can be generated.

Imaging

To create the continuum maps we used the task `INVERT`. A pixel size of 1/5 of the synthesised beam was chosen to sample the beam, i.e. a pixel size of 0.4 arcsec. A map twice the size of the primary beam was created to confirm no contamination was coming from bright sources within the primary beam. Because we want to optimise the sensitivity of our point source, we chose 'natural weighting'. Selecting multi-frequency synthesis we coadded different frequencies in the same map thereby increasing the S/N. We can then create the dirty beam and dirty map (Figure 3.6 top-left and right respectively) with `INVERT`. The resulting synthesised beams are 2.80×1.63 arcsec^2 (P.A. = 70 deg) and 2.06×1.77 arcsec^2 (P.A. = 115 deg) for SAB3037 and SAB5264 respectively.

To do the imaging deconvolution we used `CLEAN`. This task produces an output map which consists of the clean components which are restored into the clean map with `RESTOR`. Moreover, this task calculates residuals as well as convolves the model by the Gaussian beam. Once we have the clean image (Figure 3.6 bottom-left), we apply the primary beam correction with `LINMOS`. This corrects the falling sensitivity towards the edges of the primary beam by dividing the continuum map by its flux distribution. This 'clean-primary-beam-corrected' image is our final calibrated map (Figure 3.6 bottom-right). We did not apply self-calibration because the S/N for these sources was too weak and this could result in wrong solutions (see Section 2.4.4). The interval of covered frequencies, total on-source integration times, expected r.m.s. and achieved r.m.s. for each of the targets can be found in Table 3.4.

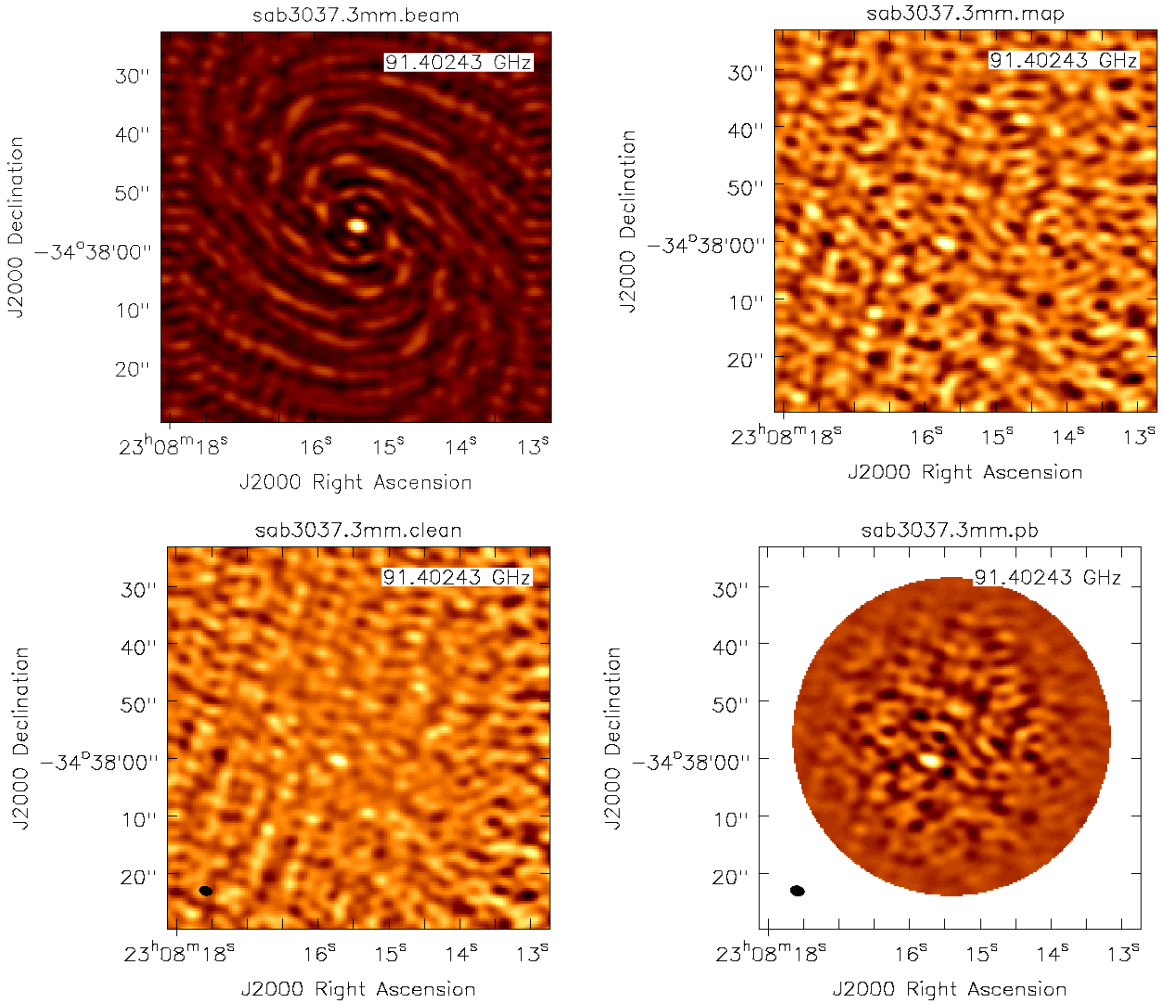

Figure 3.6 : From left to right and top to bottom, this figure shows: the dirty beam, dirty map, clean map and 'clean-primary-beam-corrected' map of SAB3037. The synthesised beam is shown in black in the bottom left corner.

Table 3.5 : Information for the observations at 3 mm for the spectral cubes. The expected r.m.s. was calculated with the ATCA sensitivity calculator under standard weather conditions. The r.m.s. is referred to the spectral cubes with a 32 MHz binning, i.e. $\sim 100\,\mathrm{km\,s^{-1}}$. Due to the variation in sensitivity at neighbouring frequencies due to weather dependency for SAB5264, it was impossible to assure whether there were CO lines in some of these frequencies.

ID	Frequencies (GHz)	Integration time (hours)	Expected r.m.s. (mJy/beam)	r.m.s. (mJy/beam)
SAB3037	90	1.38	3.11	2.45
SAB3037	92	1.38	2.86	1.74
SAB5264	86	2.63	2.61	1.50
SAB5264	88	2.63	2.54	3.42
SAB5264	90	1.97	2.61	2.03
SAB5264	92	1.97	2.39	1.46
SAB5264	94	1.97	2.10	6.06
SAB5264	96	1.97	2.39	4.89
SAB2956[a]	90	1.48	3.01	2.43
SAB2956[a]	92	1.48	2.76	1.75

[a]This source was not observed at 7 mm.

Spectral cubes

The spectral cubes were created from the visibilities using the same task as for the imaging, `INVERT`. Similar parameters were selected but in this case instead of multi-frequency synthesis we processed the channels of the bandwidth to create a cube. For those channels which were flagged a linear interpolation of two adjacent good channels was applied. Cleaning and primary beam correction must be applied analogous to the method for the continuum maps. The CO linewidth for this type of galaxies is expected to be in the range of $\sim 300-800\,\mathrm{km\,s^{-1}}$ (Harris et al., 2012), so an initial good guess of the linewidth is $\Delta v = 500\,\mathrm{km\,s^{-1}}$. The ATCA 2 GHz spectral window has 2048 channels with a resolution of $3.295\,\mathrm{km\,s^{-1}}$ (1 MHz) at 91 GHz. Thus, we can bin channels to achieve a resolution of $\sim 100\,\mathrm{km\,s^{-1}}$ (32 MHz), increasing the sensitivity by a factor of 6. The information of covered frequencies, total on-source integration times, expected r.m.s. and achieved r.m.s. for the different cubes for a channel width of 32 MHz can be found in Table 3.5.

No lines were detected at these frequencies for any of the 3 targets (Figure 3.7). However, the noise at the 3 mm band was very weather dependent as shown in Table 3.5 (see SAB5264 which has a bigger covered frequency range). At neighbouring frequency tunings the noise varied by more than a factor of 2, so the limits in poorer conditions were too high to allow detection of lines at the expected level, and did not allow us to exclude that the line could be in those frequency ranges. Additionally, the spectral windows were centred such that there

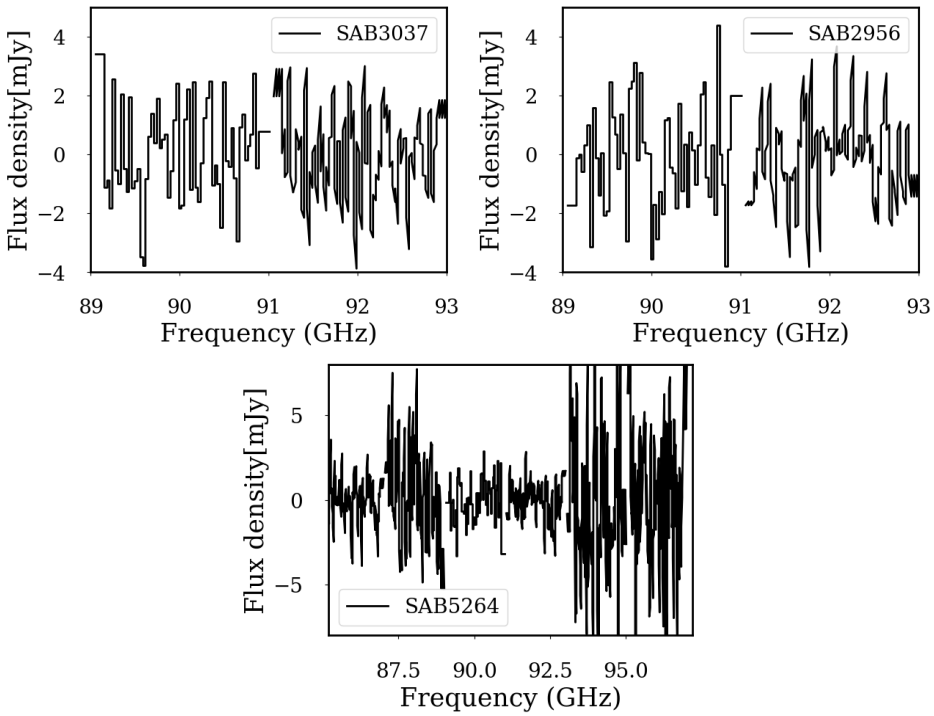

Figure 3.7 : Spectra for the three different targets at 3 mm where no line is detected for any of them. The cubes were binned achieving a resolution of ~ 100 km s^{-1} increasing the sensitivity by a factor of ~ 6. In the bottom figure we can see how the r.m.s. is much higher for some of the spectral windows. This is due to the dependency of the antennae with temperature which at 3 mm is more sensitive. Hence, this band is very weather dependent.

were a few gaps[10] in the frequency coverage due to useless channels in the edges of the spectral windows where potential lines could be located.

3.4.2 Photometry

To analyse the 3 mm continuum maps we used the software CASA because it is more interactive than MIRIAD and therefore easier to use. We detected continuum for two galaxies above 3σ, SAB3037 and SAB5264. The fluxes were measured with the task `IMFIT`, which implements a 2D-Gaussian fitting in the selected aperture around the detected source. After subtracting the source, CASA creates a residual image where we can see how the subtraction of the flux was done. A uniform background noise in the residual image is expected as a result of a good subtraction of the source. The clean maps and corresponding residual images for the two sources can be found in Figure 3.8 left and right, respectively. The flux densities, r.m.s. and S/N are shown in Table 3.6. Because the galaxies were not resolved, the peak flux in the aperture

[10] Around 64 MHz between different tunings.

Table 3.6 : Photometry of the continuum maps at 3 mm with ATCA. This table shows the averaged central frequency, peak flux density and S/N for the detected sources.

ID	Avg. Frequency (GHz)	Peak Flux density (mJy/beam)	S/N
SAB3037	91	1.02 ± 0.27	5.8
SAB5264	90	0.43 ± 0.28	4.1
SAB2956	90	–	–

instead of the integrated flux was considered. Due to the absolute flux uncertainty, we added a 10% calibration error in quadrature, which is the value recommended for the ATCA 3 mm window in the ATCA's manual.

As well as pinpointing the location of our DSFGs, these fluxes allowed us to estimate a better photometric redshift to determine where the CO lines could be located in follow-up observations as explain in Section 3.3.

3.5 Radio Observations at 7 mm

For our last two proposals we observed 7 days with a total amount of 50.5 hours. We aimed to cover $3.6 < z < 6$ at the 7 mm window. During the run the system temperature varied in good conditions between 20 - 60 K and in bad conditions $\sim$ 250 K. The same configuration and resolution as for the 3 mm band was used. This is, H214 configuration without antenna-6 and CABB 2×2 GHz bandwidth with 2048 channels, 1 MHz spectral resolution and a primary beam of $\sim$ 1 arcmin at 48 GHz. After doing the z_{phot} estimation with more bands and SEDs templates we expected the targets not to be as red as previously thought (Section 3.3). Thus, we started the observation at higher frequencies, which correspond with lower redshifts as we can see in Figure 3.4. We wanted to cover all the 7 mm band for the two targets so optimising the observations was crucial. For this purpose the reduction and analysis of the data had to be done just after the run so in case a line was detected we could change to another target. The bandpass calibrator, 1921-293, was visited three times during a 12 hours observation similarly than for the 3 mm observations. The calibrator 1934-638 was used as flux calibrator at these frequencies, and the phase calibrator 2255-282 was visited every 10 minutes for 2 minutes according to weather conditions.

A CO molecular line was detected for both targets while continuum was not detected for any of them.

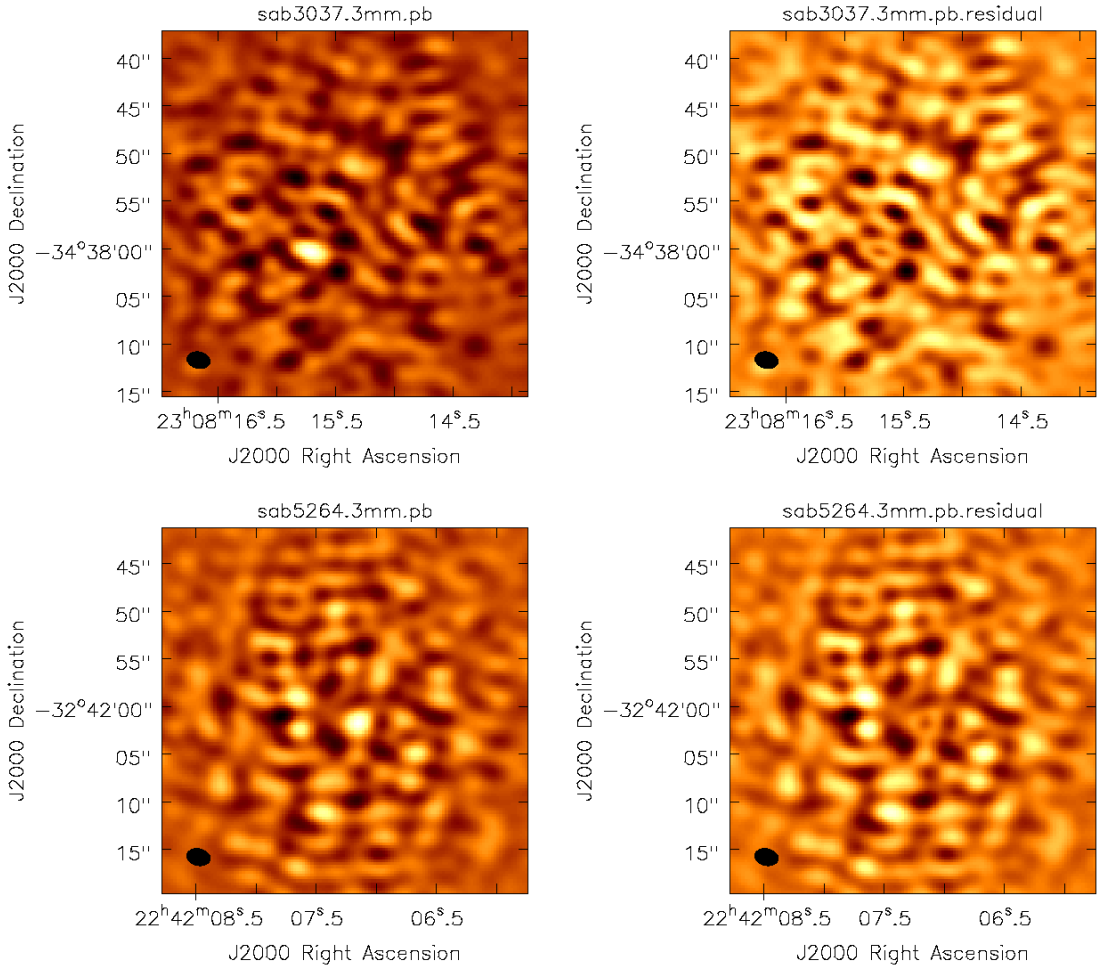

Figure 3.8 : From left to right and top to bottom, 'clean-primary-beam-corrected' continuum maps and residual images for SAB3037 and SAB5264. The residual image was created after subtracting the flux in the continuum map. The synthesised beam is shown in black in the bottom-left corner. We can see a uniform background noise in the residual images indicating a good subtraction of the flux density of the sources.

3.5.1 7 mm Data Reduction

As explained in Section 3.4.1 the data reduction was done with MIRIAD. The general steps for the 7 mm reduction are similar to the 3 mm windows, as follow:

1. The RPFITS format was converted into MIRIAD's format with `ATLOAD`. At this band this task corrects from the same defects as at 3 mm as well as for atmospheric opacity. The data were split in different directories with `UVSPLIT`.

2. Manual flagging was applied with `BLFLAG` before and after calibrating the data. The data-sets were re-calibrated when more flagging was needed after the first calibration.

3. The bandpass calibrator 1921-293 has a flux density S $\sim$ 6.69 Jy at 46.5 GHz. We corrected for bandpass with the task `MFCAL`, achieving a flux of S $\sim 7.35 \pm 0.01$ Jy at the same frequency, which means an error of around 10%. With the use of `MFCAL` we calibrated the antenna gains, passband responses and delay terms. We copied this calibration to the phase calibrator with `GPCOPY`.

4. The task `GPCAL` was used in the phase calibrator to correct from time variation in the gains. Then we copied this calibration to the flux calibrator with `GPCOPY`.

5. To do the flux calibration, first we used `GPCAL` on the flux calibrator. Then we applied `GPBOOT` in the same calibrator taking the phase calibrator as reference to scale the data to absolute flux units. At 7 mm the source PKS 1934-638 is recommended as flux calibrator[11] because it has a very well known and stable flux. `GPBOOT` compares the gains between the flux calibrator and the model and determines the factor to apply to scale the gains. At 46.5 GHz the flux of 1934-638 is S $\sim$ 0.29 Jy, and we obtained S $= 0.24 \pm 0.05$ Jy which represented an error of 17% in the flux calibration.

6. The phase calibrator was now properly flux calibrated and we copied these calibration to the targets with `GPCOPY`. The gain solutions were averaged with `GPAVER`. Continuum maps and spectral cubes were created from the calibrated visibilities with `INVERT`.

Imaging

Continuum maps were created in the same way as for the 3 mm data. With a synthesised beam of 6.5 arcsec at 47.7 GHz, a pixel size of 1.3 arcsec was selected. Multi-frequency synthesis and 'natural weighting' were chosen to create the continuum maps. Those channels with detected lines were flagged so no contribution from the CO lines affected the continuum. The resulting

[11] Note that PKS 1934-638 is a point-source at the ATCA spatial resolution at the frequency of our observations.

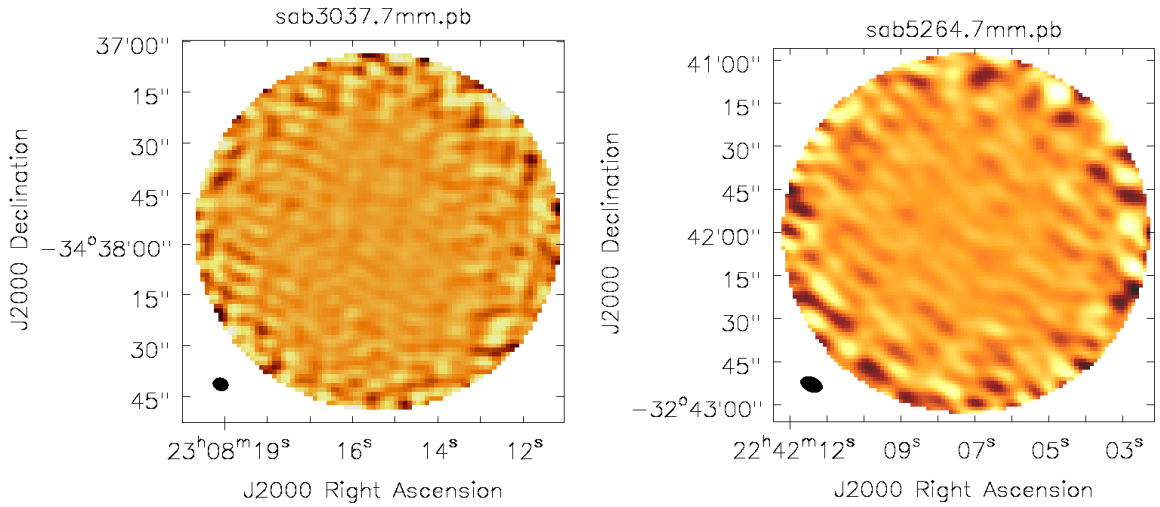

Figure 3.9 : From left to right, continuum maps at 7 mm for the sources SAB3037 and SAB5264. No continuum was detected for any of the sources.

Table 3.7 : Information of the 7 mm observations for the continuum maps. The expected r.m.s. is calculated with the ATCA sensitivity calculator in typical weather conditions.

ID	Frequencies (GHz)	Integration time (hours)	Expected r.m.s. (mJy/beam)	r.m.s. (mJy/beam)
SAB3037	47.75	12.34	0.022	0.041
SAB5264	40.20	32.89	0.007	0.013

synthesised beams were 4.51×3.76 arcsec^2 (P.A. = 68.93 deg) and 7.78×5.01 arcsec^2 (P.A. = 66.88 deg) for SAB3037 and SAB52564 respectively. The integration times, expected r.m.s. and achieved r.m.s. are shown in Table 3.7. No continuum was detected at these frequencies as shown in Figure 3.9.

Spectral cubes

The channel resolution at 49 GHz is 6.121 km s^{-1} (1 MHz). Thus, to create the spectral cubes we binned channels to achieve a resolution of ~ 100 km s^{-1} (16 MHz), increasing the sensitivity by a factor of 4. A first glance of how the spectrum looks like before and after the binning is shown in Figure 3.10[12]. The integration times, expected r.m.s. and achieved r.m.s. for the spectral windows where the lines were detected are shown in Table 3.8. CO lines were detected for both DSFGs.

[12]Note that the detected line in the right plot is a single cube, not the combined cube after the confirmation of the line (Section 3.5.2).

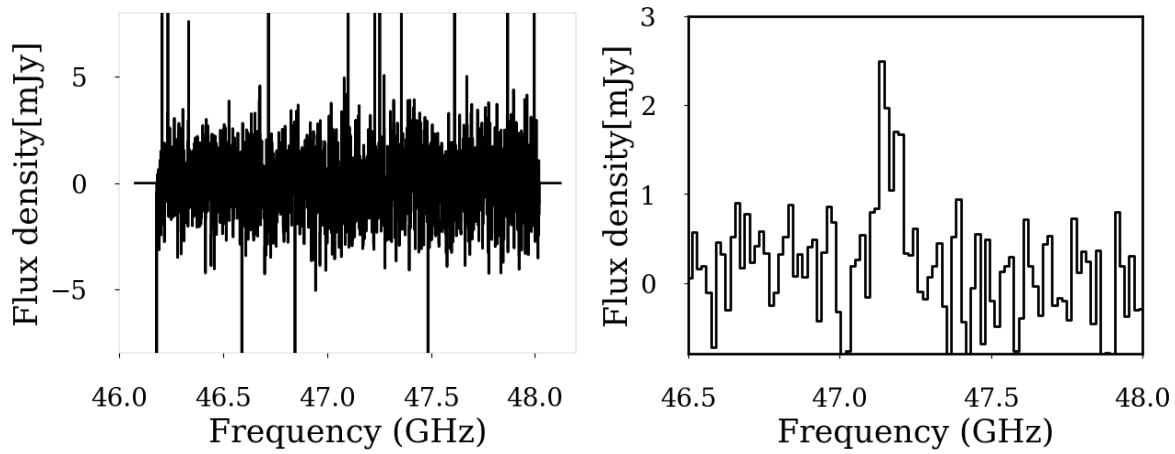

Figure 3.10 *Left*: SAB3037 spectrum before binning the channels where the resolution is $v = 6.121\,\mathrm{km\,s^{-1}}$. No line is perceivable. *Right*: SAB3037 spectrum after binning channels to achieve a resolution of $\sim 100\ \mathrm{km\,s^{-1}}$. In this case the line is clearly visible.

Table 3.8 : Information of the 7 mm observations on those spectral windows where lines were detected. The expected r.m.s. is calculated with the ATCA sensitivity calculator under typical weather conditions. The r.m.s. is calculated for a channel width of $\sim 100\ \mathrm{km\,s^{-1}}$.

ID	Frequencies (GHz)	Integration time (hours)	Expected r.m.s. (mJy/beam)	r.m.s. (mJy/beam)
SAB3037	47.1	3.29	0.44	1.02
SAB3037	46.5	2.88	0.43	0.72
SAB3037	47.4	2.88	0.49	0.76
SAB5264	49.0	3.61	0.55	0.66
SAB5264	48.5	4.93	0.44	0.55
SAB5264	49.4	4.93	0.51	0.75

Table 3.9 : Integrated and peak flux densities of the CO(2-1) lines at different tunings and final combined cube for SAB3037 are shown in this table. These values were derived from the moment-0 maps, created by selecting 17 channels (i.e. 850 $\mathrm{km\,s^{-1}}$) around the central velocity of the line. The S/N is calculated from the peak flux and the local r.m.s. Note that the peak flux is the peak of the 2D-Gaussian of the moment-0 and not the peak of the spectrum.

ID	Central ν (GHz)	Integrated flux ($\mathrm{Jy\,km\,s^{-1}}$)	Peak flux ($\mathrm{Jy\,km\,s^{-1}\,beam^{-1}}$)	S/N
SAB3037	47.1	1.35 ± 0.33	1.38 ± 0.19	4.6
SAB3037	47.4	1.46 ± 0.22	1.57 ± 0.13	7.8
SAB3037	46.5	1.36 ± 0.26	1.30 ± 0.14	7.6
SAB3037	46.38	1.39 ± 0.19	1.49 ± 0.10	9.7

3.5.2 Spectroscopy

As mentioned before, due to the weather dependency at the 3 mm window and the few gaps between covered frequencies (see Section 3.4.1), we could not exclude any redshift after the 3 mm observations and for the 7 mm band we could not rule out any frequency range. Hence, we aimed to cover the full 7 mm window.

A line for SAB3037 was detected at 46.85 GHz in a spectral window tuned at central frequency 47.10 GHz. To confirm this line we re-tuned our central frequency by an integer number of channels, i.e. 46.5 and 47.4 GHz, so we could combine the different data-sets in a final cube. Because ATCA has two spectral windows of 2 GHz each, we tried to detect the line in both spectral windows so we could increase our S/N as well. In Figure 3.11 (top) we can see the line in the 3 different central frequencies tunings, confirming the presence of a line. In Figure 3.11 (bottom) we show the line for the combined datasets[13] centred at the rest-frequency. The information of the CO lines for the different tunings can be found in Table 3.9.

The same strategy was followed for SAB5264. Initially we covered almost all the 7 mm band [49-33.7 GHz] without finding any line. Because we did not expect the redshift to be higher than 5 we did not observe the lowest frequencies of this band. We changed the search to SAB3037 where we detected the CO(2-1) line with an integrated flux density of 1.49 ± 0.10 $\mathrm{Jy\,km\,s^{-1}}$, $\sim 20\%$ fainter than the estimated flux via SED fitting. Following da Cunha et al. (2013) we thought that this could be due to the effect of the CMB, whose temperature approaches or even exceeds the temperature of cold dust and molecular gas observed in the local universe. Despite da Cunha et al. (2013) considering this effect to be relevant at galaxies with $z > 5$, we evaluated the possibility that the CMB could affect our estimations with the SEDs models. Thus, we decided to increase the sensitivity of our observations expecting to detect a line for our second

[13] When combining the cubes with MIRIAD we must cut the cubes into the same range of frequencies with the task `UVAVER`. This converts the cubes from 2048 channels into 1100 channels.

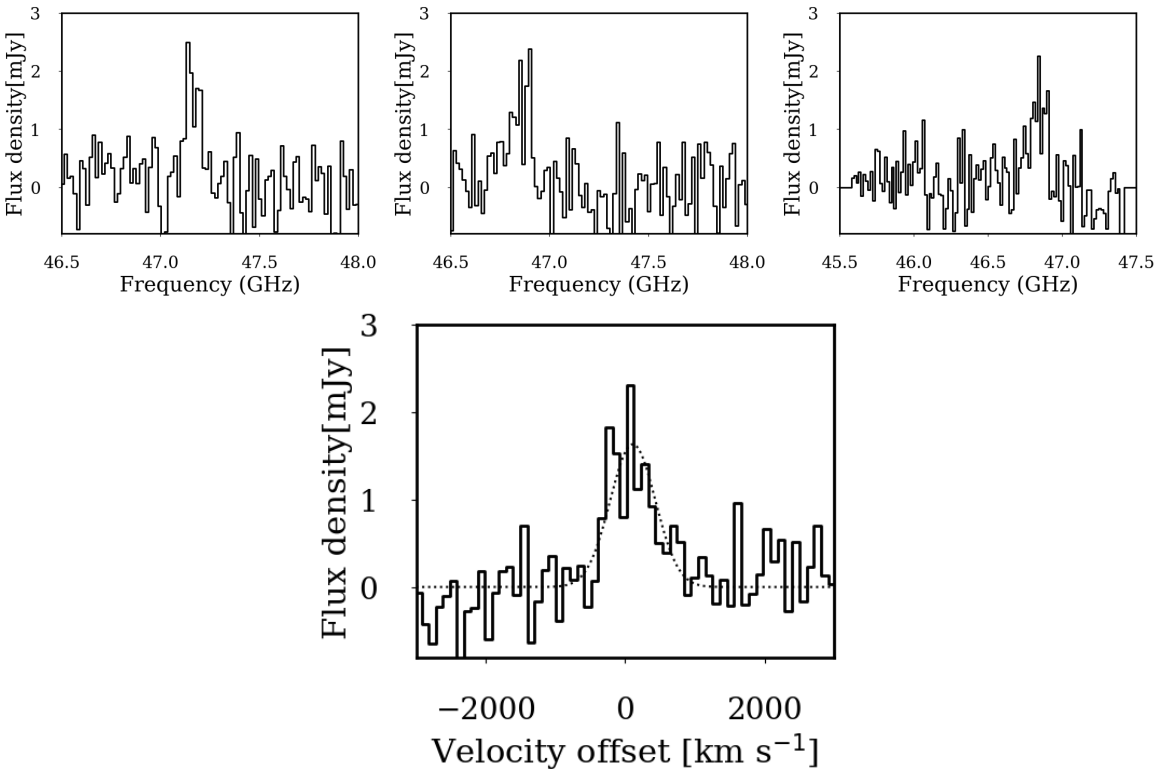

Figure 3.11 *Top:* Detected line of SAB3037 in the three spectral windows centre at different frequencies to confirm its existence. *Bottom:* SAB3037 line for the combined cubes at different tunings centred at the rest-frequency.

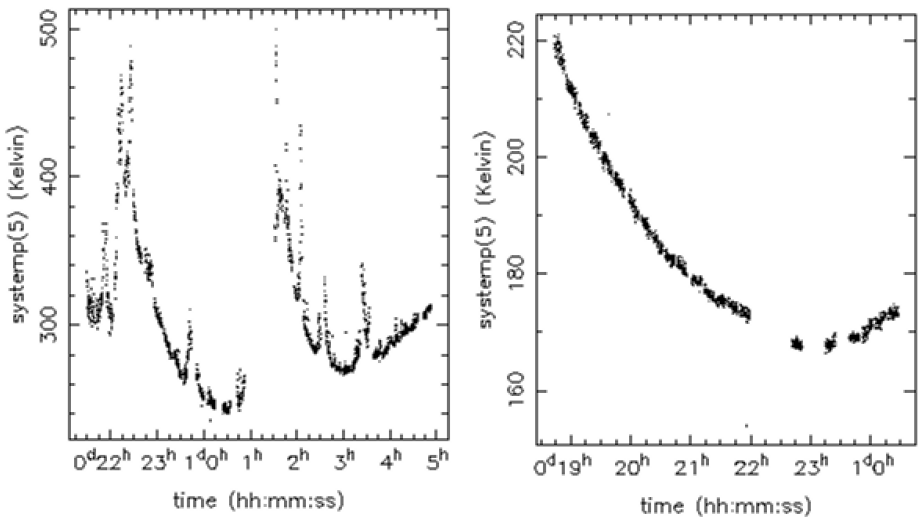

Figure 3.12 : T_{sys} during the two run observations of SAB5264. *Left*: Temperature of the system for one of the antenna the first time we observed SAB5264. We can see that the temperatures changes a lot during the run and therefore it is difficult to determine a good T_{sys}. *Right*: During the second run the temperature of the system varies smoothly and therefore a good T_{sys} can be determine.

target. Unexpectedly, after 3.61 hours of integration time on the second try versus 5.10 hours of the first one, a line was detected at 48.95 GHz whose flux was $\sim$ 50% brighter than estimated. Doing a more detailed study of the two cubes we compared the temperature of the system (T_{sys}) during both runs (Figure 3.12) and we found that T_{sys} was very unstable during the first run, when the line was not detected. However the r.m.s. of both cubes were pretty similar ($\sim$ 0.7 mJy and $\sim$ 0.9 mJy) so the source should have been detected in both cases. The most reasonable explanation is that T_{sys} was scaled incorrectly during the set-up of the antennae due to the bad weather. Therefore, we can assume that the weather ruined our observations in the first run.

To confirm the detected CO line, subsequent observations were done the following night. As we did before, we varied the central frequency tuning an integer number of channels, i.e. 48.5 GHz and 49.4 GHz. The three spectral windows where the line was detected are shown in Figure 3.13 (top) and the combine final line in Figure 3.13 (bottom). The line presents two distinguishable peaks which might indicate the presence of a merging system. We cannot differentiate between the two potential lines, so one single line was considered in this work. In Table 3.10 the information for the CO lines can be found.

To measure the integrated fluxes, we first created moment-0 maps by co-adding the channels where the CO line contributed to the flux. For SAB3037 we added 17 channels around the central velocity (i.e. 850 $\mathrm{km\,s^{-1}}$ on each side). SAB5264 had a wider line and 25 channels

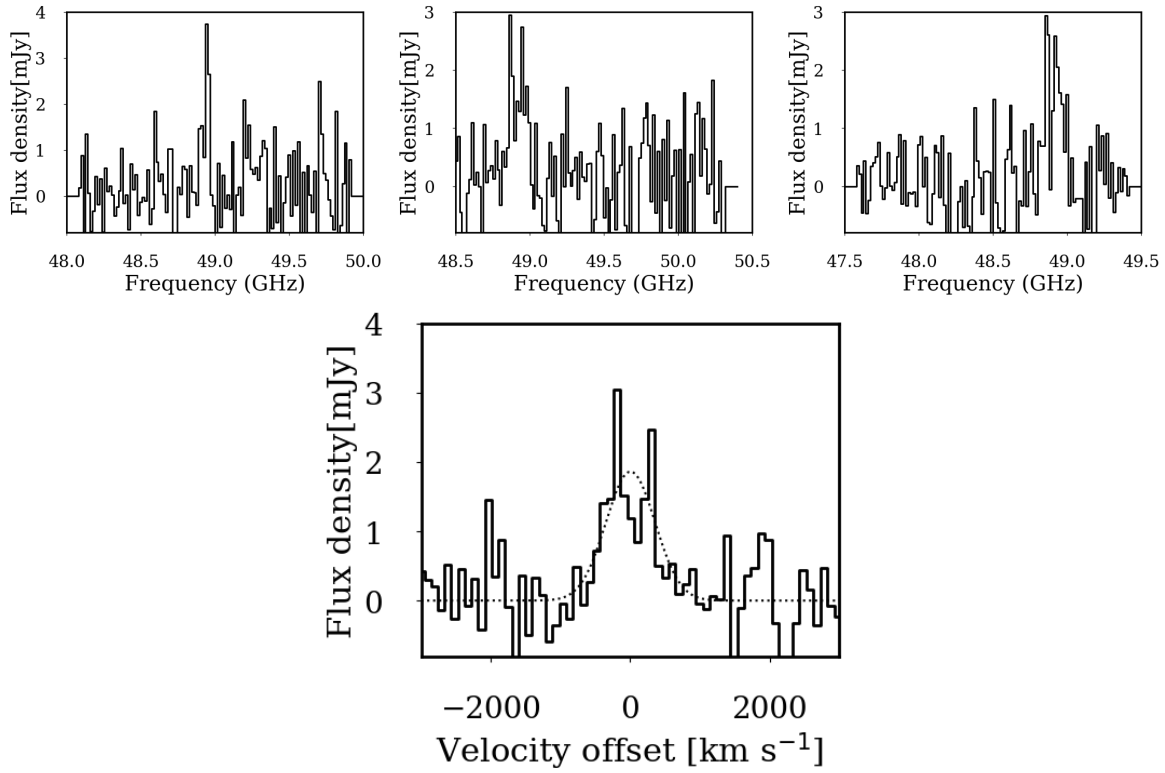

Figure 3.13 *Top:* Line detected at SAB5264 in the three different spectral windows. *Bottom:* Final line of SAB5264 where the presence of two potential lines was detected. Because we cannot be certain about the presence of two lines, we consider one single CO(2-1) line.

(1,250 km s^{-1}) were added to include all the flux. The moment-0 maps for the three tunings were then concatenated by doing a weighted average using $1/\text{r.m.s.}^2$ as the weight. This weighting results in the highest S/N for the concatenated maps. We then used `IMFIT` to measure the integrated and peak fluxes for each of the individual tunings and the concatenated maps for both sources. For SAB3037 the integrated and peak flux are close to each other, indicating a point source. However SAB5264 has a larger integrated flux for the two tunings of the second observing night, indicating an extended source. Considering the distance to the source, it would be very odd to actually observe extended emission from this galaxy. We thus suspect that the large angular size is due to the weather, especially since the first night the source was not extended.

These lines allow us to determine a potential redshift of the *Herschel*-sources. Assuming our z_{phot} was a fair estimation, the only option is that these lines correspond to CO(2-1) as we can see in Figure 3.3. Thus we can determine their redshifts: $z = 3.9198 \pm 0.0003$ and $z = 3.7135 \pm 0.0003$ for SAB3037 and SAB5264. In the case this line corresponds to CO(1-0) the redshifts would be 1.46 and 1.36 respectively, much lower than the 30% uncertainty

Table 3.10 : Integrated and peak flux densities of the CO(2-1) lines at different tunings and final combined cube for SAB5264 are shown in this table. These values were derived from the moment-0 maps, created by selecting 25 channels (i.e. $1,250\ \mathrm{km\,s^{-1}}$)) around the central velocity of the line. The S/N is calculated from the peak flux and the local r.m.s. Note that the peak flux is the peak of the 2D-Gaussian of the moment-0 and not the peak of the spectrum.

ID	Central ν (GHz)	Integrated flux ($\mathrm{Jy\,km\,s^{-1}}$)	Peak flux ($\mathrm{Jy\,km\,s^{-1}\,beam^{-1}}$)	S/N
SAB5264	49.0	1.22 ± 0.22	1.00 ± 0.12	3.9
SAB5264	49.4	3.34 ± 0.46	1.20 ± 0.11	4.6
SAB5264	48.5	2.92 ± 0.43	1.58 ± 0.13	4.2
SAB5264	48.5	2.65 ± 0.21	1.30 ± 0.07	5.0

Table 3.11 : Observational results derived from the CO(2-1) emission lines.

Parameter	SAB3037	SAB5264
z_{LSR}	3.9198 ± 0.0003	3.7135 ± 0.0003
ν_{obs} [GHz]	46.859 ± 0.004	48.910 ± 0.005
Δv_{FWHM} [$\mathrm{km\,s^{-1}}$]	688 ± 114	912 ± 116
$S_{CO}\Delta v$ [$\mathrm{Jy\,km\,s^{-1}}$]	1.49 ± 0.10	2.65 ± 0.21

expected for the estimation of z_{phot}. A similar situation occurs if we assume these lines are CO(3-2). In this case we would obtain redshifts 6.38 and 6.07 for each of the targets, much higher value than the estimated z_{phot}. To confirm these redshifts we would need to detect another emission line. The corresponding CO(4-3) lines at 3 mm would be at 93.71 GHz and 97.88 GHz for SAB3037 and SAB5264 respectively. Unfortunately, we did not cover any of these frequencies when this band was observed. To decide if another ATCA proposal would be worth it to confirm these redshifts, we estimated the necessary integration times. To calculate the CO(4-3) fluxes we did it through the coefficients $r_{4-3} = 0.4$ and $r_{2-1} = 0.8$ from Frayer et al. 2011. This resulted in $S_{peak}(4-3) = 4.04$ mJy and $S_{peak}(4-3) = 6.23$ mJy which correspond with an on-source integration time of ~ 9 and ~ 8 hours for SAB3037 and SAB5264 respectively. Adding the time needed for calibrations ~ 14 and ~ 13 hours would be required to detect these lines. Due to the big weather dependency at 3 mm band, we decided not to try with ATCA and add these targets to a sample of lenses to do the follow-up with ALMA (P.I. Serjeant).

In Table 3.11 we show the main results from the CO(2-1) detected lines. All the physical parameters we can derive from these emission lines are shown in Section 3.7.

3.6 Near Infrared Observations

To determine the origin of the sub-mm emission we observed at NIR bands. In combination with our interferometric observations deep and high quality K_s imaging might reveal either a) a counterpart for the sub-mm source consistent with NIR and sub-mm emission coming from a $z > 4$ starburst system, b) arclets in the field revealing that the sub-mm source is being lensed by a cluster of galaxies c) a single counterpart with colours consistent with a massive lens system at $z > 1$.

3.6.1 GEMINI-South Observations

To determine the NIR counterparts we observed the targets with GEMINI-South[14] located at Cerro Pachon, Chile, at an altitude of 2,722 m. The instrument FLAMINGOS-2 in K_s-band was used, covering a FOV of 6.19 arcmin^2 with a pixel size of 0.18 arcsec and an intrinsic point spread function of 0.36 arcsec across the full FOV. This telescope has two guiding options: the On-Instrument Wavefront Sensor (OIWFS) and the telescope's Peripheral Wavefront Sensors (PWFSs). It is strongly recommended to use OIWFS as default auto-guider because PWFSs creates vignetting in a large part of the science field (Figure 3.14). However, there was a problem with the default auto-guider during this semester so PWFSs was used instead. This caused a very big vignetting area in the images so special care had to be taken during the reduction of these data sets.

A total integration time of 40 minutes was used to observe both targets, SAB3037 and SAB5264. An average seeing of ~ 0.63 and ~ 0.50 arcsec, airmass of ~ 1.23 and ~ 1.07 and AB limit magnitudes of 22.17 and 23.61 at 5σ and 2 arcsec aperture for SAB3037 and SAB5264 were achieved during these observations.

3.6.2 Data Reduction

Two different software packages were used for the reduction of the images, IRAF[15] (Tody 1986 & Tody 1993) and THELI (Schirmer 2013 & Erben et al. 2005). Due to the vignetting in the images, we did two different reductions to have better uncertainties values in our photometry. Both methods are based in similar principles so no big differences were expected in our final results. In addition to the science images, we need other images to calibrate the data. Five

[14] These observations were done in service mode during the second semester of 2014 (project GS-2014A-Q-58, P.I. L. Dunne).

[15] IRAF is distributed by the National Optical Astronomy Observatories, which are operated by the Association of Universities for Research in Astronomy, Inc., under cooperative agreement with the National Science Foundation.

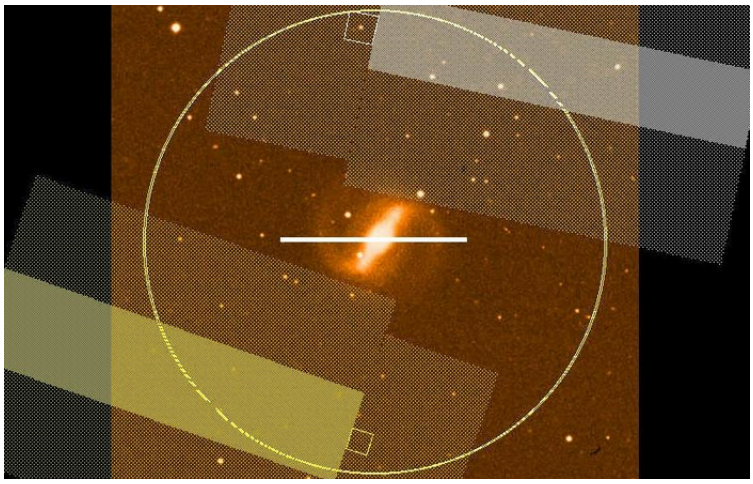

Figure 3.14 : This plot shows the vignetting caused by the PWFSs. The circle corresponds to the 7 arcmin outer radius of the PWFS patrol area. The white horizontal line in the centre shows a long-slit which we can ignore as we did not do spectroscopy observations.The vignetting patterns of PWFSs are represented as the large, shaded irregular boxes. Image credit: GEMINI

'flat-fields' and five 'darks' were taken from the archive of FLAMINGOS-2[16]. All of them at the proper filter and similar exposure times as the science images. Due to the brightness of the NIR sky it is necessary to do a 'dithering pattern' while observing to subtract the sky and identify the sources. This dithering consist of applying an offset of a few arcseconds in RA and DEC in each exposition frame. A simple example of how the sky looks like in a normal NIR exposition and after subtracting the sky is shown in Figure 3.15, where we can see the small offset in the position of the sources respect the previous one. As we mentioned before, the main steps of this process are similar for both methods (i.e. THELI and IRAF). We explain next the general steps to reduce the NIR data with both programs.

- CALIBRATION

  Calibration corrections need to be applied to the science images. To correct for dark current coming from thermal excitation in the detector, 'dark'-images are used. This dark current is different for every pixel and it changes with time. To correct for this effect we subtracted an averaged dark to all images, i.e. both 'flat-fields' and science images.
  Other effects that affect the quality of the images are variations in pixel-to-pixel sensitivity on the detector, illumination patterns, variations in the filters, artifacts,etc. To correct for these effects we need to uniformly illuminate the CCD to measure these variations. A blank area in the sky is pointed during the twilight, when the sky remains bright

[16]The instrument is pretty stable so flat-fields and darks are taken weekly or bi-monthly. The necessary calibration images can be found in the archive within a month of the data taken in the program.

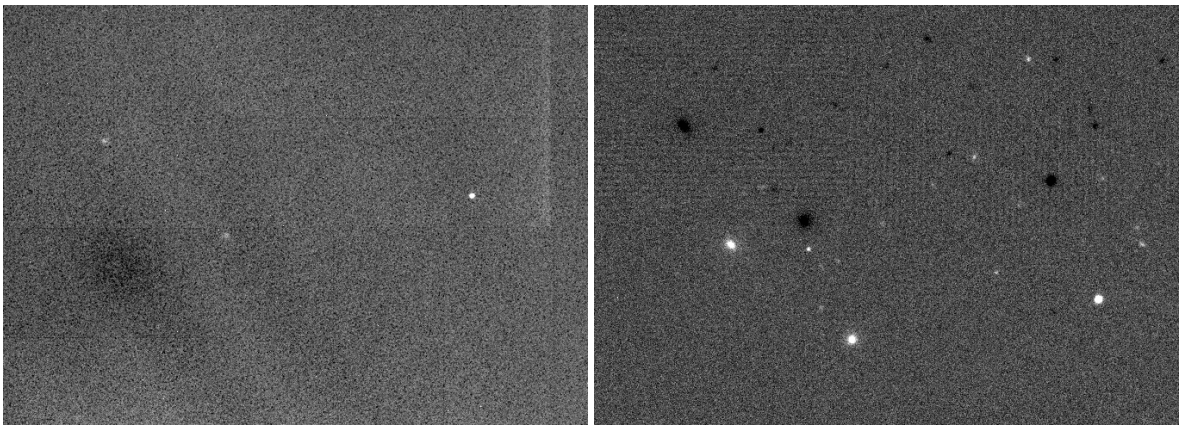

Figure 3.15 : *Left:* Example of a science image in the field SAB3037 before subtracting the sky. Due to the brightness of the NIR sky almost no sources are visible. *Right:* This image represent the subtraction of two science images with an offset between their pointings. We can see that the sources are more visible as an effect of the subtraction of the sky.

enough to hide sources but faint enough to not saturate the detector. These images are the so-called flat-fields which were downloaded from the archive. To apply the flat-field correction we created an average-normalised flat and divided our science image for it. An example of the dark and normalised flat-field is shown in Figure 3.16.

- MODELING SKY
  At NIR wavelengths the sky background is very bright, so it is necessary to subtract the sky to identify sources. The background brightness changes along the night so we need to model it in a short-logical period of time to subtract the sky from the different frames.

  – IRAF: We did the sky subtraction using the task `BGSUB` (Valentin Ivanov; *priv. comm.*). This task averages the two images surrounding the input image and subtract the averaged result from it. When there is only one neighbouring image (i.e. first and final images on the list), `BGSUB` will subtract only the nearest image. To create the background to subtract, we combined this two images with `IMCOMBINE`, selecting a percentile clipping algorithm to reject sources in the map. This algorithm is similar to a sigma clipping but instead of computing the sigma of the pixels from the CCD noise parameters or from the data values, the width of the distribution is characterised by the difference between the median value and a specified 'percentile' pixel value. This width was then multiplied by a scale factor to define the clipping thresholds above and below the median.

  – THELI: We can choose how many images, before and after the input frame, we want to use to create the background sky which will be subtracted from this frame.

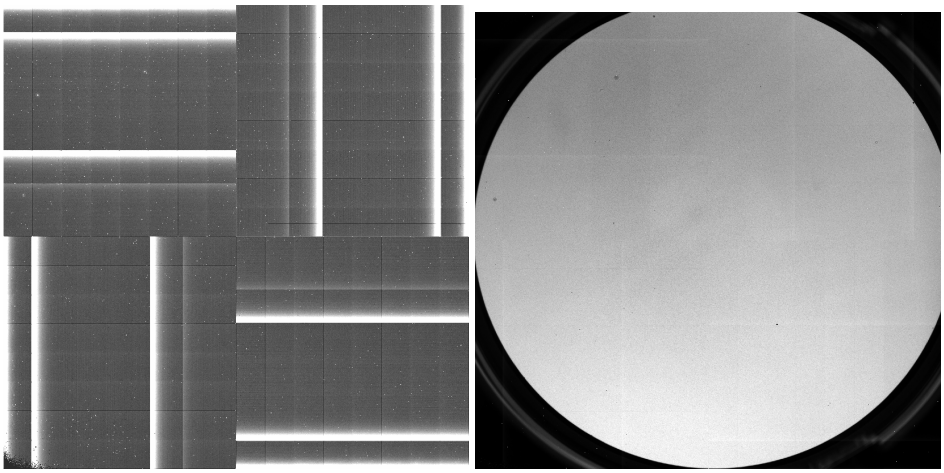

Figure 3.16 *Left:* Example of a dark frame of the Flamingos' CCD. *Right*: Example of the normalised flat-field used to be subtracted from the science images. These maps correct defects in the detector and distortions in the optical path.

In this case we chose a dynamical window of 4 images surrounding the input frame. To mask the objects so they do not contribute to the background, a threshold range was chosen. Due to the big vignetting we had on the top-left side of the FOV, a very 'soft' mask was used to avoid masking a bigger region in the frames. We selected a detection threshold per pixel (DT) of 10 sigma of the sky background noise and a minimum number of connected pixels (DMIN) of 10.

- BSCALE AND WEIGHTING

  These tasks apply different corrections to the images in IRAF and THELI. We explain each of them separately.

  – IRAF: When subtracting the sky, any old values of 'bscale' and 'bzero' are modified and hence obsolete. These two parameters are used to convert physical pixel values to FITS integer pixel values (i.e. 'bscale' is the scale factor to be applied and 'bzero' is the zero point to be subtracted before applying the scale factor). Therefore, we set 'bscale' = 1.0 and 'bzero = median'. To define the median value we selected a region of the image which was clean of 'fabric errors'.

  – THELI: To correct from bad pixels (e.g. cosmetic errors, cosmic-rays...) we applied WEIGHTING. First, a global weight image was created using the normalised 'flat-field' as reference to know the information in the pixels. Static pixel defects and those pixels whose values were outside the min-max interval in the normalised flat-field were set to zero. With this option we assured that the vignetted region or/and

underexposed areas were masked. We tried different values but not significant differences were found so default values were used (min=0.6, max=1.5). After the global weighting, we modified the weight of each image individually. This individual maps allowed us to mask the individual hot pixels as well as the cosmic-rays according with the S/N per pixel (DT = 6) and the number of connected pixels (DMIN = 1) (i.e. the smaller the value of DMIN, the fainter the objects that will be masked).

- ALIGN IMAGES

  Due to the dithering pattern during the observations the images need to be aligned before the coaddition.

  - IRAF: To calculate the offset between images we used `lintran`. This task performs a linear transformation to the list of images we used as input. This list was created with `imexam`. We took as reference the coordinates of one bright and small source from the first frame and `lintran` found the offset for the rest of the frames. Finally, to shift the individual frames to the reference frame , i.e. to align the images, we use `imshift`.
  - THELI does this automatically by connecting to online catalogues. We chose the 2MASS-NIR catalogue (Skrutskie et al. 2006) as astrometric reference. THELI read the coordinates of the images in the header and applied the necessary offset correction to align all the images at the same reference coordinates. However in our cases the astrometry was not perfectly correct so a manual astrometry correction was applied as we explain next.

- COADDITION AND ASTROMETRY CORRECTION

  Once the images are calibrated and aligned we combined all of them in a final image.

  - IRAF: To combine the different frames we used the task `imcombine`. We chose a median combination, a median additive zero level and a sigma-clipping rejection.
  - THELI: To do the coaddition THELI uses SWarp (Bertin et al., 2002) which does the final stacking of all the frames.

  These images might be astrometrically wrong so we needed to correct the astrometry. To solve this we used Starlink/GAIA[17]. Selecting the 2MASS-NIR catalogue as reference

[17]The Starlink Project was a UK Project supporting astronomical data processing, now maintained by the East Asian Observatory. GAIA is an extension of the RTD (Real Time Display tool) which has been written at ESO as part of the VLT project.

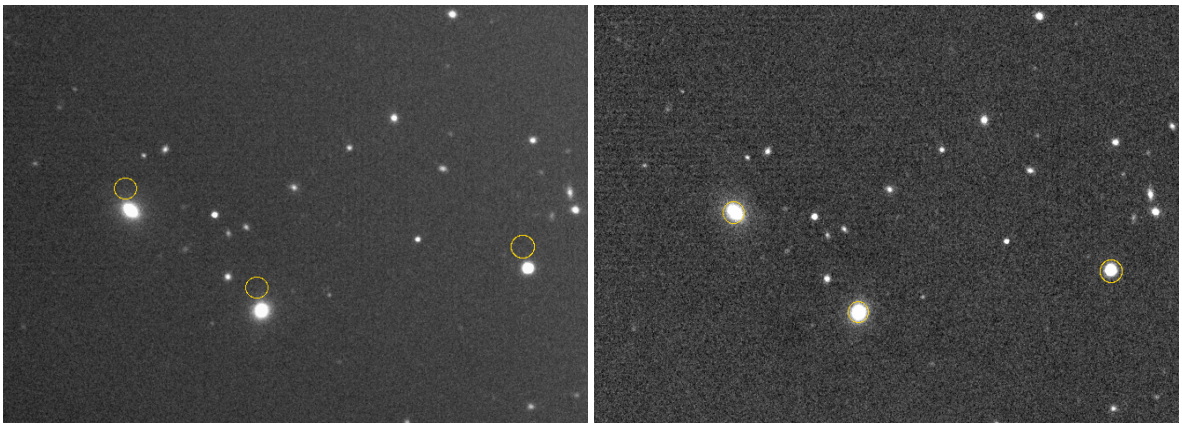

Figure 3.17 *Left:* SAB3037 map without astrometry correction. The yellow circles are the locations of the 2MASS standards. *Right:* Same map with the astrometry correction applied. We can see a good match between the coordinates of the 2MASS standards between the catalogue and our map.

we identified the standards in our image and apply the necessary offset. An example of an image before and after the astrometry correction can be found in Figure 3.17. Our final images can be found in Figure 3.18.

3.6.3 Photometry

We did aperture photometry using Starlink/GAIA for the NIR sources. Doing aperture photometry, we measured the flux inside a defined 'aperture-radius' around the target and subtracted the sky background flux. We defined an 'aperture-radius' big enough to measure all the flux coming from the target but not too big that other sources could contaminate our measurement. The flux of all the pixels inside the aperture was added to obtain the total flux in the aperture. To subtract the flux coming from the background sky we defined an 'inner' and 'outer-annulus'. These annulus surrounded the 'aperture-radius' measured the local sky background which was scaled to the same area as the source aperture and subtracted from the sum flux to yield the flux of the target. An example of the different apertures is shown in Fig. 3.19. It is important that for the sky annulus only the sky background is measured. Thus, care was taken to avoid contamination from other sources.

The pixel/units in the GEMINI maps are in ADUS/s, which were converted into fluxes and then into magnitudes. To convert the number of counts (ADU) in the detector to flux, first the zero-point (m_{zp}) needs to be calculated. By definition, the zero-point is the magnitude of an object that produces one count per second. An object producing N_{counts} in an exposure time

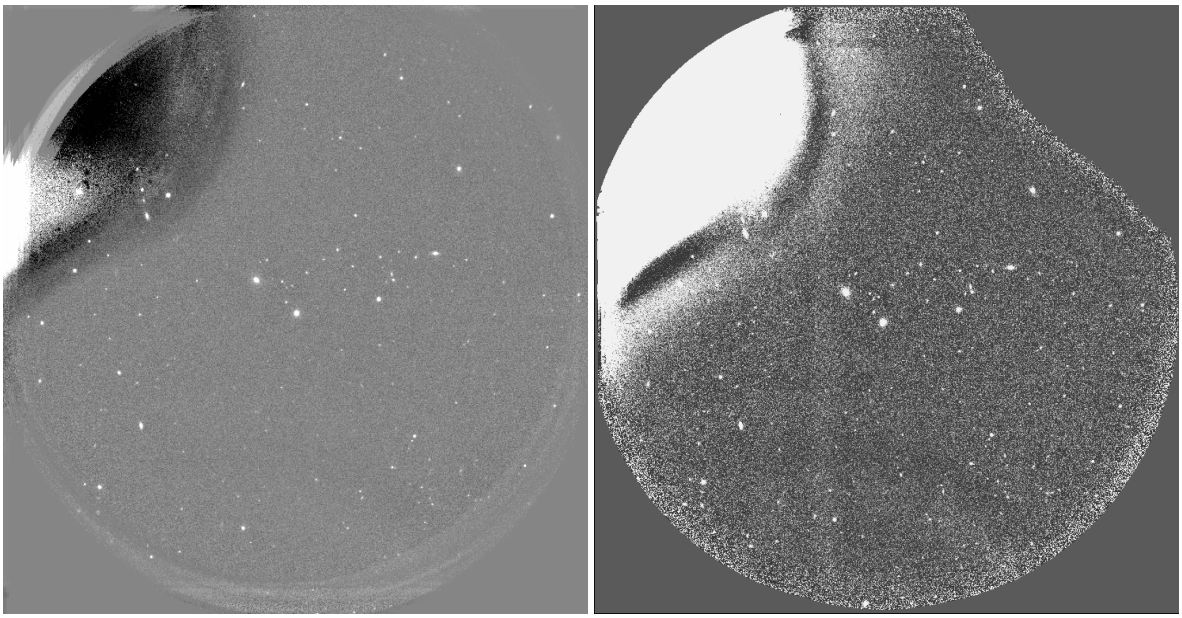

Figure 3.18 : From left to right, SAB3037 final images for IRAF and THELI reduction. The main difference in these two images is the applied mask. Because the FOV is very big and we want to focus in the central part of the image our final results should not be affected by the differences in the masks.

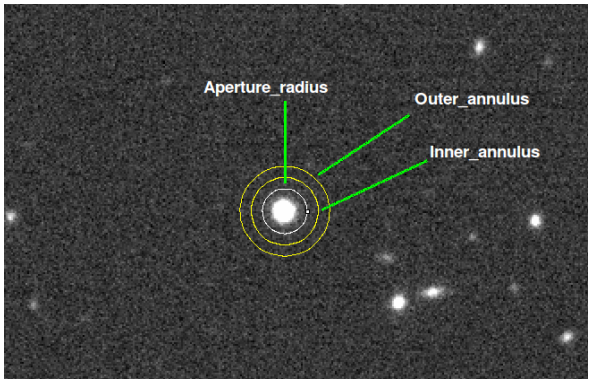

Figure 3.19 : Example of the different apertures when doing aperture photometry. An ‘inner-’ and ‘outer-annulus’ surrounding the target measure the local sky background which is subtracted from the flux measured in the target within the ‘aperture-radius’.

length t will have a magnitude of:

$$m = -2.5x\log_{10}(N_{counts}/t) + m_{zp} \tag{3.2}$$

Therefore, it is m_{zp} which determines the connection between observed counts and magnitudes. We did this connection through the standard photometric 2MASS catalogue, from where we took the magnitudes at K_s-band of the standard sources (m_{stand}) which were the reference to calculate the magnitudes of our targets. Because not many standards were found to lie in the FOV ($\sim$ 12 sources), we selected all those standards which were located in a non-corrupted area of the FOV. To calculate the zero-point another parameter is needed, the instrumental magnitude (m_{instr}). This magnitude is an uncalibrated apparent magnitude relative to the sky background, which is defined as:

$$m_{inst} = A - 2.5\log_{10}\left[\frac{(\Sigma_{i=1}^{n} C_i - nC_{sky}}{t}\right] \tag{3.3}$$

where A is an arbitrary constant which is added to the instrumental magnitudes. Normally an unrealistically high value is chosen for this constant so the instrumental and calibrated magnitudes are very different and therefore easy to distinguish. C_i is the count in the ith pixel inside the aperture, C_{sky} is the average count in a background sky pixel, n is the number of pixels in the aperture and t is the exposure time of the frame. Thus, m_{inst} is the sum of the pixels inside the aperture after subtracting the averaged sky background. We selected an 'aperture-radius' of 3 arcsec and an 'inner-' and 'outer-annulus' of 4.5 and 6 arcsec respectively. We determined the instrumental magnitude for each of the standards and averaged them. Ideally, we would want 15-20 standards with similar airmasses, magnitudes and colours than our targets. However this was not always possible in our maps. An average of only $\sim$ 7 standards were found distributed around the whole FOV. Although, the instrumental magnitude was very similar for all the standards so we assumed that the zero-point was very stable around the whole map. With the averaged m_{inst} in hand, we calculated the m_{zp} via:

$$m_{zp} = A - m_{instr} - m_{stand} \tag{3.4}$$

Once we had the zero-point, we measured the flux of our targets defining an 'aperture-radius' in a similar way than for the flux measurement of the standards. This is, the 'aperture-radius' was 1.5 arcsec and the 'inner-' and 'outer-annulus' 2.25 and 3 arcsec respectively. To determine the uncertainty in our sky subtraction, we defined 100 apertures around the central area of the field (avoiding edges and vignetting areas). We selected them manually to avoid contamination from other sources. The uncertainty on the measured flux of the targets was then given by the

Table 3.12 : Comparison of the GEMINI photometry done with two different methods, i.e. IRAF and THELI.

ID	m_{zp}	Flux (μJy)	S/N	m_{AB}
	IRAF | THELI	IRAF | THELI	IRAF | THELI	IRAF | THELI
SAB3037	24.67 | 24.68	51.45 ± 0.27 | 50.92 ± 0.20	19 | 25	19.68 ± 0.02 | 19.69 ± 0.04
SAB5264	27.02 | 24.80	12.75 ± 0.82 | 12.49 ± 0.76	15 | 16	21.20 ± 0.07 | 21.22 ± 0.06

standard deviation of the fluxes in these hundred apertures. The hundred background apertures were given the same size as the targets aperture since the variation in the background flux for each aperture does depend on its size[18]. To convert ADU to fluxes we used the next equations:

$$-2.5\log_{10}C = m_{VEGA} - m_{zp} \tag{3.5}$$

$$m_{VEGA} = -2.5\log_{10}(f/f_{zp}) \tag{3.6}$$

$$F(Jy) = f_{zp}\frac{C}{10^{m_{zp}/2.5}} \tag{3.7}$$

where f_{zp} is the flux for the 2MASS-K_s filter (666.7 ± 12.6 Jy). To convert fluxes to magnitudes we used:

$$m_{VEGA} = -2.5\log_{10}(F/f_{zp}) \tag{3.8}$$

$$m_{AB} = m_{VEGA} - 2.5\log_{10}f_{zp} + 8.9 = m_{VEGA} + 1.9 \tag{3.9}$$

In Table 3.12 we see that the photometry for both targets is very similar independently of the map (i.e. IRAF and THELI), so the reduction process is not dominating the errors. In both cases the r.m.s. is smaller in the maps obtained with THELI, so these maps were used for further analysis.

Finally, we determine the observed limiting magnitude in a sky-limited image. We considered a 2 arcsec aperture for 100 apertures distributed in the whole map obtaining $m_{AB_{lim.mag.}} = 22.56$ and $m_{AB_{lim.mag.}} = 23.82$ for SAB3037 and SAB5264 respectively.

These maps are covered with the VISTA Kilo-degree Infrared Galaxy Survey (VIKING; Edge et al., 2013). We downloaded the correspondent maps from the archive and did the photometry similarly than for the GEMINI maps obtaining $m_{AB} = 19.46$ and $m_{AB} = 21.28$ for SAB3037 and SAB5264, respectively. Therefore, our GEMINI photometry is consistent with the photometry in the VIKING maps. However, the limit magnitude of VIKING is $m_{AB} \sim 21.5$ at 5σ while our GEMINI maps are deeper, $m_{AB} \sim 23$. We observed deeper with GEMINI to confirm that the measurement of our sources with VIKING were not limited by the observations

[18]The noise in one aperture is proportional to the root of the number of pixel in the aperture.

and that the VIKING observation did not miss any arclets or direct counterparts (see next Section).

To be certain about the origin of the 3 mm emission, we would need the redshift of the NIR source to check that their redshifts are smaller than for the DSFGs. Because we do not have this information, we tried to imagine an scenario where the NIR source were at z = 3.92 with $m_{AB} = 19.69$ and see how realistic this situation would be. Thus, we calculated the absolute K_{AB} magnitude in such a situation. To do this, we used the Arp220 SED (ULIRG template) to calculate the K-correction and applied this correction to the K_s-band flux. Then we calculated the absolute magnitude (M_K) with:

$$m_K - M_K = 5\log(d/10) \tag{3.10}$$

where m_K is the apparent magnitude for the hypothetical source, and d is the distance in parsec. We obtained that the absolute K magnitude would be $M_K = -29.97$ for SAB3037 and for SAB5264 at z = 3.71 it would be $M_K = -28.13$[19]. Assuming a typical mass-to-light ratio of $0.35\,M_\odot/L_\odot$ in the K_s-band (Johnson et al., 2016), these sources would have total stellar masses of $M_* = 3 \times 10^{12}\,M_\odot$ and $7 \times 10^{11}\,M_\odot$ respectively. While SAB5264 would be consistent with a very massive starburst at z ∼ 3 (Bauer et al., 2011), SAB3037 would be consistent with a galaxy cluster, although it would be the most compact galaxy cluster found at those high redshifts. Therefore, we cannot exclude the possibility that the K_s-band emission is coming from the DSFGs at least for one of our sources. Thus, spectroscopic redshift for the NIR counterparts would be essential to determine if they are gravitationally lensed systems.

3.7 Characterisation of the Sources

To characterise the *Herschel*-sources, first we determined the origin of the 3 mm emission. The 3 mm continuum maps have a resolution of ∼ 2 arcsec, which allowed us to optically identify the DSFGs. To determine the origin of the 3 mm emission we overplotted the continuum map over the K_s-band. Figure 3.20 shows a clear offset between the lens source (background map) and the mm emission (yellow contours) for both galaxies. This indicates that our two *Herschel*-sources are good candidates to be lensed galaxies. The green contours represent the moment-0 of the CO(2-1) line which allowed us to determine the redshift of these two galaxies. Observing with GEMINI we did not find any signs of arclets indicating no presence of cluster lensing. Additionally the only NIR counterparts for the *Herschel*-sources were offset and much

[19] Different SED templates were used obtaining similar results (maximum difference of 0.8 magnitudes). This is due to the mostly flat area of the SED where the rmK_s band is located.

too bright to be at the same redshift as the *Herschel*-sources. This indicates lensed systems rather than unlensed bright starbursts with directly detected NIR counterparts.

To be certain about the offset, we studied the accuracy of the astrometry in the NIR and mm maps. To study the NIR maps, we compared the central positions of the standard sources identified by SExtractor and the corresponding coordinates in the 2MASS catalogue. We found a mean offset for the SAB3037 map of δRA $= 0.03$ arcsec and δDEC $= 0.03$ arcsec with a standard deviation of 0.16 arcsec and 0.10 arcsec respectively. For the SAB5264 map we obtained δRA $= 0.02$ arcsec and δDEC $= 0.02$ arcsec with a standard deviation of 0.13 arcsec and 0.23 arcsec respectively. The pixel size of the GEMINI maps is ~ 0.18 arcsec which means that the astrometry is good within one pixel. The astrometric accuracy in the interferometric maps was studied by creating the images of the gain calibrators and checking the astrometry in those. We used the gain calibrators to do the pointing of the antennae every hour during the observations, so any offset in these sources would imply a problem in the astrometry of our targets. As expected, the position of the gain calibrator was not offset from its original coordinates so our 3 mm maps have a good astrometry a priori. The positional measurement uncertainty due to low S/N in the mm imaging was derived from $\sigma_{\rm pos} = 0.6 \times \frac{\theta}{\rm S/N}$, where θ is the FWHM of the beam in arcseconds (Ivison et al., 2007). We obtained an uncertainty of $\sigma_{\rm pos} = 0.23$ arcsec and $\sigma_{\rm pos} = 0.28$ arcsec for SAB3037 and SAB5264 respectively. The total offset between the centre position of the two counterparts are 0.70 arcsec and 1.13 arcsec for SAB3037 and SAB5264. Therefore evidence of lensing are found for these two sources. More observations would be needed to confirm that the *Herschel*-sources are certainly gravitationally lensed.

From the detected CO(2-1) lines we calculated the line luminosities ($L'_{\rm CO}$) following Solomon & Vanden Bout (2005):

$$L'_{\rm CO} = 3.25 \times 10^7 S_{\rm CO} \Delta v \upsilon_{\rm obs}^{-2} (1+z)^{-3} D_{\rm L}^2 \tag{3.11}$$

where $\nu_{\rm obs}$ is the observed frequency of the emission line in GHz. We obtained line luminosities in the order of $L'_{\rm CO} \sim 3 \times 10^{11}$ K km s^{-1}pc^2.

Assuming these galaxies are gravitational lensing systems the measured luminosities are actually apparent luminosities affected by the magnification factor, μ. A gross approximation of their magnification was done following the next equation from Harris et al. (2012) where a study of DSFGs at $2.1 \leqslant z \leqslant 3.5$ is presented:

$$\mu = 3.5 \frac{L'_{\rm CO}}{10^{11} {\rm K\,km\ s^{-1} pc^2}} \left(\frac{400\,{\rm km\,s^{-1}}}{\Delta v_{\rm FWHM}} \right)^{1.7} \tag{3.12}$$

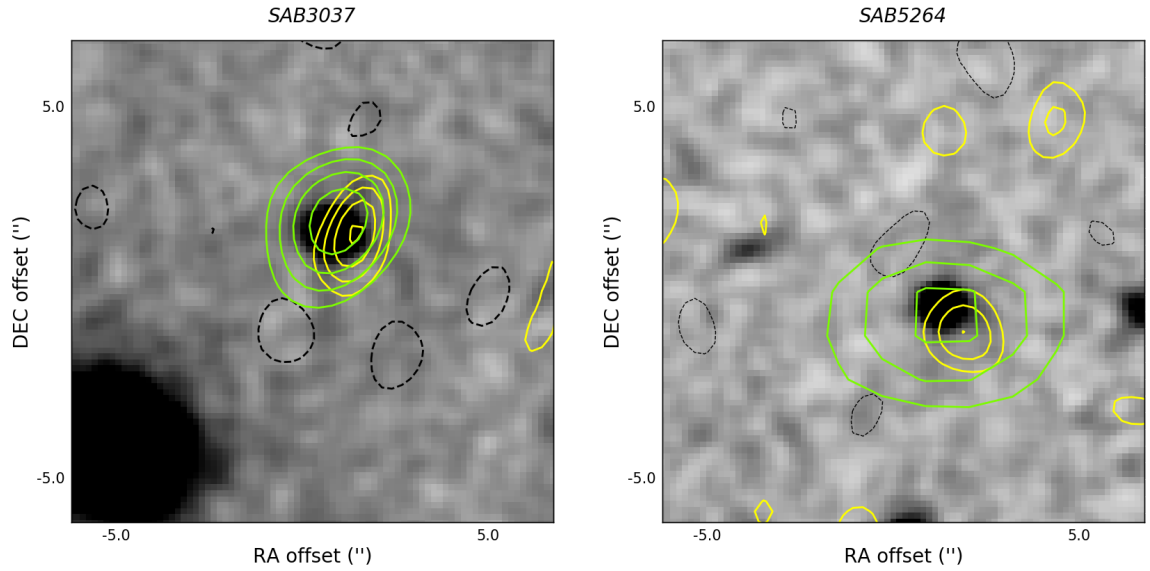

Figure 3.20 : From left to right, GEMINI K_s-band for SAB3037 and SAB5264. Overplotted in yellow contours are represented the 3 mm continuum detection ($3,5,7,9\times\sigma$; -3σ in dashed-black), and in green the moment-0 correspondent to the CO(2-1) line ($3,4,5,6\times\sigma$; -3σ in dotted-black). Note that the resolution for K_s is 0.56 arcsec while at 3 mm it is ~ 2 arcsec and at 7 mm it is ~ 5 arcsec.

With linewidths (FWHM) of $\sim 800\,\mathrm{km\,s^{-1}}$, consistent with other studies in the literature (e.g. Greve et al., 2005; Aravena et al., 2016; Huynh et al., 2017) but wider than the average value of $418\pm216\,\mathrm{km\,s^{-1}}$ found for this type of galaxies at $z\sim2-4$ (Yang et al., 2017), we found a magnification factor of $\mu\sim3.2$ for both galaxies. The intrinsic luminosity is defined as $L'_{INT}=\frac{L'_{CO}}{\mu}$, so $L'_{INT}\sim7.18\times10^{10}\,\mathrm{K\,km\,s^{-1}\,pc^2}$ and $L'_{INT}\sim11.60\times10^{10}\,\mathrm{K\,km\,s^{-1}\,pc^2}$ for the corresponding galaxies.

We calculated the total cold gas mass ($H_2+He=M_{gas}$) with $M_{gas}=\alpha L'_{INT}$, assuming a constant line temperature brightness ration $L'_{2-1}=L'_{1-0}$ and a conversion factor of CO-to-H_2 of $\alpha=0.8\,M_\odot(\mathrm{K\,km\,s^{-1}pc^2})^{-1}$ which is representative for ULIRGs and DSFGs, the kind of galaxies we are studying (e.g. Downes & Solomon, 1998; Tacconi et al., 2008). This gives us a $M_{gas}=5.75\times10^{10}\,M_\odot$ and $M_{gas}=9.28\times10^{10}\,M_\odot$, typical values for this kind of objects (e.g. Frayer et al., 1999; Coppin et al., 2010; Greve et al., 2005).

We determined the L_{TIR} and M_{dust} by fitting our *Herschel* and LABOCA photometry to a two-component MBB model (see Section 1.2.2). There are no detections at the PACS wavelengths for any of our sources above 3σ. However we still performed and included the photometry on them to have a constraint for the warmer dust as well. To do the photometry in these bands we did a 2D-Gaussian fit to the flux density in each band (for more details see Section 4.6.1). The best-fitting two-components MBB model is shown in Figure 3.21.

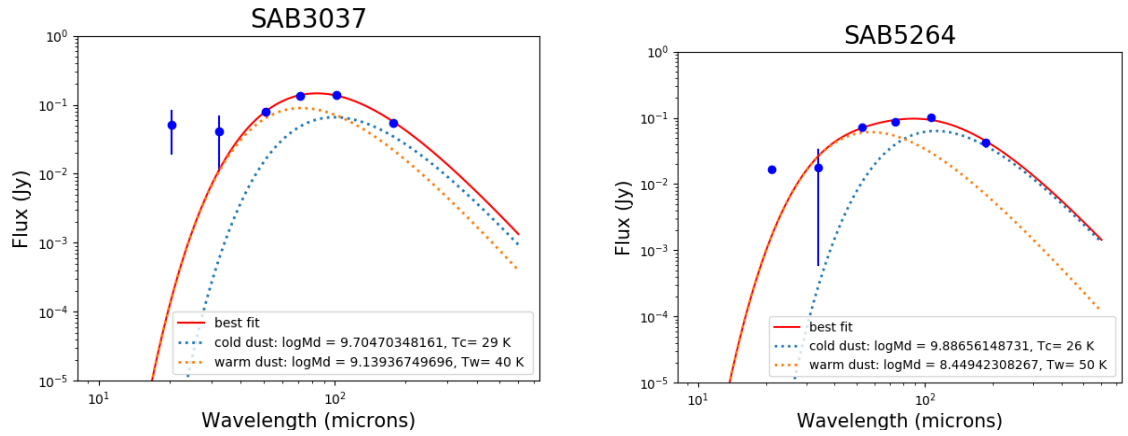

Figure 3.21 : Best-fitting model for a MBB template to estimate the L_{TIR} and constrain the T_{dust} with *Herschel* and LABOCA bands. The fitting was done weighting the error, thus the best-fitting follows the SPIRE and LABOCA bands better as it has smaller errors than PACS where there are not detections above 3σ.

Integrating the best-fitting model from $\lambda\,(8-1000\,\mu\mathrm{m})$ with:

$$L_{TIR}(8-1000\,\mu\mathrm{m}) = 4\pi D_L^2 \int_{\nu_1}^{\nu_2} S_\nu d\nu \tag{3.13}$$

the derived infrared luminosities for our two galaxies are $\mu L_{TIR} = 5.01\times10^{13}\ L_\odot$ and $\mu L_{TIR} = 3.89\times10^{13}\ L_\odot$. Correcting for the magnification factor we obtained $L_{TIR} = 1.59\times10^{13}\ L_\odot$ and $L_{TIR} = 1.22\times10^{13}\ L_\odot$ and dust masses of $M_{dust} = 2.04\times10^{9}\ M_\odot$ and $M_{dust} = 2.50\times10^{9}\ M_\odot$ for SAB3037 and SAB5264 respectively. With the best-fitting model we obtained as well a constraint on the dust temperature (T_{dust}) of the galaxies for the cold ($T_{cold-dust} \sim 27$ K) and warm ($T_{warm-dust} \sim 45$ K) components. Uncertainties on the dust masses, luminosities and temperatures were obtained from a bootstrapping analysis where 100 new sets of fluxes were created from the measured fluxes and uncertainties, and a two-component MBB was fitted to each set.

The Star Formation Rate (SFR) was calculated via L_{TIR} following Kennicutt (1998)[20] and we obtained SFR $\sim 2,400\ M_\odot yr^{-1}$ for both galaxies. With the SFR and the M_{gas} in hand, the Star Formation Efficiency[21] can be estimated obtaining SFE $\sim 45\ Gyr^{-1}$ and $\sim 20\ Gyr^{-1}$ for SAB3037 and SAB5264 respectively. Therefore, the gas depletion time (τ_{depl})[22] for these galaxies has a value of 21 and 44 Myears. These very rapid depletion times are consistent with

[20] $SFR_{TIR}\ [M_\odot yr^{-1}] = 4.510^{-44} \times L_{TIR}\ [erg\,s^{-1}]$
[21] $SFE = SFR/M_{gas}$
[22] $\tau_{depl} = SFE^{-1}$

merged or merging galaxies at high redshifts (e.g. Solomon & Sage, 1988; Genzel et al., 2015; Aravena et al., 2016; Harrington et al., 2018).

With high SFR and M_{dust} these galaxies allow us to study obscured star-formation before the epoch of peak star-formation ($z \sim 2$). A summary with all the results for the two galaxies can be found in Table 3.13.

Table 3.13 : Final results for our two galaxies.

Parameter	SAB3037	SAB5264
z_{LSR}	3.9198 ± 0.0003	3.7135 ± 0.0003
ν_{obs} [GHz]	46.859 ± 0.004	48.910 ± 0.005
Δv_{FWHM} [km s^{-1}]	688 ± 114	912 ± 116
v_{obs} [km s^{-1}]	0.0 ± 46.1	0.0 ± 44.5
$S_{CO}\Delta v$ [Jy km s^{-1}]	1.49 ± 0.10	2.65 ± 0.21
μ	3.16 ± 0.52	3.19 ± 0.41
$\log(L_{TIR})$ [$L_\odot$][a]	13.20 ± 0.01	13.09 ± 0.02
M_{dust} [$10^9 M_\odot$][a]	2.04 ± 0.82	2.50 ± 1.37
$T_{cold-dust}$ [K]	29 ± 4	26 ± 3
$T_{warm-dust}$ [K]	40 ± 9	50 ± 6
SFR [$M_\odot$ yr^{-1}] [a]	$2,700 \pm 500$	$2,100 \pm 300$
$L'_{(CO)}$ [10^{10} K km s^{-1} pc^2] [a]	7.18 ± 1.25	11.60 ± 1.54
M_{gas} [10^{10} $M_\odot$] [a]	5.75 ± 0.95	9.28 ± 1.18
SFE [Gyr^{-1}][a]	48 ± 12	23 ± 5
τ_{depl} [Myears][a]	21 ± 5	44 ± 9

[a]Corrected for magnification factor.

3.8 Conclusions

We have characterised two *Herschel*-selected DSFGs (SAB3037 and SAB5264) as potential ULIRGs that are gravitationally lensed. These galaxies were selected such that they are some of the reddest sources in the H-ATLAS survey with $S_{250} < S_{350} < S_{500}$ and $S_{500} > 100$ mJy. Our main results are:

- We have identified the *Herschel*-sources with the 3 mm continuum-maps via ATCA observations. With a resolution of 2 arcsec, it was possible to identify the origin of the sub-mm emission.
- We have determined the spectroscopic redshift of the DSFGs via CO(2-1) lines with ATCA observations. These sources have redshift $z = 3.9198 \pm 0.0003$ and $z = 3.7135 \pm 0.0003$. To confirm this, detection of a second line would be necessary.

- We have identified their NIR counterparts with GEMINI observations. With a total offset between the 3 mm emission and the NIR counterpart of ~ 0.9 arcsec, we conclude that both of our sources are good candidates of gravitationally lensed galaxies. The K_s magnitudes for the NIR lenses counterparts are $m_{AB} = 19.69 \pm 0.04$ and $m_{AB} = 21.22 \pm 0.06$. Spectroscopic redshift for the lenses would be necessary to confirm that these NIR galaxies have lower redshift than the *Herschel*-sources and therefore are acting as lenses. Because we do not have this information, we have done an estimation of what the absolute magnitude at K_s-band would be if they were not lensed galaxies. In this situation, after applying the correspondent K-correction, the absolute magnitude would be very high to be $z \sim 3-4$. Thus, the most likely option is that these NIR sources are acting as lenses for the DSFGs.

- With linewidths of ~ 800 km s^{-1} these detected lines are wider than the average value of ~ 400 km s^{-1} found in the literature. The magnification factors, μ, of these weak gravitational lensing systems, have been estimated using the linewidths and luminosities of these CO(2-1) lines. We obtained values for the magnification of ~ 3.16 and ~ 3.19.

- The line luminosities derived from the detected CO(2-1) lines give a measurement of the cold molecular gas reservoirs available for future star formation, which is $M_{gas} \sim 7 \times 10^{10}$ $M_\odot$ after applying the magnification factor correction.

- SFRs $\sim 2,400$ $M_\odot$ indicate these sources are very high star-forming galaxies. In addition, depletion times of ~ 30 Myears are consistent with merging galaxies at these high-redshifts causing startburst with high SFRs.

- Finally, we conclude that these very red *Herschel*-sources are most probably gravitationally lensed ULIRG galaxies. It is very likely that these DSFGs are merging galaxies following the width of their CO(2-1) lines and their very rapid depletion times. In addition, they are likely progenitors of two massive elliptical galaxies at $z \sim 2-3$.

The next steps in this work will be to identify the redshift of both, the NIR and the DSFGs. This means to obtain unambiguous spectroscopic redshifts for the system. After this, obtaining high resolution imaging and multiple-J CO observations will be crucial to provide us with more information to use lens modelling and to study in more detailed the ISM for high-redshift DSFGs. These sources have been added to an ALMA follow-up sample (P.I. Serjeant). This should provide the necessary sensitivity and resolution to study in more detail these two galaxies.

Chapter 4

The Thousand Lens Survey

4.1 Introduction

The use of gravitational lensing as a tool for cosmography is still not very well exploited. This is because i) the number of lensing systems is still small and ii) many searches have been based on potential lenses rather than potential lensed sources, which is a much less sensitive method for measuring cosmological parameters (Meylan et al., 2006; Treu, 2010) and has a redshift bias. A large unbiased sample of lensed systems would help to constrain Ω_Λ more accurately with only information from the lens and source redshift (Short et al., 2012). As shown in Figure 4.1, with 100 lensed systems, the error on Ω_Λ should be the order of 0.01. This value would be comparable with those obtained from the CMB and SNe methods, providing a completely independent test. In addition, studying the evolution of the equation-of-state for dark energy (Zhang et al., 2009) and testing theories of modified gravity (Zhao et al., 2011) would be possible with big samples of lensed systems. The properties of high-redshift lensed sources depend on the properties of the intervening dark-matter halos, thus a large sample of high-redshift lenses can also be used to test how the number-density of halos depends on redshift and mass (Short et al., 2012). This is a fundamental ingredient of all galaxy-evolution models, and there is currently no other way to investigate it. Finally, while existing lensing samples are dominated by elliptical galaxies because the lensing cross-section is proportional to the fourth power of the velocity dispersion, large samples should contain more spiral galaxies which would open a new frontier (Treu, 2010).

With $\sim$ 300,000 sources on 550 deg^2 observed area, H-ATLAS is the largest extragalactic *Herschel* survey. During the Science Demonstration Phase (SDP), with an area of 16 deg^2, $\sim$ 6,600 sources were detected at 5σ in at least one SPIRE waveband. As explain in Section 1.3.5 a first selection of candidates of Strongly Lensed Galaxies (SLGs) can be done with a simple flux density selection in the SPIRE band $S_{500} > 100$ mJy. DSFGs are usually at high redshifts,

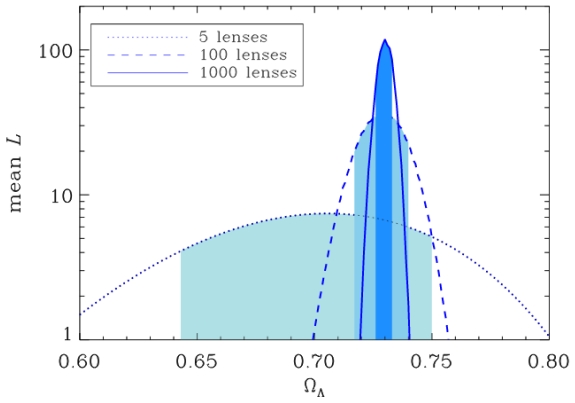

Figure 4.1 : Simulation of the constrain for Ω_Λ with the number of lensing systems. Image credit: Short et al. (2012)

so due to the large volume that is in front of these sources the chance of an alignment with a foreground galaxy increases and therefore the probability to be lensed also increases. Negrello et al. (2010) present a study of 5 candidates of lensed sources for which a close NIR counterpart were found in the *Sloan Digital Sky Survey* (SDSS) and/or UKIDSS. The probability of a chance alignment is of a few percent (Smith et al., 2011), so it was likely that the NIR object was associated with the *Herschel*-source, either because the NIR and *Herschel* emission were from the same galaxy or because the *Herschel*-source was being lensed by the NIR object. Furthermore, these objects had much lower redshifts than those estimated for the *Herschel*-sources, supporting that they were the result of lensing.

In González-Nuevo et al. (2012) a similar study is presented but for fainter *Herschel* objects in the SDP with a sample of 31 candidates. The idea was to increase the sample of SLGs to those in the bulk of the star-forming galaxy population ($z \approx 1-3$). These galaxies are fainter than the SPIRE confusion limit so without the effect of the lenses it would not be possible to study them. With SPIRE fluxes $S_{250} > 35$ mJy and $S_{350} > 85$ mJy, $S_{350}/S_{250} > 0.6$ and $S_{500}/S_{350} > 0.4$, their z_{phot} were consistent with $z_{source} > 1.2$. This corresponds with a number density of $\simeq 2\,\mathrm{deg}^{-2}$ (Figure 1.7). In this case the presence of NIR counterparts was studied with the K_s-band images from VIKING. This NIR survey was able to reveal $\simeq 90\%$ of the lensing galaxies, whereas only $\simeq 40\%$ would be visible via SDSS. Almost 50% of the selected objects turned out to be SLGs.

In this chapter we present a study of the faint *Herschel*-sources (down to 29 mJy at 500μm-band, see Section 4.3) in the H-ATLAS catalogue with a z_{phot} from SED fitting consistent with $1.5 < z < 2.5$, which together make up the TLS. With the TLS selection criteria, the bulk of the star-forming galaxy population is under scope. Using VLA radio observations we identify candidates of lensed sources and the *Herschel*-sources population.

This chapter is divided as follows. In Section 4.2 the methodology used in this chapter is explained. The sample selection and the VLA observations are explained in Section 4.3. Section 4.4 is dedicated to the general steps of the data reduction and imaging process of the radio maps. In Section 4.5 we characterise the sample and in Section 4.6 a study of the InfraRed-to-Radio Correlation (IRRC) and Star-Formation-Rates (SFRs) is presented. The caveats to consider in this analysis can be found in Section 4.7. Finally, in Section 4.8 the main conclusions of this chapter are summarised.

4.2 Methodology

The main goal of this study was to determine the presence of SLGs in H-ATLAS at the faintest regime fluxes for the 500μm-band. First, we selected the potential SLGs by defining a density flux limit in the SPIRE bands (Section 4.3). These galaxies were selected to have z_{phot} between $1.5 < z < 2.5$, so the bulk of the Star-Forming Galaxies (SFGs) population could be studied. Thus, z_{phot} were estimated with a precision of $\simeq 30\%$ from fitting SED templates to the SPIRE fluxes using a minimum χ^2 technique (Lapi et al., 2011).

To determine the origin of the emission of the selected sources a morphological study for these objects was carried out. González-Nuevo et al. (2012) showed that a gravitational lensing sample of galaxies at $z > 1.2$ had a NIR counterpart within 3 arcsec of the *Herschel* position with the probability of a chance alignment $< 10\%$. To study this scenario in our sample, we used high-resolution (~ 1.2 arcsec) radio continuum observations at 6 GHz with the VLA. Overplotting these radio maps in K_s-band images[1], it was possible to determine the origin of the radio emission. To do so, the morphology and position of the radio emission over the NIR counterparts was studied. At the spatial resolution of our radio continuum maps, if the *Herschel*-source was not lensed the radio and the NIR counterpart should be coincident. However, if the NIR object was acting as a lens, an offset between the two sources would be expected. This offset was not expected to be higher than ~ 3.5 arcsec due to the magnification factor affecting the type of galaxies in this work, similar to those in Bussmann et al. (2013). *Herschel*-sources are expected to suffer strong dust obscuration, therefore they are difficult to detect at optical and NIR wavelengths at the depth of the surveys used here. Hence confusion coming from the NIR emission should not be a problem.

In this sample of galaxies some contaminants were expected (i.e. nearby galaxies, AGNs and blazars) so in addition to a morphological study, the IRRC (Yun et al., 2001; Ivison et al., 2010) was used to identify AGNs in the sample. This correlation is followed by all SFGs not

[1]The K_s images were obtained from the VIKING survey (Edge et al., 2013) for the GAMA fields and from UKIDDS (Lawrence et al., 2007) for the NGP field.

dominated by AGNs, so outliers which did not follow the correlation were identified as such (Section 4.5.1). Furthermore, this correlation allowed us to determine if the FIR and the radio emission originated from the same source. For those galaxies which followed the correlation, either lensed or not, the Star Formation Rates (SFRs) were derived in terms of their luminosities and the results discussed.

This dataset allowed us to estimate the fraction of H-ATLAS sources that are lensed. Therefore, the use of VLA observations to detect lensed galaxies at the faintest flux densities is analysed in this work. This groundwork will be part of the lensing systems catalogue of the TLS at redshifts $1.5 < z < 2.5$ which will provide an unprecedented dataset for the modeling of individual sources and for a first cosmographic analysis.

4.3 Sample Selection and VLA Observations

As explained in Section 1.3.5, we can see in Figure 1.7 that the trend of H-ATLAS sources (black line) disperses from the unlensed DSFGs (red line) at $S_{500} \sim 60$ mJy. The probability to detect lensed galaxies above this limit is higher than at lower fluxes. However, radio observations are very time consuming due to the iterative phase calibration, therefore creating a significant sample of sources at $S_{500} > 60$ mJy would require a very high number of hours of observing time. Instead, we selected sources detected at $> 10\sigma$ at 350μm-band with $1.5 < z_{phot} < 2.5$ and close enough to share a phase calibrator (i.e. lying close to each other in the sky) in order to minimise the observing time.

The final sample consisted in 123 candidates, 63 from the GAMA fields and 60 from the NGP field (Table 4.1). From these 123 galaxies, a primary sub-sample of 39 sources at $S_{500} > 60$ mJy (likely containing both lensed and unlensed sources) was created from which 8 sources had $S_{500} > 100$ mJy (expected to be lensed DSFGs). A secondary sub-sample of 84 sources at $S_{500} < 60$ mJy was created which together with the primary sub-sample allows us to test how the fraction of lensed sources decreases as S_{500} decreases. These two sub-samples were analysed together and the results combined but for the final results.

The radio data were obtained with the VLA[2] in two different semesters. The GAMA fields were observed in November 2013 - January 2014 (project 13B-269, P.I. Ivison). These observations were done in configuration B and at C-band (4 - 8 GHz), with a primary beam of ~ 7 arcmin and a beam FWHM ~ 1.1 arcsec. The on-source integration time was ~ 21 min. As flux calibrator J1331+3030 was used for all the observations while the phase calibrators were: J0909+0121 and J0839+0319, J1150-0023 and J1224+0330, and J1505+0326 and J1404-0130 for GAMA09, GAMA12 and GAMA15 fields respectively. The achieved synthesised beam

[2]This observations were done in service mode.

for the GAMA fields was $\sim 1.5 \times 1.1$ arcsec^2. The NGP field was observed in February - May 2015 (project 14B-475, P.I. Ivison). These observations were taken in configurations B and BnA[3] at C-band and with the same angular resolution and synthesised beam $\sim 1.1 \times 1.0$ arcsec^2. The on-source integration time was $\sim$ 24 min. In this case J1331+3030 was used for both flux and phase calibration. In total 60 hours were allocated for both proposals.

4.4 Data Reduction

The data reduction, imaging and analysis of the products was done with the *Common Astronomy Software Applications* package (CASA; McMullin et al., 2007). This package is being developed by an international consortium of scientists[4] to support the data processing of the next generation of radio telescopes (e.g. VLA, ALMA, SKA). The pipeline-v.4.5.3 was used in this work. In Chapter 2 a more detailed explanation of the data reduction and imaging process for interferometric data can be found. Here we explain the main steps nominating the corresponding tasks for each purpose.

4.4.1 Calibration

1. Before any calibration is applied, the first step is to correct the antennae position with `GENCAL`. The positions of the antennae are regularly monitored and updated in a database. When this task is applied the small offset in the antennae positions are modified to their proper values. In addition, some flagging is applied with `FLAGDATA` in known wrong frequencies.

2. An initial flux density scaling for the flux calibrator is defined with `SETJY`. This task sets the flux density model in J1331+3030. The flux density scale at the VLA is updated periodically, the most recent and current default value being defined as 'Perley-Butler 2013' (Perley & Butler, 2013).

3. An initial phase calibration is applied with `GAINCAL`[5]. At certain frequencies and configurations there could be significant gain variations in the different scans of the bandpass calibrator if the scans are at much different elevations. This task averages over the

[3] An extended north arm hybrid configuration. The resolution of the hybrid configurations will be determined by the smaller configuration of the hybrid.

[4] NRAO, ESO, NAOJ, ASIAA, CASS and ASTRON under the guidance of NRAO.

[5] gaintype = 'G', calmode = 'p', solint ='int'

Table 4.1 : TLS sample at $1.5 < z_{phot} < 2.5$. Sources detected at $> 10\sigma$ at 350μm-band were selected in this study creating two sub-samples with $S_{500} < 60$ mJy and $S_{500} > 60$ mJy.

ID	RA	DEC	S_{250} (mJy)	S_{350} (mJy)	S_{500} (mJy)	z_{phot}
G09.v10.157	09:13:31.40	-00:36:43.5	175 ± 6	142 ± 7	86 ± 8	1.74
G09.v10.259	09:09:52.99	-01:08:11.3	152 ± 7	109 ± 8	83 ± 8	1.72
G09.v10.401	09:23:48.50	+01:19:08.	126 ± 7	115 ± 8	70 ± 9	1.99
G09.v10.474	09:02:44.83	+01:33:25.7	116 ± 7	109 ± 8	77 ± 9	2.06
G09.v10.493	08:37:26.12	+01:56:41.9	127 ± 7	114 ± 8	68 ± 9	2.08
G09.v10.507	09:18:52.54	+02:30:16.8	119 ± 7	103 ± 8	47 ± 9	1.64
G09.v10.576	08:38:00.75	-00:33:08.1	112 ± 7	100 ± 8	51 ± 9	2.06
G09.v10.812	08:51:19.57	+02:29:40.6	97 ± 7	86 ± 8	49 ± 9	1.79
G09.v10.825	09:21:44.13	+00:39:08.7	104 ± 7	78 ± 8	37 ± 9	1.57
G09.v10.892	08:43:47.45	+00:33:31.9	84 ± 7	57 ± 8	30 ± 8	1.81
G09.v10.1183	09:01:38.84	-01:08:55.1	76 ± 7	69 ± 8	53 ± 9	1.91
G09.v10.1186	08:46:40.85	+00:34:40.1	66 ± 6	62 ± 7	37 ± 8	2.31
G09.v10.1251	09:13:50.20	+01:45:43.5	91 ± 7	87 ± 8	50 ± 9	2.09
G09.v10.1475	08:34:34.34	+01:16:01.5	81 ± 8	74 ± 8	47 ± 9	1.79
G09.v10.1558	08:41:16.68	+02:06:36.9	74 ± 7	64 ± 8	35 ± 9	2.07
G09.v10.1569	09:08:11.65	-00:13:40.4	73 ± 7	64 ± 8	31 ± 8	2.12
G09.v10.1573	09:04:29.68	+00:29:35.9	87 ± 7	83 ± 8	56 ± 9	2.23
G09.v10.1700	08:47:40.94	+00:24:20.7	65 ± 6	68 ± 7	40 ± 8	2.36
G09.v10.1729	09:17:35.15	+00:12:03.1	65 ± 7	59 ± 8	34 ± 9	1.82
G12.v10.116	12:13:34.91	-02:03:22.9	211 ± 6	198 ± 7	130 ± 7	2.12
G12.v10.305	11:51:12.30	-01:26:38.8	141 ± 7	138 ± 8	108 ± 9	2.34
G12.v10.457	11:48:50.47	-02:01:56.6	372 ± 64	260 ± 47	113 ± 38	1.50
G12.v10.463	11:45:19.52	-00:39:00.6	111 ± 6	91 ± 7	40 ± 8	1.65
G12.v10.528	12:20:27.68	+01:28:12.9	267 ± 36	219 ± 32	123 ± 25	1.86
G12.v10.530	12:04:22.05	-01:27:36.7	110 ± 7	91 ± 8	55 ± 8	1.71
G12.v10.596	12:18:26.91	+01:24:21.9	108 ± 7	75 ± 8	54 ± 9	1.57
G12.v10.761	11:59:45.51	-00:33:29.2	85 ± 6	84 ± 7	51 ± 8	2.09
G12.v10.829	11:59:24.54	-00:24:40.5	104 ± 15	62 ± 7	48 ± 8	1.58
G12.v10.846	12:14:17.20	+00:33:04.9	96 ± 7	84 ± 8	48 ± 9	1.87
G12.v10.860	11:36:16.78	-00:46:21.2	109 ± 7	99 ± 8	55 ± 9	1.93
G12.v10.864	11:50:10.52	+00:29:44.9	109 ± 7	83 ± 8	50 ± 8	1.71
G12.v10.881	11:42:10.80	+00:39:09.7	80 ± 7	86 ± 9	55 ± 9	2.46
G12.v10.893	11:41:31.32	+01:33:55.9	101 ± 7	110 ± 8	76 ± 9	2.45
G12.v10.932	12:17:04.69	-00:09:16.7	109 ± 7	78 ± 8	43 ± 8	1.62
G12.v10.1246	11:55:40.81	-00:55:30.4	85 ± 7	92 ± 8	58 ± 8	1.63
G12.v10.1259	11:41:39.97	-00:22:35.1	96 ± 7	76 ± 8	40 ± 9	1.80
G12.v10.1504	12:16:08.14	+00:40:55.7	84 ± 7	64 ± 8	45 ± 8	2.01
G12.v10.1529	12:17:10.00	+00:28:15.1	77 ± 7	76 ± 8	46 ± 9	2.09
G12.v10.1589	11:37:39.25	-02:45:43.3	79 ± 7	74 ± 8	54 ± 9	2.13
G12.v10.1805	11:44:04.73	-01:08:39.5	84 ± 7	67 ± 8	35 ± 9	1.91
G15.v10.245	14:45:33.91	+01:05:56.4	184 ± 7	141 ± 8	70 ± 8	1.58
G15.v10.432	14:08:27.93	+01:42:08.8	134 ± 8	110 ± 8	70 ± 10	1.87
G15.v10.468	14:18:27.47	-00:17:03.6	117 ± 6	116 ± 7	80 ± 9	2.18
G15.v10.581	14:42:43.44	+01:55:05.8	123 ± 7	133 ± 8	86 ± 10	2.41
G15.v10.592	14:20:03.77	+01:40:44.7	121 ± 7	108 ± 8	77 ± 10	2.16
G15.v10.606	14:45:01.63	+00:41:31.1	117 ± 7	89 ± 8	73 ± 10	2.15
G15.v10.678	14:52:07.21	-00:33:38.3	115 ± 7	98 ± 8	41 ± 10	1.71
G15.v10.730	14:11:49.66	-00:56:32.6	112 ± 7	101 ± 8	58 ± 9	1.76
G15.v10.861	14:21:12.43	+00:52:30.2	105 ± 7	99 ± 8	74 ± 10	2.21
G15.v10.877	14:51:57.19	+00:52:44.0	100 ± 7	84 ± 8	54 ± 8	1.78
G15.v10.899	14:18:49.92	+01:03:21.9	84 ± 7	79 ± 8	40 ± 8	1.63
G15.v10.934	14:45:22.19	+01:15:15.4	106 ± 7	81 ± 8	35 ± 8	1.52
G15.v10.945	14:24:19.63	+00:14:58.3	105 ± 7	81 ± 8	66 ± 9	1.77
G15.v10.1044	14:57:33.73	-00:41:35.7	88 ± 8	65 ± 8	43 ± 9	1.55
G15.v10.1103	14:23:01.08	-00:38:17.5	78 ± 7	64 ± 8	39 ± 9	1.57
G15.v10.1138	14:33:55.34	+00:32:55.7	93 ± 7	78 ± 8	47 ± 9	1.64
G15.v10.1162	14:23:26.30	+02:07:11.9	87 ± 7	69 ± 8	30 ± 8	1.65
G15.v10.2095	14:08:44.85	-01:18:48.7	78 ± 8	72 ± 8	56 ± 9	2.24
G15.v10.2150	14:40:45.84	+00:04:33.1	57 ± 6	59 ± 7	40 ± 8	2.35
G15.v10.2160	14:35:56.62	+01:52:23.7	73 ± 7	78 ± 8	44 ± 8	2.11
G15.v10.2231	14:09:08.06	-00:51:09.0	61 ± 7	64 ± 8	49 ± 9	2.25
G15.v10.2516	14:51:07.52	-01:20:21.7	64 ± 7	67 ± 8	49 ± 10	2.30
G15.v10.4116	14:22:27.41	-01:50:58.3	68 ± 7	68 ± 8	40 ± 10	2.47

Table 4.1 *: Continued*

ID	RA	DEC	S_{250} (mJy)	S_{350} (mJy)	S_{500} (mJy)	z_{phot}
NGP-383	12:57:59.67	+22:45:57.9	272 ± 6	215 ± 6	138 ± 7	1.67
NGP-413	13:30:08.51	+24:58:59.1	271 ± 5	278 ± 6	203 ± 7	2.36
NGP-684	13:41:58.55	+29:28:31.5	174 ± 5	172 ± 5	109 ± 6	2.15
NGP-714	13:36:22.64	+34:38:05.8	192 ± 6	150 ± 6	65 ± 7	1.53
NGP-1017	13:46:54.62	+29:56:59.3	160 ± 6	125 ± 6	76 ± 7	1.66
NGP-1113	13:35:42.89	+30:04:04.5	137 ± 5	146 ± 6	125 ± 7	2.49
NGP-1128	12:59:10.95	+29:38:44.3	162 ± 6	138 ± 6	90 ± 7	1.93
NGP-1189	13:44:00.35	+34:22:42.7	146 ± 5	125 ± 6	69 ± 7	1.81
NGP-1328	13:38:34.16	+29:48:04.0	143 ± 6	109 ± 6	60 ± 7	1.50
NGP-1386	13:19:28.86	+25:58:01.0	108 ± 4	82 ± 4	37 ± 6	1.50
NGP-1401	13:10:04.85	+34:10:48.9	105 ± 5	70 ± 6	44 ± 7	1.50
NGP-1411	13:28:58.26	+30:42:18.7	132 ± 6	89 ± 6	49 ± 7	1.56
NGP-1451	13:09:36.66	+28:08:02.7	132 ± 6	102 ± 6	47 ± 7	1.50
NGP-1595	13:05:25.00	+34:28:50.6	129 ± 6	125 ± 6	77 ± 7	2.14
NGP-1632	13:05:29.24	+27:38:19.2	131 ± 6	112 ± 6	67 ± 7	2.04
NGP-1784	13:31:15.41	+32:19:14.3	107 ± 5	97 ± 5	47 ± 6	1.73
NGP-1787	12:56:53.68	+31:48:18.0	105 ± 5	90 ± 5	52 ± 6	1.69
NGP-1790	13:14:12.32	+28:17:52.7	109 ± 6	85 ± 6	46 ± 7	1.59
NGP-1801	13:32:31.60	+35:08:42.7	130 ± 6	109 ± 6	73 ± 7	2.02
NGP-1874	12:45:52.55	+32:23:04.6	115 ± 6	96 ± 6	51 ± 7	1.65
NGP-2178	13:35:25.25	+29:49:18.9	121 ± 5	94 ± 6	45 ± 7	1.51
NGP-2241	13:13:48.55	+24:24:55.5	110 ± 6	119 ± 6	74 ± 7	2.22
NGP-2353	13:04:14.49	+30:35:38.8	106 ± 6	111 ± 6	89 ± 7	2.44
NGP-2403	13:30:47.61	+35:23:40.2	90 ± 5	73 ± 5	41 ± 6	1.76
NGP-2478	12:51:53.34	+26:33:03.7	104 ± 6	83 ± 6	49 ± 7	1.70
NGP-2535	12:54:25.31	+29:36:49.4	103 ± 6	90 ± 6	65 ± 7	2.05
NGP-2555	12:53:15.50	+25:49:42.9	115 ± 6	88 ± 6	49 ± 7	1.54
NGP-2736	13:40:14.06	+23:47:14.4	93 ± 7	88 ± 6	58 ± 7	2.10
NGP-2945	12:54:34.36	+28:29:46.6	84 ± 4	81 ± 4	66 ± 6	2.29
NGP-2985	13:13:09.39	+31:31:32.8	100 ± 6	76 ± 6	53 ± 7	1.83
NGP-2995	13:39:02.95	+23:37:58.6	96 ± 6	74 ± 6	32 ± 7	1.55
NGP-3078	13:41:32.41	+25:47:49.0	100 ± 6	68 ± 6	35 ± 8	1.55
NGP-3120	12:50:30.20	+31:33:48.2	91 ± 5	77 ± 5	47 ± 6	1.86
NGP-3154	12:58:05.65	+29:48:02.1	98 ± 5	94 ± 6	53 ± 7	2.17
NGP-3196	13:30:46.02	+24:57:13.2	90 ± 5	89 ± 6	44 ± 7	1.88
NGP-3222	13:32:04.23	+30:17:47.6	104 ± 6	107 ± 6	55 ± 7	1.99
NGP-3248	13:44:54.21	+33:11:33.8	103 ± 6	81 ± 6	29 ± 7	1.51
NGP-3287	13:26:43.28	+28:06:49.7	98 ± 6	74 ± 6	52 ± 7	1.63
NGP-3394	13:20:25.46	+30:10:04.0	87 ± 6	79 ± 6	33 ± 7	1.91
NGP-3653	12:46:20.08	+33:16:13.7	89 ± 6	82 ± 6	45 ± 7	2.01
NGP-3669	13:47:59.61	+32:27:10.3	82 ± 6	68 ± 6	38 ± 7	1.73
NGP-3708	13:27:04.69	+31:31:32.5	96 ± 5	93 ± 6	56 ± 7	1.99
NGP-3746	12:54:54.06	+31:50:25.5	86 ± 5	74 ± 6	34 ± 7	1.80
NGP-3778	13:14:55.75	+30:21:01.1	91 ± 5	71 ± 6	36 ± 7	1.92
NGP-3862	13:09:56.96	+34:29:06.1	101 ± 6	82 ± 6	60 ± 8	1.90
NGP-3990	13:45:41.01	+25:28:24.1	83 ± 6	69 ± 6	44 ± 7	1.89
NGP-4201	12:51:21.65	+27:24:52.7	89 ± 6	88 ± 6	45 ± 7	2.09
NGP-4209	13:41:51.88	+33:27:19.9	94 ± 6	104 ± 6	73 ± 7	2.30
NGP-4425	13:38:07.54	+32:43:04.1	75 ± 5	77 ± 5	60 ± 6	2.40
NGP-4546	13:08:56.73	+32:36:32.2	78 ± 6	77 ± 6	53 ± 7	2.01
NGP-4690	12:56:55.50	+27:46:20.4	84 ± 6	73 ± 6	35 ± 7	1.94
NGP-4772	13:48:28.62	+25:45:50.3	79 ± 6	98 ± 6	66 ± 7	2.49
NGP-4810	13:28:18.12	+35:16:25.0	72 ± 6	66 ± 6	40 ± 7	1.96
NGP-4844	13:23:55.01	+33:59:20.4	76 ± 6	67 ± 6	45 ± 7	1.99
NGP-4870	13:17:32.95	+24:09:25.5	84 ± 6	100 ± 6	73 ± 7	2.47
NGP-5121	13:38:06.85	+35:15:27.1	83 ± 6	82 ± 6	43 ± 7	1.97
NGP-5310	13:15:53.01	+23:28:26.7	80 ± 6	78 ± 6	40 ± 7	1.93
NGP-5913	13:10:17.26	+27:44:18.3	82 ± 6	72 ± 6	36 ± 7	1.91
NGP-6110	13:37:05.98	+34:13:14.5	81 ± 6	87 ± 6	54 ± 7	2.25
NGP-6431	12:53:02.71	+24:44:54.7	76 ± 6	90 ± 6	50 ± 7	2.40

variations of phase with time in the bandpass calibrator before solving for this solution. A second `GAINCAL`[6] is used to correct from the antenna delays.

4. The bandpass calibration is applied with `BANDPASS`[7]. It corrects the gain variations with frequency.

5. To derive corrections for the antenna gains `GAINCAL`[8] is used.

6. To scale the amplitudes we use `FLUXSCALE`. This produces a new calibration table with the properly scaled amplitude gains for the phase calibrator.

7. The task `STATWT`[9] is applied to re-weight visibilities according to their scatter.

8. Finally we can apply the calibration solutions with `APPLYCAL` to the phase calibrator and the targets.

After running the pipeline for the very first time, the visibilities for the calibrators and the targets were checked. Normally a lot of RFIs were found in all the sources so flagging the data was necessary. The CASA pipeline does an automatic flagging, however it was not very effective so manual flagging was needed instead. Due to the big amount of data to reduce we tried to use a more automatic and interactive tool to speed up this process like AOFlager (Offringa et al., 2012). This software was first created to used with LOFAR data and later adapted for other radio telescopes. Because of the large size of our data sets it was practically very difficult to run AOflagger, even using specific machines at ESO[10] with big capacity of processing. Another problem was that AOflagger is not specifically set up for the VLA and we would need thus to run many iterations before finding the proper characteristics to flag the targets and the calibrators with the same parameters and not to flag too much or too little. Due to the very time consuming and the uncertainty in the set-up we decided to do the flagging manually with CASA using the task *FLAGDATA*. This process was long and hard but more reliable in the final measurements. After flagging the data the pipeline was run again to recalibrate the data. After this, even a third flagging and re-calibration was necessary for some of the data-sets.

[6] gaintype = 'K', solint ='inf'
[7] Using bandtype='B' the solution is derived on a channel-by-channel basis.
[8] gaintype='G', calmode='ap'
[9] This task is currently under experiment.
[10] European Southern Observatory

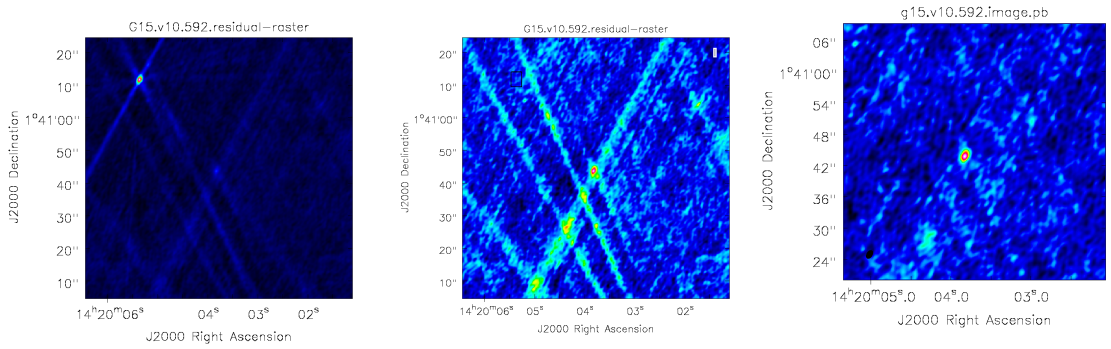

Figure 4.2 : Example of the contamination coming from bright sources within the primary beam and the different steps for the cleaning process in the map. *Left:* One bright source in the left corner of the map is clearly detected. Some other weak contamination is noticeable as well. *Middle:* When box-selecting the bright source in the left corner the noise in the map coming from other sources becomes more obvious. It is clear how other bright sources within the primary beam are contaminating our target. *Right:* After creating a bigger map and box-select all those bright sources the contamination is eliminated and our map looks cleaner.

4.4.2 Imaging

After calibrating the visibilities, continuum maps were created with the task `CLEAN`. Multi-frequency-continuum images were created with a pixel size of 0.2 arcsec, natural weighting and interactive cleaning boxing mode. The primary beam correction was done with `IMPBCOR` which divides the restore map after the cleaning by the primary beam response[11]. These calibrated 'clean-primary-beam-corrected' maps were the final radio continuum maps to analyse.

Due to the size of the primary beam ($\sim$ 7 arcmin) sometimes one or more very bright radio sources produced interferences in the maps which contaminate our targets. Doing a bigger map to box-select these sources (see Section 2.3) to remove their contamination from the map was normally sufficient to clean the maps properly (Figure 4.2). However, in some maps this cleaning process was not enough to obtain a clean map. In a few maps (4 GAMA and 7 NGP targets) there were no radio emission detections at the *Herschel* position. The noise of these maps was not much higher than the average noise of all the maps but no targets were detected (Figure 4.3). For these cases it was not possible to know if the radio emission coming from the *Herschel*-source was too faint to be detected or if the nearby bright sources were contaminating the map enough that the target was not detected. A more elaborated cleaning process for these sources would be needed, and as they represented 9% of our sample, we decided to exclude them from the sample. Thus, the final sample consisted of 112 sources out of 123.

[11] From the 7 arcmin of primary beam, only the central part, $\sim$ 40 arcsec^2, was under study. Thus the primary beam correction should not change much the measurements in the studied region.

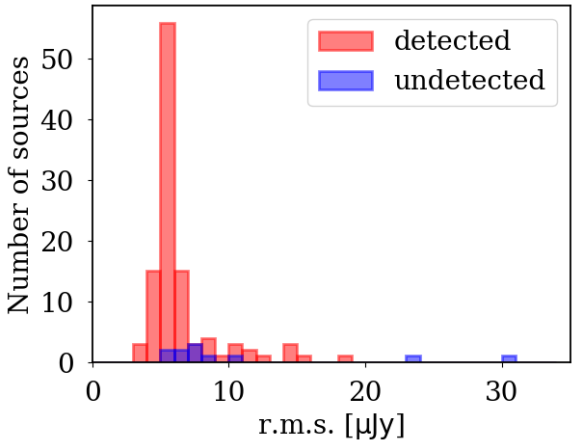

Figure 4.3 : Histogram of the r.m.s. for the 112 maps with detected radio sources in red and the 11 maps with non-detected radio sources in blue. The mean value for the detected sources is 6.66 μJy with a standard deviation of 3.18 μJy. We can see that the noisier map has an r.m.s. $\sim$ 30 μJy, it is thus understandable to not detect any source in this map. However, some of the maps where there is no radio detection do not have much higher r.m.s. than the mean value. A more careful cleaning process is needed to obtain better quality of these maps.

During this work the spectral index (α) of the sources was calculated to determine the radio luminosities, so three different maps were created from the visibilities. The 4 GHz bandwidth was divided in two different images of 2 GHz each. Thus the different images were centred at 6 GHz (total continuum map), 5 GHz and 7 GHz. The mean r.m.s. for these three maps were 7 μJy, 10 μJy and 8 μJy respectively which was in agreement with the sensitivity of the C-band across the bandwidth (Figure 4.4). In Figure 4.5 an example of the three different maps for one source is shown where we can see how the resolution improves at higher frequencies. For this target, while only one clear detection is seen at 5 GHz, two different detections are distinguishable at 6 and 7 GHz.

4.5 Classification of the Targets

To classify the *Herschel*-sources first we needed to identify the radio emission within the 250μm-band. The radio sources at 5σ in the C-band maps were identified with SExtractor (Bertin & Arnouts, 1996). The detection criteria was a 5σ standard deviation above the background, an object size of 5 pixels and a "top-hat"-1.5-3x3[12,13] filter. As explained in Section 4.2 there were some contaminants in the sample that needed to be removed. In this

[12]FWHM$\times$size, in pixels.
[13]Different filters were tested but no relevant differences were found.

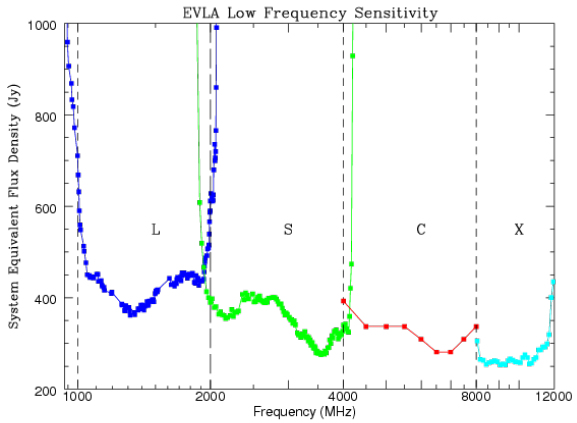

Figure 4.4 : The sensitivity of the different bands in the VLA is shown in this plot. Focussing on the C-band (red line) we see how the flux density limit is lower at higher frequencies which results in better sensitivity. This is in agreement with the average r.m.s. of our 3 different maps. Image credit: https://science.nrao.edu

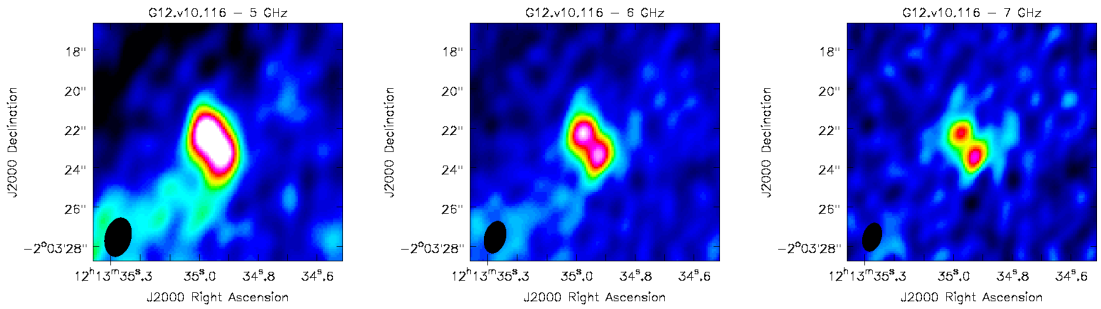

Figure 4.5 : From left to right the radio continuum maps centred at 5 GHz , 6 GHz and 7 GHz are shown for the source G12.v10.116. The image centred at 6 GHz has a bandwidth of 4 GHz while the other two have a bandwidth of 2 GHz. These maps show how the resolution changes with frequency and therefore at higher resolutions two different detections are resolved. The beam for each map is shown in the bottom-left corner. Note that this situation is not the normal case for every source.

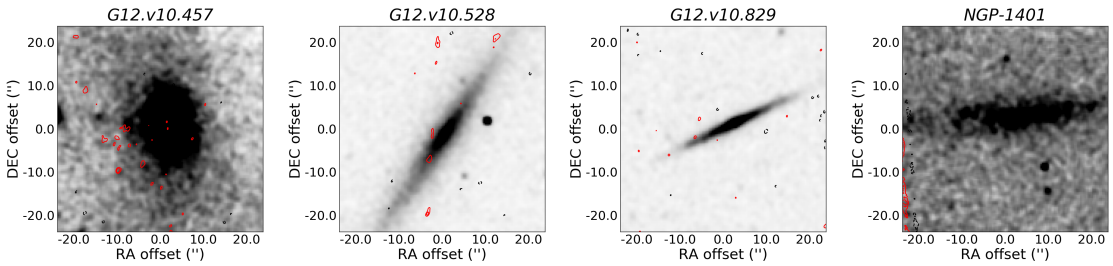

Figure 4.6 : K_s-band images of four nearby galaxies are shown. The red contours represent the radio emission from the VLA with no hint of lensing. Due to the 'largest angular scale' these sources are resolved out and no radio counterparts can be detected. These sources are excluded from the final sample.

section we explain how the contaminants were identified and show the final statistics of the sample.

4.5.1 Contaminants

Nearby galaxies

Upon visual inspection of the K_s-band images, four bright nearby galaxies were found with no hint of lensing radio emission. Due to the 'largest angular scale' effect in interferometric arrays, these galaxies were most likely resolved out and therefore no radio emission coming from the nearby galaxies was detected. The minimum baseline at configuration B with the VLA is 0.21 km, which allows a largest visible structure of 29 arcsec. These 4 nearby galaxies are extended over a range of ~ 40 arcsec so no radio counterparts can be detected. Thus, these four galaxies were removed from the sample (Figure 4.6).

Galaxy Groups and Clusters

When inspecting the K_s- and C-band images it turned out that some maps had multiple sources or even extended morphologies within the *Herschel* 250μm beam. Taking Smolčić et al. (2017a) as reference, the number density of sources in 40 arcsec^2 at this frequency was calculated. Smolčić et al. (2017a) present a catalogue for the COSMOS field with a covered area of 2.6 deg^2. This survey was carried out with the VLA at 3 GHz with a median r.m.s. ~ 2.3 μJy/beam. To calculate the density number of sources in our maps we defined as flux limit 5σ the average r.m.s. of the maps at 6 GHz, i.e 35.22 μJy. We converted this flux to the 6 GHz frequency with an $\alpha = 0.7$ ($S \propto \nu^{-\alpha}$) which corresponded to 21.68 μJy. In the COSMOS catalogue there are 6,443 sources above this flux limit in 2.6 deg^2, therefore the expected number of sources in our 40 arcsec^2 VLA maps was 0.3. Hence, those maps with more than one source were

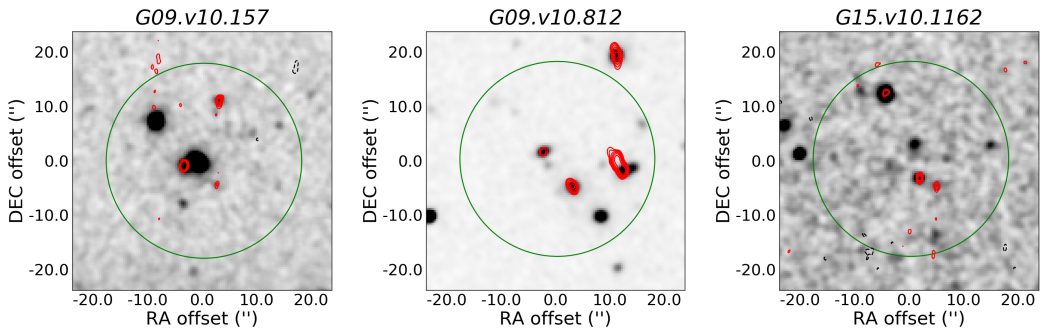

Figure 4.7 : Example of potential galaxy clusters in our sample. The green circles represent the *Herschel* 250μm beam, the background image (in grey-scale) is the K_s-band and the contours (in red) correspond to the 6 GHz radio continuum emission. The contours start at 3σ and increase by a factor of $\sqrt{2}$ (-3σ in dashed-black).

over-densities and the galaxies in the maps with 3 detected sources or more were most likely related, e.g. galaxy clusters or proto-clusters. Some examples of these complex maps are shown in Figure 4.7.

To determine the radio counterparts of the *Herschel*-sources, the 250μm-band images were examined. For instance, in Figure 4.8 (top-left) two radio sources were within the Herschel beam. Although, when inspecting the 250μm image (Figure 4.8 top-right) we can see that the FIR emission is dominated by, and centred on, one of the sources while the second source, further from the centre of the beam, is weak enough to be ignore as a contributing source of FIR emission. However in Figure 4.8 (bottom-left) the contribution from the FIR band appeared to come from both sources, hence it was not possible to determine the radio counterpart for the *Herschel* emission.

In total there were 46 maps with more than one radio detection within the *Herschel* 250μm beam and 62 with single detections. From these 46 maps, we found that there were 5 SLGs (i.e. more than one radio detection produced for the effect of the lens as shown in Figure 4.9), 39 for which it was not possible to identify them because the FIR confusion and 2 sources for which it was possible to determine the radio counterparts of the *Herschel* objects. Therefore 7 sources with multiple radio detections could be identified as counterparts of FIR sources (5 SLGs + 2 identified radio counterparts).

From the 39 unclassified sources found to have more than one radio counterpart within the *Herschel* 250μm emission, there were 10 sources with 3 or more radio counterparts. This over-densities are very good candidates of proto-cluster sources. Proto-clusters are defined as the progenitors of the massive galaxy clusters of today's universe. Located at high-redshifts ($z > 1.3$), they are formed from several halos which will merge in a final halo to create the clusters at low redshifts (Muldrew et al., 2015). They are characterized as over-densities of

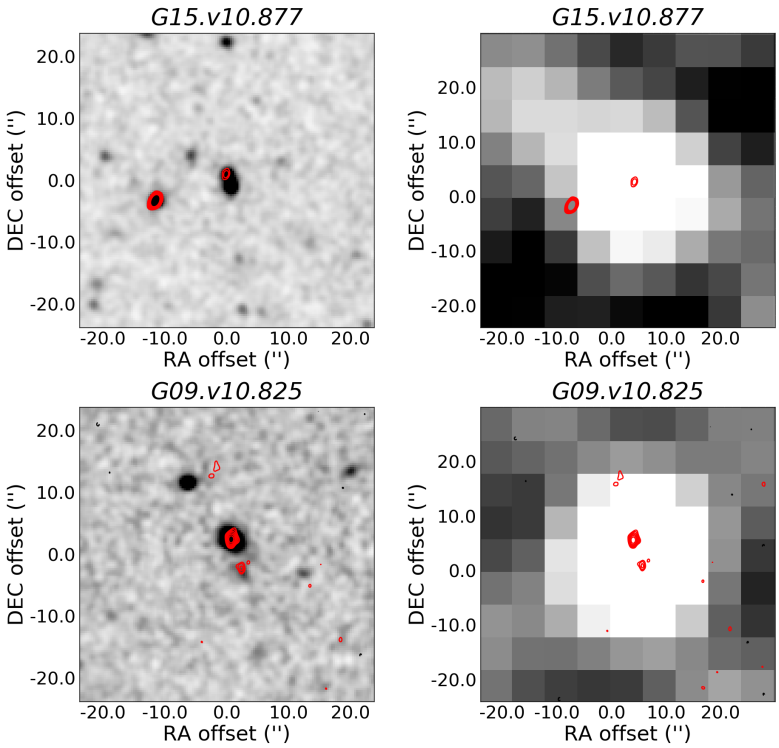

Figure 4.8 : From left to right K_s- and 250μm-band images are shown. The red contours represent the radio emission from the VLA starting at 3σ with increments of $\sqrt{2}$ (-3σ in dashed-black). In the top-right image it is possible to distinguish one of the radio sources being centred at the FIR emission while the other radio emission is in a darker area. Thus this second source might contaminate the FIR emission of our target but not significantly. However, in the bottom panels we can see that two radio sources are over the FIR emission. It is thus not possible to know if both galaxies contribute to the FIR emission or not. With no signs of lensing it is not possible to classify these galaxies with the available information.

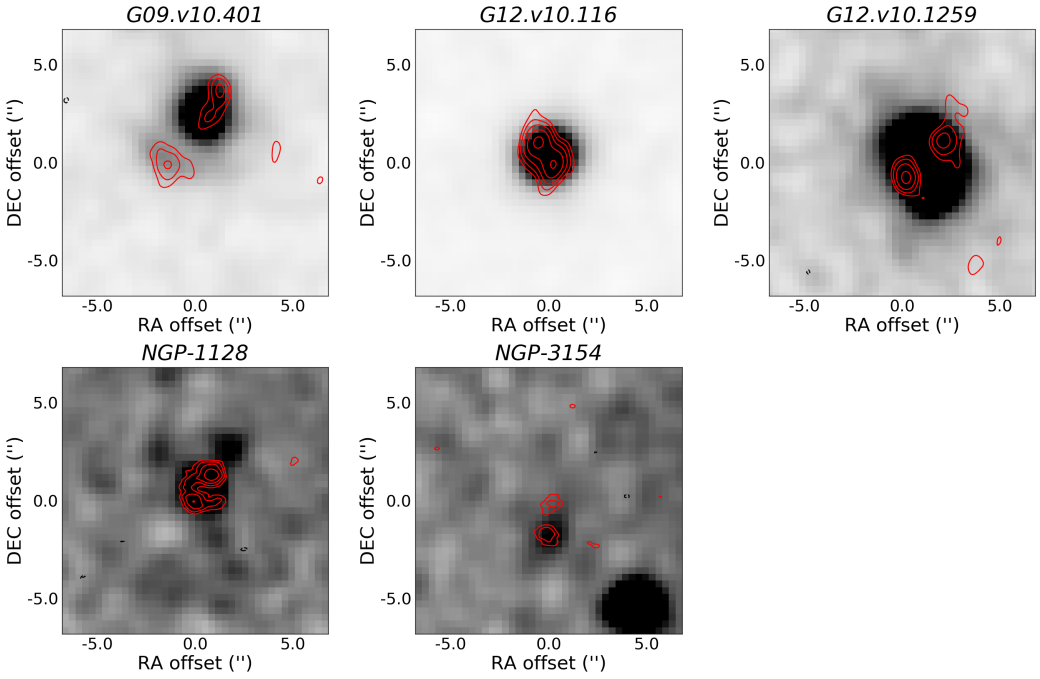

Figure 4.9 : In this figure the unconfused detected SLGs in the sample are shown. The background image correspond to the K_s-band and the red contours to the C-band starting at 3σ and increasing by a factor of $\sqrt{2}$ (-3σ is shown in dashed-black).

massive galaxies on 2-8 co-moving Mpc scales and are very difficult to detect due to their low density number and the faintness of distant galaxies. Due to their high mass density and therefore high merger rates, radio-loud galaxies are expected to exist in them (e.g. Ramos Almeida et al., 2013; Hatch et al., 2014). One of the most successful methods to detect proto-clusters is the High Redshift Radio Galaxies (HzRGs) as a tracer population to locate overdense regions (e.g. Le Fevre et al., 1996; Pentericci et al., 2000; Best et al., 2003; Hatch et al., 2011; Cooke et al., 2014). Not many proto-clusters have been found so far. If it is confirmed that this sample indeed consists of proto-clusters, it would be a relevant result which would allow us to study in more detail the formation and evolution of the galaxy clusters in today's universe and the distribution of dark matter in the high-z universe. In Figure 4.10 some examples are shown of the sub-sample of proto-cluster candidates.

For these 39 maps affected by the FIR confusion or potential galaxy clusters no further analysis was possible with the available data. Although we describe the available information and provide some potential scenarios in Appendix 4.A.

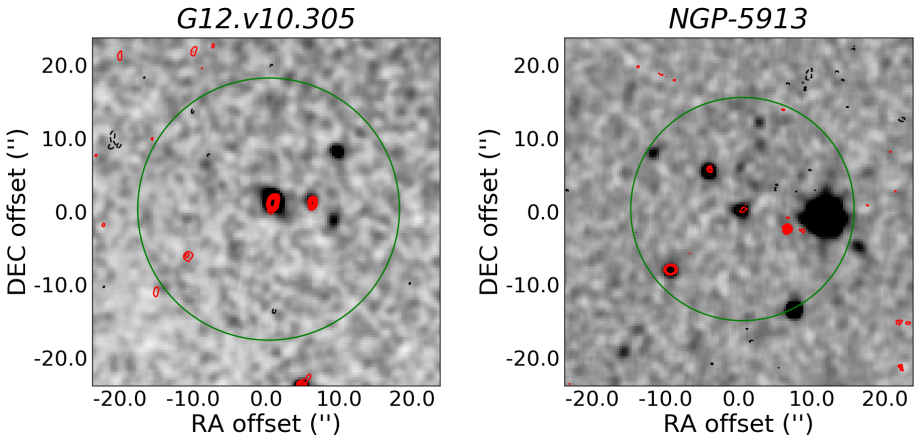

Figure 4.10 : Two examples of overdense regions that are good candidates to be proto-cluster. The background image correspond to the K_s-band, the green circle is the 250μm beam from *Herschel* and the red contours correspond to the C-band starting at 3σ and increasing by a factor of $\sqrt{2}$ (-3σ is shown in dashed-black).

AGNs

To identify the AGNs in the 69 remaining galaxies (62 single detections + 7 multiple detections) the IRRC was used. Galaxies dominated by AGNs have higher radio emission and are thus outliers in the IRRC. As we explained in Section 1.5 the IRRC is due to young stars ending their lives as SNe. These young stars heat the dust, which in turn results in augmented FIR emission. The associated SNe are as well the main sites for cosmic-ray acceleration which emits radio synchrotron emission as electrons are accelerated due to the interstellar magnetic field. Therefore, if the FIR and the radio emission are coming from the same source, and they are not AGNs, it is expected these galaxies follow this very well studied correlation. In this work, the IRRC was studied between the 250μm-band from *Herschel* (the SPIRE band with the highest resolution) and the 6 GHz continuum maps. The radio fluxes were measured with the task `IMFIT` in CASA. The selected region to measure the flux of the source was defined taking the central coordinate of the SExtractor-detected source and creating a centerbox region of 5×5 arcsec^2 width (Figure 4.11). Another centerbox region of 15×15 arcsec^2 close to the targets and without sources in it was selected to determine the r.m.s. of the maps with `IMSTAT`.

In Figure 4.12 (left) the IRRC for all the sources in the sample is shown. Some outliers are present in this figure which correspond to eleven AGNs shown in red in Figure 4.12 (right). The dashed-blue line shows the correlation for the remaining SFGs (blue dots) of the TLS sample excluding the AGNs (red dots). To determine the flux limit at which these galaxies were classified as AGNs, the difference between the measured and the estimated radio fluxes at 6 GHz were calculated (Flux_{dif}). The estimated fluxes were calculated averaging the 6 GHz

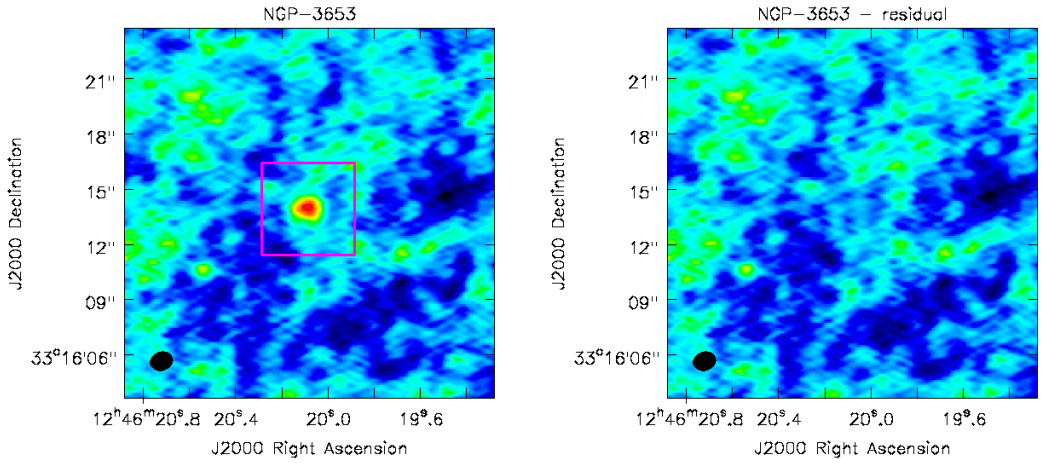

Figure 4.11 *Left:* Example of a radio detection for one of the targets. The box in magenta is the selected-region box to perform the 2D-fit Gaussian and measure the flux density. *Right:* Residual image created by CASA after subtracting the flux density. We can see that the noise in the residual image is very homogeneous with the rest of the map so the subtraction of the flux is good.

flux of four different SEDs[14] (Figure 4.13) at the z_{phot} of the target. We considered sources with $\mathrm{Flux_{dif}} > 3 \times \Delta\mathrm{Flux_{dif}}$ to be AGNs, using the following expressions:

$$\mathrm{Flux_{dif}} = \mathrm{Flux_{measured}} - \mathrm{Flux_{estimated}} \tag{4.1}$$

$$\Delta\mathrm{Flux_{dif}} = \sqrt{(\Delta\mathrm{Flux_{measured}})^2 + (\Delta\mathrm{Flux_{estimated}})^2 + (\Delta_{\mathrm{calibration}})^2)} \tag{4.2}$$

where $\Delta\mathrm{Flux_{measured}}$ is the error in the measured flux, $\Delta\mathrm{Flux_{estimated}}$ is the standard deviation of the four templates, and $\Delta_{\mathrm{calibration}}$ is a calibration error of 15%. It is important to note that this correlation does not exclusively mean that a system is star forming only, since low luminosity AGNs and hybrid AGN/SF systems can all lie on the same correlation.

The AGNs found in the sample are shown in Figure 4.14. Two of them (G12.v10.893 and NGP-413) present hints of extended radio emission most likely related with jets. Another less probable explanation might be that these two AGNs are lensed sources.

To determine whether the remaining galaxies were lensed or not, their morphology was studied in detail to determine offsets between the NIR potential lens and the radio emission. This classification is based on visual inspection[15] and thus it is not the most robust classification. One of the main concerns is whether AGN jets can be misclassified as extended emission

[14] M82, Arp220, eyelash-rest and Pearson+13.

[15] This visual inspection was done by three different people to compare our interpretation of the morphology and was discussed until agreement was reached on the classification of each object.

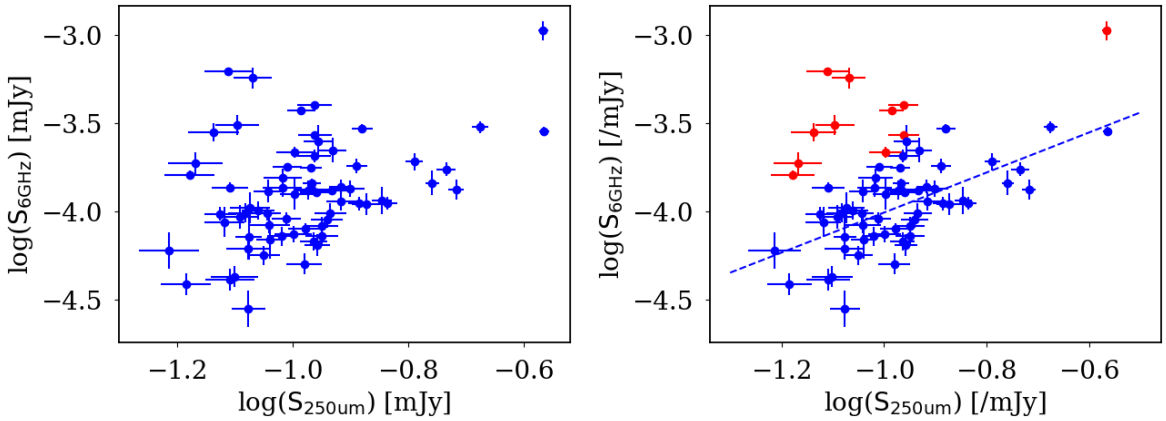

Figure 4.12 : *Left:* IRRC correlation for the remaining 69 targets which were selected after removing contaminants in the VLA maps (nearby galaxies and groups of galaxies). *Right:* IRRC with the AGNs flagged in red. The dashed-blue line shows the correlation for the SFGs (blue dots) of our TLS sample, given by $\log(S_{6GHz}) = 0.63 \times \log(S_{250}) + 1.14$ with a dispersion of 0.19 dex.

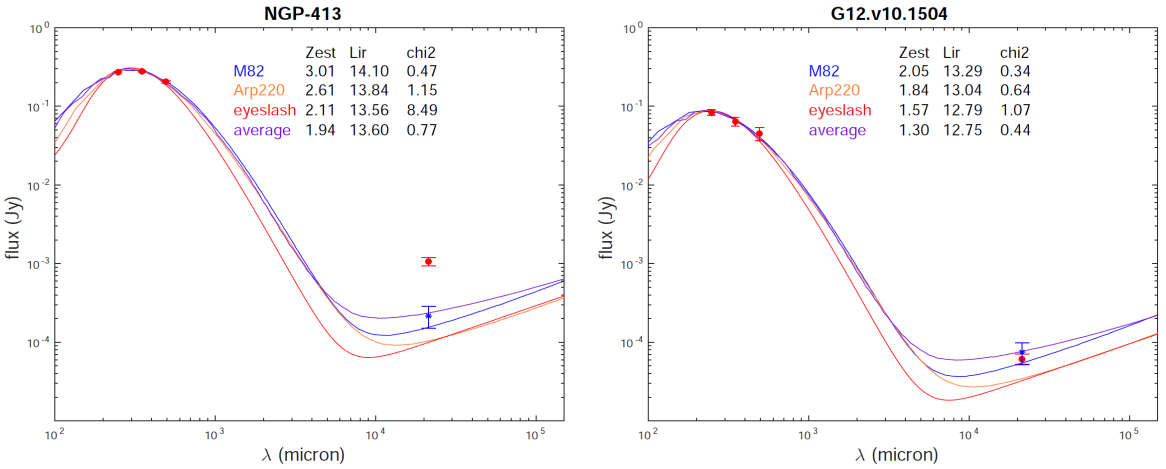

Figure 4.13 : Comparison of the estimated (blue dot) and measured (red dot) fluxes for the 6 GHz emission. SED fitting was used to obtain the estimated fluxes. *Left:* We can see how the measured flux is higher than the estimated one. We thus classify this source as an AGN. *Right:* Estimated and measured fluxes are coincident so this galaxy is classified as a SFG.

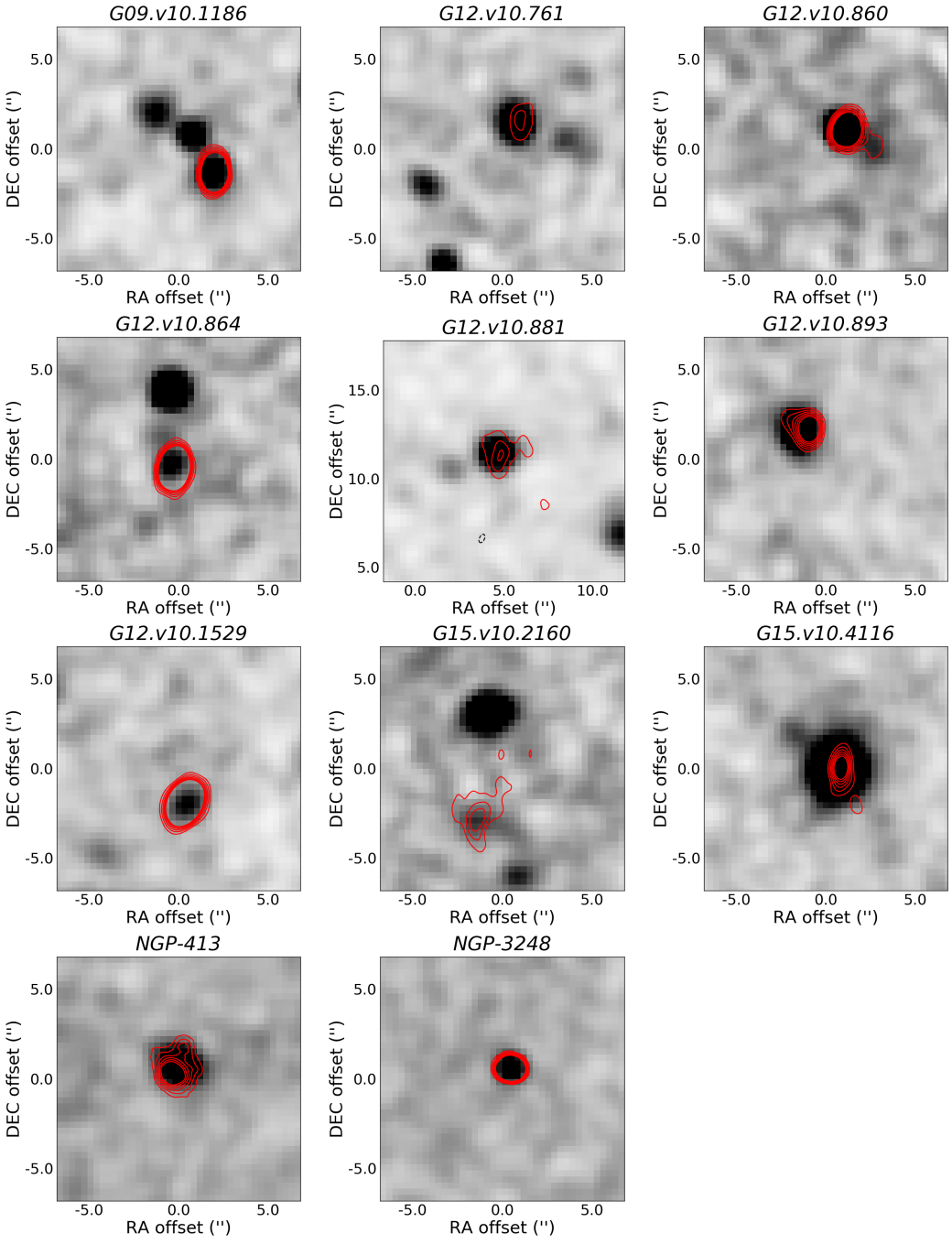

Figure 4.14 : AGNs found in the sample where the background image correspond to the K_s-band and the red contours correspond to the 6 GHz radio emission starting at 3σ and increasing in steps of $\sqrt{2}$. In dashed-black -3σ is plotted. We see that two of these galaxies (G12.v10.893 and NGP-413) present hints of extended radio emission most likely associated with jets, typically found in AGN systems. Another explanation might be that these AGNs are lensed and these asymetries are due to the lensing effect. Note that the offsets are centred on the *Herschel* position.

associated with lensing. Even if these galaxies lie on the IRRC there may still be low-luminosity AGN, and therefore this could be a source of jet emission instead of a lensing effect. When studying these cases we identified as lensing those where the morphology of the radio emission presented some kind of bending associated with lensed systems. Despite the difficulty of an unequivocal identification, our method provides a good first approximation to follow-up and provide basic statistics on the number of lensed galaxies in the sample.

4.5.2 Final Classification and Study of Herschel Fluxes

To determine if the offset between the NIR and the radio counterpart was reliable, the accuracy of the astrometry for these two bands was studied. Five random maps from each of the NIR surveys, i.e. VIKING and UKIDSS, were chosen with ~ 7 standards in each of them. Their coordinates were compared with the 2MASS catalogue positions using the coordinates obtained with SExtractor. The average offsets found between the 2MASS catalogue and the VIKING maps were $\delta\mathrm{RA} = 0.045$ arcsec and $\delta\mathrm{DEC} = 0.108$ arcsec with standard deviation of 0.15 arcsec and 0.13 arcsec respectively. The pixel size for the VIKING maps is 0.34 arcsec, so the error in the astrometry is less than one pixel for these maps. For the UKIDSS maps the average offsets found were $\delta\mathrm{RA} = 0.08$ arcsec and $\delta\mathrm{DEC} = 0.024$ arcsec with standard deviation of 0.22 arcsec and 0.17 arcsec. The pixel size of UKIDSS is 0.4 arcsec, so the error in the coordinates is less than one pixel as well. Thus the astrometry for the NIR maps was good for both surveys. To study the astrometry in the VLA, the seven calibrators used during the observations were imaged and their coordinates compared with their coordinates in the catalogues. No error was found in these positions so there was not any problem during the pointing in the VLA observations. The resolution for the VLA maps is ~ 1 arcsec, therefore the offsets between NIR and radio counterparts were accurate within this distance.

Previously in Figure 4.5 we saw that the image centre at 7 GHz had better resolution due to shorter wavelength. Although, these maps were 2 GHz bandwidth and therefore their r.m.s. were higher than the correspondent 6 GHz maps with 4 GHz bandwidth. We used the 7 GHz and 6 GHz maps to study the origin of the radio emission in more detail. Three targets showed two potential radio emissions at the 7 GHz map which might be due to the effect of the lens (Figure 4.15). To know if this deblending in the radio emission was due to the effect of better resolution at higher frequencies, we did a convolution with the task `IMSMOOTH` in CASA. The 7 GHz map was convolved to the resolution of the 5 GHz map defining the 'smoothing length' as $\sqrt{axis^2_{5GHz} - axis^2_{7GHz}}$ for the major and minor axis. For two sources in our sample the individual peaks at 7 GHz lie within the 5 GHz beam after convolving the image (and can thus appear as one source). Therefore, the single detection was simply due to the resolution limit, and evidence of lensing can be found by using the better resolved 7 GHz maps (Figure 4.16).

However there is also one source with a single detection at 5 GHz and two individual detections at 7 GHz, where contrary to the previous sources, this is not a resolution effect, as there are still 2 individual peaks after convolving the image so we cannot be certain that the separation is due to the effect of lensing. When these maps are overplotted over their NIR counterparts we see that they are consistent with lensed galaxies. The final 8 detected SLGs are shown in Figure 4.17. For the other 51 galaxies it was not possible to deblend the radio emission at higher resolution so these sources could be lensed galaxies (LGs) or simple SFGs. To study their morphology the 6 and 7 GHz maps were analysed. The morphology for these galaxies can be found in Figure 4.18 for the LGs, and in Figure 4.19 for the SFGs.

For the whole sample of 123 galaxies, 9% were undetected radio sources, contaminants (i.e. nearby galaxies, AGNs and groups or cluster galaxies) represent 44% of the sample, 21% are lensed galaxies (6% SLGs and 15% candidates of LGs) and 26% are unlensed SFGs (Figure 4.20). It is important to note that some of the sources classified as groups and cluster galaxies can be lensed galaxies, affecting our statistics. Based on a morphological study from a biased perspective (where as many sources as possible are identified as lensed) up to 25% could be lensed galaxies.

For the 58 isolated galaxies which formed part of our final sample, we had 8 SLGs (13.8%), 18 candidates to be LGs (31.0%) and 32 SFGs (55.2%). This was a total of 44.8% lensed galaxies (SLGs + LGs) of the 58 sources. Considering the *Herschel* flux limits for the 500μm-band we studied the fraction of lensed sources as S_{500} decreases. We obtained that for our primary sub-sample of 23 sources with $S_{500} > 60$ mJy there were 20% SLGs, 36% candidates to LGs and 44% SFGs. This is 56% lensed galaxies (SLGs + LGs). For the secondary sub-sample with $29 < S_{500} < 60$ mJy 35 sources were in the sample with a presence of 9% SLGs, 31% candidates to LGs and 60% SFGs. This is 40% lensed galaxies (SLGs + LGs). In addition, for those galaxies with $S_{500} > 100$ mJy we found a presence of 67% SLGs and 33% SFGs.

Therefore, to obtain the maximum number of lensed galaxies it is better to select brighter sources at 500μm. Thus the strategy followed during the VLA observations was not the best to select the largest sample of lensed galaxies. Aiming to obtain a large sample in a limited amount of observational time with the VLA, fainter sources which could share calibrators were selected instead. However, this strategy resulted in a sample with a smaller presence of lensed galaxies. Sub-arcsecond resolution would have been better as well, so the use of ALMA or SMA would have been a better option. A proposal was submitted to observe the dust emission at ~ 1.2 mm with NOEMA for some of the sources for which it was not possible to confirm whether they were lensed or not. Despite this proposal was accepted, the observations were not carried out due to the upgrade of the new NOEMA correlator Polyfix.

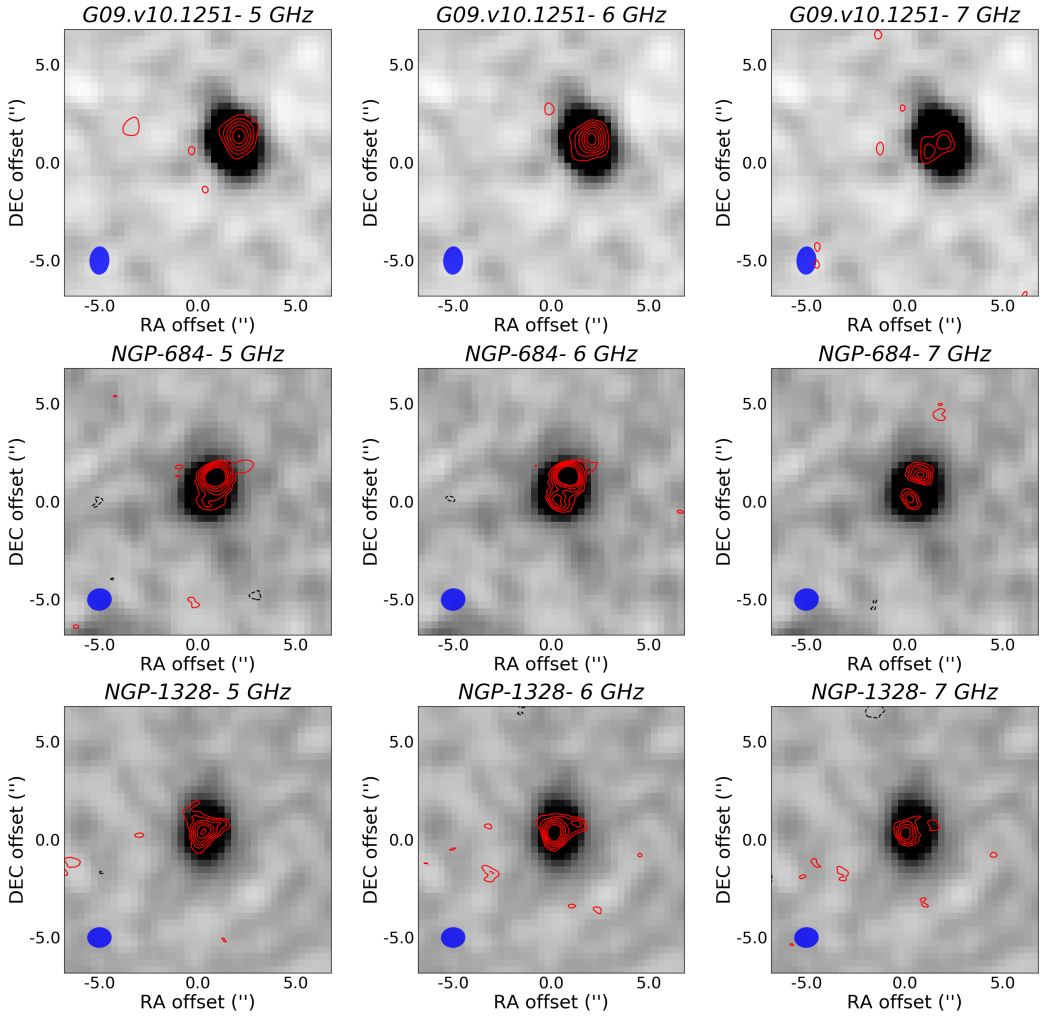

Figure 4.15 : From left to right maps at 5, 6 and 7 GHz. The beam is plotted in the bottom-left corner of each map. *Top:* In the maps at 5 and 6 GHz there is no hint of the effect of the lens while in the 7 GHz map two weak contributions are detected. *Middle:* A very weak detection at the bottom of the central source is visible at 5 and 6 GHz. When studying the 7 GHz map this second weak contribution appears more clear. *Bottom:* A very weak contribution is detected at 6 GHz map at the top-right of the main source. This weak detection splits at 7 GHz as a very weak detection. This blending could be effect of the better resolution at lower wavelengths or could be due to noise.

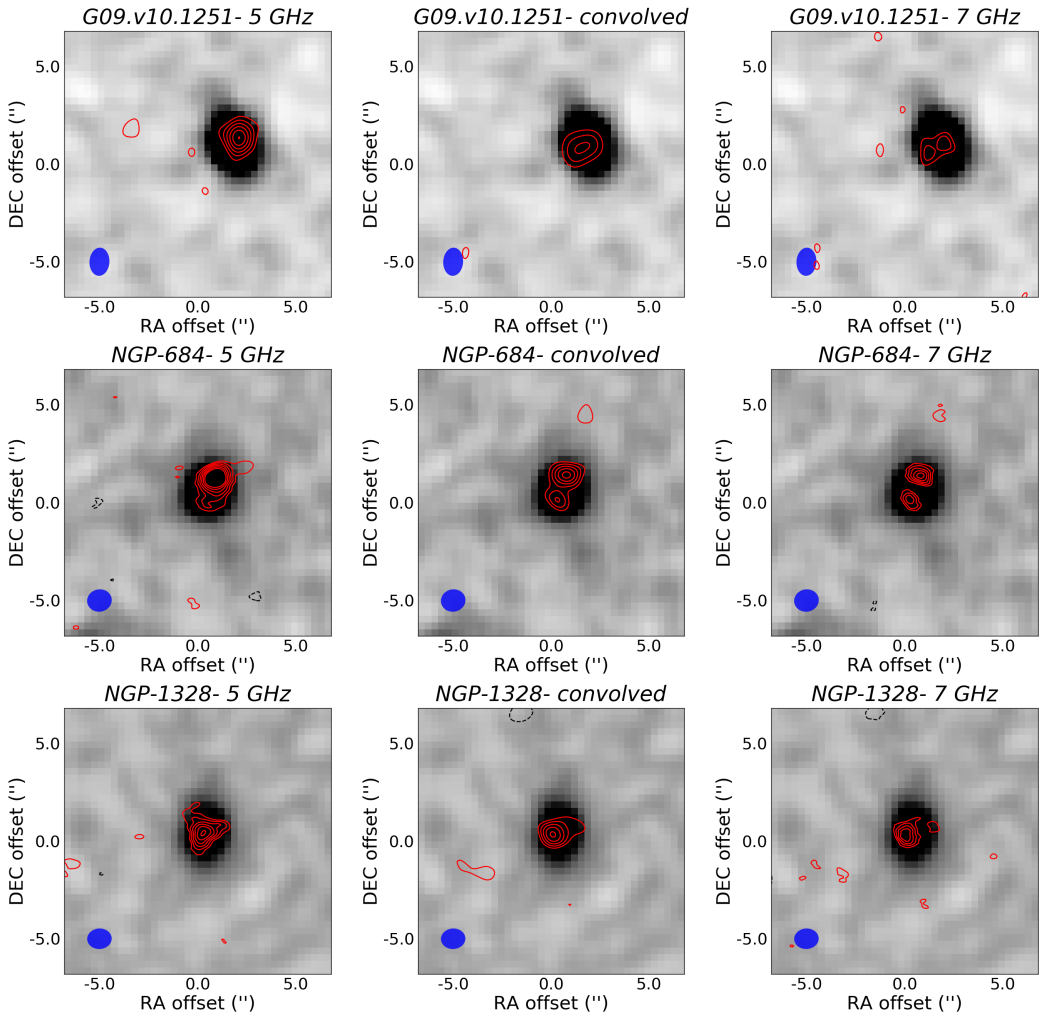

Figure 4.16 *Left:* Images at 5 GHz central frequency. We want to do the convolution to this beam. *Middle:* Convolution of the images at 7 GHz with the 5 GHz resolution. *Right:* Maps at 7 GHz with their correspondent resolution. In these three images we can see that for the top and bottom maps the two peaks at 7 GHz are within the beam in the convolved image, therefore the two peaks could be an effect of the better resolution. However, in the middle maps the two peaks in the 7 GHz map are still distinguishable in the convolved image so the single peak at 5 GHz could not be an effect of the resolution. The second peak could be noise or could be real.

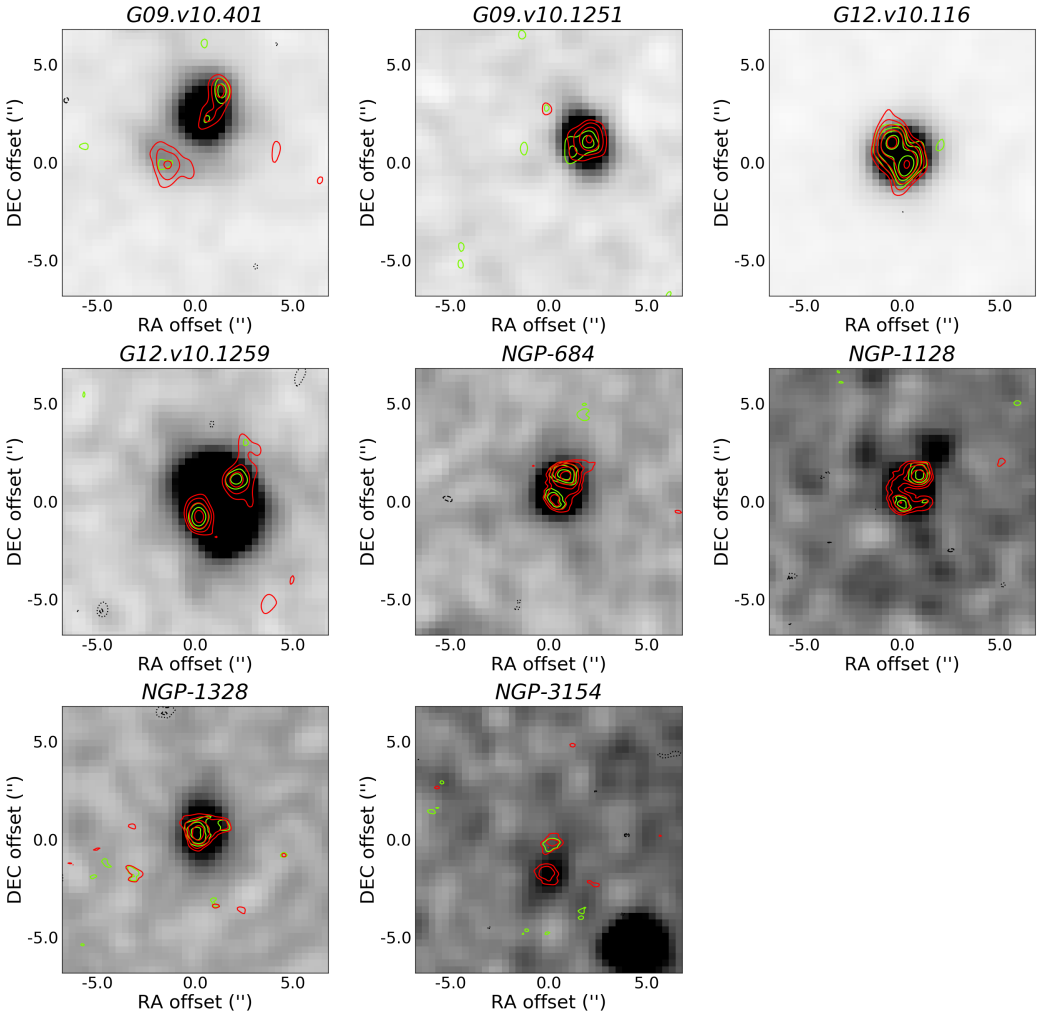

Figure 4.17 : The eight SLGs detected in the sample. The background images in grey scale correspond to the K_s-band where the NIR lenses are detected. In red contours the 6 GHz and in green the 7 GHz emission from the VLA are shown. The contours start at 3σ and increase in steps of $\sqrt{2}$ (-3σ is shown in dashed-black for 6 GHz and dotted-black for 7 GHz).

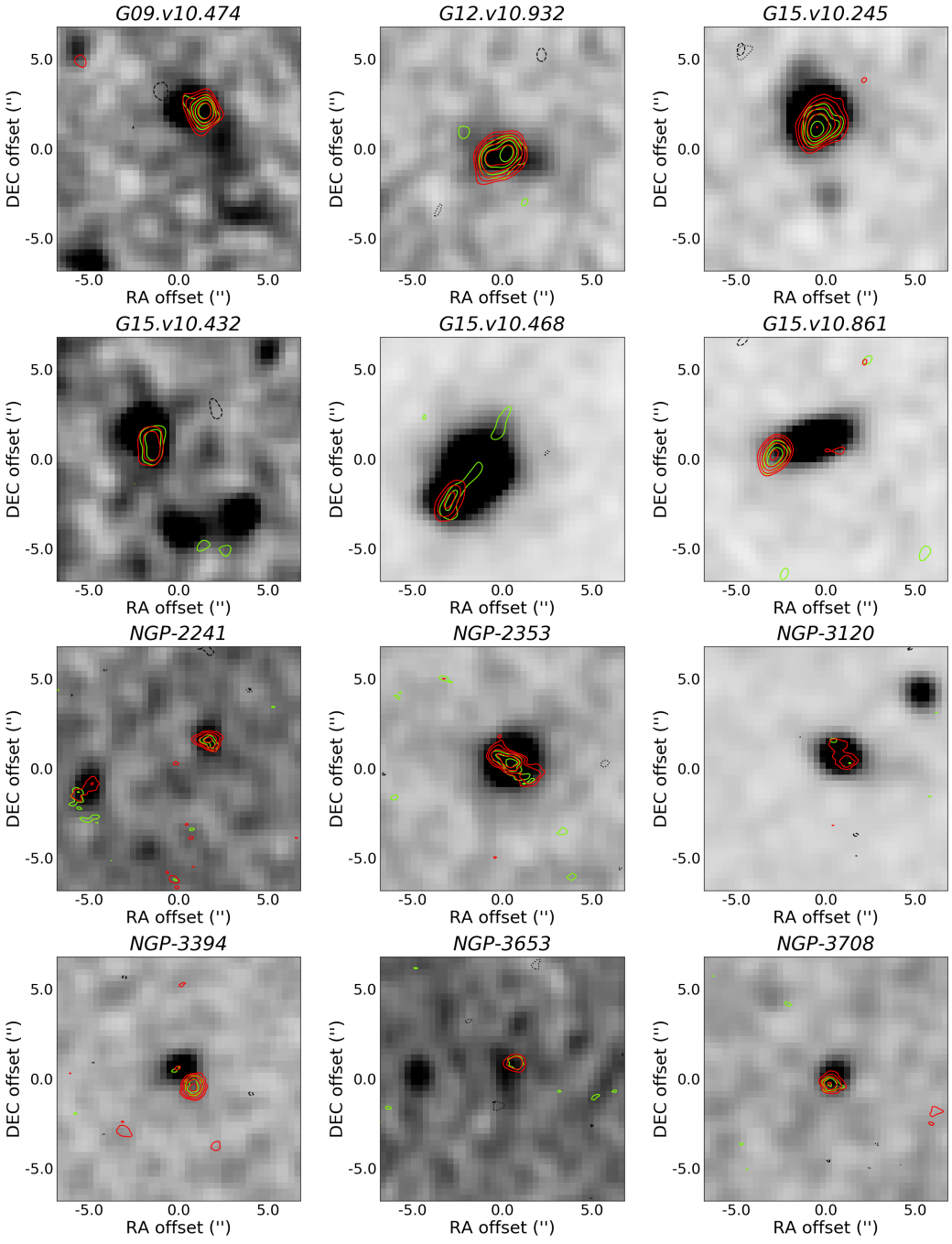

Figure 4.18 : Potential LGs in the sample. These sources are classified as LGs due to their offset between the NIR and the radio emission and/or due to their morphology. The background images in grey scale correspond to the K_s-band where the NIR lenses are detected. In red contours the 6 GHz and in green the 7 GHz emission from the VLA are shown. The contours start at 3σ and increase in steps of $\sqrt{2}$ (-3σ is shown in dashed-black for 6 GHz and dotted-black for 7 GHz).

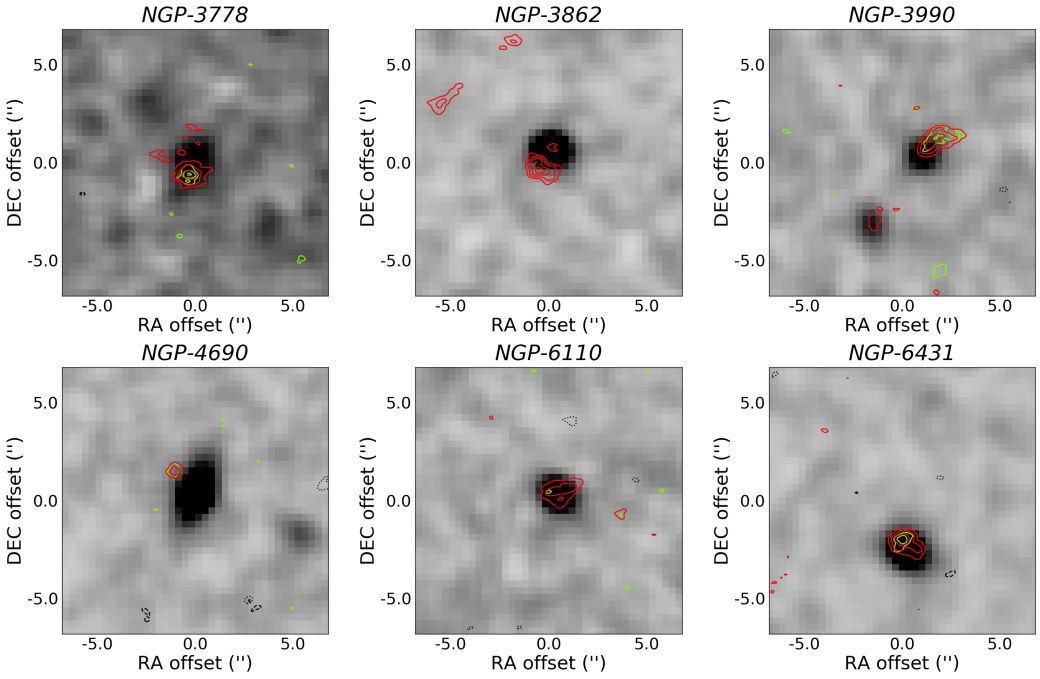

Figure 4.18 : *Continued*

From the sample of 112 radio detected sources eight galaxies had $S_{500} > 100$ mJy. Two of them were nearby galaxies and one of them and AGN, all of them considered as contaminants and deleted from the sample. For the other five galaxies we found 40% SLGs, 40% over-densities (with two and 3 radio sources) and 20% SFGs with no hint of lensing. This represents an overestimation of the SLGs compared with previous studies at $S_{500} > 100$ mJy. Negrello et al. (2010) found almost 100% fraction of SLGs in a sample of 5 sources from the SDP of H-ATLAS, and Bussmann et al. (2013) found 70%-80% fraction of lensing systems in a sample of 30 sources in H-ATLAS and HerMes[16]

To summarise, the fraction of lensed galaxies in our sample was 67% for $S_{500} > 100$ mJy, 54% for $60 < S_{500} < 100$ mJy and 40% for $29 < S_{500} < 60$ mJy. We see that the probability of detecting LGs decreases with decreasing flux at 500μm-band as we would expect.

4.6 The Infrared-to-Radio Correlation

The IRRC was studied in more detail for all the SFGs in the sample, both lensed and unlensed galaxies. Luminosities for both bands (i.e. FIR and radio) were derived and their SFRs calculated. We compared our results with Delhaize et al. (2017, hereafter D17) who present a

[16]Herschel Multi-tiered Extragalactic Survey (HerMES), Oliver et al. (2012).

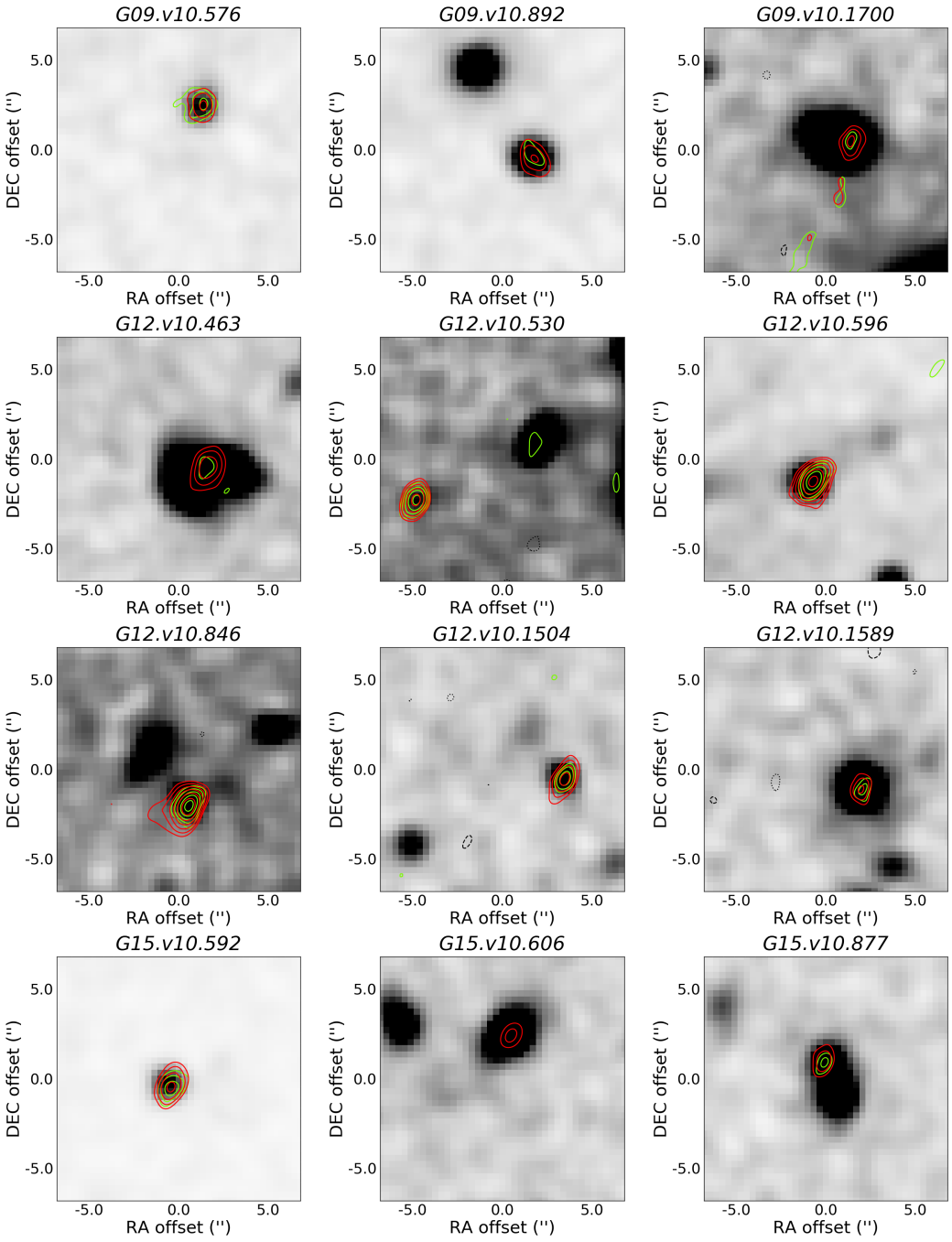

Figure 4.19 : SFGs in the sample without signs of lensing. Again, the background images in grey scale correspond to the K_s-band, in red contours the 6 GHz and in green the 7 GHz emission from the VLA are shown. The contours start at 3σ and increase in steps of $\sqrt{2}$ (-3σ is shown in dashed-black for 6 GHz and dotted-black for 7 GHz).

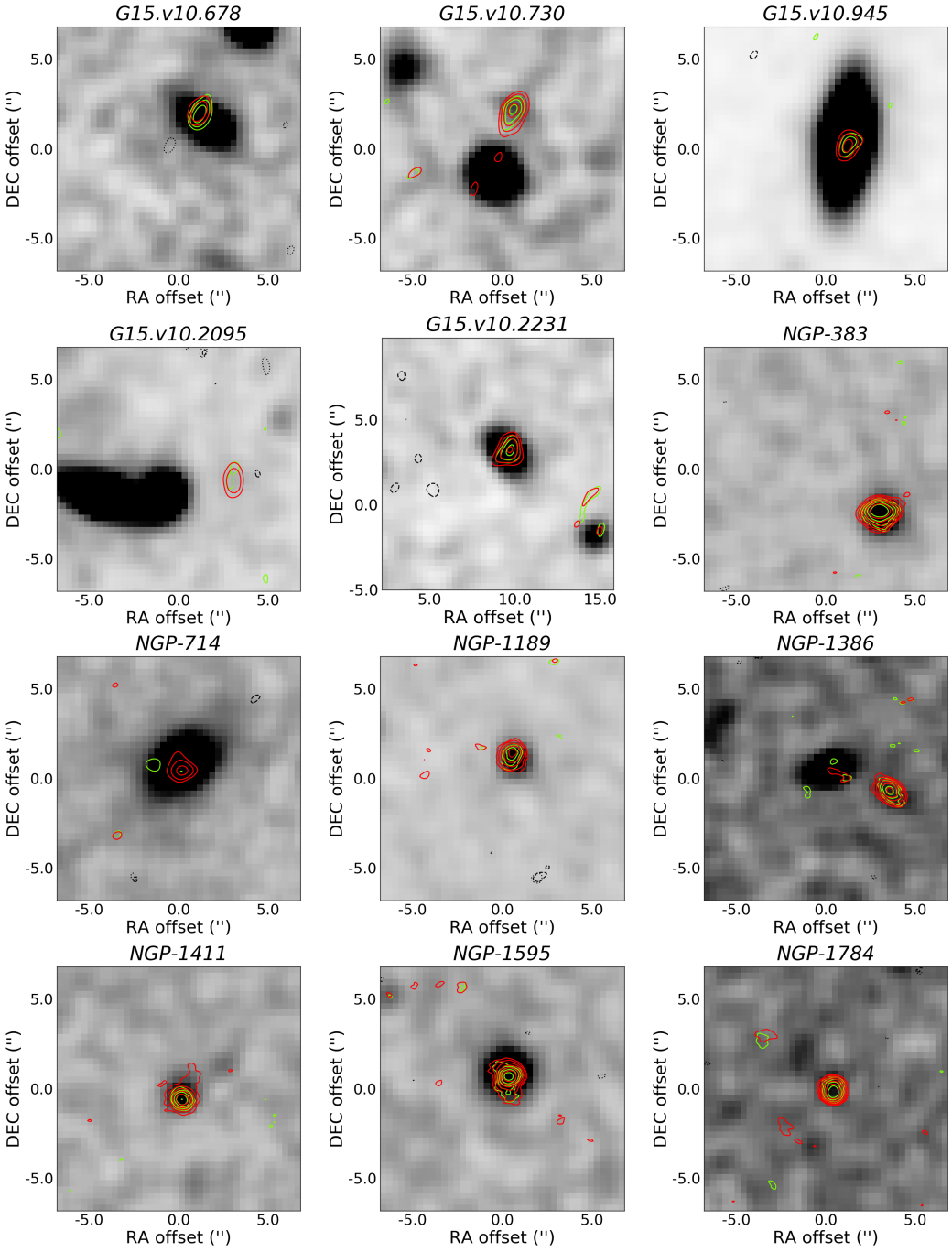

Figure 4.19 : *Continued*

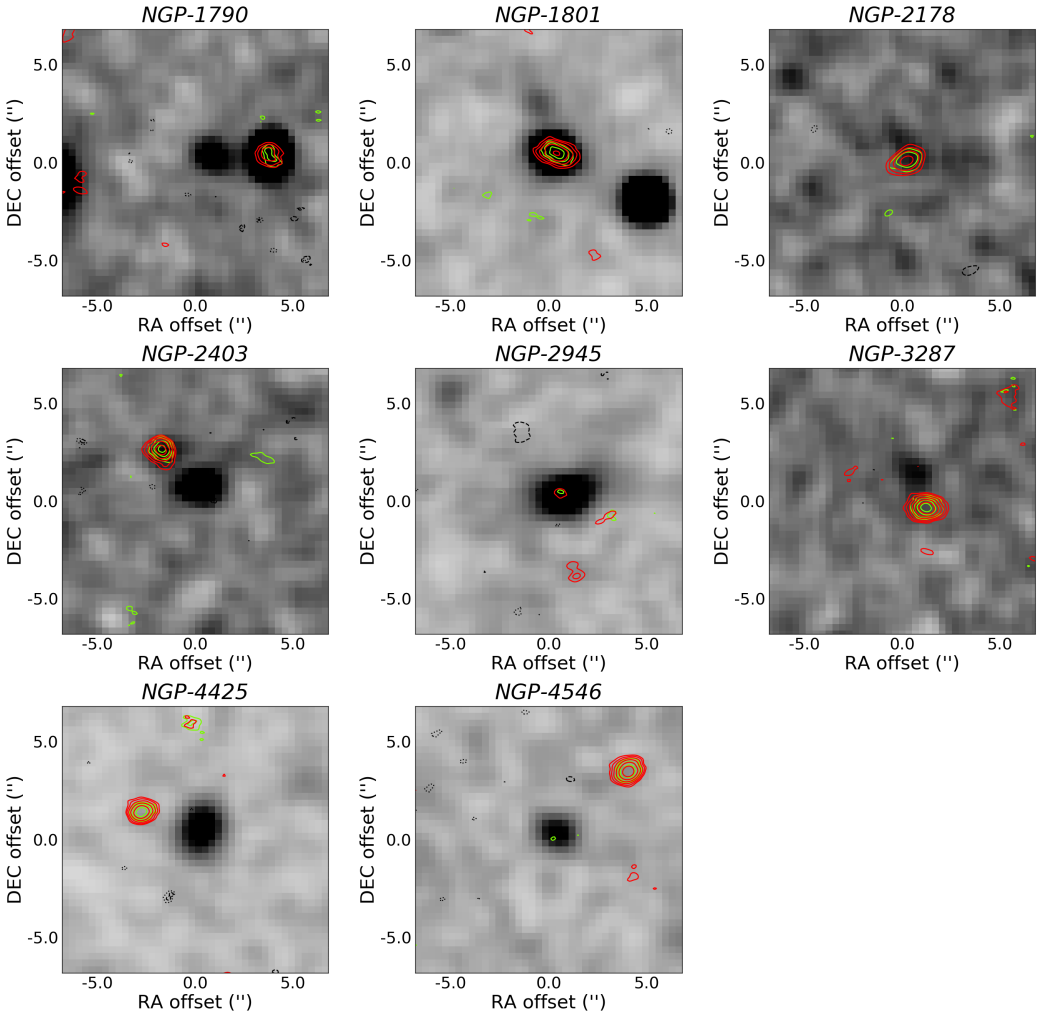

Figure 4.19 : *Continued*

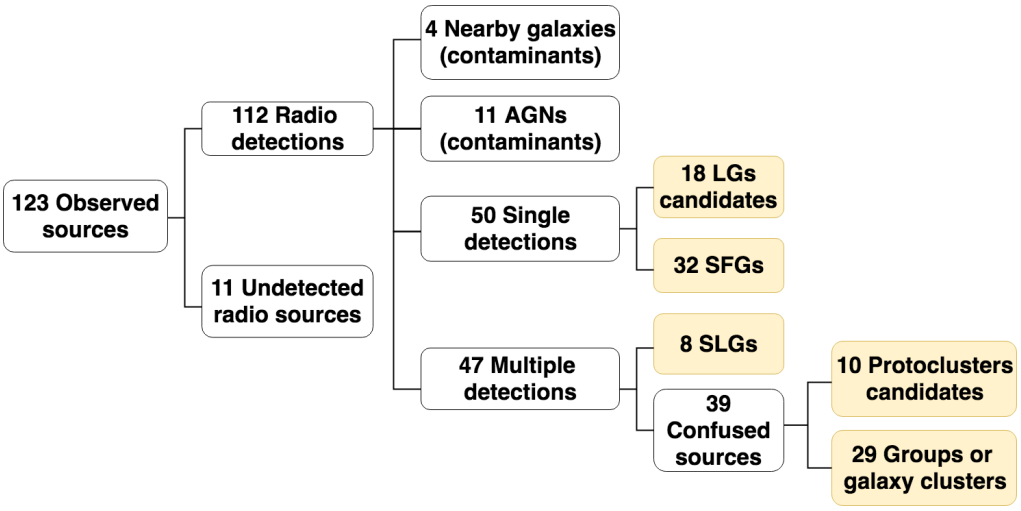

Figure 4.20 : Final classification for our 123 TLS sample at $1.5 < z_{phot} < 2.5$.

similar study for the COSMOS field with a sample of 12,333 sources. This sample consist of a combination of radio- and FIR-selected samples so the selection-bias is minimal. To derive the luminosities at FIR and 1.4 GHz different methods were used for each band. In this section we explain how the luminosities were obtained and the derived SFRs are discussed.

4.6.1 Infrared Luminosities

As explained in Section 1.2.2 the dust emission is a thermal process with dust grains emitting a MBB spectrum. Hence, the total infrared luminosity (L_{TIR}) can be derived from the integrated total IR flux at rest-frame, S_{TIR}. The total infrared flux, was calculated by fitting all the *Herschel* bands (i.e. PACS and SPIRE) with two-component MBB templates and integrating the flux from $\lambda(8-1000\ \mu m)$. The preliminary H-ATLAS catalogue used in this work had available photometry for PACS and SPIRE bands for the GAMA fields. However, for the NGP field only the SPIRE bands were available in the catalogue. For consistency, we performed our own photometry in the PACS bands of NGP (Table 4.2). In addition, this allows to better constrains the warm dust component. The PACS maps were downloaded from the archive[17] and cut-outs of 180 and 150 arcsec size where created for the 100 and 160μm maps respectively. The photometry was done by fitting a Gaussian distribution model into the flux-map with FWHM 7 and 12 arcsec, corresponding to the 100- and 160μm-bands. The source flux was then given by integrating the flux under this Gaussian. The uncertainties were calculated by selecting 100 random locations in the map, avoiding areas close to the target, and measuring the flux using

[17] http://www.h-atlas.org/data/data_release_2.html

the same Gaussian distribution as the source for each random location. The final error was given by the standard deviation of the fluxes measured in the 100 randomly placed apertures.

Since finishing the analysis performed in this work, the H-ATLAS NGP photometry catalogue has become available (Maddox et al., 2018). As a sanity test, we compared our photometry to this newly available photometry. This comparison for the 100μm-band is shown in Figure 4.21 were the blue dots represent the NGP sample of TLS, the green dots a random sample of brighter sources from the H-ATLAS NGP catalogue and the red line the one-to-one relation. We see that the TLS photometry presents a lot of scatter due to the big uncertainties for these faint sources. In addition, the photometry calculated with our code seems to be overestimated compared with those values from the catalogue. However, the two estimates are consistent within the scatter. To better test our method, we selected a random sample of brighter sources from the new NGP catalogue. When we perform our photometry method on these sources and compare them to the catalogue photometry (green dots in Figure 4.21), we find that now there is a clear correlation between the catalogue and our derived flux (especially when including both the faint and bright sources). However, our photometry for the bright sources is somewhat lower than those from the catalogue for these brighter sources. The differences are likely due to the diffences in the method in terms of background subtraction and flux extraction. In particular, our code does not apply any deblending of the flux from other sources, whereas the H-ATLAS photometry does. If this difference in deblending was systematically biasing our sources, we would expect our photometry to be systematically higher than the H-ATLAS photometry. Figure 4.21 shows this is not the case and our results for the TLS sample were thus not dominated by confusion issues. In summary, there is a reasonably good consistency between our photometry method and the H-ATLAS photometry, though the scatter is large for our TLS sources.

To determine the S_{TIR} we performed a MBB fitting at the rest-frame. The frequencies were shifted to the rest-frame by applying a (1+z) factor (the z_{phot} were taken from Table 4.1)[18]. There were five bands to be fitted in the model so two-components for the MBB were used corresponding to the warmer and colder dust (see Section 1.2.2 for more details). Therefore there were four free parameters, the temperatures (T_w, T_c) and the dust mass (M_{d_w}, M_{d_c}) for each of the components. Due to the computational difficulty of having 4 free parameters, a χ^2 minimisation on a grid of temperatures was performed. This was done by varying $T_c = 10 - 30$ K in steps of 1 K and $T_w = 30 - 80$ K in steps of 5 K. Therefore two parameters were fitted (i.e. the dust masses) with a computational χ^2 minimisation. The M_{dust} of each component was selected to be $> 10\ M_\odot$, i.e. not negative. Values of $\kappa_{850} = 0.077\ m^2 kg^{-1}$ and

[18] Given that we have intrinsically shifted the spectrum to the rest-frame, it is not necessary to apply an additional K-correction.

Table 4.2 : PACS photometry for the GAMA and NGP fields. The photometry for GAMA was taken from the catalogues while the photometry for the NGP field we performed ourselves.

ID	S_{100} (mJy)	S_{160} (mJy)	ID	S_{100} (mJy)	S_{160} (mJy)
G09.v10.157	124 ± 29	197 ± 34	NGP-383	215 ± 51	183 ± 43
G09.v10.259	169 ± 41	192 ± 48	NGP-413	134 ± 34	124 ± 31
G09.v10.401	97 ± 41	44 ± 48	NGP-684	96 ± 42	78 ± 29
G09.v10.474	13 ± 41	93 ± 48	NGP-714	143 ± 36	122 ± 31
G09.v10.493	97 ± 41	81 ± 48	NGP-1113	68 ± 24	51 ± 23
G09.v10.507[b]	-12 ± 41	122 ± 48	NGP-1128	74 ± 29	69 ± 26
G09.v10.576	103 ± 41	118 ± 48	NGP-1189	116 ± 39	99 ± 32
G09.v10.812[a]	–	–	NGP-1328	101 ± 26	88 ± 20
G09.v10.825	90 ± 41	66 ± 48	NGP-1386	76 ± 28	69 ± 21
G09.v10.892	121 ± 41	88 ± 48	NGP-1401	183 ± 49	140 ± 39
G09.v10.1186	9 ± 29	88 ± 34	NGP-1411	141 ± 46	126 ± 30
G09.v10.1251	12 ± 41	16 ± 48	NGP-1451	142 ± 38	120 ± 31
G09.v10.1475	8 ± 41	135 ± 48	NGP-1595	9 ± 34	14 ± 25
G09.v10.1558[b]	-13 ± 41	58 ± 48	NGP-1632	110 ± 36	89 ± 28
G09.v10.1569[b]	-6 ± 41	38 ± 48	NGP-1784	104 ± 30	90 ± 25
G09.v10.1573	120 ± 41	74 ± 48	NGP-1787	79 ± 39	67 ± 27
G09.v10.1700	70 ± 29	48 ± 34	NGP-1790	104 ± 42	86 ± 33
G09.v10.1729	77 ± 41	106 ± 48	NGP-1801	85 ± 35	82 ± 30
G12.v10.116	64 ± 41	84 ± 48	NGP-1874	36 ± 33	36 ± 25
G12.v10.305[b]	-1 ± 41	120 ± 48	NGP-2178	88 ± 28	81 ± 26
G12.v10.457	199 ± 552	574 ± 469	NGP-2241	80 ± 35	67 ± 29
G12.v10.463	75 ± 45	52 ± 50	NGP-2353	72 ± 31	63 ± 30
G12.v10.528	520 ± 372	513 ± 316	NGP-2403	54 ± 32	42 ± 27
G12.v10.530	148 ± 41	49 ± 48	NGP-2478	62 ± 25	52 ± 22
G12.v10.596	9 ± 41	111 ± 48	NGP-2535	36 ± 34	32 ± 26
G12.v10.761	1 ± 29	69 ± 34	NGP-2555	40 ± 33	36 ± 25
G12.v10.829	77 ± 62	85 ± 54	NGP-2736	93 ± 36	77 ± 29
G12.v10.846[b]	-9 ± 41	68 ± 48	NGP-2945	63 ± 36	52 ± 26
G12.v10.860	64 ± 41	62 ± 48	NGP-2985	36 ± 33	31 ± 27
G12.v10.864	61 ± 41	167 ± 48	NGP-2995	133 ± 42	109 ± 29
G12.v10.881	135 ± 45	114 ± 50	NGP-3078	44 ± 29	40 ± 23
G12.v10.893[b]	-1 ± 45	-4 ± 50	NGP-3120	82 ± 32	63 ± 26
G12.v10.932	79 ± 41	94 ± 48	NGP-3154	62 ± 36	53 ± 26
G12.v10.1246	113 ± 60	210 ± 63	NGP-3196[b]	-2 ± 34	-2 ± 29
G12.v10.1259	19 ± 41	57 ± 48	NGP-3222	86 ± 28	79 ± 24
G12.v10.1504[b]	-18 ± 41	140 ± 48	NGP-3248	99 ± 29	84 ± 22
G12.v10.1529[b]	-49 ± 41	210 ± 48	NGP-3287	67 ± 33	57 ± 28
G12.v10.1589	64 ± 41	82 ± 48	NGP-3394	57 ± 34	51 ± 30
G12.v10.1805[b]	-62 ± 41	42 ± 48	NGP-3653	26 ± 30	15 ± 23
G15.v10.245	149 ± 41	114 ± 48	NGP-3669	94 ± 35	77 ± 25
G15.v10.432	58 ± 41	105 ± 48	NGP-3708	47 ± 29	40 ± 22
G15.v10.468	51 ± 29	117 ± 34	NGP-3746	78 ± 37	60 ± 30
G15.v10.581	15 ± 41	49 ± 48	NGP-3778	75 ± 42	63 ± 30
G15.v10.592	95 ± 41	122 ± 48	NGP-3862[b]	-4 ± 29	-5 ± 26
G15.v10.606	77 ± 41	67 ± 48	NGP-3990	54 ± 36	51 ± 30
G15.v10.678	59 ± 41	156 ± 48	NGP-4201	1 ± 33	3 ± 27
G15.v10.730	69 ± 41	129 ± 48	NGP-4209	89 ± 35	74 ± 28
G15.v10.861	1 ± 41	80 ± 48	NGP-4425	35 ± 31	29 ± 25
G15.v10.877[b]	-4 ± 41	74 ± 48	NGP-4546	65 ± 30	56 ± 26
G15.v10.899	133 ± 41	93 ± 48	NGP-4690	60 ± 35	55 ± 28
G15.v10.934	32 ± 41	140 ± 48	NGP-4772	43 ± 34	37 ± 26
G15.v10.945	101 ± 41	143 ± 48	NGP-4810	23 ± 36	18 ± 26
G15.v10.1044[a]	–	–	NGP-4844	50 ± 31	41 ± 23
G15.v10.1103	180 ± 41	102 ± 48	NGP-4870	41 ± 29	36 ± 24
G15.v10.1138	2 ± 45	124 ± 50	NGP-5121	78 ± 36	64 ± 27
G15.v10.1162	47 ± 41	117 ± 48	NGP-5310	62 ± 30	50 ± 25
G15.v10.2095	76 ± 41	69 ± 48	NGP-5913	88 ± 39	73 ± 33
G15.v10.2150	31 ± 29	74 ± 34	NGP-6110	14 ± 34	10 ± 28
G15.v10.2160	23 ± 41	62 ± 48	NGP-6431	43 ± 34	37 ± 33
G15.v10.2231	34 ± 45	-16 ± 50			
G15.v10.2516[a]	–	–			
G15.v10.4116[a]	–	–			

[a] These sources are not inside the PACS maps.

[b] Note that these values are consistent with the flux of 0 within the error.

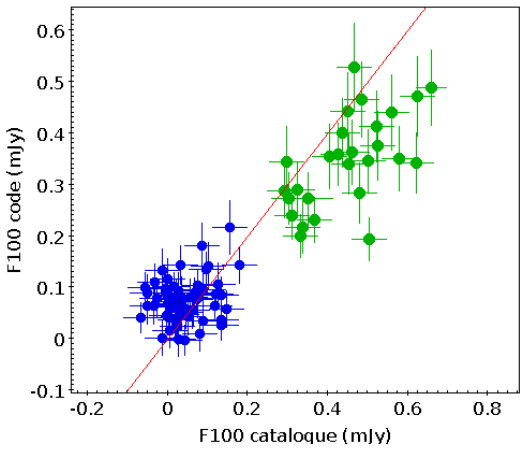

Figure 4.21 : Comparison of the photometry calculated with our code and the photometry recently released by the H-ATLAS group for the NGP field (Maddox et al., 2018). The blue dots represent the NGP sources of the TLS sample and the green dots represent a random sample of brighter sources in the H-ATLAS NGP catalogue for which we performed our own photometry to compare with. The red line represents the one-to-one relation. We found that our results do not present confusion issues and thus we can consider our photometry and the photometry from the catalogue reasonably consistent.

$\beta = 2$ (see Section 1.2.2) were chosen for both components which resulted in a mean value for the dust masses of $\log(M_{d_w}/M_\odot) = 7.68$ and $\log(M_{d_c}/M_\odot) = 9.49$ with mean temperatures of $T_w = 62$ K and $T_c = 26$ K. Finally, the total flux was calculated integrating the model SED from $\lambda(8-1000\ \mu m)$. An example of this fitting is shown in Figure 4.22. To determine the uncertainties on the S_{TIR}, a bootstrapping analysis was performed. For each flux 25 new random fluxes were generated assuming a normal distribution with the measured flux as the mean value and the measured error as the standard deviation of the distribution. In some cases there were no detections in the PACS bands but in this case the MBB fitting naturally results in bigger uncertainties and the fitting still results in the best possible statistical fit (Figure 4.22 right). This method was repeated for 15 sources with 100 iterations (instead of the usual 25). The error difference between the two number of iterations was in average $\sim 6\%$. Because this process was computationally very expensive and the difference in the error was not dominating our results, only 25 iterations were done for the whole sample.

To convert S_{TIR} into luminosity we used the expression:

$$L_{TIR} = \frac{4\pi D_L^2}{(1+z)} S_{TIR} \tag{4.3}$$

where D_L is the luminosity distance in metres and S_{TIR} is the flux in Jy. D_L was calculated from the comoving distance $D_L = (1+z)D_M$ where the comoving distance is defined for a flat

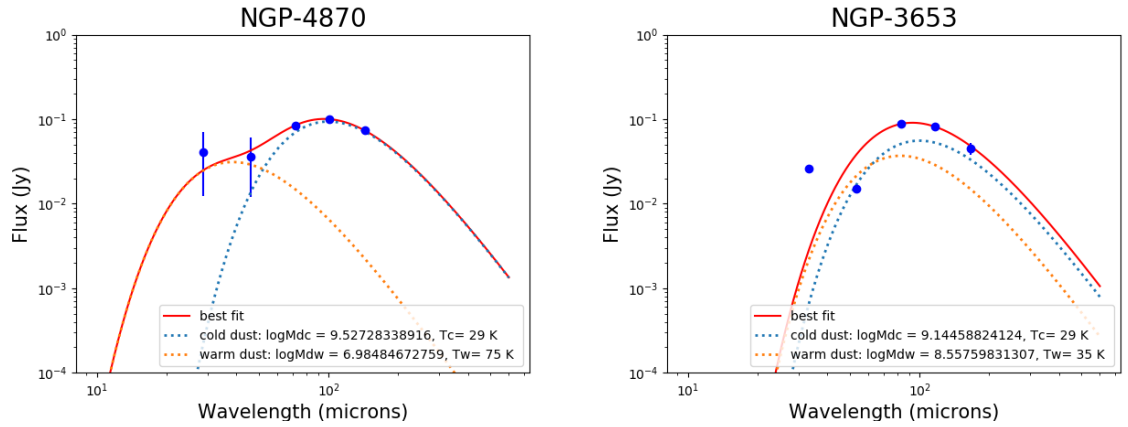

Figure 4.22 : Examples of the two MBB fitting to determine the total infrared flux integrating between $\lambda(8-1000\ \mu\mathrm{m})$. *Left:* Two components for the 5 *Herschel* bands give the best fit. *Right:* Due to the big uncertainties for the PACS bands one single component is the best fit for the 5 bands in this case, yet a second component is still formally included and adds an additional term of uncertainty to the final error.

Universe as:

$$D_M(z) = \frac{c}{H_o}\int_0^z \frac{dz}{\sqrt{\Omega_m(1+z)^3+\Omega_\Lambda}} \tag{4.4}$$

where c is the speed of light and the cosmological constants as defined in Chapter 1. Uncertainties for the redshift and therefore D_L were not considered, so the uncertainties for the luminosities were calculated with the relative errors on the integrated fluxes.

4.6.2 Radio Luminosities

The rest-frame luminosities at 1.4 GHz ($L_{1.4GHz}$) were calculated from the integrated radio fluxes densities at 6 GHz (S_{6GHz}) with the following relation:

$$L_{1.4\ GHz} = \frac{4\pi D_L^2(z)}{(1+z)^{(-\alpha+1)}}\left(\frac{1.4}{6}\right)^{-\alpha} S_{6GHz} \tag{4.5}$$

where D_L is the luminosity distance in metres at the redshift of the source and α is the spectral index ($S_\nu \propto \nu^{-\alpha}$). The spectral index is the power law slope of the synchrotron radiation which for normal SFGs an average value of $\alpha = 0.7$ is characteristic (Condon, 1992). We calculated the spectral index for each of our targets with the two spectral windows at 5 and 7 GHz. However, these two spectral windows were very close to each other and one of the maps had bigger r.m.s., therefore the measured spectral index had big uncertainties and the

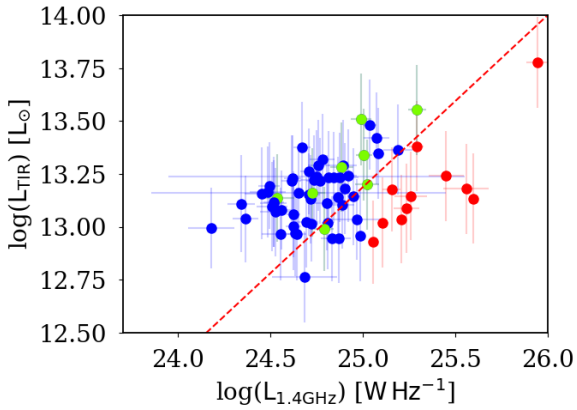

Figure 4.23 : IRRC for our sample with the correlation from D17 in dashed-red line ($\log(L_{TIR}) = 0.812 \times \log(L_{1.4GHz}) - 7.125$). The blue dots represent the SFGs, green dots the SLGs and red dots the AGNs of our sample. We see that our sample is systematically above D17 due to the FIR selection-bias. In addition, we see that the AGNs have a clear excess of radio emission laying below the correlation. Although, some of the classified AGNs have similar ratios than other SFGs. It is important to note that the contamination coming from AGNs is always difficult to eliminate unless we determine without confusion the origin of the radio emission.

average value of $\alpha = 0.7$ was used instead (more in Section 4.7). The uncertainties for the $L_{1.4GHz}$ were derived from the relative errors.

4.6.3 IRRC

D17 present a study of the IRRC in the COSMOS field for SFGs up to $z \leq 6$. Their sample is similar to ours with data at 3 GHz from the VLA and FIR data from *Herschel*. In Figure 4.23 we show our sample and the D17 correlation as a dashed-red line. An excess for L_{TIR} was observed for the SFGs (green and blue dots, where the green dots represent the SLGs and the blue dots the rest of the sample), although as our sample was FIR-selected this selection-bias was expected (Sargent et al., 2010). In this figure the AGNs are plotted in red dots to show the excess in radio emission for these sources. This plot shows that some of the sources classified as AGNs under our criteria (see Section 4.5.1) are closer to the correlation than some of the ones classified as SFGs. Therefore, contamination coming from AGN radio emission plays an important role in this correlation.

The evolution of q_{TIR} (defined as in equation 1.8) with redshift is shown in Figure 4.24. D17 find a value of $q_{TIR}(z) = (2.88 \pm 0.03)(1+z)^{-0.19 \pm 0.01}$ (dashed-red in the figure) showing that q_{TIR} decreases with increasing redshifts. Our sample follows this trend but a clear decline of this ratio with redshift was not noticeable.

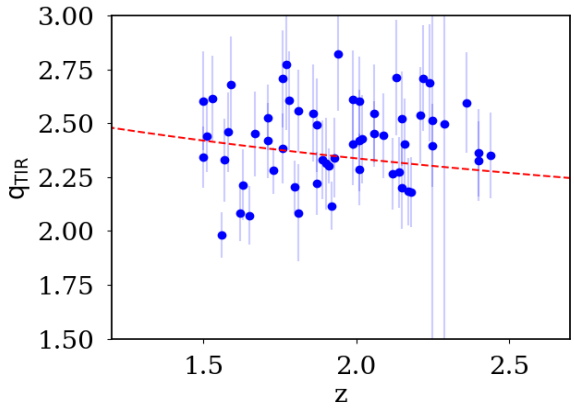

Figure 4.24 : The IR/radio ratios versus redshift is shown in this plot. The dashed-red line corresponds to D17, $q_{TIR}(z) = (2.88 \pm 0.03)(1+z)^{-0.19\pm0.01}$, showing an evolution of this parameter with redshift. We can see that our sample follows the trend of D17, but no significant evolution is found in this small range of redshifts.

Figure 4.25 (left) shows q_{TIR} versus $\log(L_{TIR})$. This figure is in agreement with Ivison et al. (2010) where they present a *Herschel*-selected sample ($S_{250} > 20$ mJy) with a mean value of $q_{TIR} = 2.40$. We obtained a q_{TIR} mean value of 2.42 ± 0.22 which indicated that our results were well sampled and that the excess of FIR in the IRRC was likely due to the selection-bias. Figure 4.25 (right) shows q_{TIR} versus $\log(L_{1.4\ GHz})$. A very strong anti-correlation is detected here that it is not necessarily representative of any physical relation. The anti-correlation is due to the selection-bias and the uncertainties in the luminosities (more details in Section 5.5.1). As the sample was FIR-selected, the range of L_{TIR} is limited as the *Herschel* fluxes are limited to > 29 mJy at 500μm. A more detail analysis of the IRRC and a comparison of the TLS with different samples is presented in Chapter 5.

4.6.4 Star Formation Rates

The SFRs were derived from the L_{TIR} following Kennicutt (1998) and from $L_{1.4GHz}$ with Murphy et al. (2011)[19]. In Table 4.3 we can see that the derived radio-SFRs ($SGR_{1.4GHz}$) are higher than the infrared-SFRs (SFR_{TIR}) for the AGNs as the radio emission is dominated by an AGN and therefore we are not measuring the real radio-SFRs of these galaxies. For the rest of the SFGs, $SFR_{1.4GHz}$ are in general lower than the correspondent SFR_{TIR}. This can be due to different reasons: i) the selection-bias of our sample results in bright FIR sources ii) the dust attenuation properties of extremely bright sources such as the ones we are studying are different than the average nearby galaxy population used in Kennicutt (1998) used to derived

[19] $SFR_{1.4GHz}\ [M_\odot yr^{-1}] = \frac{L_{1.4GHz}}{4\times10^{28}}\ [erg\,s^{-1}Hz^{-1}]$

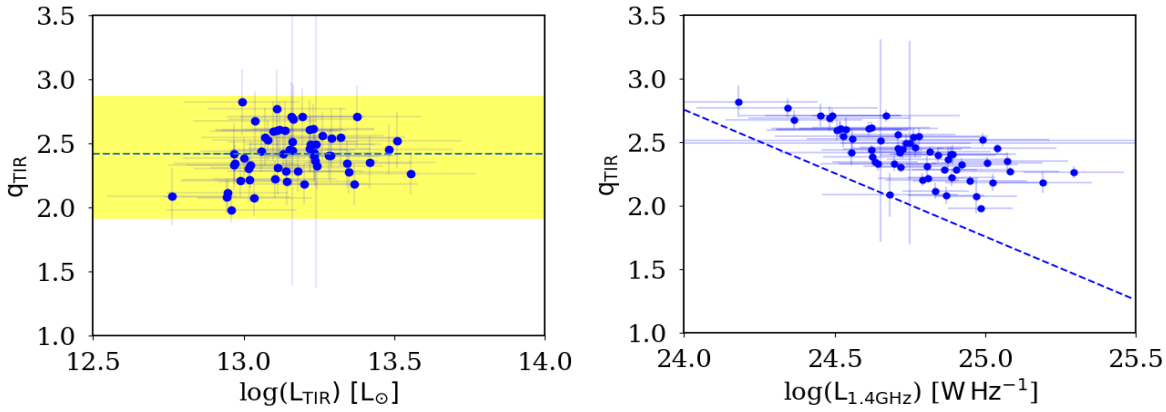

Figure 4.25 *Left:* In this plot we show q_{TIR} versus $\log(L_{TIR})$. We found a mean value of $q_{TIR} = 2.42 \pm 0.22$, plotted in dashed-blue, consistent with Ivison et al. (2010). The yellow-shadow region covers $\pm 2\sigma_q$ ($\sigma_q = 0.24$) as in Ivison et al. (2010). *Right:* The IR/radio ratio versus $\log(L_{1.4GHz})$ is shown. A strong anti-correlation is found which is likely due to the selection-bias of the sample. The dashed-blue line shows the q_{TIR} for a constant luminosity of $\log(L_{TIR}/L_\odot) = 12.75$, which corresponds to the faintest source in our sample.

SFR_{TIR}, or iii) the synchrotron radiation process might be different in these extremely bright galaxies due to different magnetic fields (see Section 5.5.1). However, the radio continuum does not suffer from dust extinction and it is possible to reach sub-arcsecond resolution from Earth, which make the radio continuum an interesting tracer of star-formation.

The measured fluxes for the SLGs are affected by the magnification factor. This magnification results in a higher value for the SFRs. Due to the differential lensing (Hezaveh et al., 2012) the magnification factor might be different at different wavelengths resulting in different derived SFRs for the FIR and the radio emission (see Section 5.5.1). Note that the SFRs in Table 4.3 are not corrected for magnification factor.

The AGNs in our sample would have $SFR_{1.4GHz} \geq 3,000 - 22,000\ M_\odot yr^{-1}$ if their radio emission were coming from star forming regions, rather than the active nucleus of the galaxy. The rest of the sample, lensed galaxies or not, have SFRs $\sim 600 - 5,000\ M_\odot yr^{-1}$ consistent with other results in the literature for DSFGs.

4.7 Caveats

1. In this study we used z_{phot} calculated by SED fitting as explain in Section 4.2. The distances derived from this parameter have not been calculated with the corresponding errors. This z_{phot} is accurate at 30% (Lapi et al., 2011) so a relative error of 50% or 0.18 dex should be considered in our final results. Spectroscopic redshifts become

Table 4.3 : Classification, luminosities and SFRs for the TLS sample at $1.5 < z_{phot} < 2.5$. The quality of the classification is indicated as A-good, B-middle, C-bad.

ID	Classification	$\log(L_{TIR})$ $[L_\odot]$	$\log(L_{1.4GHz})$ $[W\,Hz^{-1}]$	SFR_{TIR} $(M_\odot\,year^{-1})$	$SFR_{1.4GHz}$ $(M_\odot\,year^{-1})$	Quality
G09.v10.1186	AGN	13.02 ± 0.21	25.11 ± 0.03	1803 ± 1134	3204 ± 222	A
G12.v10.761	AGN	13.18 ± 0.21	25.56 ± 0.12	2603 ± 1635	9070 ± 2953	C
G12.v10.860	AGN	13.18 ± 0.20	25.16 ± 0.05	2587 ± 1512	3586 ± 422	A
G12.v10.864	AGN	13.04 ± 0.21	25.21 ± 0.02	1871 ± 1158	4050 ± 205	A
G12.v10.881	AGN	13.24 ± 0.21	25.45 ± 0.10	3000 ± 1904	7058 ± 1714	C
G12.v10.893	AGN	13.38 ± 0.21	25.29 ± 0.04	4142 ± 2627	4889 ± 464	B
G12.v10.1529	AGN	13.13 ± 0.21	25.60 ± 0.01	2338 ± 1483	9865 ± 344	A
G15.v10.2160	AGN	13.14 ± 0.21	25.26 ± 0.09	2407 ± 1488	4560 ± 1018	C
G15.v10.4116	AGN	13.09 ± 0.21	25.24 ± 0.07	2111 ± 1329	4310 ± 761	A
NGP-3248	AGN	12.93 ± 0.20	25.05 ± 0.01	1460 ± 837	2829 ± 83	A
NGP-413	AGN	13.78 ± 0.22	25.95 ± 0.06	10317 ± 6653	22083 ± 3263	B
G09.v10.576	SF	13.15 ± 0.19	24.71 ± 0.06	2449 ± 1373	1276 ± 193	B
G09.v10.892	SF	12.76 ± 0.21	24.68 ± 0.17	995 ± 634	1206 ± 599	B
G09.v10.1700	SF	13.10 ± 0.21	24.51 ± 0.08	2155 ± 1351	804 ± 168	B
G12.v10.463	SF	13.03 ± 0.19	24.97 ± 0.13	1869 ± 1023	2328 ± 851	A
G12.v10.530	SF	13.13 ± 0.21	24.72 ± 0.03	2327 ± 1433	1301 ± 92	A
G12.v10.596	SF	12.97 ± 0.22	24.64 ± 0.05	1599 ± 1049	1101 ± 139	A
G12.v10.846	SF	13.10 ± 0.21	24.89 ± 0.07	2180 ± 1320	1929 ± 324	A
G12.v10.1504	SF	12.96 ± 0.22	24.55 ± 0.10	1593 ± 1049	895 ± 239	B
G12.v10.1589	SF	13.16 ± 0.22	24.45 ± 0.09	2480 ± 1590	700 ± 160	A
G15.v10.592	SF	13.29 ± 0.22	24.89 ± 0.08	3349 ± 2171	1949 ± 375	A
G15.v10.606	SF	13.14 ± 0.23	24.95 ± 0.03	2391 ± 1665	2225 ± 183	A
G15.v10.678	SF	13.08 ± 0.18	24.56 ± 0.07	2069 ± 1097	905 ± 169	B
G15.v10.730	SF	13.19 ± 0.20	24.49 ± 0.06	2694 ± 1625	777 ± 113	A
G15.v10.877	SF	13.12 ± 0.21	24.52 ± 0.06	2256 ± 1431	823 ± 115	B
G15.v10.945	SF	13.11 ± 0.23	24.34 ± 0.07	2214 ± 1546	549 ± 103	A
G15.v10.2095	SF	13.16 ± 0.22	24.48 ± 0.10	2520 ± 1627	760 ± 190	B
G15.v10.2231	SF	13.16 ± 0.21	24.65 ± 0.80	2497 ± 1601	1124 ± 5935	B
NGP-383	SF	13.48 ± 0.21	25.03 ± 0.04	5233 ± 3329	2727 ± 242	A
NGP-714	SF	13.23 ± 0.20	24.62 ± 0.04	2930 ± 1727	1042 ± 114	A
NGP-1189	SF	13.26 ± 0.20	24.71 ± 0.05	3147 ± 1875	1278 ± 141	B
NGP-1386	SF	12.97 ± 0.20	24.63 ± 0.02	1606 ± 947	1077 ± 61	A
NGP-1411	SF	12.96 ± 0.22	24.98 ± 0.01	1568 ± 1012	2409 ± 73	A
NGP-1595	SF	13.35 ± 0.21	25.08 ± 0.03	3842 ± 2452	3014 ± 234	A
NGP-1784	SF	13.14 ± 0.19	24.86 ± 0.02	2373 ± 1327	1828 ± 98	A
NGP-1790	SF	13.04 ± 0.20	24.36 ± 0.07	1876 ± 1129	578 ± 102	C
NGP-1801	SF	13.23 ± 0.22	24.81 ± 0.04	2957 ± 1931	1630 ± 144	A
NGP-2178	SF	13.06 ± 0.20	24.62 ± 0.04	1971 ± 1175	1049 ± 95	B
NGP-2403	SF	13.00 ± 0.20	24.62 ± 0.04	1730 ± 1040	1051 ± 108	A
NGP-2945	SF	13.24 ± 0.22	24.75 ± 0.80	2983 ± 1953	1402 ± 7486	C
NGP-3287	SF	13.02 ± 0.22	24.81 ± 0.03	1793 ± 1176	1612 ± 129	A
NGP-4425	SF	13.24 ± 0.22	24.92 ± 0.04	3008 ± 1955	2091 ± 218	B
NGP-4546	SF	13.18 ± 0.21	24.90 ± 0.02	2609 ± 1672	1992 ± 109	B
G09.v10.474	LG	13.32 ± 0.21	24.78 ± 0.07	3600 ± 2307	1507 ± 258	B
G12.v10.932	LG	12.94 ± 0.21	24.87 ± 0.07	1516 ± 941	1848 ± 306	B

Table 4.3 : *Continued*

ID	Classification	$\log(L_{TIR})$ $[L_\odot]$	$\log(L_{1.4GHz})$ $[W\,Hz^{-1}]$	SFR_{TIR} $(M_\odot\,year^{-1})$	$SFR_{1.4GHz}$ $(M_\odot\,year^{-1})$	Quality
G15.v10.245	LG	13.22 ± 0.20	24.77 ± 0.07	2854 ± 1702	1459 ± 256	B
G15.v10.432	LG	13.22 ± 0.21	24.74 ± 0.07	2865 ± 1816	1360 ± 246	C
G15.v10.468	LG	13.36 ± 0.21	25.19 ± 0.08	3995 ± 2542	3875 ± 779	B
G15.v10.861	LG	13.29 ± 0.22	24.76 ± 0.06	3373 ± 2168	1438 ± 202	B
NGP-2241	LG	13.37 ± 0.21	24.67 ± 0.05	4080 ± 2607	1170 ± 133	C
NGP-2353	LG	13.42 ± 0.22	25.07 ± 0.07	4514 ± 2945	2961 ± 512	B
NGP-3120	LG	13.07 ± 0.21	24.53 ± 0.08	2021 ± 1263	843 ± 182	C
NGP-3394	LG	13.02 ± 0.18	24.72 ± 0.04	1787 ± 922	1310 ± 121	C
NGP-3653	LG	13.11 ± 0.20	24.51 ± 0.07	2221 ± 1329	819 ± 143	C
NGP-3708	LG	13.22 ± 0.21	24.61 ± 0.05	2845 ± 1813	1027 ± 132	B
NGP-3778	LG	12.94 ± 0.20	24.83 ± 0.06	1517 ± 894	1706 ± 268	B
NGP-3862	LG	13.11 ± 0.22	24.81 ± 0.08	2238 ± 1507	1602 ± 327	A
NGP-3990	LG	13.02 ± 0.21	24.70 ± 0.06	1810 ± 1149	1241 ± 190	B
NGP-4690	LG	12.99 ± 0.19	24.18 ± 0.12	1700 ± 947	377 ± 125	C
NGP-6110	LG	13.23 ± 0.21	24.84 ± 0.05	2957 ± 1883	1742 ± 231	B
NGP-6431	LG	13.23 ± 0.21	24.88 ± 0.10	2960 ± 1850	1881 ± 480	B
G09.v10.401	SLG	13.28 ± 0.21	24.88 ± 0.06	3297 ± 2056	1918 ± 292	A
G09.v10.1251	SLG	13.16 ± 0.21	24.72 ± 0.07	2501 ± 1544	1326 ± 239	B
G12.v10.116	SLG	13.55 ± 0.21	25.29 ± 0.05	6157 ± 3924	4920 ± 581	A
G12.v10.1259	SLG	12.99 ± 0.20	24.79 ± 0.05	1682 ± 987	1541 ± 200	A
NGP-684	SLG	13.51 ± 0.22	24.99 ± 0.05	5548 ± 3569	2454 ± 330	A
NGP-1128	SLG	13.34 ± 0.22	25.01 ± 0.04	3778 ± 2435	2536 ± 266	A
NGP-1328	SLG	13.14 ± 0.21	24.54 ± 0.09	2353 ± 1429	861 ± 200	B
NGP-3154	SLG	13.20 ± 0.21	25.02 ± 0.06	2729 ± 1735	2635 ± 427	C

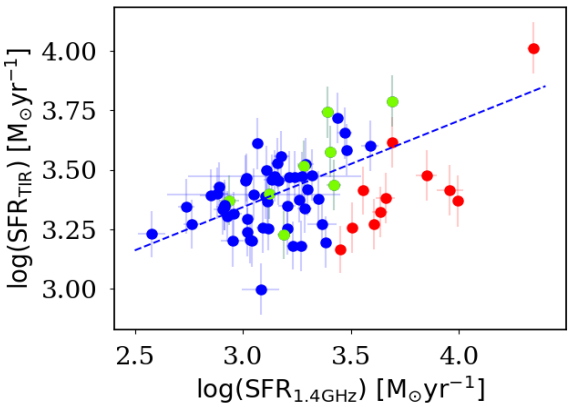

Figure 4.26 : In this plot we represent the SFRs derived from the infrared and radio luminosities. The red dots represent the AGNs, which have an excess of radio emission. The green dots correspond to the SLGs whose values are not corrected for magnification factor, and the blue dots are the other SFGs of the sample.

essential to determine the origin of this sample. Though with a sample of 112 sources we can obtain a good statistical representation of the behavior of these galaxies.

2. An spectral index of $\alpha = 0.7$, typical for SFGs, was used to calculate radio luminosities. However, we also experimented with two other prescriptions for the spectral index. The 'real' spectral indexes were measured in our maps from the two spectral windows obtained by dividing the 4 GHz bandwidth continuum maps into two spectral windows of 2 GHz each, centred at 5 and 7 GHz. This alpha was obtained following the expression:

$$\alpha = -\frac{\log(S_{5_{GHz}}/S_{7_{GHz}})}{\log(\nu_{5_{GHz}}/\nu_{7_{GHz}})} \tag{4.6}$$

Despite the small distance between these two central frequencies, resulting in an uncertain slope of the power law, we initially used the measured α as a first estimation of this parameter. Due to the higher noise at 5 and 7 GHz sometimes the targets at these frequencies were very weak or not detected, and therefore a reliable measurement was difficult to obtain. To avoid introducing too much uncertainty an $\alpha = 0.7$ was adopted when the $S/N < 5$ for any of the two spectral windows. This is:

$$\alpha_{cond} = \begin{cases} 0.7, & \text{if } S/N_{5_{GHz}} < 5 \text{ or } S/N_{7_{GHz}} < 5 \\ \alpha_{measured} = -\frac{\log(S_{5_{GHz}}/S_{7_{GHz}})}{\log(\nu_{5_{GHz}}/\nu_{7_{GHz}})} \end{cases} \tag{4.7}$$

Due to the small frequency range over which the spectral indeces were measured and the large uncertainties in the flux densities due to their low S/N, a wide range of measured spectral index values were found, $\alpha \sim [-1.82, +2.99]$. This is consistent with Smolčić et al. (2017b) who calculate the spectral index between 1.4 and 3 GHz bands for 2,420 detected sources in the COSMOS field finding a range of $\alpha \sim [-1.2, +3.5]$. To study how good the measured-α were, $L_{1.4GHz}$ were converted to fluxes ($S_{1.4}$) to analyse the IRRC in these terms. The 1.4 GHz fluxes were obtained with $S_{1.4} = S_6(\frac{1.4}{6})^{-\alpha}$ for the different scenarios of α. The different IRRC are plotted in Figure 4.27 where we can see that the best correlation corresponds to the average-α. For the other two cases, measure-α and condition-α there are no clear correlations. This indicates that our best option was to use the averaged-α despite the strong assumption that this implied.

It is important to note that more work needs to be done to measure the synchrotron radiation as it is a important feature to determine the luminosities. The synchrotron

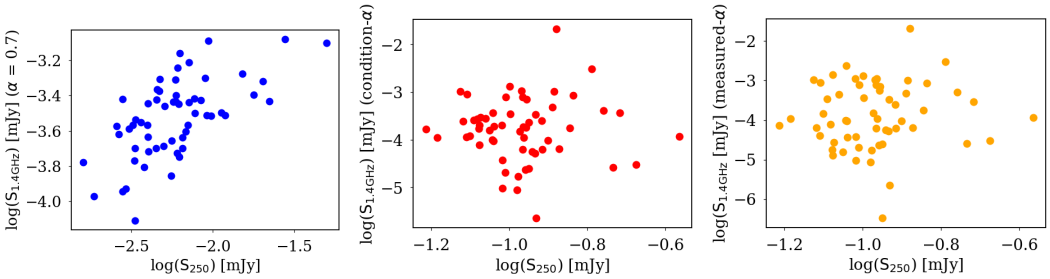

Figure 4.27 : IRRC for the converted fluxes ($S_{1.4}$) from $L_{1.4GHz}$ to study the quality of the different α. *Left:* IRRC for the converted radio-luminosities using the average $\alpha = 0.7$ where a clear IRRC is obtained. *Middle:* Correlation for the condition-α where the found correlation is less clear. *Right:* Correlation for measured-α where no clear correlation is obtained either. Therefore, we consider our best option to use the averaged-α in our analysis.

radiation can be dominated by the thermal free-free emission, changing the slope of the SED.

3. To classify the sources we did a morphological study of the sample but in most of the cases this was not sufficient to identify the targets beyond any doubt. Better resolution would be necessary to resolve the lensed galaxies as well as spectroscopic-redshift for the NIR counterparts and the radio sources. It is very risky to assure that the classified SFGs are not possible LGs or that the LGs are certainly so.

4.8 Conclusions

We have studied faint H-ATLAS sources to determine what fraction of SLGs are detected following a flux limit criteria ($S_{500} > 29$ mJy). This sample spans the faintest regime of 500μm fluxes for which lensing has ever been studied. Our main results are:

- A sample of 123 FIR-selected sources were observed with the VLA at 6 GHz to obtain radio counterparts for them. NIR maps from VIKING and UKIDSS were used to determine the lenses galaxies of the gravitationally lensed system.

- After deleting contaminants such as nearby galaxies and groups of galaxies, a final sample of 58 galaxies were found to be candidates of LGs. We found 13.8% SLGs, 31.0% good candidates to be LGs and 55.2% SFGs.

- The presence of lensed galaxies decreases with decreasing 500μm-band fluxes as expected. 67% lensed galaxies were found for $S_{500} > 100$ mJy, 54% for $60 < S_{500} < 100$ mJy and 40% for $29 < S_{500} < 60$ mJy. It is important to note here that multiple-J

CO observations and spectroscopic redshifts for both- the NIR and the *Herschel*-sources would be needed to confirm these gravitational lensing systems.

- Eight sources with $S_{500} > 100$ mJy were in the main sample, of which two were nearby galaxies and one was an AGN. After subtracting these contaminants, we found 40% SLGs, 40% over-densities (with two and 3 radio sources) and 20% SFGs with no hint of lensing. This sample has an under presence of gravitational lenses compared with Negrello et al. (2010) who found an almost 100% fraction of gravitational lensing systems in the SDP of H-ATLAS, or Bussmann et al. (2013) who found 70%-80% rate of lensing systems in H-ATLAS and HerMes.

- Studying the IRRC we found consistency between our results and Ivison et al. (2010) who study a FIR-selected sample of DSFGs. This indicates a systematic trend towards higher q_{TIR} when comparing with Delhaize et al. (2017) as was predicted in Sargent et al. (2010).

- SFRs $\gtrsim 1,000$ $M_{\odot}yr^{-1}$ are found for the sample, consistent with the type of galaxies we are studying. Higher SFRs for the infrared emission than for radio were obtained for those SFGs not dominated by an AGN. This is likely due to the selection-bias towards bright infrared sources.

- This work allowed us to obtain a sample of 10 proto-cluster candidates to study spectroscopically in the future to confirm their origin and their redshift.

- The strategy followed during the VLA observations turned out not to be the best one to select a maximum number of lensed systems. To obtain a large sample in a limited amount of observational time at radio wavelengths, fainter sources near the same phase calibrators were selected. To increase the number of lensed galaxies it would have been better to study less galaxies and select brighter sources, even if this means more time needs to be spend to observe these objects. A better resolution of sub-arcseconds would be desired as well, so the use of ALMA or SMA would have been a better option for this work.

This work is a first step to determine the origin of these systems in the faintest regime of the H-ATLAS sources. Additionally, we have made significant progress towards selecting a relatively large sample of lensed galaxies to use in a cosmography study. Spectroscopic redshifts for the lenses and lensed galaxies would be crucial to determine unequivocally the origin of these systems.

Appendix 4.A

Groups and Cluster Galaxies

As mentioned before, there were 39 maps which had more than one radio detection within the 250μm beam and were classified as galaxy groups or potential proto-clusters. However, we highlight that spectroscopic redshifts would be needed to give a definite answer, and the multiple radio components might be also coming from sources at different redshifts (and thus might be physically unrelated). The classification in this appendix is thus somewhat speculative, and it is likely at least a few of these galaxies are lensed. From left to right the following figures represent: i) K_s-band in grey scale and the *Herschel* 250μm beam as the green-circle and ii) *Herschel* image at 250μm. The red contours in all the maps correspond to the radio emission at 6 GHz (3, 4, 5,.. $\times\sigma$ in red and -3σ in dashed-black).

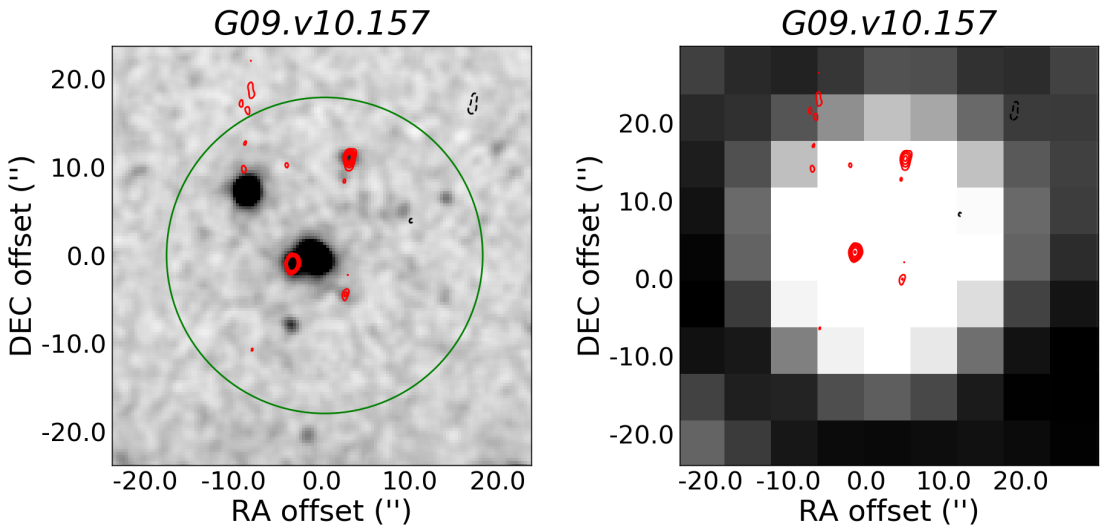

Figure 4.A.1 : This source was first studied in González-Nuevo et al. (2012). It was classified as a potential gravitational lensing system due to the spectroscopic measurements of its optical counterpart (z = 0.30). In this plot we can see three radio sources within the Herschel beam each of them with a NIR counterpart. Therefore, the contamination in the FIR emission coming from other sources could bias the z_{phot} calculated for the *Herschel*-source. Spectroscopic redshift for the radio sources would be necessary to determine the origin of these group of galaxies or proto-cluster candidate.

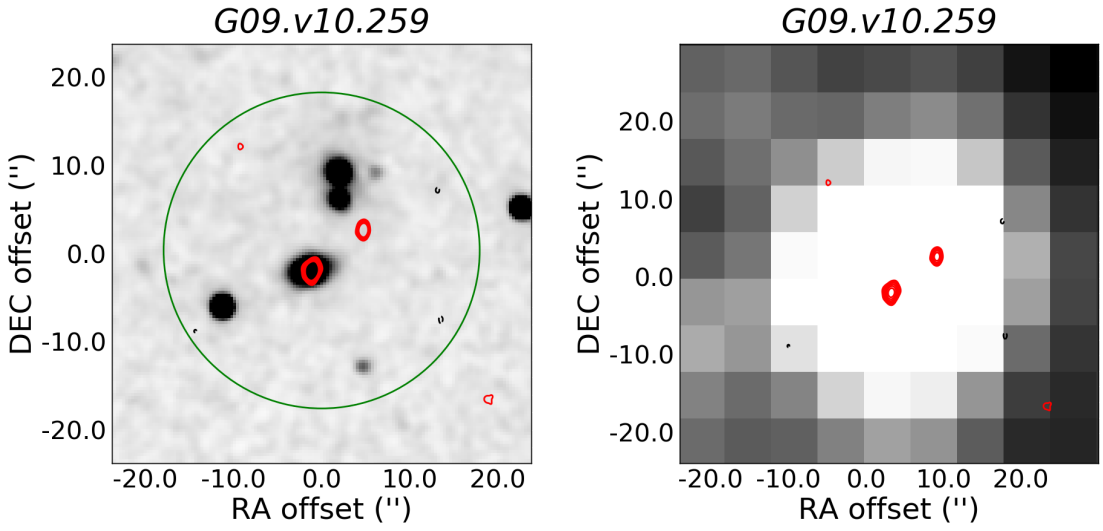

Figure 4.A.2 : Classified as potential lensed in González-Nuevo et al. (2012) because of the photometric VIKING redshift (z = 0.22), the *Herschel*-source has two radio counterparts with similar brightness which might indicate that these two sources are part of the same system. The distance between both radio emissions, their morphology and their location with respect to the NIR counterpart make us think that this galaxy is not lensed.

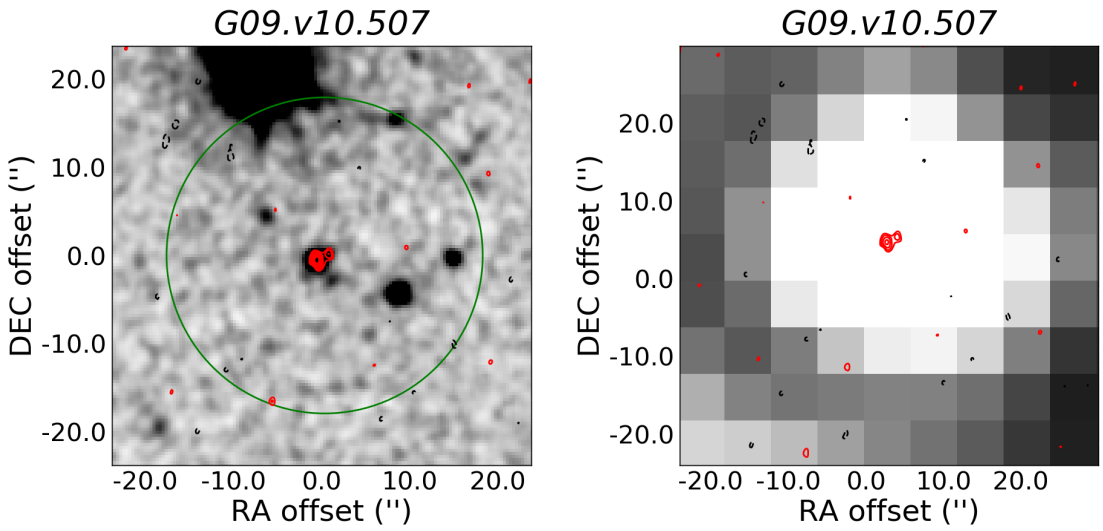

Figure 4.A.3 : This source is classified as a quasar in the catalogue from Adelman-McCarthy & et al. (2009) with spectroscopic redshift ~ 2.03. In the VLA radio map we can distinguish two nearby sources with NIR counterpart with the same 'double' shape. One of the radio sources could be the jet coming from the quasar. High-resolution radio spectroscopy would be necessary to know more about the relation between these two sources.

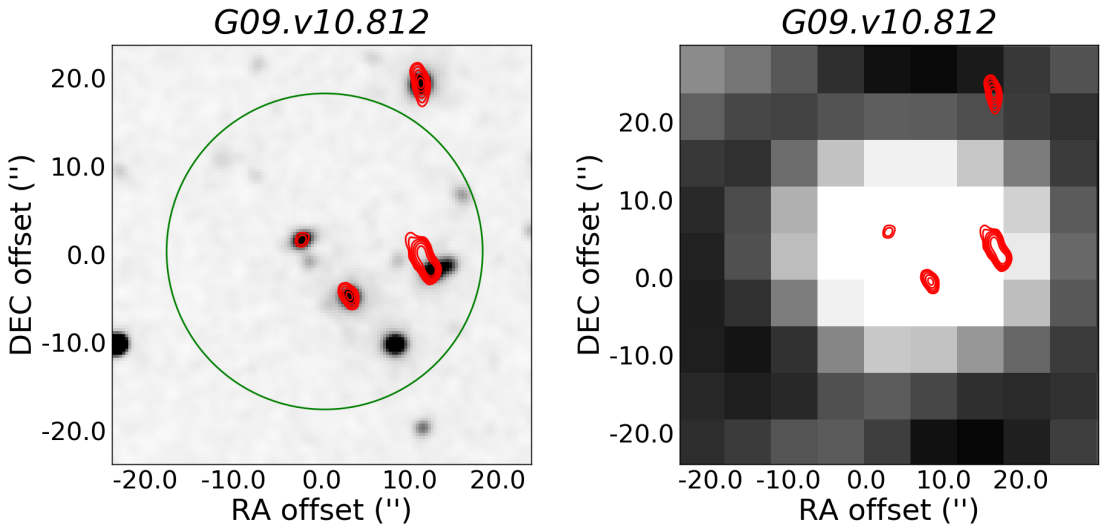

Figure 4.A.4 : At photometric redshift ~ 0.4046 this galaxy cluster was identified by Wen et al. (2009). Three radio sources are detected within the *Herschel* beam and one outside towards the north of it, all of them with similar brightness and NIR counterparts, so it is likely all the radio emissions belong to the same galaxy cluster.

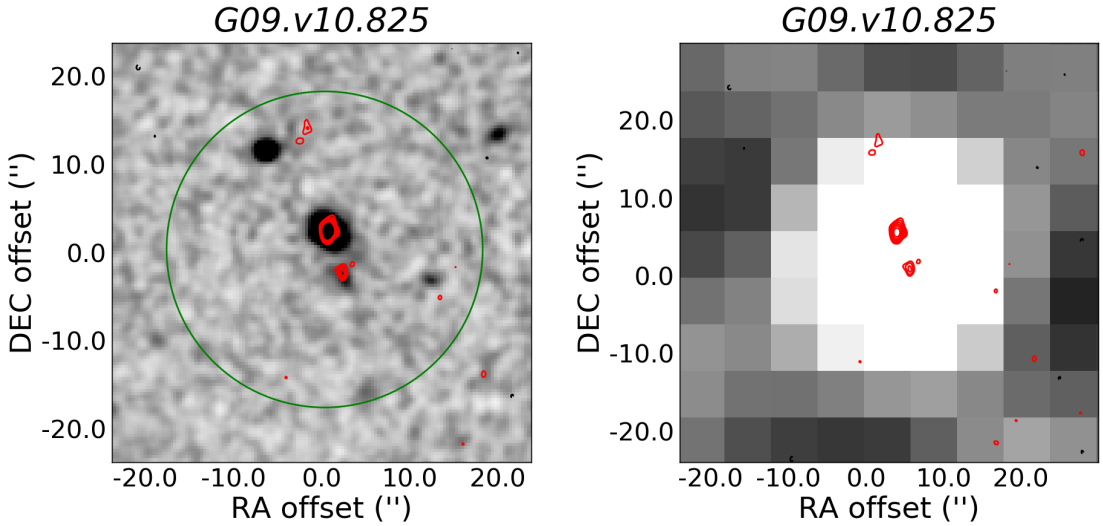

Figure 4.A.5 : Two radio sources both with NIR counterparts are detected as radio counterparts of the FIR emission. One of them seems an AGN and the other one could be a LG or a SFG.

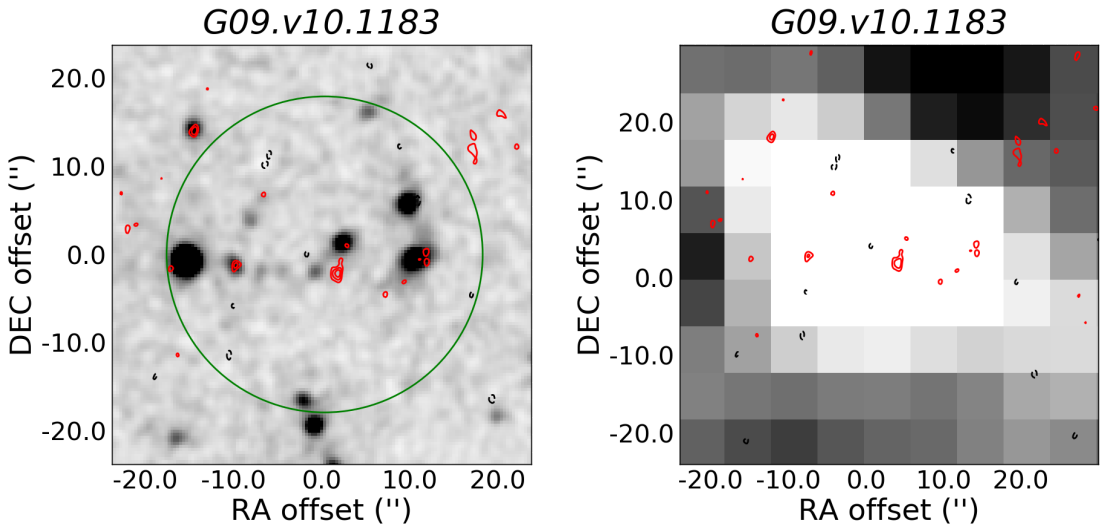

Figure 4.A.6 : Three sources are contributing to the extended FIR emission in this map (one of them at the top-left outside the green-circle). With faint radio detections these sources could be related forming a galaxy cluster or a proto-cluster.

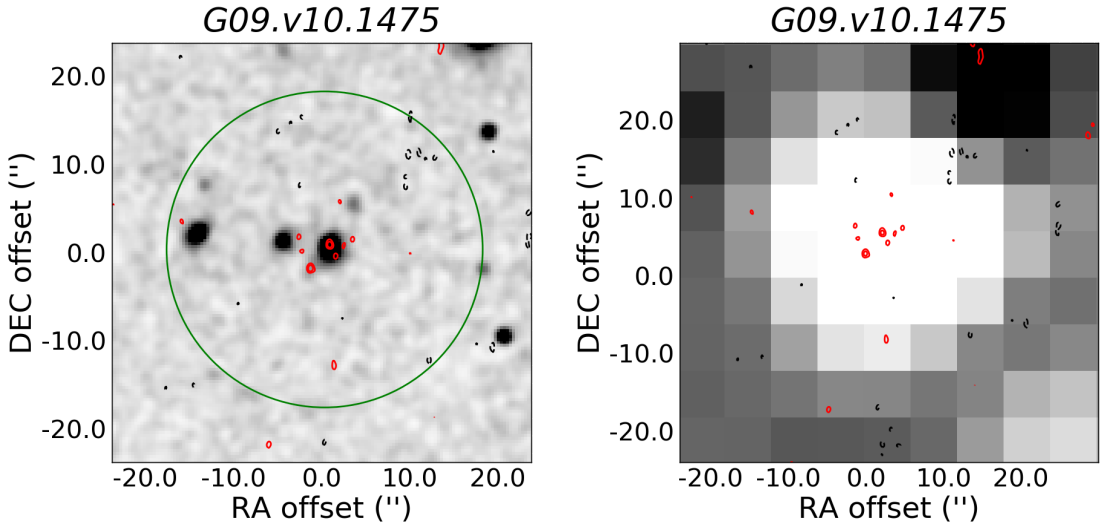

Figure 4.A.7 : Despite of the high r.m.s. of this map, two faint radio sources within the *Herschel* emission are detected. These two galaxies can be part of the same system, a group of galaxies.

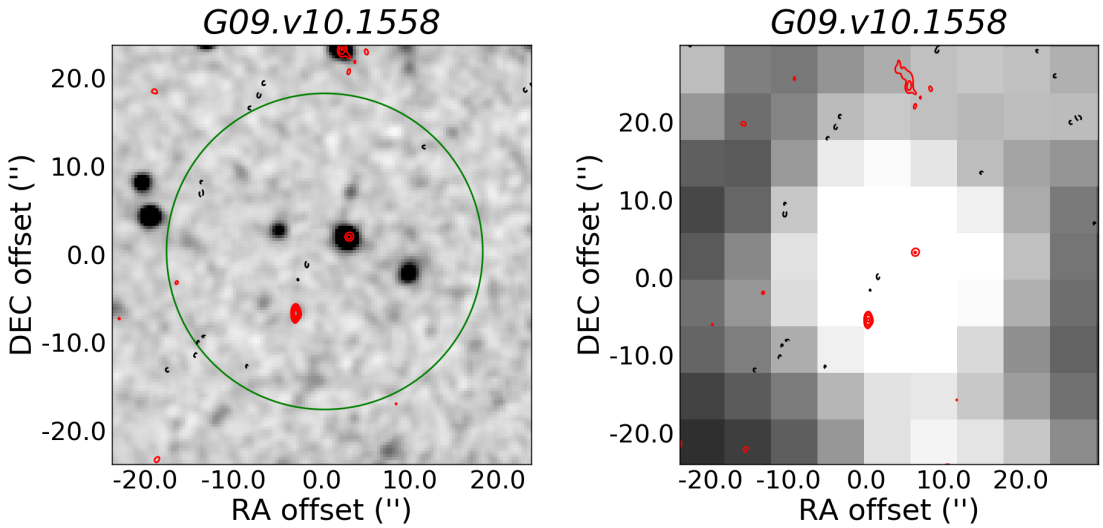

Figure 4.A.8 : Two radio sources with apparent different brightness are detected in this map. In addition, a third source at the north of the map seems to slightly contribute to the FIR emission. Therefore these three sources could be part of a proto-cluster.

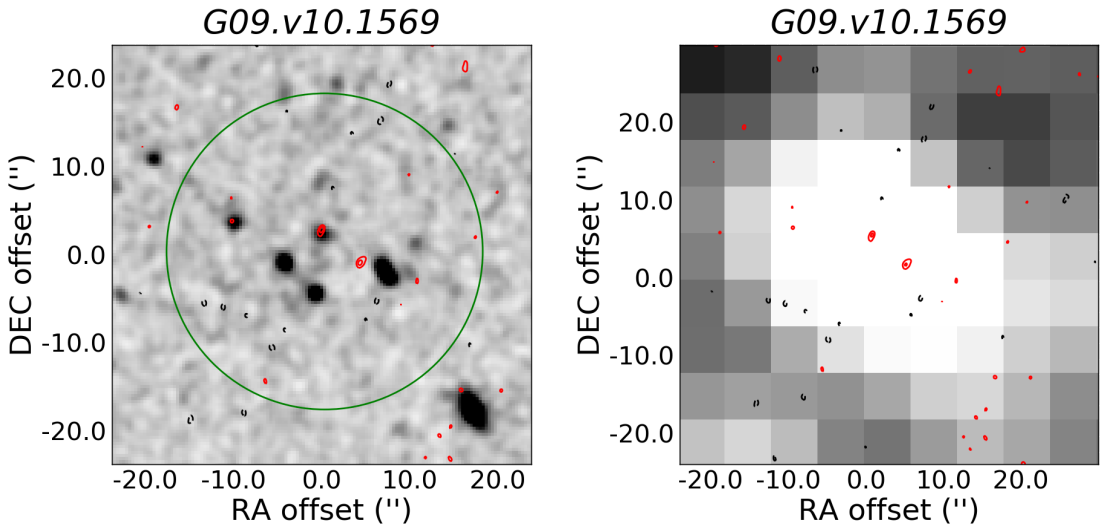

Figure 4.A.9 : An over-density of two radio sources with similar brightness are present in this map within the extended 250μm emission.

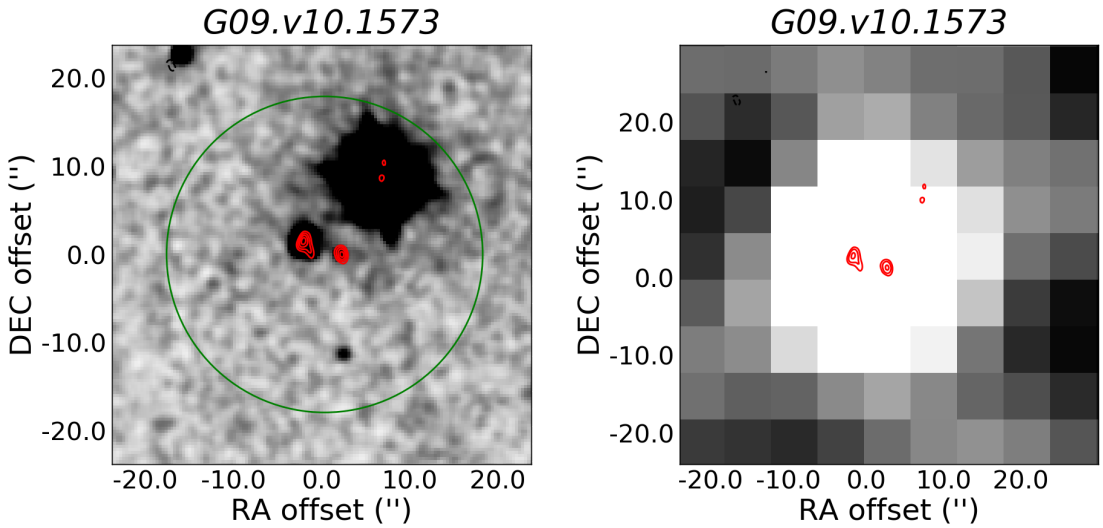

Figure 4.A.10 : Studied in González-Nuevo et al. (2012) this source was classified as potential gravitationally lensed due to its VIKING photometric redshifts (z = 0.18). Two radio sources with similar radio brightness and NIR counterparts for both indicate that these galaxies can be a galaxy cluster. Another possibility is that the source at the left of the map is being lensed while the other source is a normal SFG.

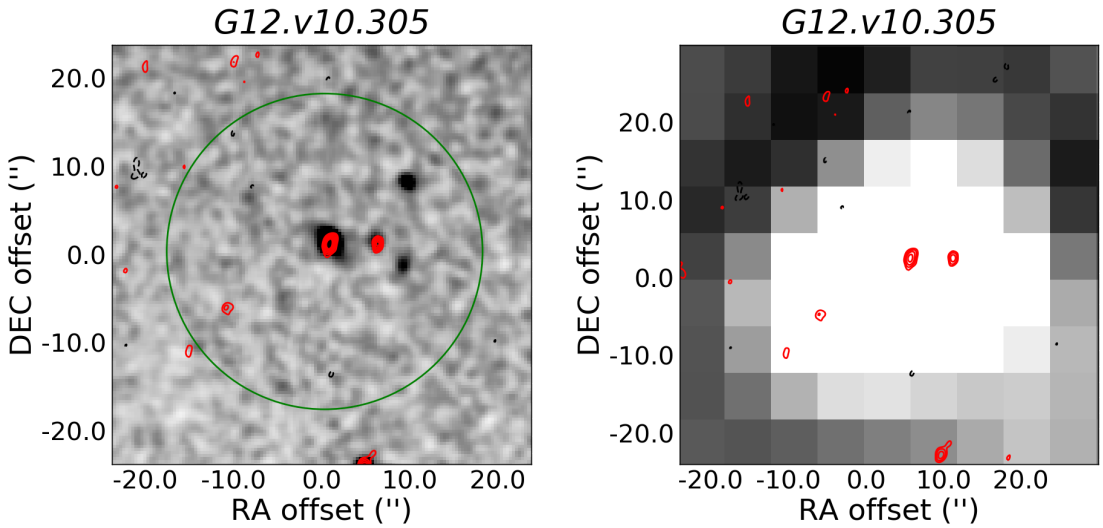

Figure 4.A.11 : This source was studied in Harris et al. (2012) to determine its spectroscopic redshift in a range of $2.1 < z < 3.5$ via CO(1-0) molecular line. No emission lines were detected and therefore the redshift is still unknown. Two radio sources with similar radio brightness are located in the centre of the FIR emission. In addition a third source with less brightness is located in the bottom-left part of the *Herschel* beam while a fourth source is detected at the very bottom of the map. With extended FIR emission this over-density of radio sources is a good candidate for a galaxy cluster or proto-cluster.

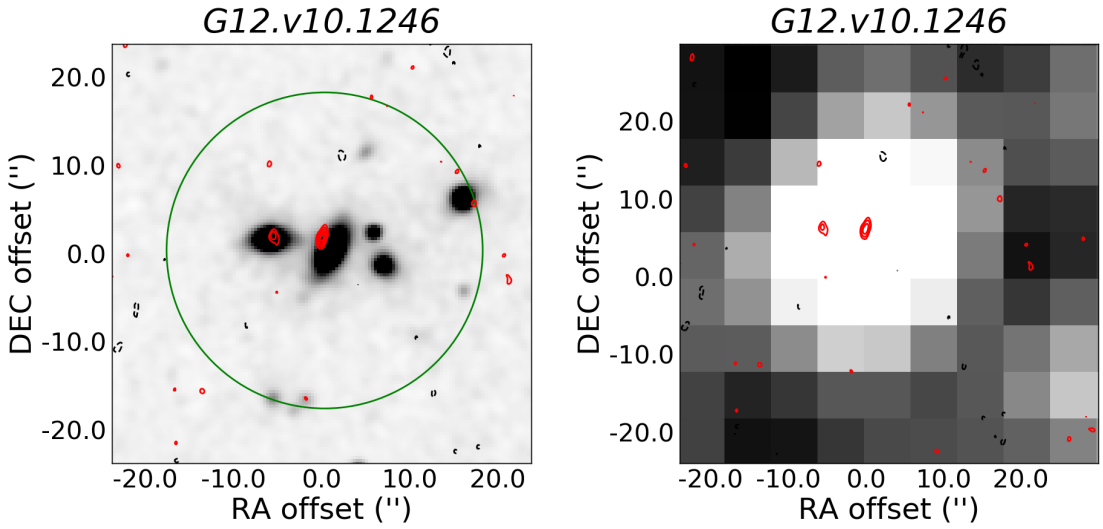

Figure 4.A.12 : Classified as a compact group of galaxies at $z = 0.1857$ (Lee et al., 2004), the two radio sources with similar brightness are consistent with a group of galaxies. The right radio source seems lensed, while the left source might be part of the group of galaxies. It is possible as well that the central source is being lensed by the group of galaxies.

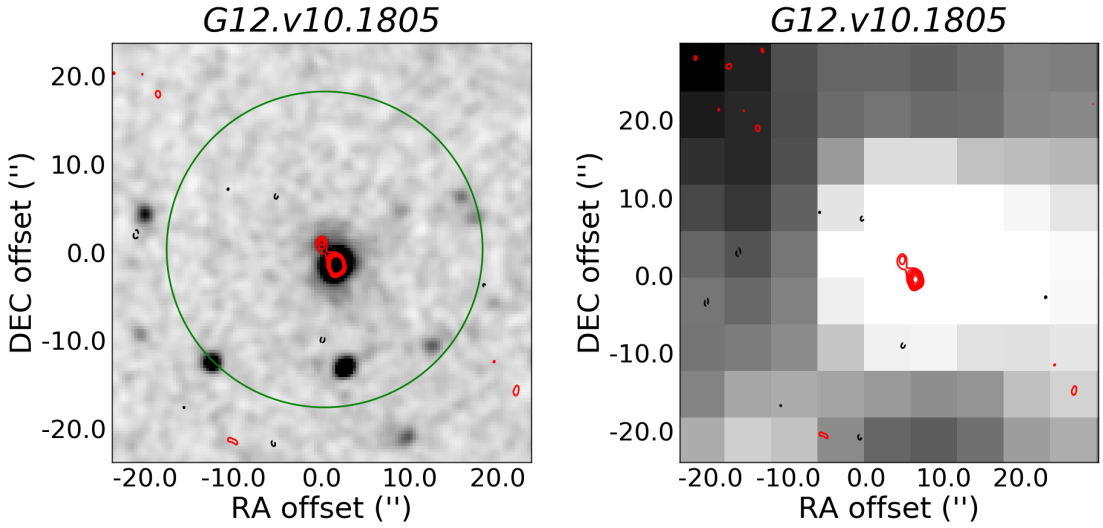

Figure 4.A.13 : Identified as an AGN at z = 0.3484 (Véron-Cetty & Véron, 2010), this radio map reveals a second fainter radio source with a NIR counterpart. Spectroscopic redshift would be necessary for this second source to confirm its origin.

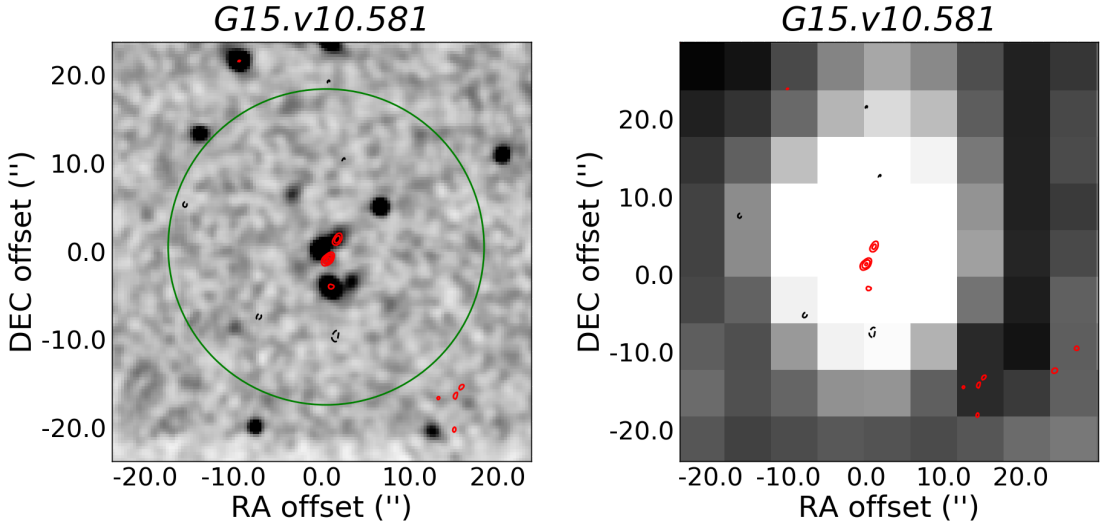

Figure 4.A.14 : Three radio sources are detected within the FIR emission. Two of them can be part of a galaxy group while the third source might be a lensed galaxy.

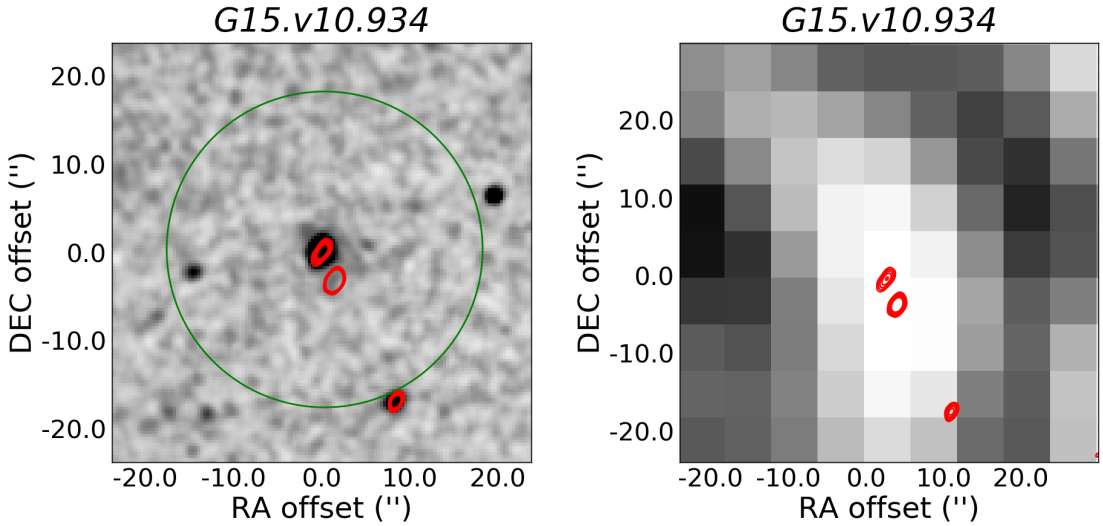

Figure 4.A.15 : Three radio sources with similar brightness are coming from the extended *Herschel*-source. These galaxies are good candidates to be a galaxy cluster or a proto-cluster.

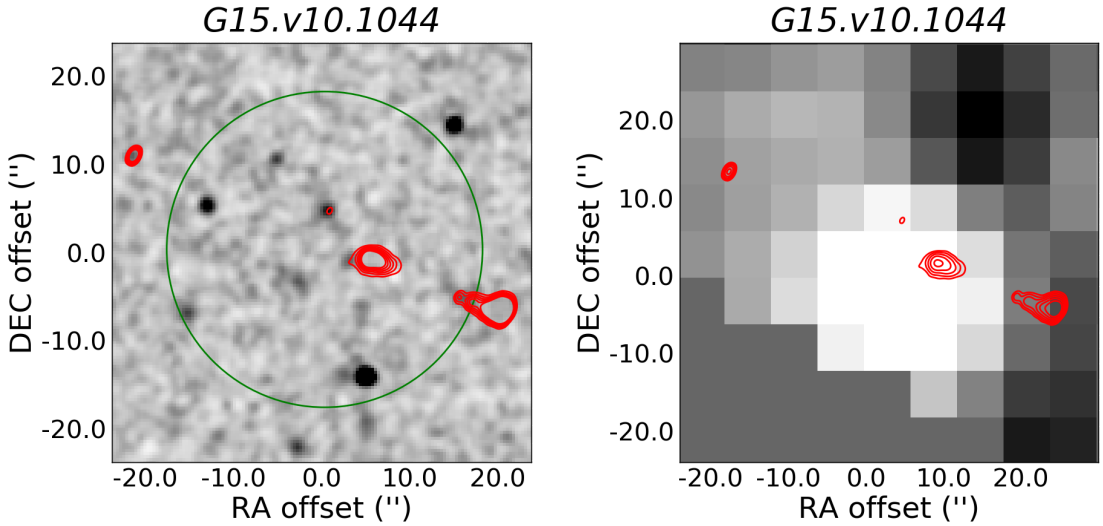

Figure 4.A.16 : Located in the edge of the *Herschel* map, this source presents radio emission consistent with a jet while other very faint source is located within the *Herschel* emission which seems to be extended.

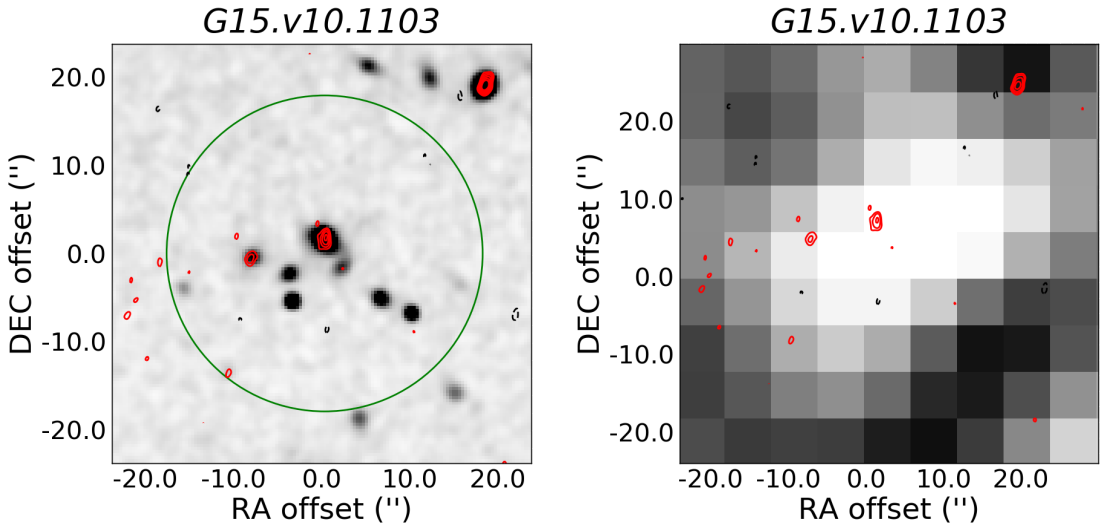

Figure 4.A.17 : A group of galaxies in the NIR map is detected with radio counterparts for some of them. Most likely the radio emission is part of the group of galaxies at NIR.

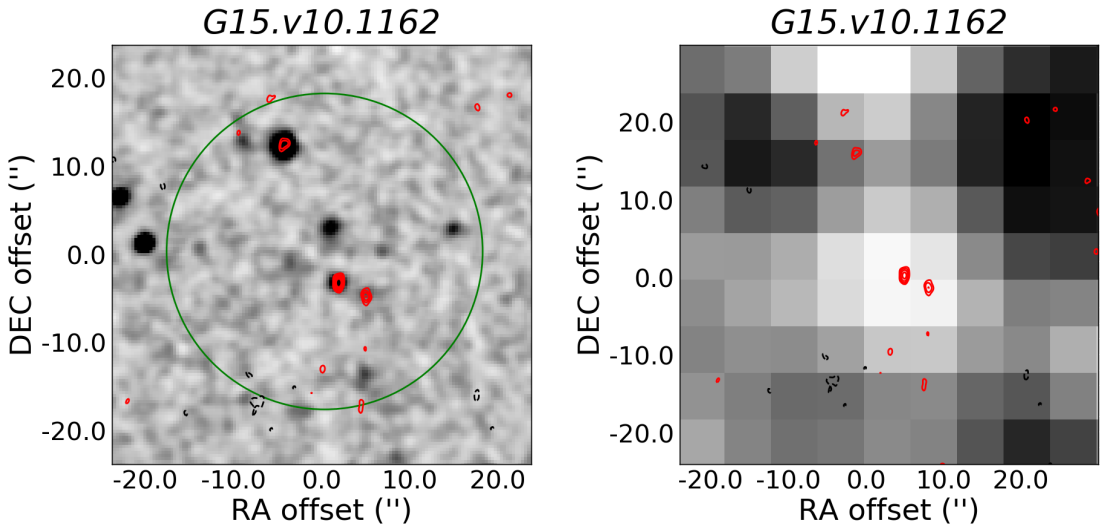

Figure 4.A.18 : A faint and extended FIR emission has three radio sources within its beam. Two of them have NIR counterparts which indicate this over-density could be a galaxy cluster.

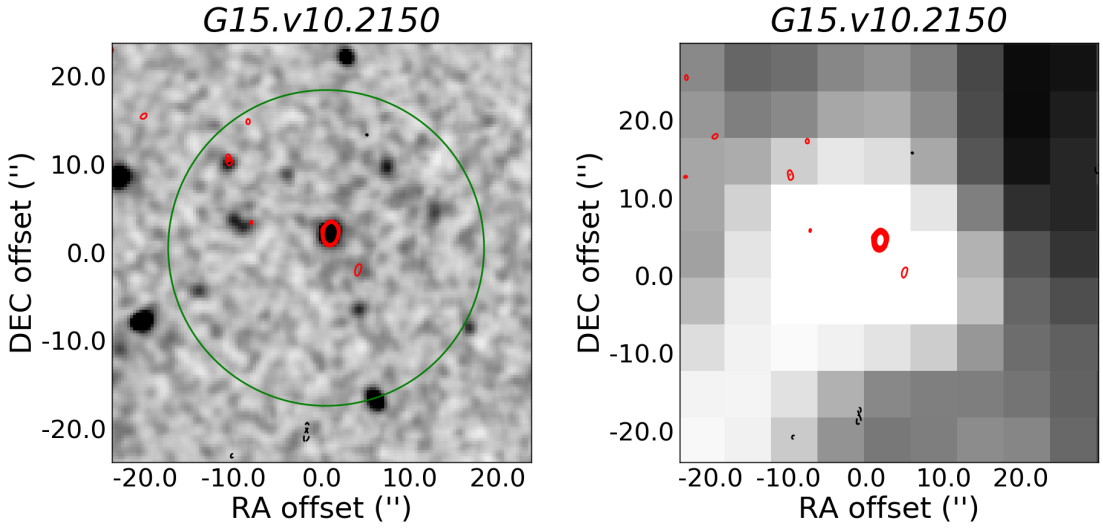

Figure 4.A.19 : A very bright radio source in the centre of the map, likely an AGN, and a very faint source are detected here. They both have NIR counterparts so they can be part of a galaxy group.

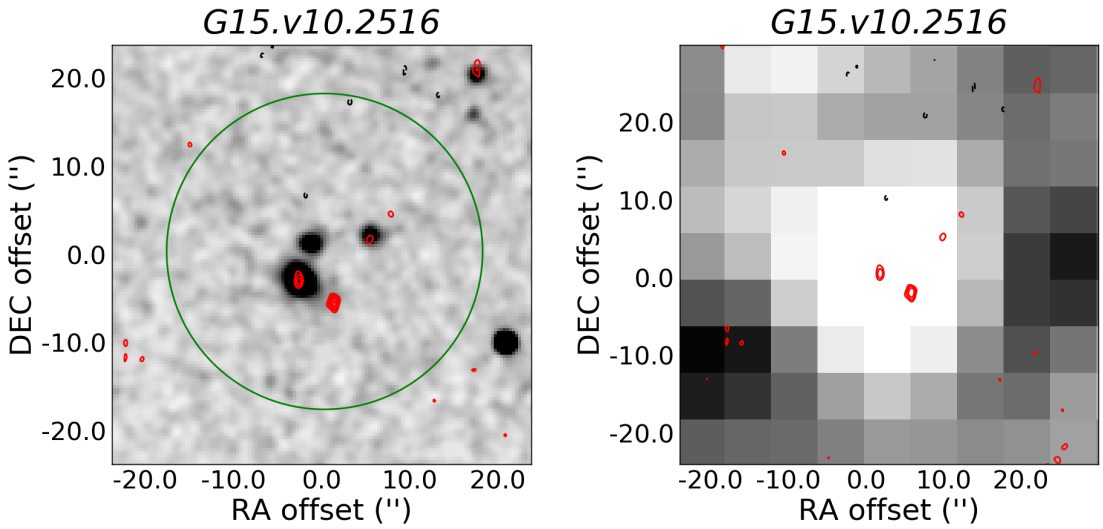

Figure 4.A.20 : Three radio detections are found in this map, which can be a potential galaxy group or proto-cluster.

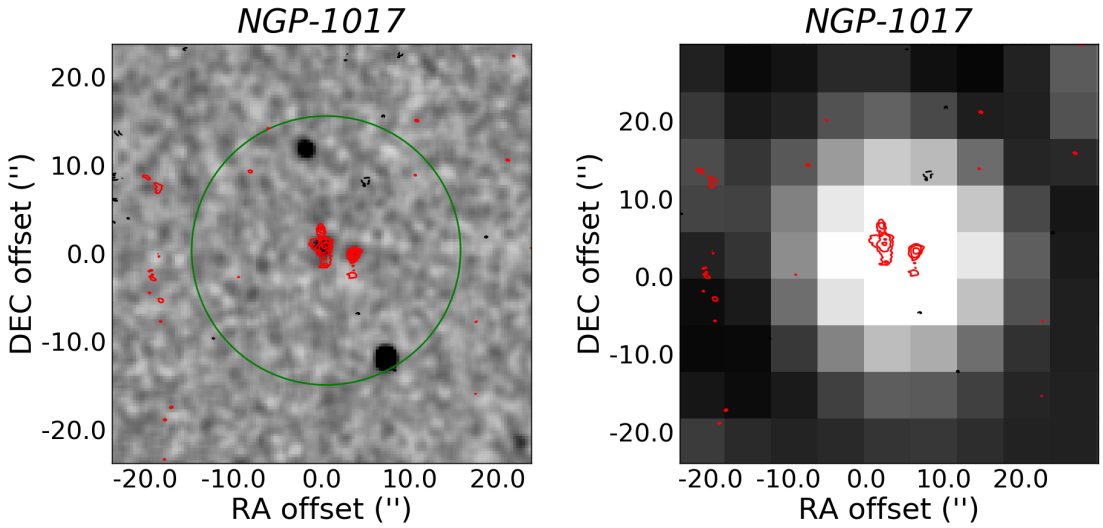

Figure 4.A.21 : With similar features than the next source, this galaxy could be a lensed massive dusty starbursting galaxy.

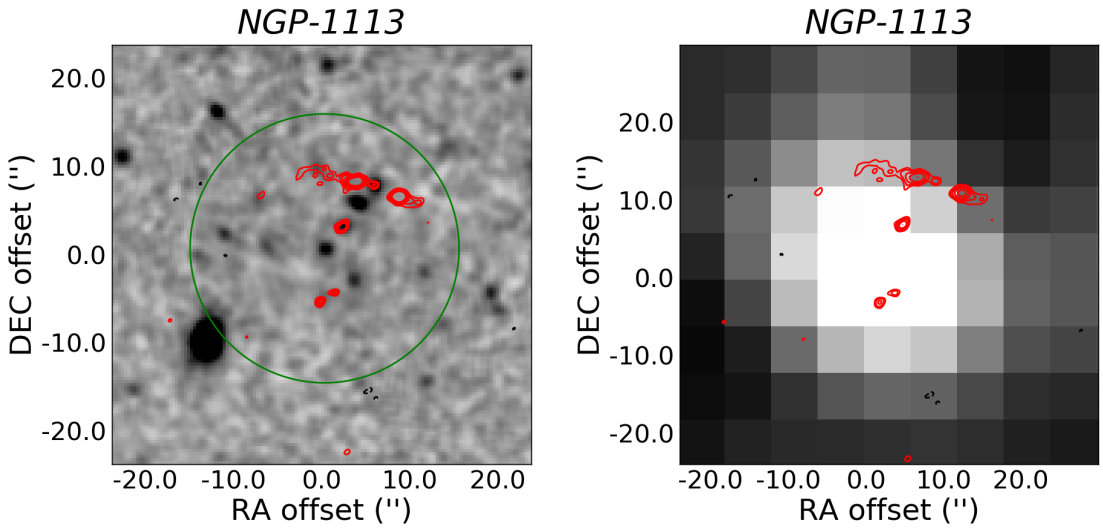

Figure 4.A.22 : This source is a studied lensed massive dust starbursting galaxy at z = 2.685 (Nayyeri et al., 2017).

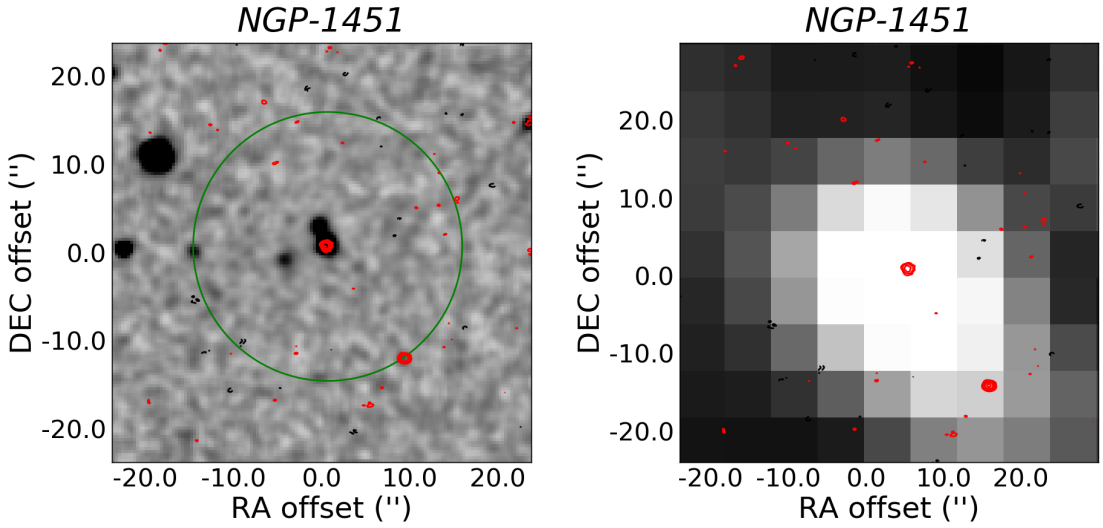

Figure 4.A.23 : An extended FIR emission is consistent with the two radio emissions of similar brightness. This might indicate the presence of a galaxy group.

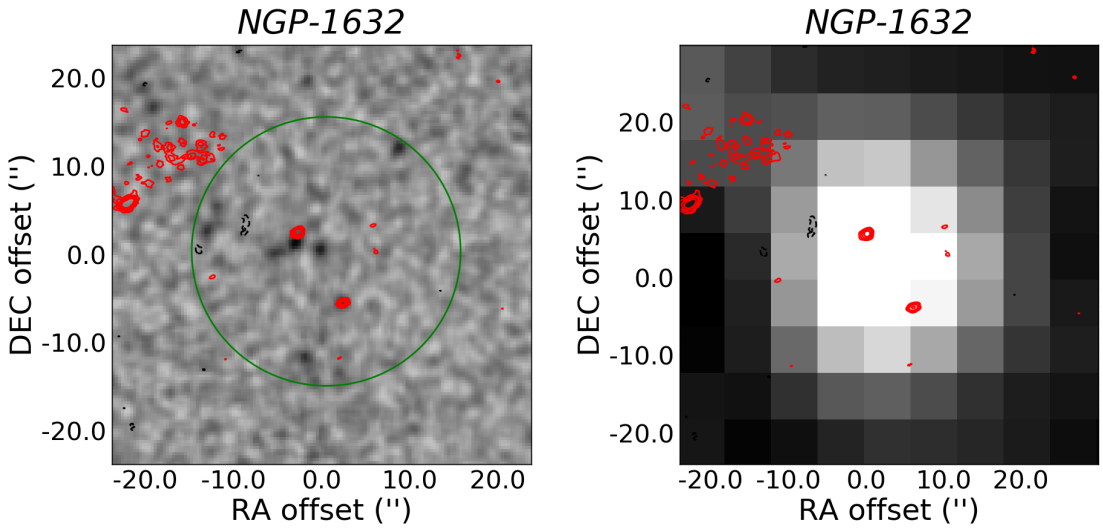

Figure 4.A.24 : Two radio sources are observed within the FIR emission with similar brightness at radio, being good candidates to be a group of galaxies. In the top-left part of the map some noise is detected coming from another very bright galaxy located inside the primary beam.

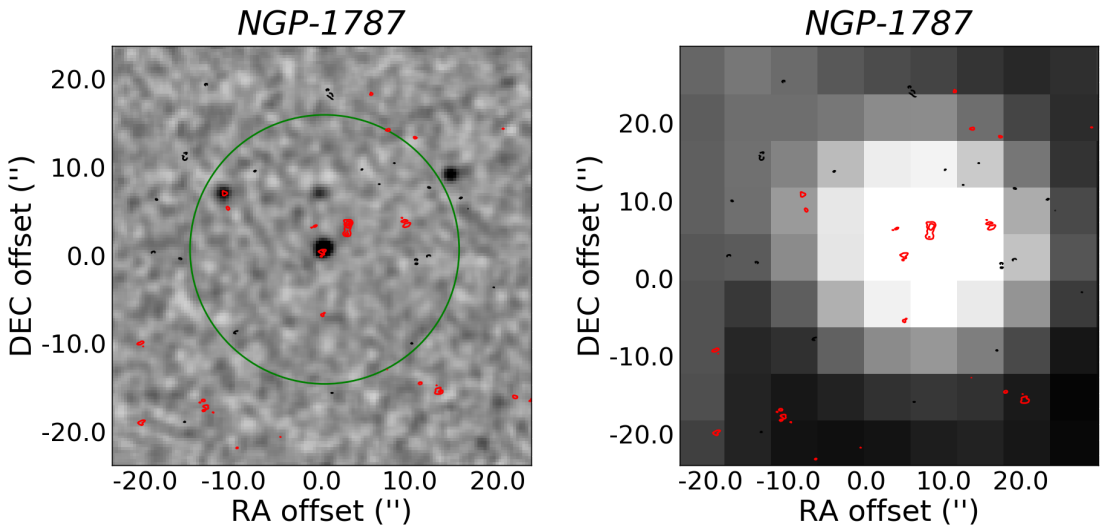

Figure 4.A.25 : Two very faint radio sources seems to be detected in this map. Although, due to the high r.m.s. in the radio map we cannot be certain about the reliability of the central source.

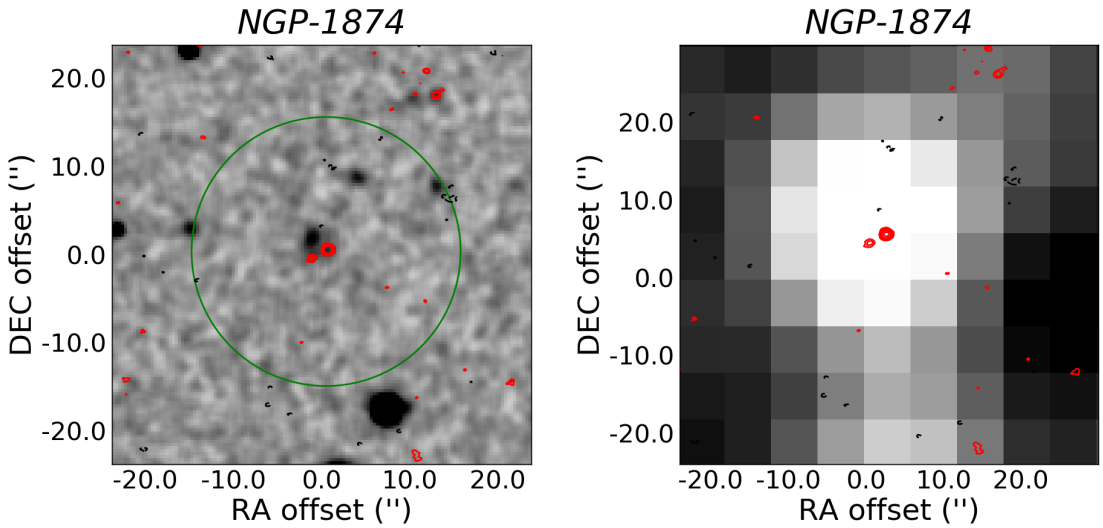

Figure 4.A.26 : Two radio sources with different brightness are detected in this map. The brightest source is likely an AGN, while the fainter galaxy could be lensed. Another two faint sources are detected at the north of the map with weak FIR emission. This over-density is a good candidate of galaxy cluster or proto-cluster.

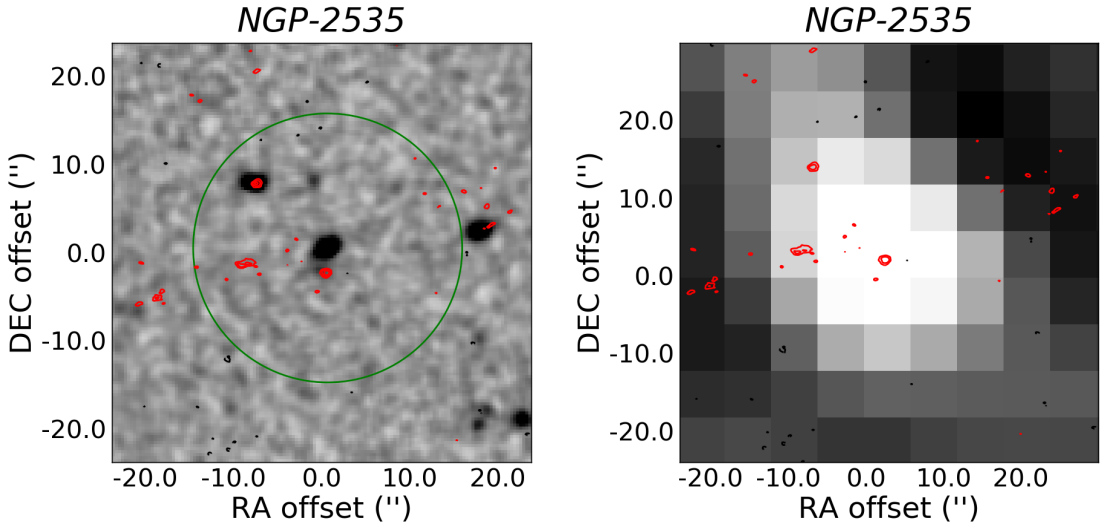

Figure 4.A.27 : Two radio sources with similar brightness are detected in this noisy map. The extended FIR emission make us think that these two galaxies can be members of a galaxy group.

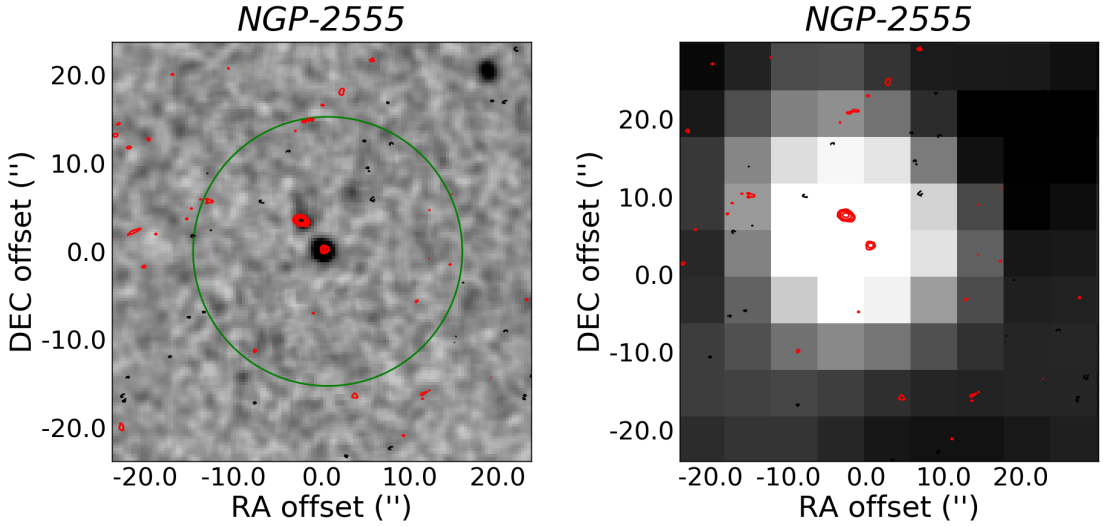

Figure 4.A.28 : A potential galaxy group is found in this map with two radio emissions with similar brightness and NIR counterparts for both of them.

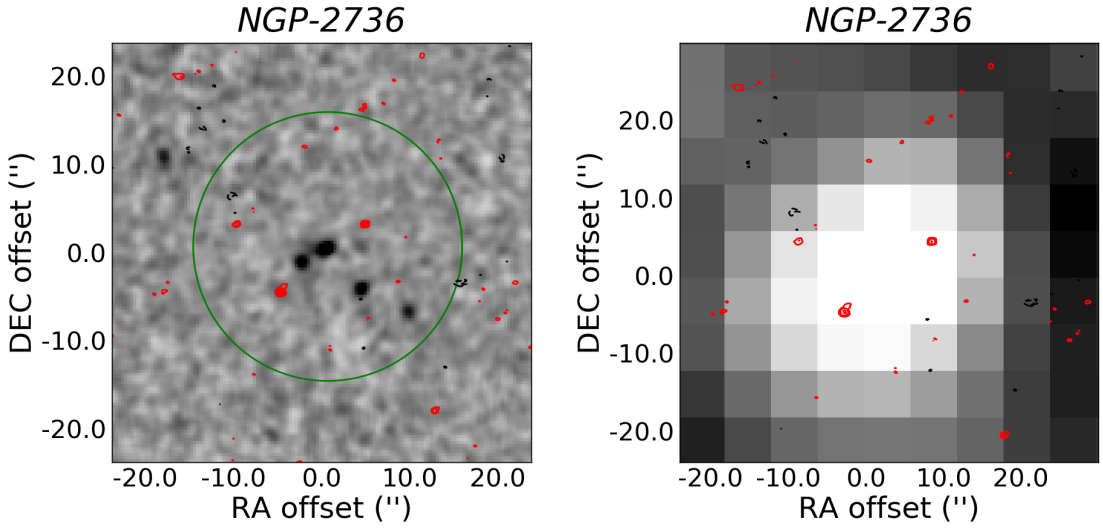

Figure 4.A.29 : Four radio sources with similar brightness are contributing to the FIR emission which has an extended appearance. A potential galaxy group or proto-cluster is detected here.

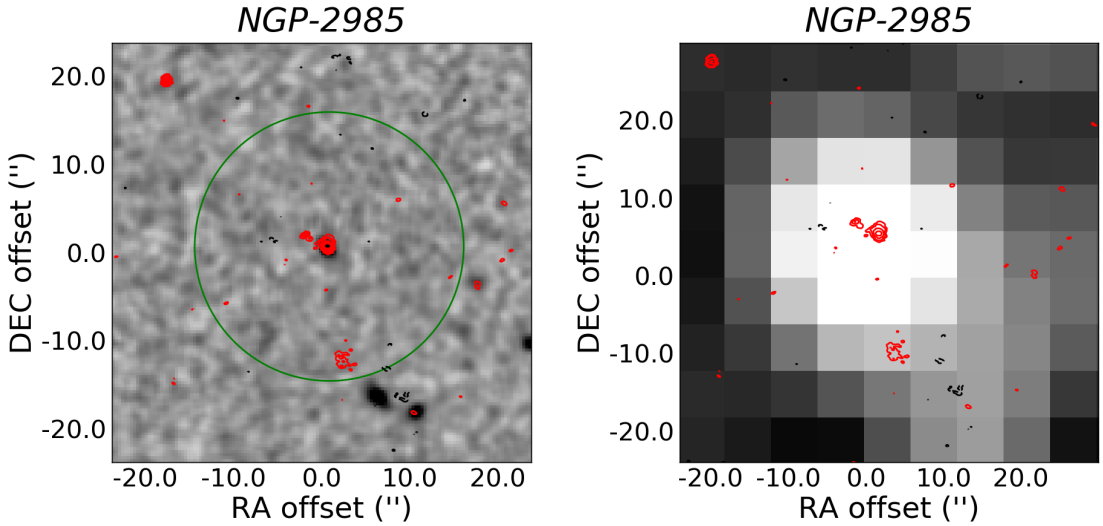

Figure 4.A.30 : A very bright radio source with a NIR counterpart, likely an AGN, is detected in the centre of the map. In addition another faint radio emission nearby the central source is detected.

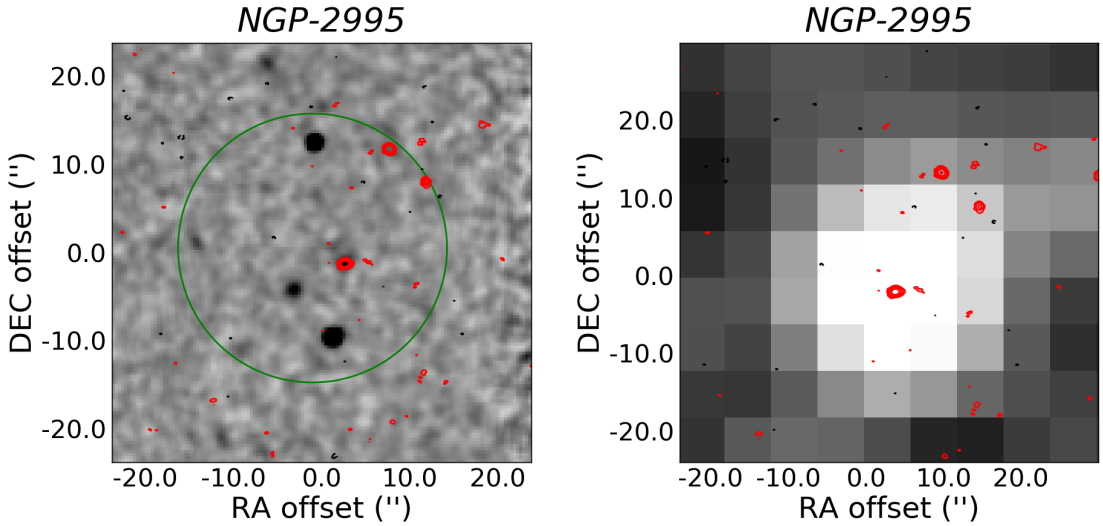

Figure 4.A.31 : Three radio sources with similar brightness are detected over the extended *Herschel*-source. These galaxies could form a galaxy group or a proto-cluster.

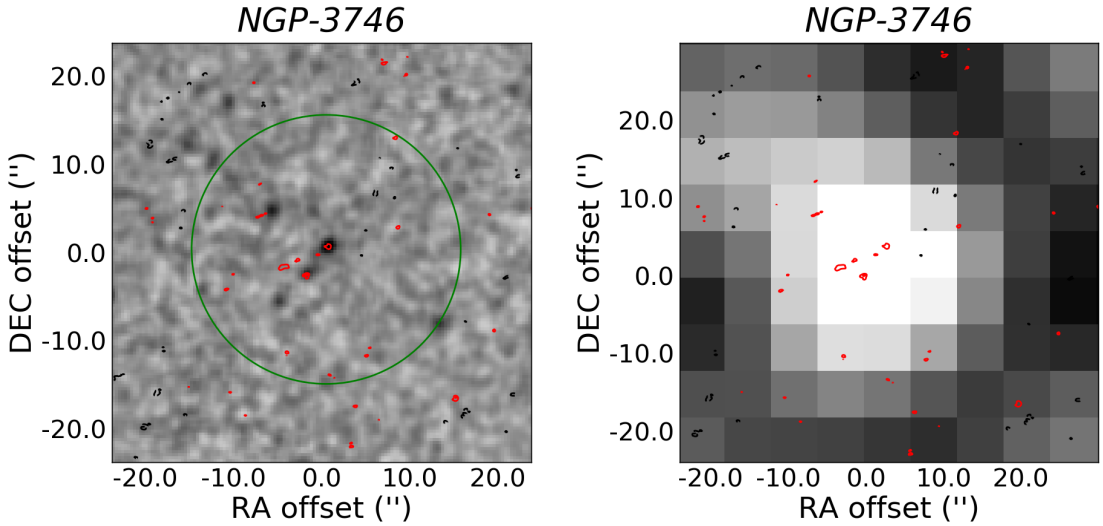

Figure 4.A.32 : Two very faint radio sources with NIR counterparts are detected in this map. Although, due to the high r.m.s. of the map we cannot be certain about the reliability of these two sources.

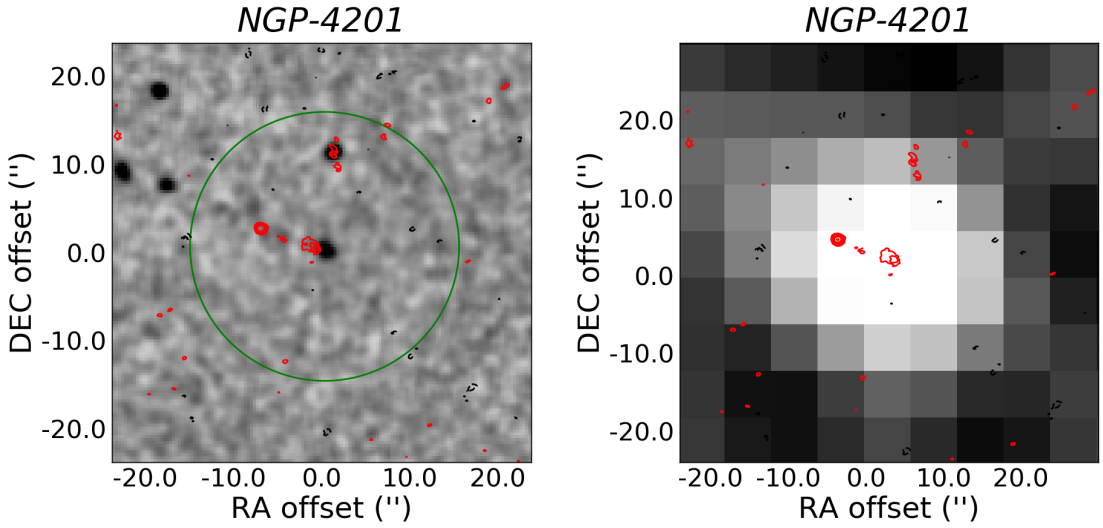

Figure 4.A.33 : Three radio sources are detected in this map. A very bright source, likely an AGN, a faint source with a NIR counterpart, and a potential lensed galaxy. This over-density could be formed for galaxies at different redshifts.

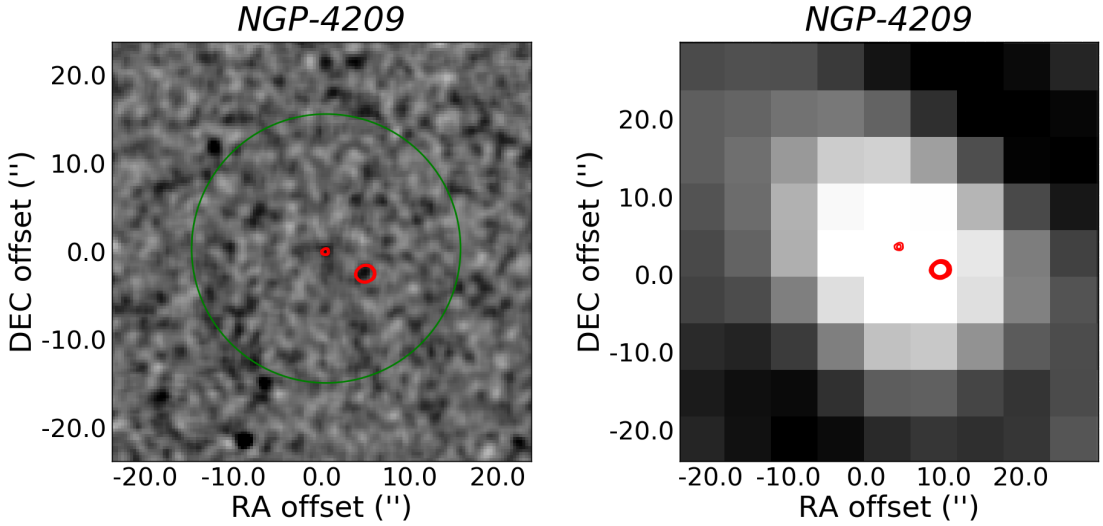

Figure 4.A.34 : Two radio sources are detected in this map. A very bright source, likely an AGN, and a faint source, both of them with NIR counterparts.

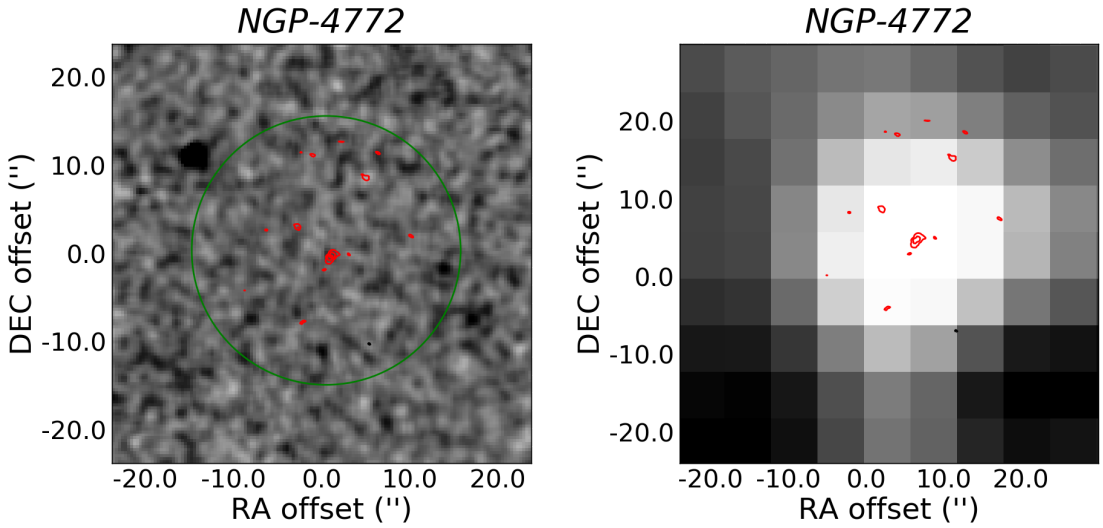

Figure 4.A.35 : Two faint radio emissions at similar brightness are detected in this map which can be two SFGs forming a galaxy group.

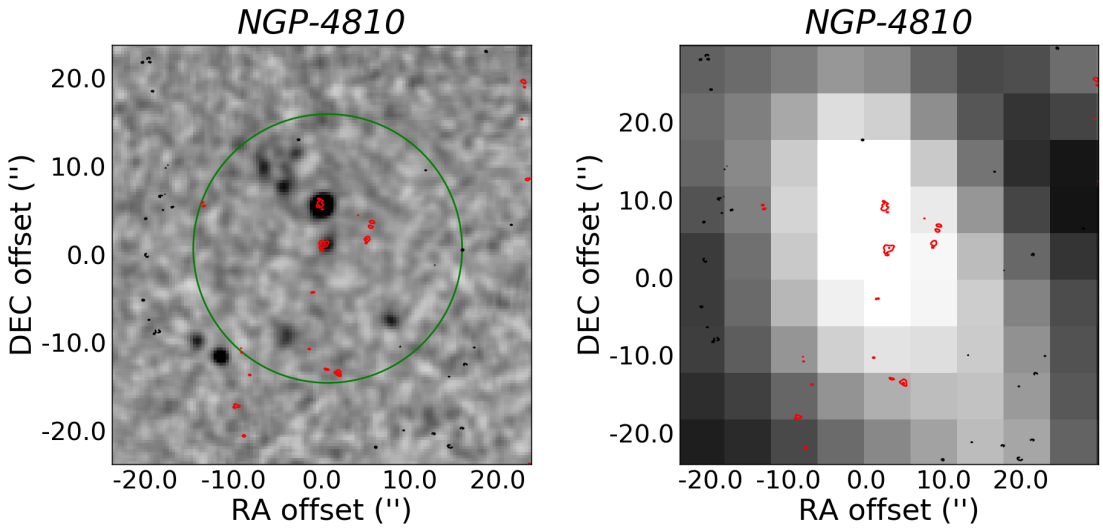

Figure 4.A.36 : Three radio sources are detected within the extended FIR emission. All of them have similar brightness so they are good candidates to be a group of galaxies or a proto-cluster.

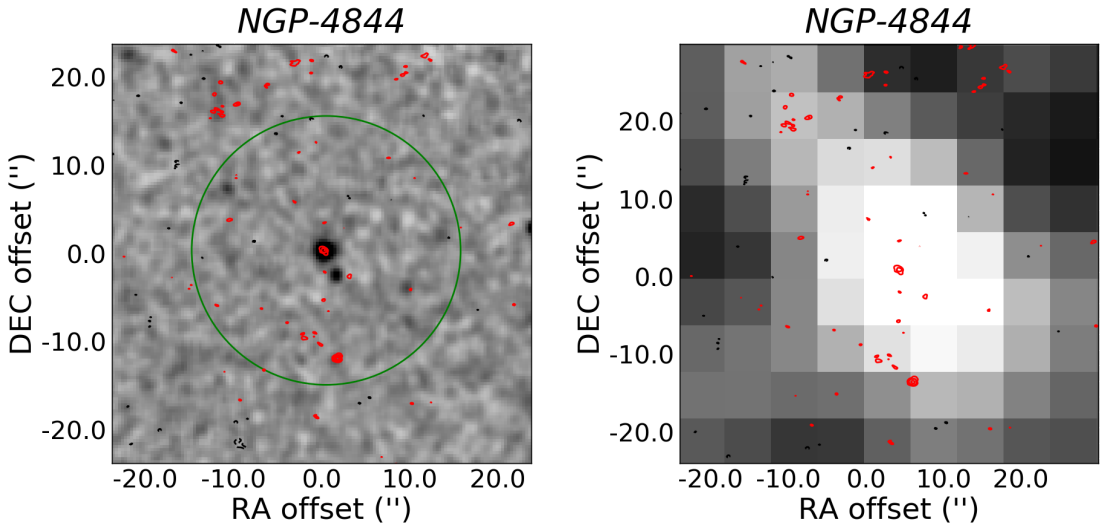

Figure 4.A.37 : Two radio sources with similar brightness are clearly detected in this noisy radio map. Located over the extended FIR emission, they can be part of a galaxy group.

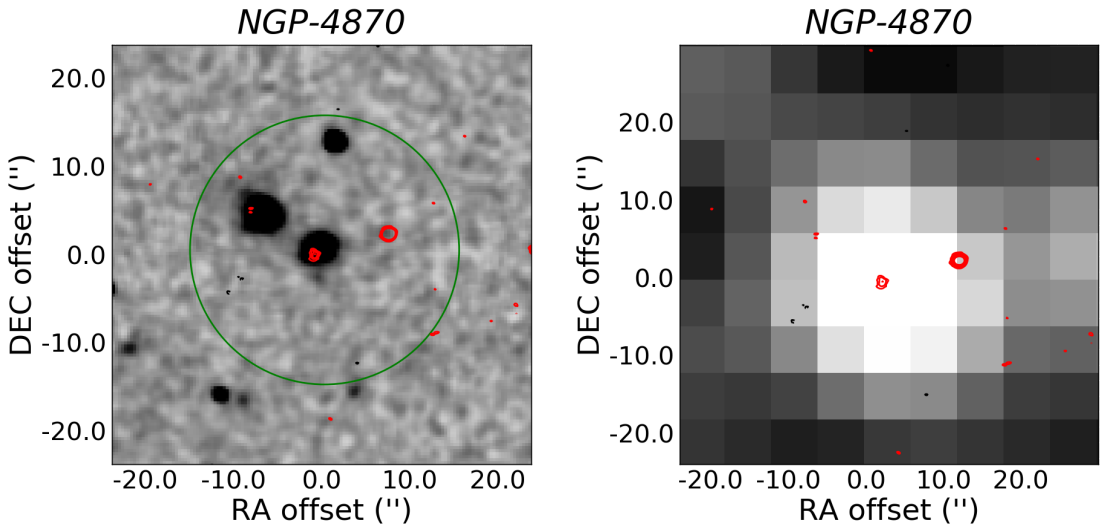

Figure 4.A.38 : A very bright radio source without NIR counterpart, probably an AGN, and a fainter radio source centred on the FIR emission, which can be lensed, are detected in this map.

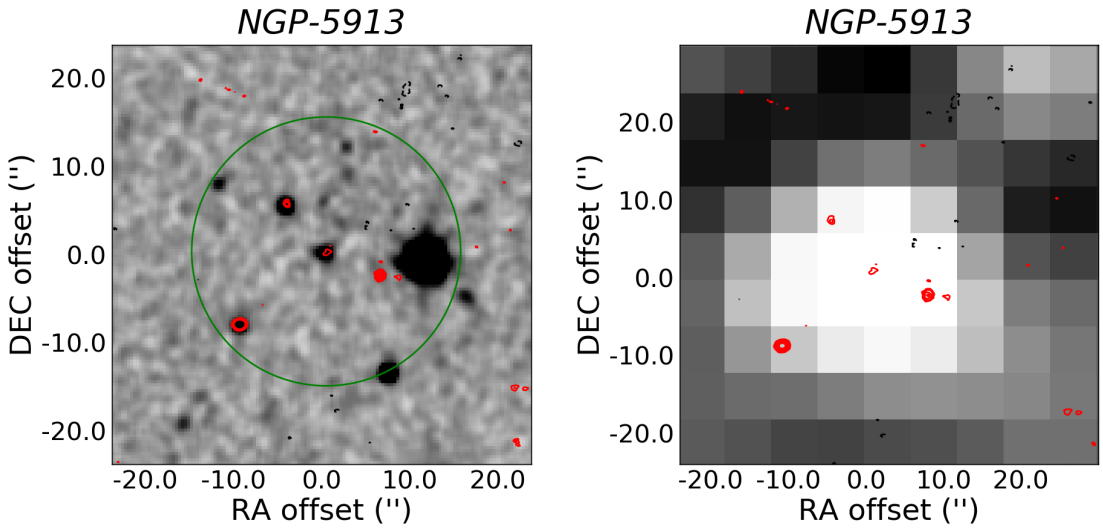

Figure 4.A.39 : Four different radio sources are detected in this map. One very bright potential AGN with a NIR counterpart, two very faint sources with NIR counterparts and a brighter source with no NIR counterpart. These galaxies could be part of the same galaxy cluster or proto-cluster.

Chapter 5

The Infrared-to-Radio Correlation in the Hubble Frontier Fields

5.1 Introduction

The tight correlation between infrared and radio emission from galaxies at all redshifts is very striking. Followed by all SFGs not dominated by AGNs, this correlation extends over 5 orders of magnitude. The most accepted theory is that young stars emitting UV radiation heat the dust which absorbs and re-emits radiation at IR wavelengths, while SNe remnants of these stars ending their lives emit cosmic-rays that in their way through magnetic fields produce synchrotron radiation at radio frequencies. It is thus not straightforward to understand why the thermal far-infrared and the non-thermal radio emission would correlate over such a wide range of galaxy types and luminosities, despite changing magnetic fields, attenuation properties, etc. (more in Section 1.5). This correlation has been very well studied in the nearby universe for cluster and isolated SFGs (e.g. Yun et al., 2001; Reddy & Yun, 2004; Andersen & Owen, 1995; Miller & Owen, 2001). An excess of radio emission was found in the correlation for rich cluster galaxies in comparison with the field galaxies, likely due to the different processes which drive the evolution in cluster galaxies, i.e. gravitational interactions and ram-pressure stripping, resulting in transforming blue SFGs into red quiescent galaxies that dominate the population of today's clusters. The proposed explanation for this excess of radio emission for the low-redshift clusters is that the ISM of galaxies in rich clusters is being compressed via ram-pressure as the galaxies move through the ICM resulting in greater radio emission. Not many studies have been done for high-redshifts clusters, where there is an increase in the number of SFGs and AGNs which can modify this correlation (Randriamampandry et al., 2015).

The Hubble Frontier Fields (HFF) program (P.I. Jennifer Lotz) consists of Hubble Space Telescope (HST) observations of six massive clusters at intermediate-redshifts ($0.33 < z < 0.55$), chosen on the basis of their gravitational lensing strength, the availability of complementary observations from ground-based telescopes such as ALMA or the VLA, and the avoidance of bright stars in their FOV. The Jansky-VLA Legacy Survey of the Frontier Fields (P.I Eric Murphy) was designed to provide some of the deepest (1 μJy/beam) radio dual-band imaging at 3 and 6 GHz (S- and C-bands respectively) over the full HST for the six clusters. Three clusters have been observed so far: MACSJ0717, MACS1149 and MACS0416 ($0.3 < z < 0.6$) at A and C configurations generating maps with resolutions 0.65 and 0.33 arcsec for the S- and C-bands respectively. In addition, a census of *Herschel*-detected sources in the HFF is presented in Rawle et al. (2016, hereafter R16), where parallel observations with PACS and SPIRE were done for the 6 clusters achieving a minimum and maximum infrared luminosity of $\log(L_{TIR}/L_{\odot}) \sim 7.66$ and ~ 12.83 respectively.

With the use of these two data sets, in this chapter we study the IRRC variation as a function of environment in these clusters at intermediate-redshifts. Two different scenarios are analysed, galaxy members and galaxies lensed by the cluster which are compared with isolated field galaxies and galaxy-galaxy lensed sources respectively. Analysing this correlation for intermediate stages of the evolution of galaxy clusters, we study how the ICM affects this correlation, both in the core and outer region of the cluster.

This chapter is divided as follows. In Section 5.2 the methodology used in this study is presented. In Section 5.3 we explain how the different samples were created from the HFF and from the literature. The calculation of the infrared and radio luminosities is explained in Section 5.4 and in Section 5.5 the analysis of the IRRC for the different samples is performed. Section 5.7 is dedicated to the caveats of this study, and finally the main conclusions are listed in Section 5.8.

5.2 Methodology

To study the IRRC for the different scenarios, we first compile several samples. Using the VLA observations in the HFF, two cluster samples were created, containing 'Galaxy-Cluster Lensed' (GCLs) sources and 'Cluster Members' galaxies (CMs). The HFF-VLA catalogue was created by Ian Heywood (*priv. comm.*, Heywood et al., 2018 in prep). The source extraction was performed with the source finder Python Blob Detection and Source Management (PyBDSM; Mohan & Rafferty, 2015). This algorithm first calculates the variation of the image noise and determines the r.m.s. close to each target. Then sources with a peak detection of 5σ and a secondary island threshold of 3σ were selected, where σ is the local value of

the r.m.s. (for more details see Section 3.2 in Heywood et al. 2016). The cross-matching between the radio and optical catalogues was done by visual examination to remove spurious detections from the VLA catalogue. The typical r.m.s. for the three maps and their restoring beam sizes were: MACSJ0416 - r.m.s. $= 0.7$ μJy/beam, 0.95×0.47 arcsec^2 (P.A. 8 deg), MACSJ0717 - r.m.s. $= 0.5$ μJy/beam, 0.68×0.58 arcsec^2 (P.A. 90 deg), and MACSJ1149 - r.m.s. $= 0.6$ μJy/beam, 0.47×0.45 arcsec^2 (P.A. 30 deg). Using SUBARU photometric redshifts ($z_{phot_{SUBARU}}$), or spectroscopic redshift when available, the lensing magnification factors were computed based in the radio position with lens models (Heywood et al., 2018 in prep). In addition, a few sources presented in Magnelli et al. (2012) were added to this GCLs sample. The other two samples, 'Galaxy-Galaxy Lensed' (GGLs) sources and 'Field Galaxies' (FGs), were created from a search in the literature and by taking the available SFGs and SLGs from Chapter 4 of this thesis.

Photometry at FIR and 1.4 GHz bands was required to derive the corresponding luminosities. The FIR data were obtained from the *Herschel* bands and used to derive the L_{TIR} from a MBB fitting with integrating flux λ $(8-1000$ μm), in the same way as in the previous chapter of this thesis (Section 4.6.1). For consistency, luminosities for the different samples were derived with the same method, comparing the accuracy of these values with those in the literature. The radio continuum data were obtained with the VLA, either available in the literature or calculated from the maps of the Faint Images of the Radio Sky at Twenty-cm survey (FIRST; Becker et al., 1995). The radio fluxes were converted into absolute radio luminosities applying the correspondent K-correction.

Once all the luminosities were calculated, the analysis of the IRRC was done for the different scenarios. First, we analysed the evolution of the IRRC for cluster galaxies at intermediate-redshifts and compared it with field galaxies. Second, we analysed if there was any difference in the IRRC for galaxies being lensed by a cluster or by other galaxy. A study of the SFR was derived from the IR and radio luminosities and the results discussed for the different samples.

5.3 Sample Selection

This section provides details on the selection of the four different samples under study: 'Cluster Members' galaxies (CMs), 'Galaxy-Cluster Lensed' sources (GCLs), 'Galaxy-Galaxy Lensed' sources (GGLs), and 'Field Galaxies' (FGs).

Cluster Members: The cluster members of the three available HFF clusters were obtained from the catalogue provided by Ian Heywood, as explained in the previous section. The line-of-sight velocity distribution of clusters are approximately Gaussian in shape, hence the vast majority of the cluster members have a velocity within $\pm 3\sigma_v$ (Girardi et al., 1993), which for

redshift range corresponds to $\Delta z \leq 0.015 \times (1+z)$ (Ramella et al., 2000). The cluster members were selected on the basis of their photometric redshift, as obtained from $z_{phot_{SUBARU}}$. The accuracy of these photometric redshifts compared with the available spectroscopic redshifts was found to have a normalised median absolute deviation of 2.7% with an outlier fraction of 9.5%. (Umetsu et al., 2014; Medezinski et al., 2013). As a result, 36 cluster members were found for MACSJ1149, 93 for MACSJ0717, and 23 for MACSJ0416, yielding a sample of 152 cluster members. To find FIR counterparts for these sources we cross-matched this data with R16, resulting in only nine CMs galaxies having FIR counterparts in *Herschel* with redshifts $0.34 < z < 0.62$ (Table 5.1).

The difference between the amount of CMs found with the VLA and with *Herschel* is due to the combination of the sensitivities and the K-correction. In Figure 5.1 (left) the fluxes at 250μm and 3 GHz for an infrared luminosity of $L_{TIR} = 10^{11.2}$ $L_{\odot}$ (typical value for the CMs in the HFF) versus redshifts are shown for different templates of SFGs. In dotted-blue lines the flux limit at 5σ for the VLA and *Herschel* in the HFF are shown. We see that a $L_{TIR} = 10^{11.2}$ $L_{\odot}$ galaxy can be detected out to redshifts of ~ 0.3 for *Herschel* and ~ 0.6 for the VLA. Given that the HFF clusters lie at $0.3 < z < 0.6$ many galaxies are detected at 3 GHz, yet only the brightest members galaxies are detected in the clusters with *Herschel*, resulting in a small sample of CMs galaxies. For comparison, Figure 5.1 (right) shows the same plot for an infrared luminosity of $L_{TIR} = 10^{13}$ $L_{\odot}$, typical value for the DSFGs studied in Chapter 2. In this case the detected redshift is slightly higher for *Herschel* ($z \sim 3.5$) than for the VLA ($z \sim 3$) due to the negative K-correction (see Section 1.3.2).

Randriamampandry et al. (2015, hereafter RAN15) presented a study of the Far-Infrared-to-Radio correlation for the massive cluster MS0451-03 ($z \sim 0.54$) with a sample of 12 members in the cluster. They derived the total infrared luminosities, L_{TIR}, only from the *SPITZER* 24μm-band which could result in these values being poorly constrained as indicated in RAN15. However, Elbaz et al. (2010; 2011) found that below $z \sim 1.5$ mid-IR extrapolations to determine L_{TIR} are correct with a dispersion of 0.15 dex. Radio luminosities were derived from the VLA observations assuming an $\alpha \sim 0.8$ ($S_{\nu} \propto \nu^{-\alpha}$). Identifying as AGNs those sources with five times greater radio fluxes than expected at that redshifts, they found three AGNs in their cluster members sample. However these sources are not specified in the paper, and therefore we identified as AGN only one source due to the clear outlier in the IRRC. No other data with similar characteristics and at similar redshifts were found in the literature, so RAN15 was used to compare with this study. Our final CMs sample consisted in 20 galaxies. More data would be desirable to get better constraints and a better understanding of this type of sources and the influence of their environment in the IRRC.

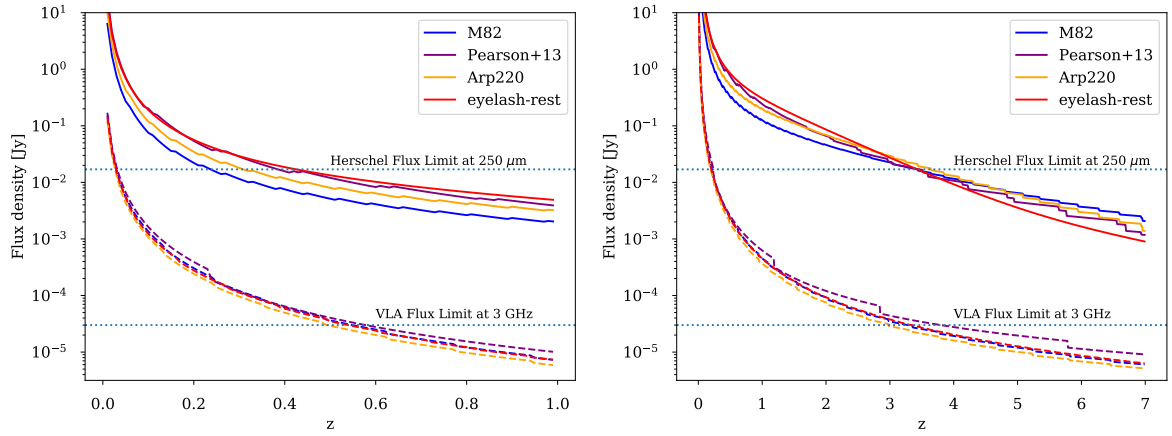

Figure 5.1 : *Left:* Representation of the fluxes at 250μm and 3 GHz vs. redshifts for an infrared luminosity of $L_{TIR} = 10^{11.2}$ $L_{\odot}$ for different templates of SFGs. The average 5σ flux limit for the three clusters in VLA and *Herschel* for the HFF is shown in dashed-blue lines. We see that for this kind of galaxy the redshift detection limit for *Herschel* is ~ 0.3, so only the brightest galaxies in the cluster will be detected at FIR. *Right:* In this case the representation is done considering an infrared luminosity of $L_{TIR} = 10^{13}$ $L_{\odot}$ typical for DSFGs. The negative K-correction allow us to detect high-redshifts galaxies at FIR frequencies.

Table 5.1 List of 'Cluster Members' galaxies in the HFF clusters with FIR counterparts in *Herschel*.

ID	S_{100} (mJy)	S_{160} (mJy)	S_{250} (mJy)	S_{350} (mJy)	S_{500} (mJy)	S3 GHz (μJy)	S6 GHz (μJy)
VLAHFF-J071722.31+375107.8	$--$	$--$	21.3 ± 5.3	14.2 ± 3.9	$--$	43.30 ± 0.82	$--$
VLAHFF-J071727.53+374441.2	13.6 ± 1.2	26.8 ± 2.4	21.4 ± 3.2	8.3 ± 3.9	$--$	42.67 ± 1.20	21.20 ± 1.84
VLAHFF-J071736.12+374309.4	5.4 ± 1.0	7.8 ± 1.7	7.1 ± 3.1	6.0 ± 3.6	$--$	5.86 ± 0.66	$--$
VLAHFF-J041610.60-240407.4	10.3 ± 1.1	9.2 ± 1.8	10.5 ± 3.1	$--$	$--$	25.04 ± 1.51	12.03 ± 1.72
VLAHFF-J114937.99+222427.7	8.2 ± 0.9	10.8 ± 1.5	$--$	$--$	$--$	15.19 ± 1.30	0.023 ± 0.002
VLAHFF-J114938.81+222531.8	3.7 ± 0.8	4.4 ± 1.0	$--$	$--$	$--$	4.55 ± 0.73	$--$
VLAHFF-J114939.46+221853.2	$--$	$--$	12.2 ± 2.8	7.1 ± 4.0	4.8 ± 2.4	60.04 ± 0.52	$--$
VLAHFF-J114943.72+222412.7	9.0 ± 1.0	10.7 ± 1.5	$--$	$--$	$--$	29.45 ± 0.96	0.020 ± 0.001
VLAHFF-J114946.11+222414.5	23.2 ± 1.9	33.5 ± 3.2	31.4 ± 3.0	14.6 ± 3.5	5.7 ± 3.6	63.28 ± 0.54	0.080 ± 0.004

Table 5.2 : List of 'Galaxy-Cluster Lensed' sources in the HFF clusters with FIR counterparts in *Herschel*.

ID	S_{100} (mJy)	S_{160} (mJy)	S_{250} (mJy)	S_{350} (mJy)	S_{500} (mJy)	S3 GHz (μJy)	S6 GHz (μJy)
VLAHFF-J071710.65+375121.8	$--$	$--$	32.4 ± 3.7	17.5 ± 5.3	9.9 ± 7.4	27.09 ± 1.15	$--$
VLAHFF-J071717.35+374830.4	$--$	$--$	10.5 ± 5.3	5.5 ± 3.4	$--$	15.63 ± 0.75	$--$
VLAHFF-J071719.48+374941.4	$--$	$--$	17.1 ± 3.5	14.5 ± 3.8	3.7 ± 3.1	14.00 ± 0.75	$--$
VLAHFF-J071722.31+375107.8	$--$	$--$	21.3 ± 5.3	14.2 ± 3.9	$--$	43.30 ± 0.82	$--$
VLAHFF-J071725.83+375018.8	$--$	$--$	14.3 ± 4.0	14.9 ± 3.7	$--$	10.72 ± 0.75	$--$
VLAHFF-J071730.40+374617.0	7.6 ± 0.9	15.4 ± 1.7	12.5 ± 3.7	$--$	$--$	12.06 ± 0.82	$--$
VLAHFF-J071730.65+374443.1	4.2 ± 2.6	15.0 ± 5.7	25.5 ± 5.1	20.1 ± 5.7	17.5 ± 14.8	5.46 ± 0.71	$--$
VLAHFF-J071734.46+374432.2	2.0 ± 0.6	11.1 ± 1.5	8.0 ± 2.9	5.9 ± 3.9	2.8 ± 2.6	17.40 ± 0.86	$--$
VLAHFF-J071735.30+374447.3	6.3 ± 1.0	6.9 ± 2.3	7.8 ± 5.0	5.9 ± 5.6	$--$	5.18 ± 0.73	$--$
VLAHFF-J071736.66+374506.5	4.3 ± 0.7	6.3 ± 2.3	$--$	$--$	$--$	16.48 ± 0.99	$--$
VLAHFF-J071740.44+374527.2	2.7 ± 1.8	7.6 ± 3.6	16.1 ± 6.2	9.4 ± 6.3	$--$	9.91 ± 0.73	$--$
VLAHFF-J041605.02-240424.2	5.0 ± 0.7	4.8 ± 0.9	$--$	$--$	$--$	6.17 ± 0.88	$--$
VLAHFF-J041606.36-240451.2	9.9 ± 1.0	12.0 ± 1.6	7.1 ± 3.1	$--$	$--$	20.70 ± 1.54	9.78 ± 1.83
VLAHFF-J041607.89-240623.4	7.4 ± 0.9	12.8 ± 1.6	11.0 ± 3.3	$--$	$--$	36.97 ± 1.30	23.10 ± 1.76
VLAHFF-J041609.12-240459.3	4.1 ± 0.7	5.4 ± 0.9	$--$	$--$	$--$	6.42 ± 0.94	7.34 ± 1.00
VLAHFF-J041610.60-240407.4	10.3 ± 1.1	9.2 ± 1.8	10.5 ± 3.1	$--$	$--$	25.04 ± 1.51	12.03 ± 1.72
VLAHFF-J041610.79-240447.5	5.1 ± 1.0	12.6 ± 2.0	9.7 ± 3.1	6.8 ± 2.6	$--$	12.12 ± 0.85	6.04 ± 0.99
VLAHFF-J041611.61-240221.6	3.8 ± 1.0	4.8 ± 1.4	$--$	$--$	$--$	9.44 ± 0.91	$--$
VLAHFF-J041614.84-240451.5	6.8 ± 0.9	4.8 ± 4.4	$--$	$--$	$--$	6.22 ± 1.63	4.83 ± 1.93
VLAHFF-J041629.52-240550.0	$--$	$--$	25.9 ± 4.3	17.3 ± 3.6	11.5 ± 4.3	8.14 ± 0.89	$--$
VLAHFF-J041629.66-240630.3	$--$	$--$	25.0 ± 4.3	10.1 ± 3.3	4.5 ± 3.3	54.81 ± 2.62	39.20 ± 6.22
VLAHFF-J041636.19-240759.7	$--$	$--$	14.0 ± 4.1	15.9 ± 3.7	5.4 ± 4.4	24.02 ± 1.09	$--$
VLAHFF-J114929.35+222407.8	10.0 ± 1.1	18.7 ± 2.2	21.5 ± 4.6	13.8 ± 2.7	6.1 ± 3.5	30.95 ± 0.90	0.030 ± 0.002
VLAHFF-J114929.81+222425.9	20.6 ± 1.8	34.1 ± 3.0	26.0 ± 3.4	15.2 ± 3.0	6.4 ± 6.0	47.27 ± 1.31	0.034 ± 0.004
VLAHFF-J114930.67+222427.6	7.0 ± 0.9	16.4 ± 1.8	32.3 ± 3.2	30.3 ± 3.2	21.4 ± 2.8	13.59 ± 0.96	$--$
VLAHFF-J114932.03+222439.3	2.4 ± 0.6	9.3 ± 1.4	14.9 ± 3.1	7.4 ± 1.3	$--$	24.08 ± 0.92	0.012 ± 0.003
VLAHFF-J114934.42+222445.3	7.7 ± 1.0	18.4 ± 1.9	23.7 ± 3.7	14.2 ± 3.0	6.1 ± 3.9	18.34 ± 1.32	0.010 ± 0.001
VLAHFF-J114936.09+222424.4	3.7 ± 0.7	7.9 ± 1.5	5.9 ± 2.5	$--$	$--$	14.84 ± 1.10	$--$
VLAHFF-J114936.98+222542.0	3.0 ± 0.7	4.4 ± 1.3	4.9 ± 2.4	$--$	$--$	20.89 ± 0.87	0.016 ± 0.001
VLAHFF-J114940.57+222415.5	6.3 ± 0.8	10.1 ± 2.0	13.8 ± 3.2	11.5 ± 3.1	5.7 ± 3.6	8.12 ± 0.71	0.013 ± 0.002
VLAHFF-J114940.87+222307.3	4.2 ± 1.2	5.2 ± 1.1	$--$	$--$	$--$	6.99 ± 0.74	$--$
VLAHFF-J114944.33+222408.6	4.2 ± 0.7	8.3 ± 1.9	16.1 ± 2.6	9.2 ± 3.3	4.4 ± 3.7	7.55 ± 0.71	$--$

Galaxy-Cluster Lensed: In order to build a sample of lensed galaxies in the HFF all galaxies with an associated magnification factor $\mu > 1$ in the HFF-VLA catalogue were selected. This resulted in 702 sources of which 32 were found to have FIR counterparts when cross-matched with R16 with redshifts $0.18 < z < 1.63$ (Table 5.2). In addition, we added 5 well studied GCLs sources gathered in Magnelli et al. (2012) from several studies in the literature (e.g. Ivison et al., 2000; Weiß et al., 2009a; Valiante et al., 2007). These galaxies are located in three different clusters (A370, A1835, CL0024) with a range of redshifts $1.06 < z < 2.93$ (Table 5.3).

Field Galaxies: To create the FGs sample we used data from Jarvis et al. (2010, hereafter JAR10, *priv. comm.*) where the IRRC at $z < 0.5$ is studied. This sample was created from the SDP of H-ATLAS finding 2,334 sources at $z < 0.5$, from which radio counterpart were detected for 104 sources. The infrared luminosities were derived from *Herschel* via SED templates from Siebenmorgen & Krügel (2007), and the radio luminosities from NVSS ($z < 0.2$) and FIRST

Table 5.3 : List of 'Galaxy-Cluster Lensed' sources in Magnelli et al. (2012).

Cluster	ID	S_{100} (mJy)	S_{160} (mJy)	S_{250} (mJy)	S_{350} (mJy)	S_{500} (mJy)	$S_{1.4GHz}$ (μJy)
A1835	SMMJ14009+0252	4.90 ± 0.7	27.7 ± 1.9	66.4 ± 6.0	65.8 ± 3.8	53.7 ± 4.2	0.529 ± 0.030
A1835	SMMJ14011+0252	11.6 ± 0.8	33.5 ± 1.4	61.7 ± 6.0	63.1 ± 3.8	48.5 ± 4.0	0.115 ± 0.030
A370	SMMJ02399-0134	45.8 ± 0.8	111.1 ± 1.9	125.8 ± 6.1	89.8 ± 3.9	41.7 ± 4.4	0.500 ± 0.010
A370	SMMJ02399-0136	13.0 ± 0.8	30.1 ± 1.8	65.7 ± 6.1	72.0 ± 3.9	62.8 ± 4.6	0.526 ± 0.010
CL0024	SMMJ00266+1708	4.79 ± 0.7	24.5 ± 2.2	52.8 ± 7.2	61.3 ± 4.5	44.6 ± 4.7	0.094 ± 0.015

($z > 0.2$)[1]. Contamination from AGNs at these redshifts begins to dominate at $L_{1.4GHz} > 10^{23}$ W Hz^{-1} (Mauch & Sadler, 2007). Because we wanted to avoid this contamination as much as possible we did not consider sources brighter than this limit, resulting thus in a sample of 55 sources. In RAN15 27 FGs at $0.22 < z < 0.90$ were available of which eleven were classified as AGNs. Studying the clear outliers in the IRRC, we could only identified five AGNs which were excluded from the final sample, resulting in 22 FGs (though with some likely contamination from AGNs). In addition, 50 SFGs from TLS with photometric redshifts $1.5 < z < 2.5$ (Table 4.1) were added. This makes a total FGs sample of 127 sources.

Galaxy-Galaxy Lensed: In order to compare galaxies being lensed by a cluster or by other galaxy, a sample of GGLs sources was created. A search in the literature was done looking for lensed sources with FIR and 1.4 GHz data available, as well as magnification factors and redshifts. Four papers (listed below) were found with FIR *Herschel* data as well as magnification factors and redshifts. However, radio fluxes were not always available in these papers, so new measurements were done for those. The cut-outs for these sources were downloaded from the VLA FIRST survey[2] and the fluxes measured with the task `IMFIT` in CASA[3].

- Negrello et al. (2017): A sample of 18 SLGs was studied in this work. They were selected by their high fluxes at the SPIRE band ($S_{500} > 100$ mJy) from the H-ATLAS survey. Spectroscopic or photometric redshifts were available as well as magnification factors obtained from lens models. Radio luminosities were not available for these sources, so $S_{1.4GHz}$ fluxes were obtained from the FIRST survey. Eight sources out of eighteen were found to have radio counterparts at 1.4 GHz and were therefore included in our sample.

- Conley et al. (2011): The source HerMESJ105751.1+573027 was studied in detail in this paper. This source is a multiply lensed DSFG which was FIR-selected ($S_{250} > 400$ mJy) in the *Herschel* SDP from HerMES. Spectroscopic redshift, derived magnification factor and radio continuum flux at 20 cm were available.

[1]The NVSS was carried out in the VLA D-configuration with a beam of 45 arcsec, larger than the *Herschel* beam so little flux is expected to be missing. For FIRST the beam equates to a galaxy size of $\gtrsim 16$ kpc.

[2]https://third.ucllnl.org/cgi-bin/firstcutout

[3]The synthesised beam for the FIRST maps was 6.40×5.40 arcsec^2 or 5.40×5.40 arcsec^2.

- Wardlow et al. (2013): A list of 13 FIR-selected sources ($S_{500} > 100$ mJy) candidates of lensed DSFGs from HerMES were presented in this work. Only three of them have spectroscopic redshifts, magnification factors as well as $S_{1.4GHz}$ fluxes available. Applying the same criteria to identify AGNs as in Section 4.5.1 one source out of three was found to have an excess of radio emission compared with its estimated flux. Therefore two galaxies were added to the sample from this work.

- Dye et al. (2017): Identified as lensed in other studies (H-ATLAS and HeLMS[4]), 6 SLGs were studied in this work. Spectroscopic redshifts were available from follow-up observations, and magnification factors from lens models. Radio fluxes were obtained from the FIRST survey, yielding 3 sources with radio counterpart at this band.

In all, these 14 galaxies ($1.026 < z < 3.675$) from the literature together form part of the GGLs sample (Table 5.4). In addition, the 8 SLGs from TLS were added to this sample. Despite the fact that the redshifts for TLS were photometric (i.e. not very accurate) and no magnification factors were known at the time of this work, these sources were added to the final sample. However, it is important to remark that to be consistent with the other samples, all the plots in terms of luminosities should be corrected from μ for the SLGs of TLS. Our final sample of GGLs sources consists of 22 galaxies.

Summarising, the final samples consist of 20 CMs, 127 FGs, 37 GCLs and 22 GGLs, covering a wide range of redshifts ($0.011 < z < 3.675$).

[4]The largest field in HerMES.

Table 5.4 : List of 'Galaxy-Galaxy Lensed' sources created from literature. Note that in addition the SLGs from TLS were added to this sample.

Paper	ID	S_{100} (mJy)	S_{160} (mJy)	S_{250} (mJy)	S_{350} (mJy)	S_{500} (mJy)	S1.4 GHz (μJy)
Negrello et al. (2017)[a]	HATLASJ090302.9-014127	–	–	354.1 ± 7.2	338.8 ± 8.1	220.0 ± 8.6	0.546 ± 0.203
	HATLASJ091043.0-000322	–	–	420.8 ± 6.5	370.5 ± 7.4	221.4 ± 7.8	0.758 ± 0.244
	HATLASJ133649.9+291800	–	–	294.1 ± 6.7	286.0 ± 7.6	194.1 ± 8.2	0.484 ± 0.120
	HATLASJ085358.9+015537	–	–	396.4 ± 7.6	367.9 ± 8.2	228.2 ± 8.9	0.622 ± 0.128
	HATLASJ090311.6+003907	–	–	133.2 ± 7.4	186.1 ± 8.2	165.2 ± 8.8	0.479 ± 0.143
	HATLASJ125135.3+261457	–	–	157.9 ± 7.5	202.3 ± 8.2	206.8 ± 8.5	0.887 ± 0.180
	HATLASJ090740.0-004200	–	–	477.6 ± 7.3	327.9 ± 8.2	170.6 ± 8.5	0.822 ± 0.108
	HATLASJ134429.4+303034	–	–	462.0 ± 7.4	465.7 ± 8.6	343.3 ± 8.7	1.120 ± 0.280
Conley et al. (2011)	Hermes:J10575.1+573027	–	–	425.0 ± 10.0	340.0 ± 10.0	233.0 ± 11.0	1.800 ± 0.700
Wardlow et al. (2013)	Hbootes01	–	–	158.0 ± 6.0	191.0 ± 7.0	160.0 ± 33.0	0.26 ± 0.040
	HXMM02	–	–	92.0 ± 7.0	122.0 ± 8.0	113.0 ± 7.0	1.200 ± 0.500
Dye et al. (2017)[a]	H-ATLASJ142935.3-002836	911.0 ± 29.0	1254.0 ± 34.0	802.0 ± 7.0	438.0 ± 7.0	200.0 ± 7.0	1.410 ± 0.180
	HELMSJ001615.7+032435	23.0 ± 11.0	92.0 ± 24.0	195.0 ± 6.0	221.0 ± 6.0	149.0 ± 7.0	1.420 ± 0.160
	HELMSJ004714.2+032454	82.0 ± 11.0	164.0 ± 22.0	312.0 ± 6.0	244.0 ± 7.0	168.0 ± 8.0	0.490 ± 0.163

[a] Sources for which we performed our own photometry from the FIRST maps.

5.4 Infrared and Radio continuum Luminosities

5.4.1 Infrared Luminosity

Total infrared luminosities, L_{TIR}, were derived from the *Herschel*-FIR maps using all available bands, i.e. 2 to 5 bands, depending on the source. A MBB with one- or two-temperature components was used with an emissivity index of $\beta = 2.0$. The total flux was calculated by integrating the SED over $\lambda(8 - 1000\ \mu\mathrm{m})$. The number of components needed to sample properly the dust of the galaxy was determined by the number of FIR-bands available. That is, when a source had detections in 4 or 5 bands, a two-components MBB fit resulted in a better constraint on the dust SED (e.g. Figure 5.2). In reality, dust in galaxies has a range of temperatures, yet can be described successfully using two components (see Section 1.2.2). However, when only 2 detections were available a single component was used instead, as not enough information was available in this case to sample both the warm and cold dust. In this situation large systematic biases and uncertainties can be introduced by a MBB component that is not sufficiently constrained by the photometry. Special care was taken when analysing the results of these sources with only 2 available bands. When 3 bands were available the best fitting model was found on a case-by-case basis. For instance, Figure 5.3 (top) shows the fits for one- (left) or two- (right) components when three SPIRE bands are available. We see that the two-components model likely overestimates the contribution from the warm dust quite significantly where there are no actual detections in the PACS bands. Since the peak of the warm dust was not sampled by any of the photometry, we deemed this fit unreliable and instead used the single-component MBB. However, in Figure 5.3 (bottom) with the same number of bands using one- (left) or two- (right) components did not change our final results significantly. Here the peak of the both MBB components was constrained by the photometry. In this specific case, the two-components model was selected as in general a two-contribution model is better justified physically. Therefore, the SED fits were inspected visually for each source and the best fit was selected for each individual case. To estimate the uncertainties, a bootstrapping method of 25 iterations taking the flux errors into account was used. Only 25 iterations were used due to the already expensive computational process involved. However, a run with 100 iterations was done for the GGLs sample, for both one- and two-components MBB. We found a mean difference in the uncertainties of 14% with a standard deviation of 6.9% when a single-component MBB was used. The difference between uncertainties was found to be much smaller when two-components MBB were used, $\sim 2\%$ with a standard deviation of 1%. In this case, this shows that with just 25 iterations, the uncertainties have already converged to their best-estimate value. More about the MBB fitting can be found in Section 4.6.1. Finally, a

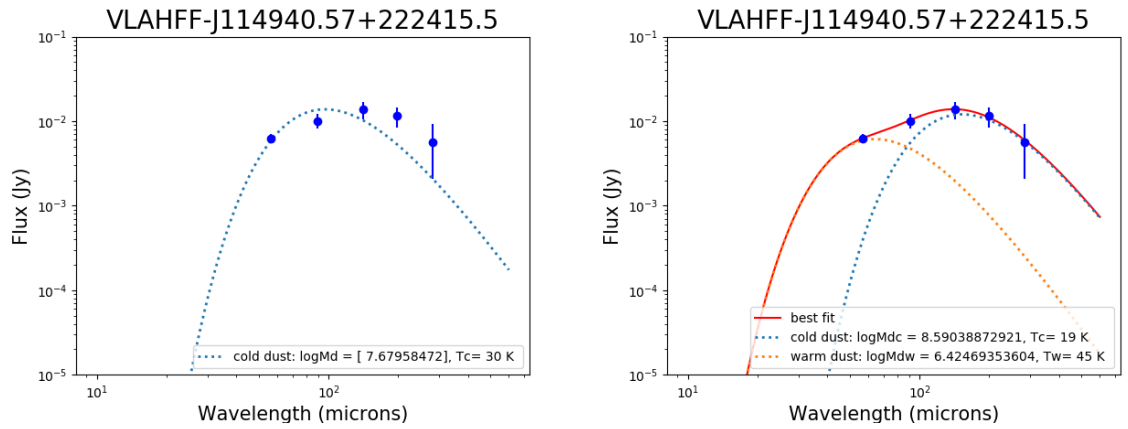

Figure 5.2 : From left to right, SED fitting for one- and two-components temperature respectively when 5 bands are available for the target. A better constrain of the dust is achieved with two-components MBB for cases where 4 or 5 bands are available.

comparison between our calculated luminosities and those in the literature was done, which we describe next[5].

First, we compared R16 with our measured fluxes for all sources in the HFF, i.e. CMs and GCLs galaxies. L_{TIR} in R16 were derived from the best-fitting Rieke et al. (2009) template integrating the SED from $\lambda\,(8-1000\ \mu\mathrm{m})$[6]. The uncertainties were calculated with a bootstrap method via 1,000 Monte Carlo simulations based on the estimated error in flux, redshift and template-to-template variation. The redshifts in R16 are photometric ($z_{photo_{FIR}}$) for all sources and therefore different in some cases to the available $z_{photo_{subaru}}$. To consistently compare our L_{TIR} with those in R16, the $z_{photo_{FIR}}$ calculated in R16 were used together with our method to obtain the corresponding luminosities. The comparison between both methods can be found in Figure 5.4 (left), where a reasonable good match can be seen.

A similar comparison was carried out for the GGLs sample. Photometry for 3 or 5 bands was available in the literature for the different galaxies using one- or two-components MBB model respectively to obtain the infrared luminosities. To do a fair estimation of how accurate our measurements were compared to those in the literature, the different dust characteristics used in the various papers had to be considered. In Table 5.5 these characteristics as well as the cosmological constants are displayed to show the difficulty of comparing different works in the literature. With this in mind we analysed the accuracy of our measurements. In Figure 5.4 (right) we see that, in general, our L_{TIR} are below the line denoting a one to one correspondence. This is likely due to the different emissivity indices used in the different studies. We see that Dye et al. (2017) in blue, who used a value of $\beta = 2$, shows a better match to our luminosities

[5] Negrello et al. (2017) did not show the numerical values for L_{TIR} so no comparison was possible in this case.
[6] These SEDs are based on eleven local LIRGs and ULIRGs.

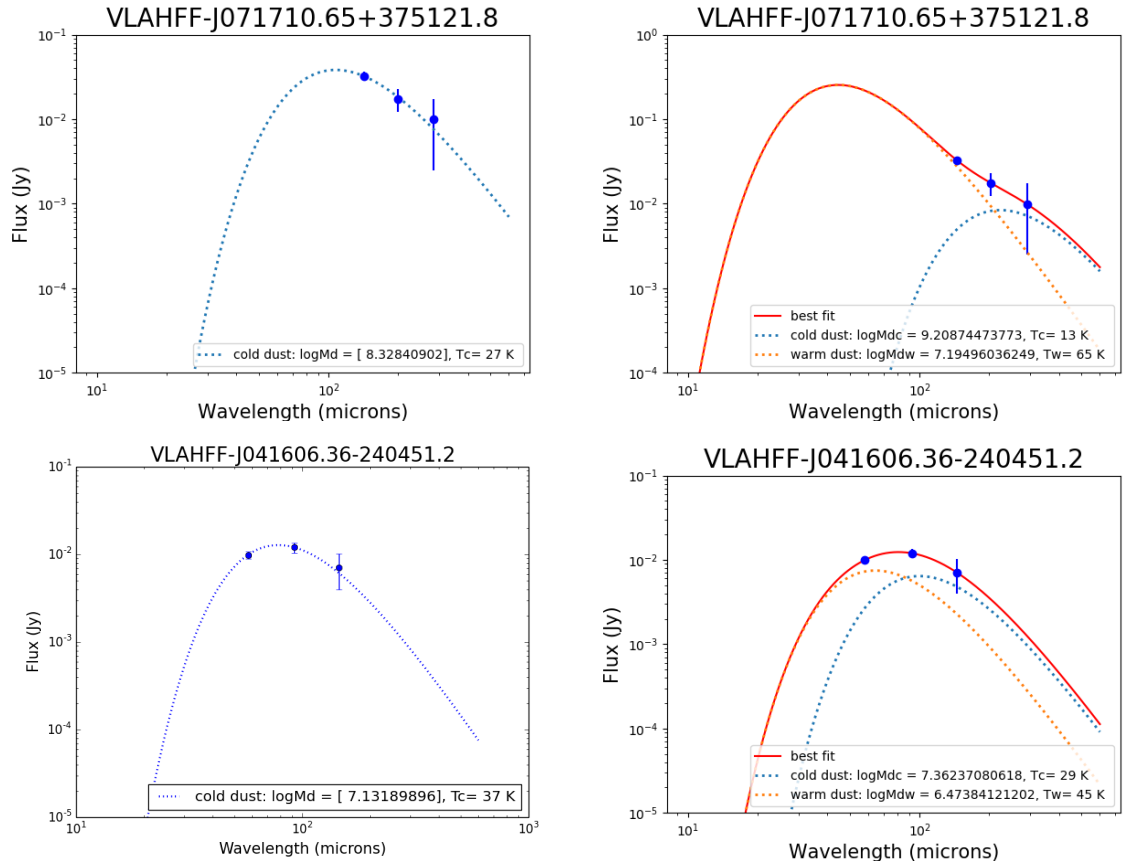

Figure 5.3 : From left to right, MBB fitting with one- or two- components MBB respectively when 3 bands were available. *Top:* We can see at the right that the two-components fitting overestimate the contribution coming from the warm dust, where there are no detections for the PACS bands. *Bottom:* In this case, we see that similar results are obtained for one- or two-components for the 3 SPIRE-bands. Therefore the best fit for each individual case was selected after visual inspection for each source.

($\sim 4.4\%$ difference) than those from Magnelli et al. (2012) in light green ($\sim 26\%$ difference), who used $\beta = 1.5$ and derived the total infra-red luminosity from $L_{FIR}[40-120\ \mu m]$ instead of $\lambda(8-1000\ \mu m)$.

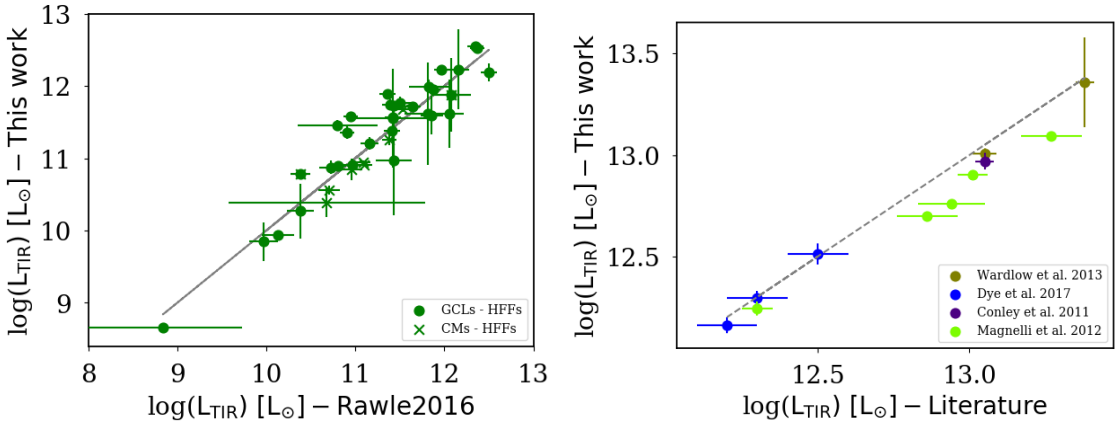

Figure 5.4 : *Left:* Comparison between the L_{TIR} calculated with our model and those obtained by R16 for the HFF. Both measurements are in good agreement. *Right:* Comparison between the L_{TIR} calculated with our model and those obtained from the literature. A good agreement between them is shown, but with the systematically lower luminosity for most of the sources probably due to different values for the emissivity index (see Table 5.5 for details).

Table 5.5 : Differences in the derived infrared luminosity, emissivity index and cosmological parameters for the papers in the literature and this work.

Paper	Luminosity	β	H_0 [km s^{-1} Mpc^{-1}]	Ω_m	Ω_Λ
Negrello et al. (2017)	$\lambda(8-1000\ \mu m)$	1.5	$H_0 = 67.7$	$\Omega_m = 0.308$	$\Omega_\Lambda = 0.69$
Wardlow et al. (2013)	$\lambda(8-1000\ \mu m)$	1.5	$H_0 = 71$	$\Omega_m = 0.27$	$\Omega_\Lambda = 0.73$
Conley et al. (2011)	$\lambda(8-1000\ \mu m)$	1.6	$H_0 = 70$	$\Omega_m = 0.27$	$\Omega_\Lambda = 0.73$
Magnelli et al. (2012)	$L_{FIR}[40-120\mu m]$	1.5	$H_0 = 71$	$\Omega_m = 0.27$	$\Omega_\Lambda = 0.73$
Dye et al. (2017)	$\lambda(3-1100\ \mu m)$	2	$H_0 = 67$	$\Omega_m = 0.32$	$\Omega_\Lambda = 0.68$
Rawle et al. (2016)	$\lambda(8-1000\ \mu m)$	2	$H_0 = 70$	$\Omega_m = 0.30$	$\Omega_\Lambda = 0.70$
This work	$\lambda(8-1000\ \mu m)$	2	$H_0 = 70$	$\Omega_m = 0.30$	$\Omega_\Lambda = 0.70$

5.4.2 Radio Luminosity

To calculate the radio luminosities the following expression was used for the HFF, where the spectral indices were calculated from the two observed VLA-bands at 6 and 3 GHz:

$$L_{1.4GHz} = \frac{4\pi D_L^2}{(1+z)^{(1-\alpha)}} \left(\frac{1.4}{3}\right)^{-\alpha} S_{3GHz} \tag{5.1}$$

where D_L is the luminosity distance in meters, $(1+z)^{(\alpha+1)}$ is related with the K-correction and α is the spectral index defined as:

$$\alpha = -\frac{\log(S_{6GHz}/S_{3GHz})}{\log(\nu_{6GHz}/\nu_{3GHz})} \tag{5.2}$$

The statistical errors for $L_{1.4GHz}$ were obtained via bootstrapping with 1,000 iterations considering the error fluxes of the C- and S- bands. The range of measured spectral indices varied between $\alpha \sim [-0.8, +1.24]$. As mentioned before, the FOV of the 3 GHz map is bigger than the 6 GHz map and therefore some observed sources in the S-band did not have an observed C-band counterpart. For those sources where there was no detection in one of the bands either because the source was not detected or because it was outside the primary beam, a typical value for SFGs of $\alpha = 0.7$ was used (Condon, 1992). In this case the uncertainties were derived from the available flux errors and an assumed uncertainty in α of a Gaussian distribution with a standard deviation of 0.3 (Delhaize et al., 2017).

For those sources taken from the literature the available fluxes were at 1.4 GHz. Therefore the radio luminosities were calculated with the following equation considering $\alpha = 0.7$:

$$L_{1.4GHz} = \frac{4\pi D_L^2}{(1+z)^{(1-\alpha)}} S_{1.4GHz} \tag{5.3}$$

The error in the $S_{1.4GHz}$ flux and a Gaussian distribution of α with a standard deviation of 0.3 were considered in the bootstrap calculation of the uncertainties using 1,000 iterations. RAN15 and JAR10 derived their luminosities with an $\alpha = 0.8$. For consistency, we scaled these luminosities to $\alpha = 0.7$ maintaining the same relative errors.

The final IR and radio luminosities for the whole sample of galaxies were corrected for magnification factor and are shown in Table 5.10.

5.5 The Infrared-to-Radio Correlation

5.5.1 IRRC for the complete sample

Before studying the differences in the IRRC for the two different scenarios, all our samples were merged and plotted together in order to compare our results with those from D17. In Figure 5.5 the IRRC is shown for all our samples combined, with the D17 correlation overplotted in dashed-red ($\log(L_{TIR}) = 0.812 \times \log(L_{1.4GHz}) - 7.12$). Our correlation in dashed-cyan, $\log(L_{TIR}) = 0.99 \times \log(L_{1.4GHz}) - 11.35$ with a dispersion of 0.36 dex, indicates good agreement between both correlations. We can see that all samples follow the trend from D17, but RAN15 and

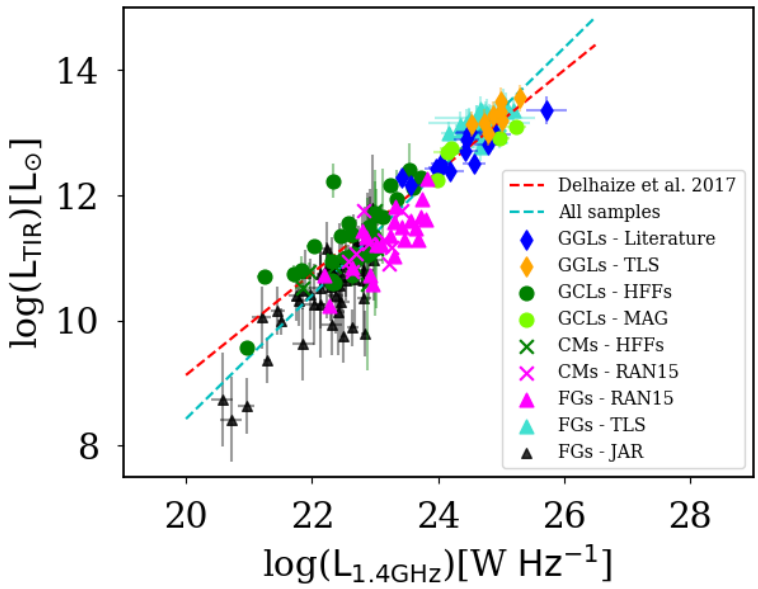

Figure 5.5 : IRRC for all the samples used in this work.The dashed-red line is the correlation from D17 and the dashed-cyan line the correlation from all our samples. A good agreement between both correlations is found.

JAR10 which are systematically below. This is due to the flux limit of the different samples. The $L_{1.4GHz}$ and L_{TIR} as a function of redshift are shown for the different samples in Figure 5.6 top and bottom respectively. In the top figure we have added the flux limit as dashed lines for the different samples. We can see how JAR10 (dashed-black) with a typical r.m.s. of 0.45 mJy for the NVSS maps and RAN15 (dashed-magenta) with a flux limit of 0.36 mJy are less sensitive than D17 (dashed-red) with a value of 0.01 mJy. Therefore these two samples have radio-flux limit which locates these sources systematically below the correlation from D17. In addition, note that the FIR selection-bias in TLS results in brighter L_{TIR} for this sample as explained in Section 4.6.3.

Figure 5.7 shows the evolution of q_{TIR} with z, which is found to be in agreement with previous results in the literature (e.g. D17, Sargent et al., 2010; Magnelli et al., 2015). Again, the dashed-red line is defined in D17 as $q_{TIR} = (2.88 \pm 0.03)(1+z)^{(-0.19\pm0.01)}$ with $\alpha = 0.7$. This is well followed by all our samples but RAN15 and JAR10 which present lower IR/radio ratios due to the selection-bias of these two samples. JAR10 performed a stacking analysis with those sources not detected at 5σ at radio wavelengths to obtain statistical detections. Slightly higher values of q_{TIR} were found when stacking, which makes these results more consistent with our study.

In Figure 5.8 the IR/radio ratios versus luminosities are plotted. We see that for q_{TIR} vs. $\log(L_{TIR})$ no clear correlation is obtained, while for q_{TIR} vs. $\log(L_{1.4GHz})$ we can see a clear

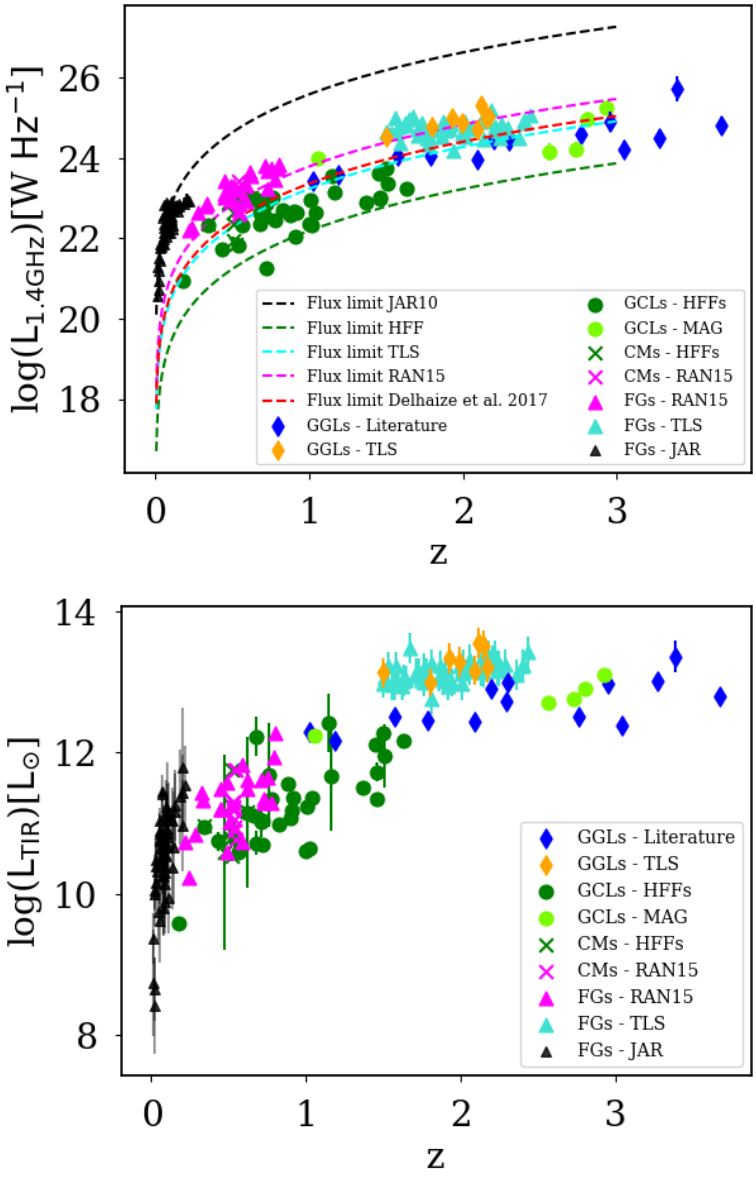

Figure 5.6 : From top to bottom we can see the logarithmic scales of $L_{1.4GHz}$ and L_{TIR} versus redshift for all the galaxies in this work. Both luminosities increase with z as an effect of the selection-bias. Note that the TLS is not corrected for magnification. The dashed lines in the top graph represent the flux limit for the different samples.

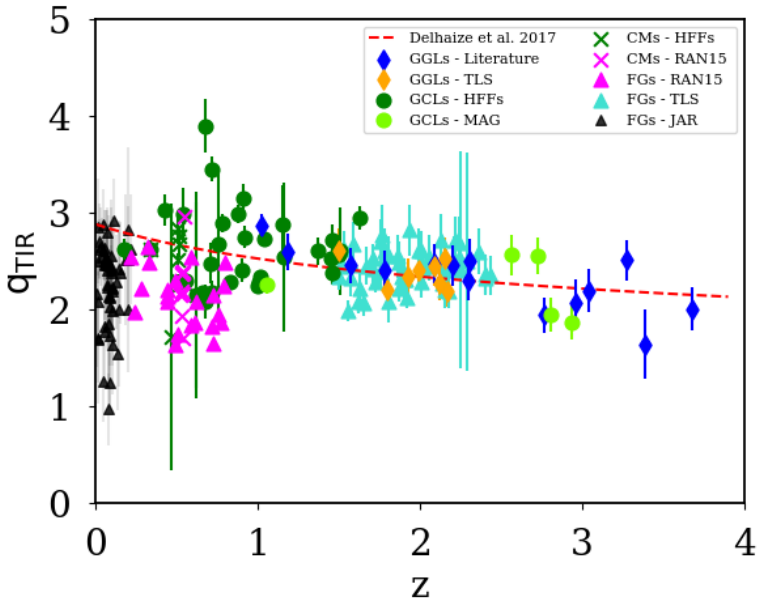

Figure 5.7 : In this plot the evolution of q_{TIR} with redshift is shown for all the samples. The dashed-red line is the correlation form D17 which we see is nicely followed by our samples of galaxies but RAN15 and JAR10 which present lower IR/radio ratios due to selection-bias towards bright radio sources.

anticorrelation for the individual samples (and for the combined sample if RAN15 and JAR10 are not considered). Due to the dependency of the q_{TIR} factor on both luminosities, these plots can be affected by their uncertainties, resulting in a change of the apparent slope of the D17 correlation. To show that the trends in the observed datasets can be a consequence of these random uncertainties we used simple Monte Carlo (MC) simulations. Assuming the null hypothesis that the data follows the D17 correlation, we generated random data and added random scatter for a given fixed error. We took the median error from the different samples and divided them into two groups following these values. This method allowed us to determine how the slope of D17[7] changes with the uncertainties for both luminosities. Figure 5.8 (top) shows how the slope of D17 changes when plotting q_{TIR} versus $\log(L_{TIR})$ (the intercept of the simulated lines was chosen manually to fit the relevant samples). The solid-red line represent D17, the dashed-red line the MC simulations with an uncertainty of 0.5 dex (typical error for JAR10), and the dotted-red line the MC simulation with a typical error of 0.08 dex (similar value than the median error for the rest of the samples). In this plot we see that JAR10 (black triangles) seems to have a positive correlation, consistent with the MC simulations for the big errors (dashed-red line). The rest of the samples seem not to have any correlation which is

[7]The slope of D17 for these plots is defined by $q_{TIR} = -0.188 \times \log(L_{TIR}) + 4.950$ and $q_{TIR} = -0.231 \times \log(L_{1.4GHz}) + 8.192$ and they are equivalent to the slope in Figure 5.5.

consistent with the MC simulations for the smaller error (dotted-red line). Doing the same study for the radio luminosities we obtained similar results as shown in Figure 5.8 (bottom) though contrary to above, the slope now is more negative as a result of the uncertainties. With errors of 0.06 dex, typical for each of the samples but those obtain in the literature (blue and light-green dots), we obtain a similar correlation (dashed-red) as for D17 (solid-red line). For bigger uncertainties of 0.2 dex (such as those for data obtained in the literature) the correlation seems to be much stronger as predicted for the MC simulations (dotted-red line). In summary, in spite of the different samples seeming to follow different correlation in the q_{TIR} vs. $L_{1.4GHz}$ compared to the q_{TIR} vs. L_{TIR} plots, they are all consistent with the anti-correlation given by the D17 line. Bright galaxies thus have lower q_{TIR} in general, which could be result of the different conditions in massive galaxies (e.g. larger magnetic fields, different attenuation properties or larger contributions from AGNs).

5.5.2 IRRC for the Cluster-Members galaxies

Previous results of nearby galaxies showed an excess of radio emission for the cluster galaxies compared with field galaxies likely due to the cluster environment, as mentioned in Section 1.5.2. In this section, we study the same scenario for intermediate-redshift galaxy clusters ($0.34 < z < 0.62$) and compare those with field galaxies ($z < 2.5$). The IRRC for our sample of CMs and isolated FGs is shown in Figure 5.9. As in previous figures, the dashed-red line corresponds to D17, plotted here as reference. We can see that all the different samples are consistent with their selection criteria, i.e. RAN15 and JAR10 below the trend while TLS is above it. The dashed-green line represents the correlation for the CMs galaxies ($\log(L_{TIR}) = 0.53 \times \log(L_{1.4GHz}) - 1.00$ with 0.27 dex dispersion). An excess of radio emission is found in this plot, although the large uncertainties make our correlation almost consistent with D17 within the errors, as shown in a green-shaded region in the plot. A mean value of $q_{TIR} = 2.33 \pm 0.18$ for the CMs at $0.34 < z < 0.62$ was found. For the isolated FGs different studies have found ratios of $2.40 < q_{TIR} < 2.66$ at $0 < z < 5$ (e.g. JAR10, Ivison et al., 2010; Sargent et al., 2010; Murphy, 2009; Bourne et al., 2011). At the redshifts of the clusters, the results from D17 suggest a $q_{TIR} = 2.63 - 2.73$. It is important to note that as highlighted in Section 5.5.1, selection effects (flux density limits) can have a significant impact on the value of q_{TIR} inferred for a population, especially where two mismatched limits in the radio and the infrared are at work as it is in our case for JAR10 and TLS. Due to this effect in our sample of sources from the literature we considered the IR/radio ratios obtained by D17 to compare with our sample of cluster member galaxies. Therefore tentative evidence of radio excess for the CMs was found compared with FGs. This result is consistent with results for nearby galaxies (include a ref) and at intermediate-redshift (RAN15) indicating an enhancement

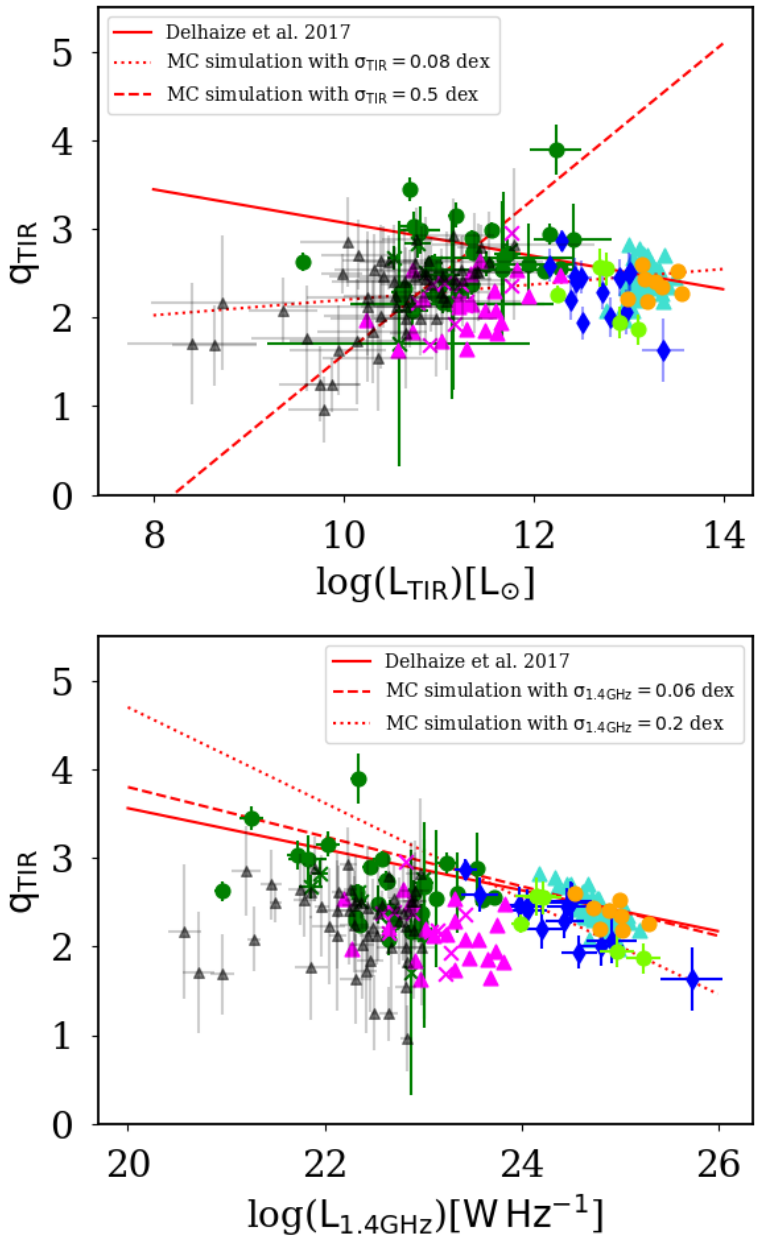

Figure 5.8 : From top to bottom the IR/radio ratio versus the infrared and radio luminosities are represented respectively. Here we can see how the value of the uncertainties can vary the slope of the D17 correlation according with MC simulations. The solid-red line correspond to D17 in both plots, and the dashed- and dotted-red lines the MC simulations for smaller are bigger uncertainties respectively.

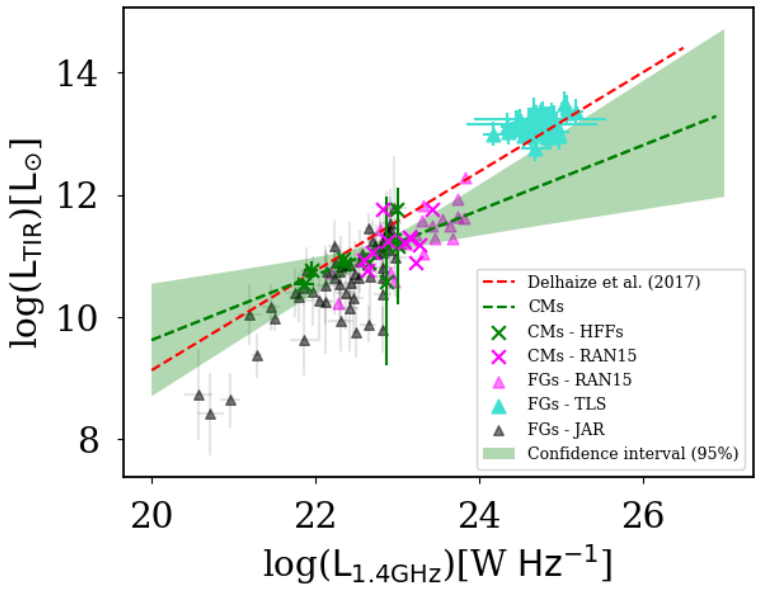

Figure 5.9 : The IRRC for the CMs in dashed-green line is shown in this plot. A less strong correlation than D17 (dashed-red) was found for the CMs, indicating an excess of radio emission in cluster environments compare with FGs. However this result cannot be taken as conclusive due to the big uncertainties as shown by the green-shaded region.

of radio emission in cluster environments due to the different processes occurring in cluster galaxies, i.e. gravitational interactions and ram-pressure stripping. Only 20 sources were used for this correlation and all of them at very similar redshifts, so this result cannot yet be taken as conclusive. A bigger sample of CMs and a bigger range of redshifts would be necessary to confirm this.

To analyse the effect of environment on the IRRC, we studied the q_{TIR} ratio vs. projected radius. We define $R_{core} \leqslant 0.5$ Mpc and $R_{ring} = 0.5 - 1.5$ Mpc as projected distances from the cluster centre. In Figure 5.10 (top) the IR and radio luminosities vs. projected radius are shown, where the dashed-red lines represent R_{core} and R_{ring}. It is important to note that the uncertainties for the CMs in the outer region of the cluster are much larger at FIR wavelengths due to the lack of data in the PACS bands[8] and very weak detections in the SPIRE bands. RAN15 did not find a preference of radio excess objects at different distances from the centre of the cluster. In this study, we found a very slight increment in the radio luminosities in the outer regions of the cluster. This implies a lower q_{TIR} in this region as shown in Figure 5.10 (bottom). However, due to the big uncertainties discussed above we should not take this as a very reliable result. At radio frequencies some galaxies with lower $L_{1.4GHz}$ in the inner part of the cluster were detected, but not at FIR. One possible explanation is that L_{TIR} is been overestimated, due

[8]These areas were not covered with PACS.

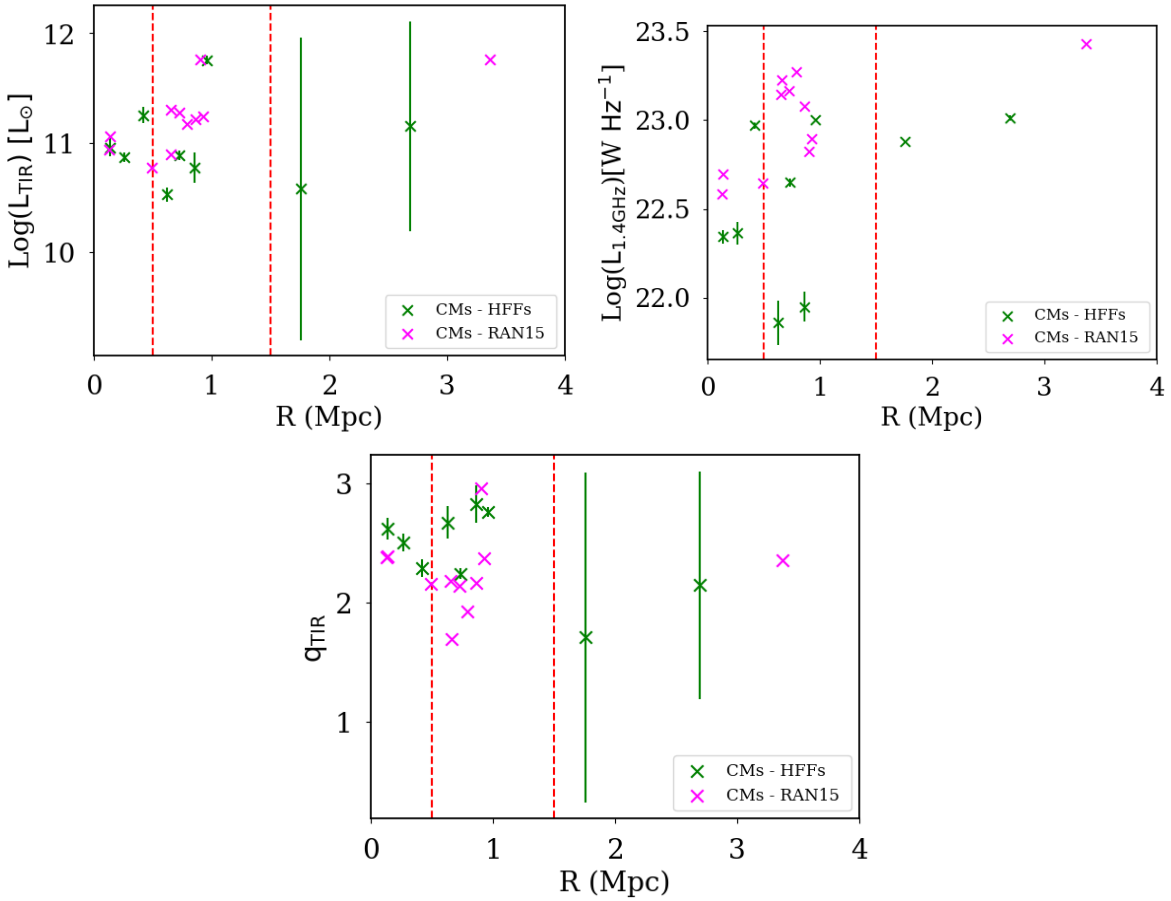

Figure 5.10 : *Top:* From left to right, L_{TIR} and $L_{1.4GHz}$ luminosities in logarithmic scale as a function of distance to the centre of the cluster. The dashed-red lines represent the inner and outer rings at 0.5 and 1.5 Mpc from the centre of the cluster. Some tentative excess in the radio luminosities is found in the outer region of the cluster. *Bottom:* q_{TIR} vs. projected radius where no clear trend is detected due to the big uncertainties in the measurements of the outer region.

to these galaxies being dominated by old stars heating the dust, as is often the case for cluster galaxies, which are on average more evolved due to environmental processes.

5.5.3 IRRC for the Galaxies-Cluster Lensed galaxies

In this section we compare the IRRC correlation for the GCLs and the GGLs sources. Figure 5.11 (top) shows the IRRC for all the lensed galaxies in this study where the dashed-blue line represents the correlation for the GGLs ($\log(L_{TIR}) = 0.75 \times \log(L_{1.4GHz}) - 5.48$ with a dispersion of 0.19 dex) and the dashed-green line corresponds to the GCLs correlation ($\log(L_{TIR}) = 0.79 \times \log(L_{1.4GHz}) - 6.36$ with a dispersion of 0.35 dex). No differences were

found between either of these two samples and D17 (in dashed-red) indicating no contamination in the measurements due to the environment of the cluster or the lensing effect.

Figure 5.11 (bottom) shows the evolution of q_{TIR} with redshift where all lensed galaxies nicely follow the trend from D17 (dashed-red line). For the GCLs sample we obtained an average $q_{TIR} = 2.58 \pm 0.20$ at $0.18 < z < 2.93$ while for the GGLs sources $q_{TIR} = 2.33 \pm 0.20$ at $1.026 < z < 3.675$[9]. This second value is slightly lower, which is consistent with higher redshifts in the sample. We found an evolution of this ratio with redshifts of $q_{TIR} = (2.90 \pm 0.06)(1+z)^{-0.18\pm0.05}$ very consistent with D17. The uncertainties on these values were calculated via bootstrapping of 1,000 iterations with a Gaussian distribution. The evolution of q_{TIR} with z could be due to only being able to observe brighter sources at higher-redshifts, which could have lower IR/radio ratios due to more radio emission coming from AGNs or larger magnetic fields (Section 5.5.1).

Because both correlations (D17 and this study) are similar, we do not expect the environment to affect our measurements with distance. To be sure about this we studied the effect of the cluster environment on the galaxies being lensed by the cluster, i.e. we looked at the correlation with angular distance to the cluster centre. Because the clusters are at different z, the angular distance from each source was calculated and divided by the corresponding R_{core}, thus yielding a consistent dimensionless measure of relative distance. First we analysed how the magnification factor changes with distance to the cluster centre. Figure 5.12 shows how μ increases with the distance to the centre of the cluster up to R_{core}, then decreases steeply towards the outer regions until being practically $\mu \gtrsim 1.01$. This is in agreement with the magnification maps presented in Johnson et al. (2014).

In Figure 5.13 (top-left) no evidence is found for a change in L_{TIR} with the relative distance to the centre of the clusters. However, for $L_{1.4GHz}$ (Figure 5.13 top-right) there are five sources with lower radio luminosities ($\log(L_{1.4GHz}/W\,Hz^{-1}) < 22.1$) which were detected in the core of the cluster. Because the magnification factor is bigger in the core, intrinsically fainter sources are expected to be detected in this region[10]. No faint L_{TIR} counterparts were found for 4 out of 5 of the sources implying a value of $q_{TIR} \gtrsim 3$ (Figure 5.13 bottom), bigger than the mean value of the sample. This might be due to a bad constraint on L_{TIR}. Only PACS bands were detected for these sources, making it impossible to obtain a good constrain for the dust temperature of the galaxies. To be sure that the increment in luminosity towards the outside part of the cluster was not due to a biases redshift distribution, we plotted in Figure 5.14 the distribution of z vs. the relative distance and see that the sources were homogeneously distributed around the cluster with a bigger number of lensed sources in the core as would be expected. No sign

[9]Note that this value can be affected by the selection effects (flux density limits) as explained in Section 5.5.1.
[10]Note that these galaxies were corrected for magnification factor.

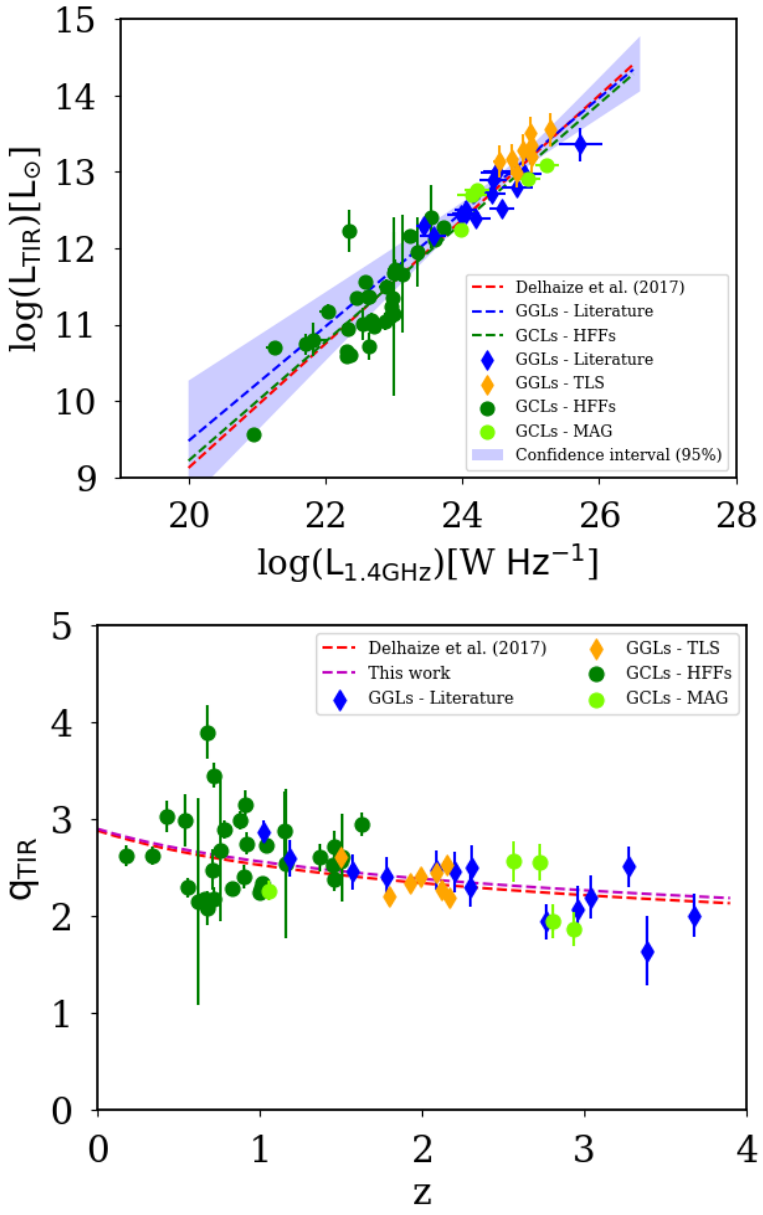

Figure 5.11 : *Top*: IRRC for the GCLs (dashed-green line) and for GGLs sources (dashed-blue line) which are similar to D17 correlation. The blue-shaded region represents the uncertainty in the correlation for the GGLs, consistent with D17. Bottom: q_{TIR} vs. z is showed here as well over the relation from D17. We see that all the samples follow the trend pretty good indicating lower ratios of q_{TIR} at higher redshifts.

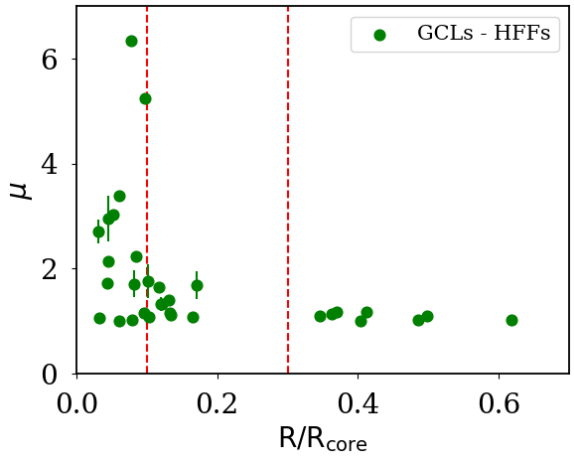

Figure 5.12 : Magnification factor vs. relative angular distance for the lensed galaxies in the HFF. The dashed-red lines represent the core and inner ring boundaries of the relative distance in the cluster. The magnification factor increases with distance from the centre of the cluster to R_{core} where it decreases towards the outer regions of the clusters.

of evolution in the IRRC was found as a function of the angular distance to the centre of the cluster (Figure 5.13 bottom).

5.5.4 Star Formation Rates

The SFRs from the IR and radio luminosities were derived from Kennicutt (1998) and Murphy et al. (2011), respectively. The typical SFR_{TIR} values for the CMs were $SFR_{TIR} = 6 - 30\ M_{\odot}yr^{-1}$. One source (VLAHFF-J114946.11+222414.5, located at 1 Mpc from the centre of the cluster MACSJ1149) was found to have $SFR_{TIR} = 98 \pm 9\ M_{\odot}yr^{-1}$, indicating a much higher SFR at this wavelength. The corresponding $SFR_{1.4GHz} = 25.1 \pm 0.4\ M_{\odot}yr^{-1}$ was only slightly higher than the $SFR_{1.4GHz}$ of the other members of this cluster ($SFR_{1.4GHz} = 2 - 19\ M_{\odot}yr^{-1}$). This might indicate that the FIR emission is being contaminated by other sources because of the relatively large extent of the Herschel beams, or that the FIR emitting dust is being heated by old stars and therefore the SFR_{TIR} is being overestimated. For the GCLs galaxies we found a range of $SFR_{TIR} = 0.6 - 445\ M_{\odot}yr^{-1}$ and $SFR_{1.4GHz} = 0.2 - 133\ M_{\odot}yr^{-1}$, consistent with higher redshifts.

Five out of 22 galaxies in the GGLs sample and two out of 5 from Magnelli et al. (2012) were found to have $SFR_{1.4GHz} > SFR_{TIR}$ (26% of the high-redshift galaxies in this study). This can be understood as an indicator of AGN contamination in the samples. Therefore using the IRRC as a tool to separate AGNs from SFGs seems to be only valid for the most powerful radio-loud AGNs (Morić et al., 2010).

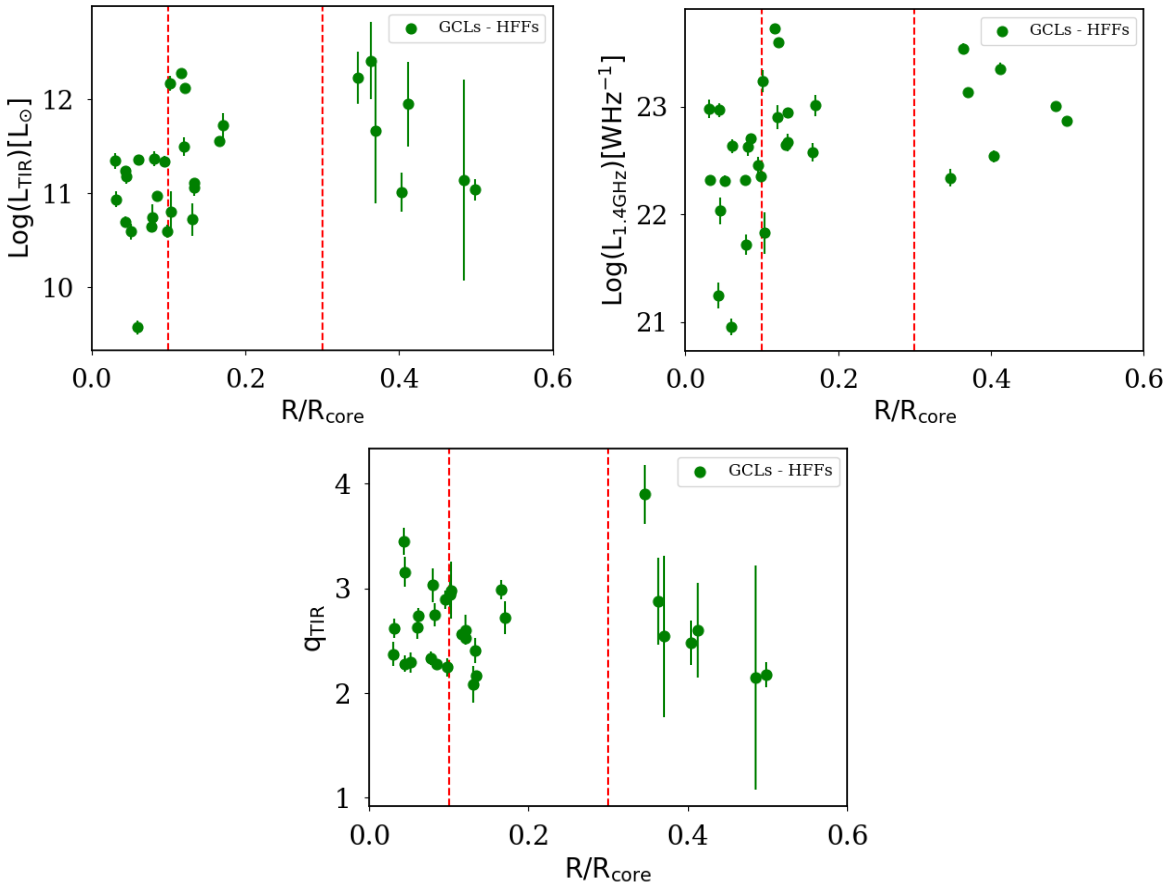

Figure 5.13 : *Top:* Luminosity vs. relative distance for the lensed galaxies in the cluster. A small trend is detected for L_{TIR} and $L_{1.4GHz}$ to increase from the centre of the cluster to the R_{ring} ($\sim$ 1.5 Mpc). This might be due to μ being higher in the core of the cluster and therefore allowing to detect fainter galaxies in this region. The uncertainties in the external part of the cluster are bigger for the FIR due to the lack of data at PACS bands. *Bottom*: No evolution was found for q_{TIR} with the relative distance to the centre of the cluster for the GCLs galaxies.

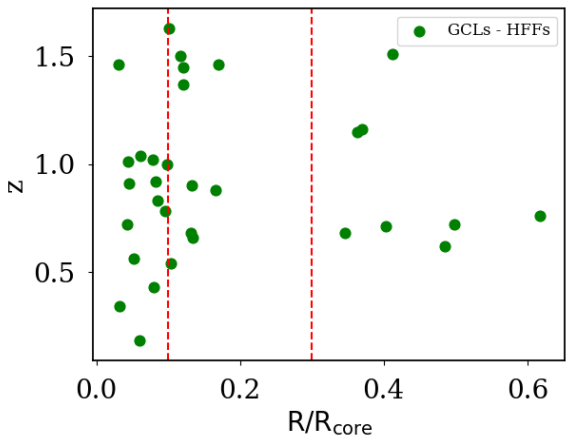

Figure 5.14 : Redshift vs. relative distance to the centre of the clusters where we can see an homogeneous distribution of redshifts for the lensed galaxies and a bigger presence of lensed galaxies in the core of the cluster.

Overestimation in the SFR_{TIR} can occur at low- and high-redshifts due to dust heating by the old stellar populations (see next Section 5.7). SFRs derived from radio luminosities are not affected by dust obscuration or contribution from old stellar populations which makes them a good tracer of SFR. In this study we are considering a mean spectral index $\alpha = 0.7$ for most our galaxies. However, different strength in the magnetic fields can result in different SFR and there is no reason to think that galaxies at high redshift have similar magnetic fields than low-redshift galaxies. Due to the advantage of it being possible to observe these frequencies from ground telescopes due to atmosphere being mostly transparency at radio wavelengths and since radio emission does not suffer from obscuration, it would be relevant to determine the radio spectrum so a better constrain than a simple power-law with a fixed α can be used to reliably determine $L_{1.4GHz}$ and the corresponding SFRs. Our derived SFRs are listed in Table 5.10.

5.6 Stacking

Numerous studies have shown that improving statistical results of undectected sources can be achieved using a stacking technique. This technique has been successfully used in different studies in the literature for continuum (e.g. Fernandez-Conde et al., 2010; Bourne et al., 2012; Man et al., 2016) as well as spectroscopic lines (e.g. Fabello et al., 2012; Delhaize et al., 2013).

Due to the small sample of *Herschel*-detected CMs galaxies in this work, we were not able to put stringent constraints on our relations. In order to improve our statistics, we therefore stack all those CMs detected in the VLA-catalogue with non-detected counterparts in the *Herschel*

maps. Even though these galaxies have no FIR-detections, the *Herschel* maps can still be extracted and stacked. In addition, to test the stacking results as well as to improve the statistics for the cluster lensed sources, we stacked as well all cluster lensed sources non-detected at FIR wavelenghts. In total, 651 GCLs and 111 CMs in the radio detected VLA-catalogue were found not to have FIR counterparts.

To produce stacked *Herschel* images, we first extracted a 300 arcsec $\times$ 300 arcsec cut-out centered on the radio counterpart, for each of the PACS and SPIRE bands. These cut-outs were then averaged to produce the final image. We then performed photometry on each of these maps in the same way as in Section 4.6.1 and determined luminosities using the average stacked redshift and distance. Finally we performed a 2-component MBB fit as in Section 5.4.1 to obtain the stacked infrared lumnosities. To obtain scaling relations, we divided our sample in seperate bins and repeated this process for each of the bins.

Both SPIRE and PACS bands were used to create the final stacking images. Although, some of the sources were outside the *Herschel* maps and therefore did not contribute to the stacked images. The HFF PACS maps are smaller than the SPIRE maps and therefore less sources were included in the stacked images, so the final images at different bands were created using a different number of maps.

Due to the large beam sizes of the *Herschel* bands, there were often multiple galaxies contributing to the flux of a particular taget galaxy. This 'confusion' was expected as some of the galaxies in our sample lied close enough to be within one *Herschel* beam of another galaxy in our sample. We thus needed to correct for this confusion. To do this we determined the average amount of SF galaxies that lied within the beam for each band. For each galaxy that was close to the target galaxy, we determined how much it contributed to the flux based on a gaussian radial profile. Each galaxy contributes:

$$S_{contr} = S_0 \, e^{-\frac{\theta^2}{2(FWHM/2.3548)^2}} \tag{5.4}$$

Where S_{contr} is the contributed flux, S_0 is the galaxy flux, θ is the angular separation in radians and FWHM is the beamsize of each band. We considered the different beam sizes for the different bands to determine the number of confused sources within the different beams. Each image was then corrected by this factor to account for the confusion. On average, the stacked images were divided by a factor of 1.1, 1.2, 1.3, 1.6 and 2.0 for 100, 160, 250, 350 and 500μm respectively.

For the 651 GCLs we stacked the undetected FIR sources selecting radio fluxes in 5 different bins of radio luminosities. The different number of stacked maps, average redshift and L_{TIR} are shown in Table 5.6. In Figure 5.15 the IRRC for all the lensed sources in our sample is shown

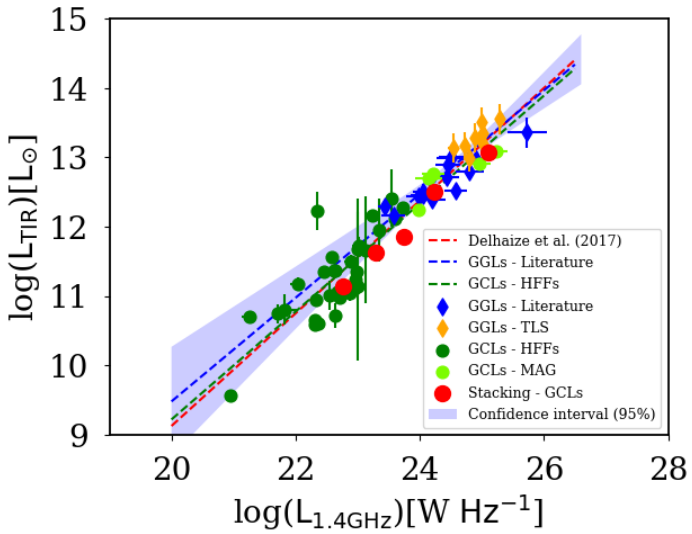

Figure 5.15 : IRRC for all the lensed sources in the sample. The red dots correspond to the stacked undetected FIR sources were we can see that the stacked sources follow the trend but are systematically below it due to the lack of a selection bias towards bright FIR fluxes.

with the stacked sources plotted as red dots. We can see that the stacked maps are consistent with our previous results but systematically below the trend. This is due to these sources not having a selection criteria towards being bright in the FIR. Additionally by only selecting undetected sources, we are not selecting the bright FIR sources, and our stacked average is thus lower than the one expected for the full sample.

Table 5.6 : Stacking bins for the GCLs. This table shows the number of sources included in the stacked maps for the PACS and SPIRE bands, the average redshift of the stacked maps, the chosen bins in terms of radio luminsities, the average radio luminosity and the infrared luminosity obtained via SED fitting.

Num. lensed sources PACS|SPIRE	$\langle z \rangle$	Radio lum. bins ($W\,Hz^{-1}$)	$\langle \log(L_{1.4GHz}) \rangle$ ($W\,Hz^{-1}$)	$\log(L_{TIR})$ ($L_\odot$)
36|71	0.65	0.0 - 23.0	11.14 ± 0.08	22.76 ± 0.03
74|146	0.83	23.0 - 23.5	11.62 ± 0.05	23.28 ± 0.01
63|120	1.01	23.5 - 24.0	11.85 ± 0.04	23.74 ± 0.01
38|92	1.44	24.0 - 24.5	12.50 ± 0.04	24.24 ± 0.01
48|113	2.15	24.5 - 99.0	13.07 ± 0.03	25.11 ± 0.05

For the 111 CMs we have 17 members for MACSJ0416, 66 sources for MACSJ0717 and 28 sources for MACSJ1149. We stacked them in radio luminosity bins and into radial distances bins to study the dependency within the cluster.

The stacking characteristics are shown in Table 5.7. In Figure 5.16 the red crosses represent the stacking sources for the CMs of our sample. We can see that as explained in Section 5.5.2,

the IRRC present an excess of radio emission compare with field galaxies. This is in the line of reasoning that ram pressure stripping by the ICM compresses the galaxies' ISM and therefore an increase of radio emission is detected in the cluster environments. When we study the radial dependency within the cluster we cannot be conclusive in our results as we do not have enough sources distributed throughout the cluster. In Figure 5.17 we show the q_{TIR} factor vs. radial distance in the cluster. The red crosses represent the stacked sources where we can see that only two dots are present. A bigger sample of cluster member galaxies would be necessary to study the radial dependency of the IRRC in cluster galaxies.

Table 5.7 : Stacking bins for the CMs sources. This table shows the number of source included in the stacked maps for the PACS and SPIRE bands, the average redshift of the stacked maps, the chosen bins in terms of radio luminsities, the averaged radio luminosity and the infrared luminosity obtained via SED fitting.

Num. member sources PACS|SPIRE	$\langle z \rangle$	Radio lum. bins ($W\,Hz^{-1}$)	$\langle \log(L_{1.4GHz}) \rangle$ ($W\,Hz^{-1}$)	$\log(L_{TIR})$ ($L_\odot$)
25|32	0.505	0.0 - 22.5	10.62 ± 0.18	22.29 ± 0.03
21|36	0.535	22.5 - 23.0	10.93 ± 0.10	22.66 ± 0.02
14|26	0.540	23.0 - 99.0	11.32 ± 0.09	23.38 ± 0.07

Table 5.8 : Stacking bins of radial distance from the center of the cluster for the CMs sources. This table shows the number of source included in the stacked maps for the PACS and SPIRE bands, the average redshift of the stacked maps, the chosen bins in terms of radial distances to the center of the cluster, the average radial distance for each bin, the average radio luminosities and the infrared luminosity obtained via SED fitting.

Num. member sources PACS|SPIRE	$\langle z \rangle$	Radial distance bins (Mpc)	$\langle$radial distance $\rangle$ (Mpc)	$\langle \log(L_{1.4GHz}) \rangle$ ($W\,Hz^{-1}$)	$\log(L_{TIR})$ ($L_\odot$)
10|10	0.545	0.0 - 1.5	1.05	10.21 ± 0.36	22.58 ± 0.22
43|45	0.52	1.5 - 4.0	2.51	11.08 ± 0.16	22.51 ± 0.07
7|39	0.54	4.0 - 99.0	5.62	11.27 ± 0.20	22.86 ± 0.08

5.7 Caveats

1. A mean value of $\alpha = 0.7$ was used for most sources. We are thus considering the same SED slope at different redshifts, which means similar magnetic fields for all the different type of galaxies we are studying. Different magnetic fields strengths can result in different slopes for the radio synchrotron radiation and therefore this assumption of a constant α can influence the shape and normalization of the IR/radio ratios as we do not consider the spectral index being dominated by the free-free emission in any case.

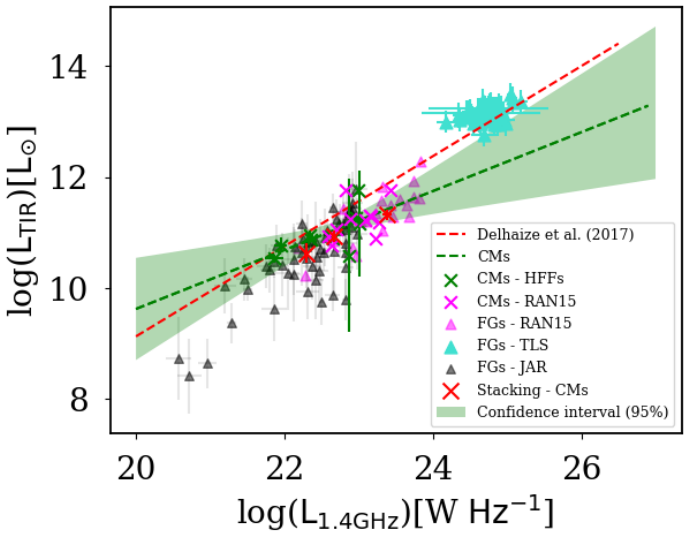

Figure 5.16 : IRRC for the cluster members and field galaxies of the sample. The red crosses represent the stacked images of the undetected cluster members sources in the *Herschel* maps. We see that there is indeed an excess of radio emission for the cluster members compared with the relation from D17. This result is in agreement with those from local clusters galaxies (e.g. Miller & Owen, 2001).

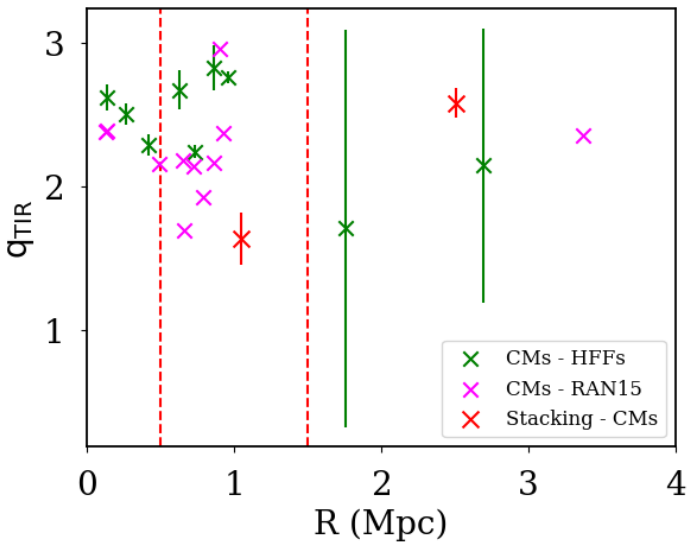

Figure 5.17 : q_{TIR} factor vs. radial distance of the cluster. The red crosses correspond to the CMs staked sources. Only two sources were found within the cluster which does not allow us to make any conclusions about the dependency of the IRRC on the radial distance within the clusters at intermediate redshifts.

2. The total infrared luminosities were derived from (Kennicutt, 1998). While for most galaxies the dust heating is dominated by star-formation, very evolved galaxies (as those typically found in clusters) can present contamination from old stellar populations heating the dust. This results in an overestimation of the SFR for these galaxies. In addition, simulations have shown that for major mergers with strong starburst, the instantaneous SFR can be overestimated as well during the post-starburst phase. Despite of the SFR decreases rapidly after the starburst, stars formed during this process can remain dust-obscured and produce an overestimation of the SFR. Therefore only the use of IR luminosity to derived SFRs can overestimate the presence of star-forming galaxies while they could be quenched galaxies (Hayward et al., 2014).

3. The magnification produced by the lens source is the same independently of the wavelength. However, this effect is geometric and therefore a change in the position can result in different magnification factors when applying lens models. Thus, spatial variations in the physical conditions of the background galaxy can result in different magnification factor at different wavelengths (e.g. Krips et al., 2007; Hezaveh et al., 2012) and can thus slightly affect q_{TIR}.

5.8 Conclusions

A study of the IRRC for two different scenarios has been performed in this chapter. Samples of CMs and FGs were compared in order to investigate the potential enhancement of radio emission within the clusters as compared to isolated galaxies. Furthermore, GGLs and GCLs sources were compared to study if the IRRC changes due to FIR contamination. Four different samples of radio-detected sources with *Herschel*-FIR counterparts for the HFF-VLA, and *Herschel*-FIR sources with radio counterparts from the literature were created to study possible differences between different environments in the galaxies. The final samples consist of 20 CMs, 127 FGs, 37 GCLs and 22 GGLs, covering a range of redshifts $0.011 < z < 3.675$. Consistent luminosities were calculated for the FIR and radio bands for all the galaxies under study. MBB fitting was done from $\lambda(8-1000\ \mu\mathrm{m})$ to obtain total infrared luminosities and the radio luminosities were derived considering $\alpha = 0.7$ and applying the corresponding K-correction. Our main conclusions are:

- The IRRC for all the samples followed the trend found in previous results in the literature and no differences in the evolution of this correlation was found between the different samples when considering all of them as a whole.

- Evolution of the IRRC with redshift was found ($q_{TIR} = (2.90 \pm 0.06)(1+z)^{-0.18\pm0.05}$) for lensed galaxies, consistent with previous results in the literature for non-lensed galaxies indicating an excess of radio emission at high redshifts.

- When studying the CMs we found that the IRRC is not as steep as in previous results, indicating an excess of radio emission for CMs at intermediate-redshifts. This is consistent with studies of nearby galaxies, where the different environment in the cluster or isolated galaxies produces a similar difference. We find an average value $q_{TIR} = 2.33 \pm 0.18$ for our sample of CMs, slightly lower than the q_{TIR} for D17 (2.63 - 2.73) at similar redshifts. The small sample used in this study makes this result not conclusive. A bigger sample and a wider range of redshifts would be desirable to constrain this scenario better.

- A stacking analysis of the undetected FIR counterparts of the radio detected VLA-catalogue was done to confirm this excess of radio emission in cluster galaxies at intermediate redshifts. Stacking the maps in three different bins of radio luminosities and excess of radio emission is found for cluster members galaxies. This is most likely due to the ISM being compressed by the ram pressure stripping by the ICM, increasing the detected radio emission in the cluster environment.

- Studying this excess in radio emission with respect to the distance to the centre of the cluster, no clear correlation was found due to the big uncertainties at large distances from the centre of the cluster.

- No differences between GCLs and GGLs sources were found. These two samples are consistent with D17 within the errors which indicates that the measured IR emission is not dominated by contamination coming from the foreground galaxy.

- The different IR/radio ratios for these four samples can be found in Table 5.9. These values are in good agreement with previous results in the literature. Therefore, no clear differences have been found between the different samples.

- SFRs have been derived from infrared and radio luminosities finding in general higher values for SFR_{TIR}. This might be due to an overestimation of the star-formation derived from infrared luminosities and/or not considering differences in the magnetic field when deriving $SFR_{1.4GHz}$. For our high-redshift sample we found 26% of the galaxies to have $SFR_{1.4GHz} > SFR_{TIR}$. Hence, using the IR/radio ratios to classify AGNs out of SFGs seems only valid for the most radio-loud AGNs. It is likely then that contamination coming from AGNs is not always possible to identify, resulting in higher $SFR_{1.4GHz}$.

Future work should be directed at obtaining a bigger sample of CMs at different redshifts to study this correlation independently and study the relation with the distance to the centre of the cluster. Better mechanisms to identify AGNs would be important to have a clean sample of SFGs. In addition, to study the slope of the radio spectrum would be crucial to obtain a more realistic representation of the IRRC.

Table 5.9 : List of q_{TIR} mean values for the different samples in this study and the correspondent interval of redshifts.

Reference	Environment	Redshift	q_{TIR}
GCLs	Cluster Lensing	$0.18 < z < 1.63$	2.58 ± 0.20
GGLs	Field Lensing	$1.03 < z < 3.67$	2.33 ± 0.20
CMs	Cluster	$0.34 < z < 0.62$	2.33 ± 0.18
RAN15	Cluster	$z \sim 0.54$	2.10 ± 0.53
FGs	Field	$1.5 < z < 2.5$	2.42 ± 0.23
JAR10	Field	$0 < z < 0.5$	2.40 ± 0.12
RAN15	Field	$0.23 < z < 0.9$	1.92 ± 0.45
TLS	Field	$1.5 < z < 2.5$	2.42 ± 0.22

Table 5.10 : This table shows redshifts, magnification factors, infrared and radio luminosities, IR/radio ratios and SFRs for all the samples. Luminosities and SFRs have been corrected for magnification factor when available. The last two columns show the angular distance (in arcmin) to the center of the cluster and the physical distance R (in Mpc) to the center, where available.

	ID	z	μ	$\log L_{TIR}$ ($L_\odot$)	$\log L_{1.4GHz}$ (W/Hz)	q_{TIR}	SFR_{TIR} ($M_\odot yr^{-1}$)	$SFR_{1.4GHz}$ ($M_\odot yr^{-1}$)	Angular Dist. (arcmin)	R (Mpc)
HFF-GCLs	VLAHFF-J071725.83+375018.8	0.71	1.01 ± 0.03	11.01 ± 0.21	22.54 ± 0.05	2.48 ± 0.21	17.7 ± 10.8	8.7 ± 1.2	5.3	−−
	VLAHFF-J071710.65+375121.8	0.76	1.02 ± 0.01	11.68 ± 0.73	23.01 ± 0.03	2.68 ± 0.73	83 ± 362	25.4 ± 2.2	8.0	−−
	VLAHFF-J071722.31+375107.8	0.62	1.02 ± 0.01	11.14 ± 1.07	23.00 ± 0.01	2.15 ± 1.07	24 ± 258	25.3 ± 0.8	6.3	−−
	VLAHFF-J071735.30+374447.3	0.43	1.02 ± 0.01	10.74 ± 0.14	21.72 ± 0.10	3.03 ± 0.16	9.5 ± 3.6	1.3 ± 0.3	1.0	−−
	VLAHFF-J071736.66+374506.5	1.0	5.24 ± 0.01	10.60 ± 0.07	22.36 ± 0.05	2.25 ± 0.08	6.8 ± 1.2	5.7 ± 0.7	1.3	−−
	VLAHFF-J071734.46+374432.2	1.02	6.34 ± 0.01	10.64 ± 0.05	22.32 ± 0.04	2.33 ± 0.06	7.6 ± 0.9	5.2 ± 0.6	1.0	−−
	VLAHFF-J071719.48+374941.4	1.51	1.17 ± 0.02	11.95 ± 0.45	23.35 ± 0.06	2.60 ± 0.45	152 ± 279	56.1 ± 7.8	5.4	−−
	VLAHFF-J071717.35+374830.4	1.16	1.18 ± 0.01	11.66 ± 0.77	23.13 ± 0.05	2.54 ± 0.77	80 ± 389	33.8 ± 3.8	4.8	−−
	VLAHFF-J071740.44+374527.2	1.46	1.68 ± 0.26	11.72 ± 0.13	23.01 ± 0.10	2.72 ± 0.16	91.0 ± 32.5	25.6 ± 6.5	2.2	−−
	VLAHFF-J071730.40+374617.0	0.92	1.71 ± 0.26	11.37 ± 0.09	22.62 ± 0.08	2.75 ± 0.11	40.0 ± 7.9	10.5 ± 2.2	1.1	−−
	VLAHFF-J071730.65+374443.1	0.91	2.95 ± 0.43	11.18 ± 0.08	22.03 ± 0.12	3.15 ± 0.14	26.1 ± 5.5	2.7 ± 0.9	0.6	−−
	VLAHFF-J041605.02-240424.2	0.18	1.01 ± 0.01	9.57 ± 0.08	20.95 ± 0.08	2.62 ± 0.11	0.6 ± 0.1	0.2 ± 0.0	0.9	−−
	VLAHFF-J041606.36-240451.2	0.56	3.03 ± 0.01	10.59 ± 0.09	22.31 ± 0.05	2.29 ± 0.10	6.7 ± 1.5	5.1 ± 0.6	0.8	−−
	VLAHFF-J041609.12-240459.3	0.72	1.72 ± 0.01	10.69 ± 0.06	21.25 ± 0.12	3.45 ± 0.13	8.5 ± 1.2	0.4 ± 0.1	0.7	−−
	VLAHFF-J041610.79-240447.5	1.01	2.13 ± 0.01	11.24 ± 0.04	22.97 ± 0.07	2.28 ± 0.08	30.0 ± 3.3	23.2 ± 3.8	0.7	−−
	VLAHFF-J041610.60-240407.4	0.34	1.05 ± 0.01	10.94 ± 0.08	22.32 ± 0.04	2.62 ± 0.09	14.9 ± 3.2	5.2 ± 0.4	0.5	−−
	VLAHFF-J041614.84-240451.5	0.54	1.07 ± 0.05	10.80 ± 0.22	21.83 ± 0.19	2.98 ± 0.27	10.9 ± 7.1	1.7 ± 0.9	1.6	−−
	VLAHFF-J041636.19-240759.7	0.72	1.09 ± 0.01	11.04 ± 0.11	22.87 ± 0.04	2.17 ± 0.12	18.8 ± 5.6	18.6 ± 1.7	7.8	−−
	VLAHFF-J041629.52-240550.0	0.68	1.10 ± 0.01	12.23 ± 0.27	22.34 ± 0.08	3.90 ± 0.28	292 ± 257	5.5 ± 1.1	5.4	−−
	VLAHFF-J041607.89-240623.4	0.66	1.12 ± 0.03	11.11 ± 0.03	22.95 ± 0.03	2.17 ± 0.04	22.2 ± 1.6	22.2 ± 1.5	2.1	−−
	VLAHFF-J041629.66-240630.3	1.15	1.13 ± 0.01	12.41 ± 0.41	23.54 ± 0.05	2.88 ± 0.41	444 ± 701	86.7 ± 10.2	5.7	−−
	VLAHFF-J041611.61-240221.6	0.9	1.15 ± 0.03	11.07 ± 0.09	22.67 ± 0.08	2.40 ± 0.12	20.0 ± 4.7	11.6 ± 2.4	2.1	−−
	VLAHFF-J114940.57+222415.5	0.78	1.15 ± 0.00	11.34 ± 0.05	22.46 ± 0.07	2.89 ± 0.09	37.9 ± 4.8	7.2 ± 1.3	1.2	−−
	VLAHFF-J114940.87+222307.3	1.37	1.32 ± 0.13	11.50 ± 0.10	22.90 ± 0.11	2.60 ± 0.14	54.0 ± 14.4	19.8 ± 5.7	1.6	−−
	VLAHFF-J114929.35+222407.8	1.45	1.33 ± 0.04	12.12 ± 0.04	23.60 ± 0.03	2.52 ± 0.05	225 ± 20.6	99.3 ± 7.9	1.6	−−
	VLAHFF-J114936.98+222542.0	0.68	1.40 ± 0.03	10.72 ± 0.17	22.64 ± 0.03	2.08 ± 0.18	9.0 ± 4.5	11.0 ± 0.8	1.7	−−
	VLAHFF-J114929.81+222425.9	1.5	1.64 ± 0.00	12.28 ± 0.02	23.73 ± 0.03	2.56 ± 0.03	328 ± 17	133 ± 9.0	1.5	−−
	VLAHFF-J114930.67+222427.6	1.63	1.76 ± 0.32	12.17 ± 0.07	23.24 ± 0.10	2.94 ± 0.12	255 ± 48	43.0 ± 11.4	1.3	−−
	VLAHFF-J114932.03+222439.3	0.83	2.23 ± 0.01	10.97 ± 0.04	22.70 ± 0.03	2.28 ± 0.05	16.3 ± 1.5	12.7 ± 0.9	1.1	−−
	VLAHFF-J114936.09+222424.4	1.46	2.71 ± 0.23	11.35 ± 0.08	22.98 ± 0.09	2.37 ± 0.11	38.0 ± 7.6	23.7 ± 5.3	0.4	−−
	VLAHFF-J114934.42+222445.3	1.04	3.38 ± 0.01	11.36 ± 0.04	22.63 ± 0.06	2.73 ± 0.07	39.6 ± 3.9	10.7 ± 1.7	0.8	−−
	VLAHFF-J114944.33+222408.6	0.88	1.08 ± 0.01	11.56 ± 0.03	22.57 ± 0.09	2.99 ± 0.09	62.1 ± 5.2	9.4 ± 2.0	2.2	−−

Table 5.10 : *Continued*

	ID	z	μ	$\log L_{TIR}$ ($L_\odot$)	$\log L_{1.4GHz}$ (W/Hz)	q_{TIR}	SFR_{TIR} ($M_\odot yr^{-1}$)	$SFR_{1.4GHz}$ ($M_\odot yr^{-1}$)	Angular Dist. (arcmin)	R (Mpc)
HFF-CMs	VLAHFF-J071722.31+375107.8	0.62	−−	11.15 ± 0.96	23.01 ± 0.01	2.15 ± 0.96	24.5 ± 198.4	25.8 ± 0.9	−−	2.691
	VLAHFF-J071727.53+374441.2	0.51	−−	11.25 ± 0.07	22.97 ± 0.02	2.29 ± 0.07	30.9 ± 5.5	23.3 ± 1.1	−−	0.420
	VLAHFF-J071736.12+374309.4	0.51	−−	10.77 ± 0.14	21.95 ± 0.08	2.83 ± 0.16	10.2 ± 3.9	2.2 ± 0.5	−−	0.861
	VLAHFF-J041610.60-240407.4	0.34	−−	10.96 ± 0.08	22.34 ± 0.04	2.62 ± 0.09	15.6 ± 3.3	5.5 ± 0.5	−−	0.140
	VLAHFF-J114937.99+222427.7	0.51	−−	10.86 ± 0.04	22.36 ± 0.06	2.51 ± 0.07	12.6 ± 1.3	5.8 ± 0.9	−−	0.264
	VLAHFF-J114938.81+222531.8	0.52	−−	10.53 ± 0.06	21.86 ± 0.12	2.67 ± 0.13	5.8 ± 0.9	1.8 ± 0.6	−−	0.627
	VLAHFF-J114939.46+221853.2	0.47	−−	10.58 ± 1.38	22.88 ± 0.01	1.71 ± 1.38	6.5 ± 151.0	18.9 ± 0.2	−−	1.759
	VLAHFF-J114943.72+222412.7	0.51	−−	10.89 ± 0.04	22.65 ± 0.02	2.24 ± 0.05	13.3 ± 1.4	11.2 ± 0.6	−−	0.731
	VLAHFF-J114946.11+222414.5	0.52	−−	11.76 ± 0.04	23.00 ± 0.01	2.76 ± 0.04	98.4 ± 9.8	25.1 ± 0.4	−−	0.964
Negrello	HATLASJ090302.9-014127	2.3049	4.9 ± 0.0	12.99 ± 0.02	24.50 ± 0.23	2.50 ± 0.23	1695 ± 100	795 ± 563	−−	−−
Negrello	HATLASJ091043.0-000322	1.786	10.9 ± 1.3	12.45 ± 0.06	24.05 ± 0.20	2.40 ± 0.21	481 ± 68	279 ± 165	−−	−−
Negrello	HATLASJ133649.9+291800	2.2024	4.4 ± 0.8	12.90 ± 0.08	24.45 ± 0.20	2.45 ± 0.21	1370 ± 264	709 ± 415	−−	−−
Negrello	HATLASJ085358.9+015537	2.0925	15.3 ± 3.5	12.43 ± 0.09	23.97 ± 0.19	2.47 ± 0.20	468 ± 111	233 ± 128	−−	−−
Negrello	HATLASJ090311.6+003907	3.042	16.0 ± 0.7	12.38 ± 0.03	24.20 ± 0.22	2.19 ± 0.22	418 ± 30	393 ± 257	−−	−−
Negrello	HATLASJ125135.3+261457	3.675	11.0 ± 1.0	12.80 ± 0.04	24.80 ± 0.22	2.00 ± 0.22	1092 ± 109	1596 ± 1064	−−	−−
Negrello	HATLASJ090740.0-004200	1.577	8.8 ± 2.2	12.50 ± 0.11	24.05 ± 0.16	2.45 ± 0.19	546 ± 159	283 ± 127	−−	−−
Negrello	HATLASJ132427.0+284449	1.676	2.8 ± 0.0	12.88 ± 0.02	25.17 ± 0.14	1.72 ± 0.14	1312 ± 75	3695 ± 1425	−−	−−
Conley	Hermes:J10575.1+573027	2.958	10.86 ± 0.68	12.97 ± 0.04	24.91 ± 0.25	2.06 ± 0.25	1604 ± 156	2050 ± 1607	−−	−−
Wardlow	Hbootes01	3.274	5.0 ± 0.0	13.01 ± 0.03	24.51 ± 0.21	2.51 ± 0.21	1750 ± 107	802 ± 492	−−	−−
Wardlow	HXMM02	3.39	1.5 ± 1.0	13.36 ± 0.22	25.73 ± 0.32	1.64 ± 0.35	3929 ± 2627	13307 ± 14323	−−	−−
Dye	H-ATLASJ142935.3-002836	1.026	23.6 ± 1.3	12.29 ± 0.04	23.43 ± 0.11	2.87 ± 0.11	338 ± 29	67 ± 19	−−	−−
Dye	HELMSJ001615.7+032435	2.765	15.9 ± 1.0	12.51 ± 0.05	24.58 ± 0.18	1.94 ± 0.19	560 ± 70	953 ± 499	−−	−−
Dye	HELMSJ004714.2+032454	1.19	8.3 ± 0.6	12.16 ± 0.04	23.57 ± 0.19	2.59 ± 0.19	248 ± 22	93 ± 51	−−	−−
Magnelli	SMMJ14011+0252	2.565	3.0 ± 0.0	12.70 ± 0.02	24.14 ± 0.21	2.56 ± 0.21	864 ± 37	346 ± 215	−−	−−
Magnelli	SMMJ02399-0134	1.06	2.5 ± 0.0	12.24 ± 0.03	23.99 ± 0.09	2.26 ± 0.10	301 ± 24	242 ± 59	−−	−−
Magnelli	SMMJ02399-0136	2.81	2.5 ± 0.0	12.90 ± 0.02	24.97 ± 0.18	1.94 ± 0.18	1383 ± 62	2326 ± 1180	−−	−−
Magnelli	SMMJ14009+0252	2.934	1.5 ± 0.0	13.09 ± 0.02	25.23 ± 0.17	1.86 ± 0.17	2136 ± 98	4285 ± 2117	−−	−−
Magnelli	SMMJ00266+1708	2.73	2.4 ± 0.0	12.76 ± 0.02	24.21 ± 0.19	2.55 ± 0.19	985 ± 55	406 ± 217	−−	−−

Chapter 6

Conclusions

6.1 Summary and Conclusions

In this thesis an IR-radio study of galaxies at different evolutionary states and in different environments is presented. We carried out different investigations using data from *Herschel*, ATCA and the VLA to study different samples of gravitational lensing systems and galaxy-members of galaxy clusters. This thesis is divided in three different projects with the following results:

Dusty Star-Forming Galaxies: In Chapter 3 we study some of the reddest ($S_{250} < S_{350} < S_{500}$) sources in H-ATLAS with fluxes $S_{500} > 100$ mJy to determine if they are lensed galaxies or intrinsic HyLIRGs (Negrello et al., 2007). A colour-selection was applied to select the reddest sources in the catalogue, which resulted in galaxies with $z_{phot} > 3.5$ via SED fitting. Follow-up of three H-ATLAS sources was carried out with the use of ATCA and GEMINI-South. 3 mm continuum maps via ATCA observations allowed us to determine the origin of the sub-mm emission with 2 arcsec resolution for two out of three of our targets. In additions, 7 mm ATCA observations resulted in the detection of $^{12}CO(2-1)$ lines for both these galaxies, yielding spectroscopic redshifts of $z = 3.9198 \pm 0.0003$ and $z = 3.7135 \pm 0.0003$. Though more emission lines would be necessary to unambiguously confirm these redshifts. Deep NIR observations at K_s-band with GEMINI (limit magnitude $m_{AB} \sim 23$) were done to determine NIR counterparts for the *Herschel*-sources. With the probability of a chance alignment between the radio and the NIR source being below $< 10\%$ (González-Nuevo et al., 2012) these two sources are most likely related. With very bright K_s-band counterparts ($m_{AB} \sim 20$) for these high-redshifts, and a small offset between the 3 mm imaging and the NIR sources, these galaxies are most likely gravitationally lensed.

Assuming these galaxies are gravitationally lensed, a gross estimation of the magnification factor was done via linewidths and luminosities of the $^{12}CO(2-1)$ lines, yielding magnification

factors of ~ 3.2 for both galaxies. These lines were found to be wider (~ 800 km s^{-1}) than the average value found in the literature (~ 400 km s^{-1}). The cold molecular gas reservoir available for future star-formation was calculated to be $M_{gas} \sim 7 \times 10^{10}$ $M_{\odot}$.

We fitted the infrared SED using two-component MBB, obtaining total infrared luminosities of $\sim 10^{13}$ $L_{\odot}$ and dust masses of $\sim 2 \times 10^{9}$ $M_{\odot}$ for both sources. The SFRs were derived from Kennicutt (1998) resulting in SFRs $\sim 2,400$ $M_{\odot}$yr^{-1}. With depletion times of ~ 30 Myears these two sources are consistent with merging systems galaxies causing a startburst. Therefore these very red *Herschel*-sources are most probably gravitationally lensed ULIRG galaxies, progenitors of two massive elliptical galaxies at $z \sim 2-3$.

The Thousand Lens Survey: In Chapter 4 a sample of H-ATLAS sources at $1.5 < z_{phot} < 2.5$ was studied to determine the fraction of Strongly Lensed Galaxies (SLGs) detected at lower fluxes ($S_{500} > 29$ mJy) following the criteria from Negrello et al. (2007). Observations with the VLA in configuration B at C-band were carried out to determine radio counterparts of the *Herschel*-sources with resolution ~ 1.1 arcsec and average r.m.s.~ 6.66 μJy. NIR maps from VIKING (for the GAMA fields) and UKIDSS (for the NGP field) were used to determine potential gravitationally lensed system via offsets between the radio counterparts and the NIR potential lenses. With the use of the InfraRed-to-Radio Correlation (IRRC) we identified the AGNs in the sample, selecting those sources whose measured radio fluxes were 5σ times brighter that estimated via SED fitting. From the sample of 112 sources with radio detections, 3% were found to be contaminants (nearby galaxies), 8% AGNs, 29% sources were classified as Star-Forming Galaxies (SFGs), 18% as potential lensed galaxies (LGs) and 7% as SLGs. 35% galaxies of the sample were found to have more than one radio source within the *Herschel* 250μm-beam and were therefore classified as potential galaxy groups or clusters. 25% of those were classified as proto-clusters due to the presence of over-densities of at least 3 radio sources and extended FIR emissions. This sample of proto-cluster candidates needs to be studied spectroscopically to confirm their origin and their redshifts. We cannot assure that there are no lensed sources in the groups and clusters, which might affect the statistics of fraction of lensed galaxies.

Focussing on the reddest sources of our TLS sample with $S_{500} > 100$ mJy, 8 sources were present in the sample from which 2 were contaminants. From the other six sources, 33% were found to be SLGs, 17% potential LGs, 33% over-densities (with 2-3 radio sources) and 17% SFGs with no hint of lensing. This implies an under presence of SLGs compared to Negrello et al. (2010) and Bussmann et al. (2013) who found almost 100% and 70%-80% fraction of gravitational lensing systems respectively in the SDP of H-ATLAS and HerMes. Although this result is somewhat uncertain due to the small sample and not very high-resolution of our radio observations.

IRRC: In Chapter 5 we present a study of the IRRC in different galaxy environments. With the use of the Jansky-VLA Legacy Survey of the Frontier Fields we obtained some of the deepest radio dual-band imaging (r.m.s.$\sim 0.6\ \mu$Jy/beam). This catalogue is formed by continuum maps at S- and C-band with resolutions 0.65 and 0.33 arcsec respectively. We crossed-match this catalogues with the catalogue of FIR sources in the HFF presented by Rawle et al. (2016) to create our final samples of Custer Members (CMs) and Galaxy-Cluster Lensed (GCLs) sources. In addition, a sample of isolated Field Galaxies (FGs) and Galaxy-Galaxy Lensed (GGLs) sources was created from the literature and from our TLS sample. Thus, the different samples are formed by 20 CMs, 127 FGs, 37 GCLs and 22 GGLs, covering a range of redshifts $0.011 < z < 3.675$.

Studying all the samples as a whole, no differences were found in the IRRC for the different galaxies. An evolution of the IR/radio ratios with redshifts was found for lensed galaxies ($q_{TIR} = (2.90 \pm 0.06)(1+z)^{-0.18\pm0.05}$), consistent with other studies of unlensed galaxies. This indicates an excess of radio emission at high redshifts, which can be due to stronger magnetic fields for these galaxies or AGNs dominating the radio emission at high redshifts and therefore contaminating our sample of intrinsic SFGs, or to the simple assumption of a mean spectral index $\alpha = 0.7$ taken from most of our galaxies. These lower q_{TIR} ratios at high redshifts might be due as well to the simple fact that the IRRC is not a one-to-one correlation and brighter galaxies in the correlation have lower IR/radio ratios. The selection-bias towards brighter galaxies at high redshifts could therefore be responsible for the evolution of the q_{TIR} with redshifts.

The IRRC for CMs and FGs were compared to study the presence of radio enhancement in intermediate-redshift galaxy clusters. This enhancement has been found in many different studies of nearby cluster galaxies, most likely due to the different physical processes that drive the evolution of galaxies in clusters, i.e. ram-pressure stripping and gravitational interactions. For our sample of CMs we indeed found tentative evidence of an excess of radio emission for cluster galaxies when comparing with FGs. Although because of the relatively large uncertainties, this result should not be taken as conclusive. An average value $q_{TIR} = 2.33 \pm 0.18$ for the CMs was found, slightly lower than the $q_{TIR} \simeq 2.68$ found for the COSMOS field at similar redshifts (Delhaize et al., 2017). Additionally, due to the big uncertainties at larger distances from the centre of the clusters, no clear correlation was found between the excess of radio emission and distance to the centre of the cluster.

A stacking analysis was done to confirm this excess of radio emission for the CMs. A sample of 111 radio detected sources with FIR undetected FIR counterparts were used to do the stacking. Indeed, an enhancement of radio emission was found in the environment of these clusters at intermediate-redshifts when comparing with field galaxies. Although, no correlation

was found between the FIR/radio ratios and the distance to the centre of the cluster. This is most likely due to the big uncertainties at large distances from the centre of the cluster. A bigger sample would be needed to carry on this study.

The IRRC for GGLs and GCLs sources were compared without finding any difference between them, indicating that the measured IR emission is not dominated by contamination coming from the foreground galaxies for either the cluster or the isolated galaxies.

Infrared and radio luminosities were derived and compared finding, in general, higher values for the derived SFR_{TIR}. For very evolved galaxies, as those in galaxy clusters, this might be due to an overestimation of the infrared luminosity due to old stellar population heating the dust. In addition, the post-starburst phase can yield to an overestimation of the SFR due to stars formed during this process remain dust-obscured. Another reason to obtain higher SFR_{TIR} is considering the same magnetic fields to calculate $SFR_{1.4GHz}$. There is no reason to believe that galaxies at different redshifts (and different brightness) present the same strength in their magnetic fields.

In conclusion, in this thesis we have studied the FIR and radio properties of high redshift DSFGs in three separate projects. DSFGs are a very important population of galaxies since they are some of the most actively star-forming and brightest galaxies in the universe. They provide a significant contribution to the star fomrmation rate density of the universe, and form the likely progenitors of the abundant early type galaxies in the local universe. By studying the star-formation properties of these galaxies, we can learn about the physical processes that drive galaxy evolution in the most extreme environments. The high star-formation in these kind of galaxies is traced both by their FIR and radio emission. In Chapter 3, we combined this information with molecular gas masses traced by CO (at the same time providing spectroscopic redshift) for two (lensed) high redshift DSFGs. We find the star fomatation efficiency (SFR/M_{gas}) is very high in these galaxies, meaning they will cosume their gas reservoir quickly (timescales ~ 30 Myr). After this time, these galaxies will become gas-poor and the star-forming will be quenched. For the galaxies in Chapter 4 and Chapter 5, we unfornutately do not have CO measurements available, but by comparing the FIR and 1.4GHz emission, we can still learn about the star-formation and the conditions within these galaxies. The IRRC is a tight relation that holds over 5 orders of magnitude that is followed by both lensed and non-lensed sources. However for cluster galaxies, our observations confirm there is an enhancement of the radio emission relative to the FIR, likely as a result of the interaction of the ICM with the ISM, which in turn cause compression of the ISM and an increase in the magnetic field strength. This work has also focussed on lensed galaxies. In particular we have identified a large number of likely candidates to be lensed galaxies. These lensed galaxies allow to study galaxies to fainter luminosities (both FIR and 1.4GHz) than would be possible without

lensing. These fainter galaxies are still found to follow the expected IRRC. In addition, this work has also considerable contributed towards obtaining a large sample of lensed galaxies at various redshifts (TLS), which will enable important cosmological studies.

6.2 Future Work

To further our study of the FIR and radio properties of high redshift DSFGs, we would need to fill in a few missing pieces of the puzzle and address some of our caveats. In particular, spectroscopic redshift for our sources as well as their molecular gas masses would be of paramount importance to study the depletion timescales and the relation between the Kennicutt-Schmidt law and the IRRC. For the lensed sources, we would also greatly benefit from higher resolution data to observe the arclets and spectroscopic redshifts for the foreground lens sources. ALMA observations would thus be ideal to achieve most of these science goals. Modelling of the lensing systems as well as the cosmographic studies planned for the TLS would be the longer term goals for this work. In the rest of this section we provide some more details of the immediate next steps to this work.

This thesis has presented a first classification of some H-ATLAS potential gravitationally lensed galaxies at $1.5 < z < 4.0$. Spectroscopic redshifts for both- the NIR and the *Herschel*-sources would be the next step to determine unambiguously the lensing systems. Continuum maps with sub-arcsecond resolution and multiple-J CO observations would allow to model the lensing system, and to study in more detail the ISM in high-redshift galaxies. With the use of ALMA the necessary sensitivity and resolution should be achieved for this study. For this purpose several proposal have been submitted at the time of this thesis (P.I. Serjeant and P.I. Oteo).

In addition, this thesis has presented a study of the IRRC in different environmental scenarios. Further work in this topic should be focussed in different aspects. First, a sample of SFGs with null AGN contamination would be desirable mostly at higher-redshifts. Complementary X-ray or optical spectroscopy for instance, would help us to identify AGNs, as has been successfully done in many studies with the use of Chandra and XMM-Newton for example. Second, a more detailed study of the radio spectrum would be necessary. We are assuming a simple power-law to define this part of the spectrum, with a mean spectral index value of $\alpha = 0.7$, which is a strong assumption. Different strength in the magnetic fields can yield different synchrotron emission strength and therefore the free-free emission could dominate the slope in this case, which can result in a bigger scatter in the correlation.

To study the physical processes driving evolution in galaxy cluster at intermediate-redshift through the IRRC, a much bigger sample and with a wider range of redshifts would be needed.

This would allow us to study if there is an enhancement of radio emission in high-redshift galaxy clusters and if this radio emission is related with the distance to the centre of the cluster.

References

Adebahr, B., Krause, M., Klein, U., et al. 2013, A&A, 555, A23

Adelman-McCarthy, J. K. & et al. 2009, VizieR Online Data Catalog, 2294

Amblard, A., Cooray, A., Serra, P., et al. 2010, A&A, 518, L9

Andersen, V. & Owen, F. N. 1995, AJ, 109, 1582

Ao, Y., Weiß, A., Downes, D., et al. 2008, A&A, 491, 747

Aravena, M., Spilker, J. S., Bethermin, M., et al. 2016, MNRAS, 457, 4406

Babyk, I., Melnyk, O., & Elyiv, A. 2012, Advances in Astronomy and Space Physics, 2, 56

Barger, A. J., Cowie, L. L., & Wang, W.-H. 2007, ApJ, 654, 764

Barlow, M. J. 1978, MNRAS, 183, 367

Barlow, M. J., Krause, O., Swinyard, B. M., et al. 2010, A&A, 518, L138

Barnes, J. E. & Hernquist, L. 1992, Nature, 360, 715

Basu, A. & Roy, S. 2013, MNRAS, 433, 1675

Batejat, F., Conway, J. E., Hurley, R., et al. 2011, ApJ, 740, 95

Bauer, A. E., Conselice, C. J., Pérez-González, P. G., et al. 2011, MNRAS, 417, 289

Becker, R. H., White, R. L., & Helfand, D. J. 1995, ApJ, 450, 559

Bernardi, M., Sheth, R. K., Nichol, R. C., Schneider, D. P., & Brinkmann, J. 2005, AJ, 129, 61

Bertin, E. & Arnouts, S. 1996, A&AS, 117, 393

Bertin, E., Mellier, Y., Radovich, M., et al. 2002, in Astronomical Society of the Pacific Conference Series, Vol. 281, Astronomical Data Analysis Software and Systems XI, ed. D. A. Bohlender, D. Durand, & T. H. Handley, 228

Best, P. N., Lehnert, M. D., Miley, G. K., & Röttgering, H. J. A. 2003, MNRAS, 343, 1

Blain, A. W. 1996, MNRAS, 283, 1340

Blain, A. W. 1999, MNRAS, 304, 669

Bolatto, A. D., Wolfire, M., & Leroy, A. K. 2013, ARA&A, 51, 207

Boselli, A. & Gavazzi, G. 2006, PASP, 118, 517

Bourne, N., Dunne, L., Ivison, R. J., et al. 2011, MNRAS, 410, 1155

Bourne, N., Maddox, S. J., Dunne, L., et al. 2012, MNRAS, 421, 3027

Bower, R. G., Lucey, J. R., & Ellis, R. S. 1992, MNRAS, 254, 601

Bravo-Alfaro, H., Cayatte, V., van Gorkom, J. H., & Balkowski, C. 2000, AJ, 119, 580

Bussmann, R. S., Pérez-Fournon, I., Amber, S., et al. 2013, ApJ, 779, 25

Butcher, H. & Oemler, Jr., A. 1978, ApJ, 219, 18

Camps, P., Misselt, K., Bianchi, S., et al. 2015, A&A, 580, A87

Carilli, C. L., Daddi, E., Riechers, D., et al. 2010, ApJ, 714, 1407

Carilli, C. L. & Walter, F. 2013, ARA&A, 51, 105

Carlstrom, J. E. & Kronberg, P. P. 1991, ApJ, 366, 422

Carniani, S., Maiolino, R., Pallottini, A., et al. 2017a, A&A, 605, A42

Carniani, S., Maiolino, R., Smit, R., & Amorín, R. 2017b, ArXiv e-prints

Casey, C. M., Berta, S., Béthermin, M., et al. 2012, ApJ, 761, 140

Casey, C. M., Narayanan, D., & Cooray, A. 2014, Physics Reports, 541, 45

Cerulo, P., Couch, W. J., Lidman, C., et al. 2017, MNRAS, 472, 254

Chapman, S. C., Blain, A. W., Ivison, R. J., & Smail, I. R. 2003, Nature, 422, 695

Chapman, S. C., Blain, A. W., Smail, I., & Ivison, R. J. 2005, ApJ, 622, 772

Chapman, S. C., Smail, I., Blain, A. W., & Ivison, R. J. 2004, ApJ, 614, 671

Chattopadhyay, T., Debsarma, S., Karmakar, P., & Davoust, E. 2015, New Astronomy, 34, 151

Clark, B. G. 1999, in Astronomical Society of the Pacific Conference Series, Vol. 180, Synthesis Imaging in Radio Astronomy II, ed. G. B. Taylor, C. L. Carilli, & R. A. Perley, 1

Clemens, M. S., Negrello, M., De Zotti, G., et al. 2013, MNRAS, 433, 695

Condon, J. J. 1992, ARA&A, 30, 575

Conley, A., Cooray, A., Vieira, J. D., et al. 2011, ApJ, 732, L35

Cooke, E. A., Hatch, N. A., Muldrew, S. I., Rigby, E. E., & Kurk, J. D. 2014, MNRAS, 440, 3262

Coppin, K. E. K., Chapman, S. C., Smail, I., et al. 2010, MNRAS, 407, L103

Cortese, L., Marcillac, D., Richard, J., et al. 2007, in IAU Symposium, Vol. 235, Galaxy Evolution across the Hubble Time, ed. F. Combes & J. Palouš, 198–198

Courtois, H. M., Pomarède, D., Tully, R. B., Hoffman, Y., & Courtois, D. 2013, AJ, 146, 69

Cox, P., Krips, M., Neri, R., et al. 2011, ApJ, 740, 63

Crook, A. C., Huchra, J. P., Martimbeau, N., et al. 2007, ApJ, 655, 790

Croton, D. J., Springel, V., White, S. D. M., et al. 2006, MNRAS, 365, 11

Crowl, H. H., Kenney, J. D. P., van Gorkom, J. H., & Vollmer, B. 2005, AJ, 130, 65

da Cunha, E., Groves, B., Walter, F., et al. 2013, ApJ, 766, 13

da Cunha, E., Walter, F., Smail, I. R., et al. 2015, ApJ, 806, 110

de Jong, J. T. A., Kuijken, K., Applegate, D., et al. 2013, The Messenger, 154, 44

de Jong, T., Klein, U., Wielebinski, R., & Wunderlich, E. 1985, A&A, 147, L6

De Lucia, G., Poggianti, B. M., Aragón-Salamanca, A., et al. 2004, ApJ, 610, L77

De Lucia, G., Poggianti, B. M., Aragón-Salamanca, A., et al. 2007, MNRAS, 374, 809

De Vis, P., Dunne, L., Maddox, S., et al. 2017a, MNRAS, 464, 4680

De Vis, P., Gomez, H. L., Schofield, S. P., et al. 2017b, MNRAS, 471, 1743

Delhaize, J., Meyer, M. J., Staveley-Smith, L., & Boyle, B. J. 2013, MNRAS, 433, 1398

Delhaize, J., Smolcic, V., Delvecchio, I., et al. 2017, ArXiv e-prints

Devlin, M. J., Ade, P. A. R., Aretxaga, I., et al. 2009, Nature, 458, 737

Dowell, C. D., Conley, A., Glenn, J., et al. 2014, ApJ, 780, 75

Downes, D. & Solomon, P. M. 1998, ApJ, 507, 615

Draine, B. T. 2003, ARA&A, 41, 241

Draine, B. T. & Salpeter, E. E. 1979, ApJ, 231, 77

Dressler, A. 1980a, ApJS, 42, 565

Dressler, A. 1980b, ApJ, 236, 351

Dressler, A., Oemler, Jr., A., Couch, W. J., et al. 1997, ApJ, 490, 577

Driver, S. P., Norberg, P., Baldry, I. K., et al. 2009, Astronomy and Geophysics, 50, 5.12

Driver, S. P., Wright, A. H., Andrews, S. K., et al. 2016, MNRAS, 455, 3911

Dunne, L., Eales, S., Edmunds, M., et al. 2000, MNRAS, 315, 115

Dunne, L., Eales, S., Ivison, R., Morgan, H., & Edmunds, M. 2003, Nature, 424, 285

Dunne, L. & Eales, S. A. 2001, MNRAS, 327, 697

Dunne, L., Gomez, H. L., da Cunha, E., et al. 2011, MNRAS, 417, 1510

Dye, S., Furlanetto, C., Dunne, L., et al. 2017, ArXiv e-prints

Eales, S., Dunne, L., Clements, D., et al. 2010, PASP, 122, 499

Ebeling, H., Stephenson, L. N., & Edge, A. C. 2014, ApJ, 781, L40

Edge, A., Sutherland, W., Kuijken, K., et al. 2013, The Messenger, 154, 32

Elbaz, D., Dickinson, M., Hwang, H. S., et al. 2011, A&A, 533, A119

Elbaz, D., Hwang, H. S., Magnelli, B., et al. 2010, A&A, 518, L29

Emonts, B. H. C., Feain, I., Mao, M. Y., et al. 2011, ApJ, 734, L25

Erben, T., Schirmer, M., Dietrich, J. P., et al. 2005, Astronomische Nachrichten, 326, 432

Fabello, S., Kauffmann, G., Catinella, B., et al. 2012, MNRAS, 427, 2841

Fall, S. M. & Efstathiou, G. 1980, MNRAS, 193, 189

Fasano, G., Poggianti, B. M., Couch, W. J., et al. 2000, ApJ, 542, 673

Fernandez-Conde, N., Lagache, G., Puget, J.-L., & Dole, H. 2010, A&A, 515, A48

Ferrarotti, A. S. & Gail, H.-P. 2006, A&A, 447, 553

Fixsen, D. J., Cheng, E. S., Gales, J. M., et al. 1996, ApJ, 473, 576

Fouqué, P., Solanes, J. M., Sanchis, T., & Balkowski, C. 2001, A&A, 375, 770

Frayer, D. T., Harris, A. I., Baker, A. J., et al. 2011, ApJ, 726, L22

Frayer, D. T., Ivison, R. J., Scoville, N. Z., et al. 1999, ApJ, 514, L13

Fudamoto, Y., Ivison, R. J., Oteo, I., et al. 2017, MNRAS, 472, 2028

Gall, C., Hjorth, J., Watson, D., et al. 2014, Nature, 511, 326

Gavazzi, G. & Boselli, A. 1999, A&A, 343, 86

Genzel, R., Tacconi, L. J., Lutz, D., et al. 2015, ApJ, 800, 20

Girardi, M., Biviano, A., Giuricin, G., Mardirossian, F., & Mezzetti, M. 1993, ApJ, 404, 38

Glazebrook, K. 2013, Publications of the Astronomical Society of Australia, 30, e056

Gomez, H. & Matsuura, M. 2012, Astronomy and Geophysics, 53, 6.19

González-Nuevo, J., Lapi, A., Fleuren, S., et al. 2012, ApJ, 749, 65

Gould, R. J. & Salpeter, E. E. 1963, ApJ, 138, 393

Greve, T. R., Bertoldi, F., Smail, I., et al. 2005, MNRAS, 359, 1165

Griffin, M. J., Abergel, A., Abreu, A., et al. 2010, A&A, 518, L3

Gunn, J. E. & Gott, III, J. R. 1972, ApJ, 176, 1

Harrington, K. C., Yun, M. S., Magnelli, B., et al. 2018, MNRAS, 474, 3866

Harris, A. I., Baker, A. J., Frayer, D. T., et al. 2012, ApJ, 752, 152

Hatch, N. A., De Breuck, C., Galametz, A., et al. 2011, MNRAS, 410, 1537

Hatch, N. A., Wylezalek, D., Kurk, J. D., et al. 2014, MNRAS, 445, 280

Hauser, M. G. & Dwek, E. 2001, ARA&A, 39, 249

Hayward, C. C., Lanz, L., Ashby, M. L. N., et al. 2014, MNRAS, 445, 1598

Helou, G. & Bicay, M. D. 1993, ApJ, 415, 93

Heywood, I., Jarvis, M. J., Baker, A. J., et al. 2016, MNRAS, 460, 4433

Hezaveh, Y. D., Marrone, D. P., & Holder, G. P. 2012, ApJ, 761, 20

Högbom, J. A. 1974, A&AS, 15, 417

Holland, W. S., Bintley, D., Chapin, E. L., et al. 2013, MNRAS, 430, 2513

Holland, W. S., Robson, E. I., Gear, W. K., et al. 1999, MNRAS, 303, 659

Huynh, M. T., Emonts, B. H. C., Kimball, A. E., et al. 2017, MNRAS, 467, 1222

Ivison, R. J., Greve, T. R., Dunlop, J. S., et al. 2007, MNRAS, 380, 199

Ivison, R. J., Magnelli, B., Ibar, E., et al. 2010, A&A, 518, L31

Ivison, R. J., Smail, I., Barger, A. J., et al. 2000, MNRAS, 315, 209

James, A., Dunne, L., Eales, S., & Edmunds, M. G. 2002, MNRAS, 335, 753

Jarvis, M. J., Smith, D. J. B., Bonfield, D. G., et al. 2010, MNRAS, 409, 92

Johnson, H. L., Harrison, C. M., Swinbank, A. M., et al. 2016, MNRAS, 460, 1059

Johnson, T. L., Sharon, K., Bayliss, M. B., et al. 2014, ApJ, 797, 48

Jones, A. P. 2004, in Astronomical Society of the Pacific Conference Series, Vol. 309, Astrophysics of Dust, ed. A. N. Witt, G. C. Clayton, & B. T. Draine, 347

Jones, A. P. & Nuth, J. A. 2011, A&A, 530, A44

Jones, A. P., Tielens, A. G. G. M., & Hollenbach, D. J. 1996, ApJ, 469, 740

Jones, A. P., Tielens, A. G. G. M., Hollenbach, D. J., & McKee, C. F. 1994, ApJ, 433, 797

Karachentseva, V. E., Mitronova, S. N., Melnyk, O. V., & Karachentsev, I. D. 2010, Astrophysical Bulletin, 65, 1

Kemp, S. N., de la Fuente, E., Franco-Balderas, A., & Meaburn, J. 2005, ApJ, 624, 680

Kennicutt, R. C. & Evans, N. J. 2012, ARA&A, 50, 531

Kennicutt, Jr., R. C. 1998, ARA&A, 36, 189

Kessler, M. F., Steinz, J. A., Anderegg, M. E., et al. 1996, A&A, 315, L27

Kilbinger, M. 2015, Reports on Progress in Physics, 78, 086901

Kim, S.-H., Martin, P. G., & Hendry, P. D. 1994, ApJ, 422, 164

Klein, U., Wielebinski, R., & Morsi, H. W. 1988, A&A, 190, 41

Krips, M., Neri, R., Eckart, A., et al. 2007, in Astronomical Society of the Pacific Conference Series, Vol. 375, From Z-Machines to ALMA: (Sub)Millimeter Spectroscopy of Galaxies, ed. A. J. Baker, J. Glenn, A. I. Harris, J. G. Mangum, & M. S. Yun, 250

Lacki, B. C., Thompson, T. A., & Quataert, E. 2010, ApJ, 717, 1

Lake, G., Katz, N., & Moore, B. 1998, ApJ, 495, 152

Lapi, A., González-Nuevo, J., Fan, L., et al. 2011, ApJ, 742, 24

Laporte, C. F. P. & White, S. D. M. 2015, MNRAS, 451, 1177

Lawrence, A., Warren, S. J., Almaini, O., et al. 2007, MNRAS, 379, 1599

Le Fevre, O., Deltorn, J. M., Crampton, D., & Dickinson, M. 1996, ApJ, 471, L11

Lee, B. C., Allam, S. S., Tucker, D. L., et al. 2004, AJ, 127, 1811

Lehnert, M. D., Nesvadba, N. P. H., Cuby, J.-G., et al. 2010, Nature, 467, 940

Liddle, A. 2003, An Introduction to Modern Cosmology, Second Edition, 188

Lilly, S. J., Eales, S. A., Gear, W. K. P., et al. 1999, ApJ, 518, 641

Lonsdale, C. J., Persson, S. E., & Matthews, K. 1984, ApJ, 287, 95

Maddox, S. J., Valiante, E., Cigan, P., et al. 2018, ApJS, 236, 30

Magnelli, B., Ivison, R. J., Lutz, D., et al. 2015, A&A, 573, A45

Magnelli, B., Lutz, D., Santini, P., et al. 2012, A&A, 539, A155

Makarov, D. & Karachentsev, I. 2011, MNRAS, 412, 2498

Man, A. W. S., Greve, T. R., Toft, S., et al. 2016, ApJ, 820, 11

Martin, C. & GALEX Team. 2005, in IAU Symposium, Vol. 216, Maps of the Cosmos, ed. M. Colless, L. Staveley-Smith, & R. A. Stathakis, 221

Mauch, T. & Sadler, E. M. 2007, MNRAS, 375, 931

McMullin, J. P., Waters, B., Schiebel, D., Young, W., & Golap, K. 2007, in Astronomical Society of the Pacific Conference Series, Vol. 376, Astronomical Data Analysis Software and Systems XVI, ed. R. A. Shaw, F. Hill, & D. J. Bell, 127

Medezinski, E., Umetsu, K., Nonino, M., et al. 2013, ApJ, 777, 43

Meylan, G., Jetzer, P., North, P., et al., eds. 2006, Gravitational Lensing: Strong, Weak and Micro

Mihos, J. C. & Hernquist, L. 1994, ApJ, 431, L9

Miller, N. A. & Owen, F. N. 2001, AJ, 121, 1903

Mohan, N. & Rafferty, D. 2015, PyBDSF: Python Blob Detection and Source Finder, Astrophysics Source Code Library

Morić, I., Smolčić, V., Kimball, A., et al. 2010, ApJ, 724, 779

Moss, C. & Whittle, M. 1993, ApJ, 407, L17

Muldrew, S. I., Hatch, N. A., & Cooke, E. A. 2015, MNRAS, 452, 2528

Murphy, E. J. 2009, ApJ, 706, 482

Murphy, E. J., Condon, J. J., Schinnerer, E., et al. 2011, ApJ, 737, 67

Murphy, E. J., Kenney, J. D. P., Helou, G., Chung, A., & Howell, J. H. 2009, ApJ, 694, 1435

Nayyeri, H., Cooray, A., Jullo, E., et al. 2017, ApJ, 844, 82

Negrello, M., Amber, S., Amvrosiadis, A., et al. 2017, MNRAS, 465, 3558

Negrello, M., Hopwood, R., De Zotti, G., et al. 2010, Science, 330, 800

Negrello, M., Perrotta, F., González-Nuevo, J., et al. 2007, MNRAS, 377, 1557

Neugebauer, G., Habing, H. J., van Duinen, R., et al. 1984, ApJ, 278, L1

Nidever, D. L., Ashley, T., Slater, C. T., et al. 2013, ApJ, 779, L15

Niklas, S. & Beck, R. 1997, A&A, 320, 54

Niklas, S., Klein, U., & Wielebinski, R. 1995, A&A, 293, 56

Oesch, P. A., Brammer, G., van Dokkum, P. G., et al. 2016, ApJ, 819, 129

Offringa, A. R., van de Gronde, J. J., & Roerdink, J. B. T. M. 2012, A&A, 539

Oliver, S. J., Bock, J., Altieri, B., et al. 2012, MNRAS, 424, 1614

Omar, A. & Dwarakanath, K. S. 2005, Journal of Astrophysics and Astronomy, 26, 89

Oteo, I., Ivison, R. J., Dunne, L., et al. 2018, ApJ, 856, 72

Oteo, I., Ivison, R. J., Negrello, M., et al. 2017, ArXiv e-prints

Pearson, E. A., Eales, S., Dunne, L., et al. 2013, MNRAS, 435, 2753

Pentericci, L., Kurk, J. D., Röttgering, H. J. A., et al. 2000, A&A, 361, L25

Perley, R. A. & Butler, B. J. 2013, ApJS, 204, 19

Pilbratt, G. L., Riedinger, J. R., Passvogel, T., et al. 2010, A&A, 518, L1

Poglitsch, A., Waelkens, C., Geis, N., et al. 2010, A&A, 518, L2

Pope, A., Bussmann, R. S., Dey, A., et al. 2008, ApJ, 689, 127

Postman, M., Franx, M., Cross, N. J. G., et al. 2005, ApJ, 623, 721

Rahvar, S. 2015, International Journal of Modern Physics D, 24, 1530020

Ramella, M., Biviano, A., Boschin, W., et al. 2000, A&A, 360, 861

Ramos Almeida, C., Bessiere, P. S., Tadhunter, C. N., et al. 2013, MNRAS, 436, 997

Randriamampandry, S. M., Crawford, S. M., Cress, C. M., et al. 2015, MNRAS, 447, 168

Rasmussen, J., Ponman, T. J., & Mulchaey, J. S. 2006, MNRAS, 370, 453

Rawle, T. D., Altieri, B., Egami, E., et al. 2016, MNRAS, 459, 1626

Reddy, N. A. & Yun, M. S. 2004, ApJ, 600, 695

Rengarajan, T. N., Karnik, A. D., & Iyengar, K. V. K. 1997, MNRAS, 290, 1

Riechers, D. A., Bradford, C. M., Clements, D. L., et al. 2013, Nature, 496, 329

Riechers, D. A., Capak, P. L., Carilli, C. L., et al. 2010, ApJ, 720, L131

Rieke, G. H., Alonso-Herrero, A., Weiner, B. J., et al. 2009, ApJ, 692, 556

Rudnick, G., von der Linden, A., Pelló, R., et al. 2009, ApJ, 700, 1559

Sanders, D. B., Mazzarella, J. M., Kim, D.-C., Surace, J. A., & Soifer, B. T. 2003, AJ, 126, 1607

Sargent, M. T., Schinnerer, E., Murphy, E., et al. 2010, ApJS, 186, 341

Sault, R. J., Teuben, P. J., & Wright, M. C. H. 1995, in Astronomical Society of the Pacific Conference Series, Vol. 77, Astronomical Data Analysis Software and Systems IV, ed. R. A. Shaw, H. E. Payne, & J. J. E. Hayes, 433

Schinnerer, E., Carilli, C. L., Capak, P., et al. 2008, ApJ, 689, L5

Schirmer, M. 2013, ApJS, 209, 21

Schleicher, D. R. G. & Beck, R. 2013, A&A, 556, A142

Schober, J., Schleicher, D. R. G., & Klessen, R. S. 2016, ApJ, 827, 109

Short, J., Pearson, E., Coles, P., & Eales, S. 2012, ArXiv e-prints

Siebenmorgen, R. & Krügel, E. 2007, A&A, 461, 445

Siringo, G., Kreysa, E., Kovács, A., et al. 2009, A&A, 497, 945

Skrutskie, M. F., Cutri, R. M., Stiening, R., et al. 2006, AJ, 131, 1163

Smail, I., Ivison, R. J., & Blain, A. W. 1997, ApJ, 490, L5

Smith, D. J. B., Dunne, L., Maddox, S. J., et al. 2011, MNRAS, 416, 857

Smith, D. J. B., Hardcastle, M. J., Jarvis, M. J., et al. 2013, MNRAS, 436, 2435

Smith, L., Lucas, P. W., Burningham, B., et al. 2014, MNRAS, 437, 3603

Smith, M. W. L., Ibar, E., Maddox, S. J., et al. 2017, ApJS, 233, 26

Smolčić, V., Delvecchio, I., Zamorani, G., et al. 2017a, A&A, 602, A2

Smolčić, V., Karim, A., Miettinen, O., et al. 2015, A&A, 576, A127

Smolčić, V., Novak, M., Bondi, M., et al. 2017b, A&A, 602, A1

Soifer, B. T., Neugebauer, G., Helou, G., et al. 1984, ApJ, 283, L1

Solomon, P. M. & Sage, L. J. 1988, ApJ, 334, 613

Solomon, P. M. & Vanden Bout, P. A. 2005, ARA&A, 43, 677

Springel, V., Di Matteo, T., & Hernquist, L. 2005, MNRAS, 361, 776

Stach, S. M., Swinbank, A. M., Smail, I., et al. 2017, ApJ, 849, 154

Sutherland, W., Emerson, J., Dalton, G., et al. 2015, A&A, 575, A25

Swinbank, A. M., Chapman, S. C., Smail, I., et al. 2006, MNRAS, 371, 465

Swinbank, A. M., Webb, T. M., Richard, J., et al. 2009, MNRAS, 400, 1121

Tacconi, L. J., Genzel, R., Smail, I., et al. 2008, ApJ, 680, 246

Tody, D. 1986, in Proceedings of the SPIE, Vol. 627, Instrumentation in astronomy VI, ed. D. L. Crawford, 733

Tody, D. 1993, in Astronomical Society of the Pacific Conference Series, Vol. 52, Astronomical Data Analysis Software and Systems II, ed. R. J. Hanisch, R. J. V. Brissenden, & J. Barnes, 173

Treu, T. 2010, ARA&A, 48, 87

Tully, R. B. 1987, ApJ, 321, 280

Umetsu, K., Medezinski, E., Nonino, M., et al. 2014, ApJ, 795, 163

Valiante, E., Lutz, D., Sturm, E., et al. 2007, ApJ, 660, 1060

Valiante, E., Smith, M. W. L., Eales, S., et al. 2016, MNRAS, 462, 3146

Veilleux, S., Kim, D.-C., & Sanders, D. B. 2002, ApJS, 143, 315

Venemans, B. P., Walter, F., Decarli, R., et al. 2017, ApJ, 851, L8

Véron-Cetty, M.-P. & Véron, P. 2010, A&A, 518, A10

Voelk, H. J. 1989, A&A, 218, 67

Wall, J. V., Pope, A., & Scott, D. 2008, MNRAS, 383, 435

Walsh, D., Carswell, R. F., & Weymann, R. J. 1979, Nature, 279, 381

Wardlow, J. L., Cooray, A., De Bernardis, F., et al. 2013, ApJ, 762, 59

Weiß, A., De Breuck, C., Vieira, J. D., et al. 2013, in Astronomical Society of the Pacific Conference Series, Vol. 476, New Trends in Radio Astronomy in the ALMA Era: The 30th Anniversary of Nobeyama Radio Observatory, ed. R. Kawabe, N. Kuno, & S. Yamamoto, 33

Weiß, A., Downes, D., Walter, F., & Henkel, C. 2005, A&A, 440, L45

Weiß, A., Ivison, R. J., Downes, D., et al. 2009a, ApJ, 705, L45

Weiß, A., Kovács, A., Coppin, K., et al. 2009b, ApJ, 707, 1201

Wen, Z. L., Han, J. L., & Liu, F. S. 2009, ApJS, 183, 197

Werner, M. W., Roellig, T. L., Low, F. J., et al. 2004, ApJS, 154, 1

Wirth, G. D., Koo, D. C., & Kron, R. G. 1994, ApJ, 435, L105

Wright, E. L., Eisenhardt, P. R. M., Mainzer, A. K., et al. 2010, AJ, 140, 1868

Wunderlich, E., Wielebinski, R., & Klein, U. 1987, A&AS, 69, 487

Xu, C. & Sulentic, J. W. 1991, ApJ, 374, 407

Yamamoto, T. & Hasegawa, H. 1977, Progress of Theoretical Physics, 58, 816

Yang, C., Omont, A., Beelen, A., et al. 2017, A&A, 608, A144

Yun, M. S., Reddy, N. A., & Condon, J. J. 2001, ApJ, 554, 803

Zhang, Q.-J., Cheng, L.-M., & Wu, Y.-L. 2009, ApJ, 694, 1402

Zhao, G.-B., Li, B., & Koyama, K. 2011, Physical Review Letters, 107, 071303